JANUARY 1960 VOLUME 6 (1960) No. 2

GREGG M. SINCLAIR LIBRARY
UNIVERSITY OF HAWAII
8-7-63

NUCLEAR INSTRUMENTS & METHODS

A JOURNAL ON ACCELERATORS, INSTRUMENTATION AND TECHNIQUES IN NUCLEAR PHYSICS

EDITOR: K. SIEGBAHN - UPPSALA

CONTENTS

B. L. COHEN, H. G. BLOSSER, E. D. HUDSON, R. S. LORD and R. S. BENDER, The Oak Ridge relativistic isochronous cyclotron, Part II. Magnetic field design for the isochronous cyclotron 105
PIERRE GRIVET et ALBERT SEPTIER, Les lentilles quadrupolaires magnétiques (I) 126
R. H. RITCHIE, J. S. CHEKA and R. D. BIRKHOFF, The spherical condenser as a high transmission particle spectrometer. I. Point source 157
A. W. PRYOR, The input stage of a transistor pulse amplifier 164
HANNO BRÜCKMANN, Ein Modulator für das Synchrozyklotron Bonn mit ferroelektrischer Keramik 169
A. E. LITHERLAND and D. A. BROMLEY, A two-dimensional pulse-height analyser 176
W. M. LAYSON, J. MALOS and D. D. MILLAR, Angular selectivity of a geiger telescope arrangement for cosmic ray air showers 179
P. SZABÓ, On the effect of total reflection on the optimum dimensions of collimators for neutron crystal spectrometers and diffractometers 183
J. B. GARG, A fast coincidence unit of variable resolving time 187
C. CERNIGOI, I. GABRIELLI and G. IERNETTI, Behaviour of photomultipliers against high-frequency modulated light 192

(continued on p. 3 of cover)

NORTH-HOLLAND PUBLISHING COMPANY - AMSTERDAM

NUCLEAR INSTRUMENTS AND METHODS

A journal on accelerators, instrumentation and techniques in nuclear physics

EDITOR: K. SIEGBAHN, UPPSALA

EDITORIAL BOARD:

J. B. ADAMS (CERN)
F. A. ALSINA (Buenos Aires)
E. AMALDI (Rome)
H. L. ANDERSON (Chicago)
K. T. BAINBRIDGE (Cambridge, Mass.)
C. J. BAKKER (CERN)
P. R. BELL (Oak Ridge)
R. E. BELL (Montreal)
A. BERTHELOT (Saclay)
H. BRINKMAN (Groningen)
E. H. COOKE-YARBOROUGH (Harwell)
S. DE BENEDETTI (Pittsburgh)
M. DE HEMPTINNE (Louvain)
A. DE-SHALIT (Rehovoth)
M. DEUTSCH (Cambridge, Mass.)
S. DU TOIT (Pretoria)
B. S. DŽELEPOV (Leningrad)
W. GENTNER (Heidelberg)
P. C. GUGELOT (Amsterdam)
H. HALBAN (Paris)
O. HAXEL (Heidelberg)
P. HUBER (Basel)
D. J. HUGHES (Brookhaven)
S. KIKUCHI (Tokyo)
J. KOCH (Copenhagen)
M. S. KOZODAEV (Moscow)
S. LIVINGSTON (Cambridge, Mass.)
E. M. MCMILLAN (Berkeley)
M. G. MEŠČERJAKOV (Moscow)
P. B. MOON (Birmingham)
M. L. OLIPHANT (Canberra)
W. PAUL (Bonn)
A. S. RAO (Bombay)
G. SALVANI (Rome)
P. SAVIĆ (Belgrade)
P. SCHERRER (Zürich)
CH. SCHMELZER (CERN)
H. W. B. SKINNER (Liverpool)
R. TANGEN (Oslo)
D. TAYLOR (Northampton)
V. I. VEKSLER (Moscow)
G. VON DARDEL (CERN)
O. WERNHOLM (Stockholm)
R. R. WILSON (Cornell)
S. D. WINTER (Saclay)

INSTRUCTIONS FOR CONTRIBUTORS

Contributions may be sent to the Editor, Professor K. Siegbahn, Institute of Physics, University of Uppsala, Sweden, either directly or through the intermediation of one of the members of the Editorial Board. Contributions may be written in English, French or German but should always, except for very short papers, be supplied with a brief abstract in English. Figures should be in inked original drawings or glossy prints and they should be sufficiently large. Contributors should make sure that important details in drawings and photographs will show up clearly in the diminished copy used by the publisher.

Books for review should be sent to Professor Siegbahn.

Objective and descriptive material on endeavours and product developments from the industry for the section "Spotlight on Industry" should be sent directly to the publishers, North-Holland Publishing Company, P.O. Box 103, Amsterdam.

Nuclear Instruments and Methods is published monthly. The subscription price of a volume of 360 pages is $ 17.00 (130 s), postage free.

Subscriptions should be sent to the publishers, North-Holland Publishing Company, P.O. Box 103, Amsterdam or to any subscription-agent.

No part of this issue may be reproduced in any form, by print, photoprint, microfilm or any other means without written permission from the publisher. Reprints, photoprints or microfilms are obtainable at cost from the publisher.

PHILIPS

equipment for Nuclear Physics and Atomic Energy

- Synchro-cyclotrons for various final energies.
- Cockcroft-Walton accelerators.
- Generators for very high d.c. voltages.
- Linear electron accelerators.
- Reactor control instrumentation
- Radiation measuring and detection equipment.
- Civil defence instruments.
- Area monitoring instrumentation.
- Geiger counter tubes.
- Photomultipliers.
- Radio-active isotopes.
- Air & gas liquefiers.
- Vacuum measuring equipment.

This panel permits the continuous programmed measurement and recording of the fast neutron and Gamma radiation levels at 8 different points in the building of the 150 MeV synchro-cyclotron of the "Laboratoire de Physique Nucléaire" in Orsay, France. It provides for "warning" or "alarm" signals, the latter with provision to switch off the cyclotron at a preset level of intensity.
Similar systems designed to your specific requirements can be supplied.

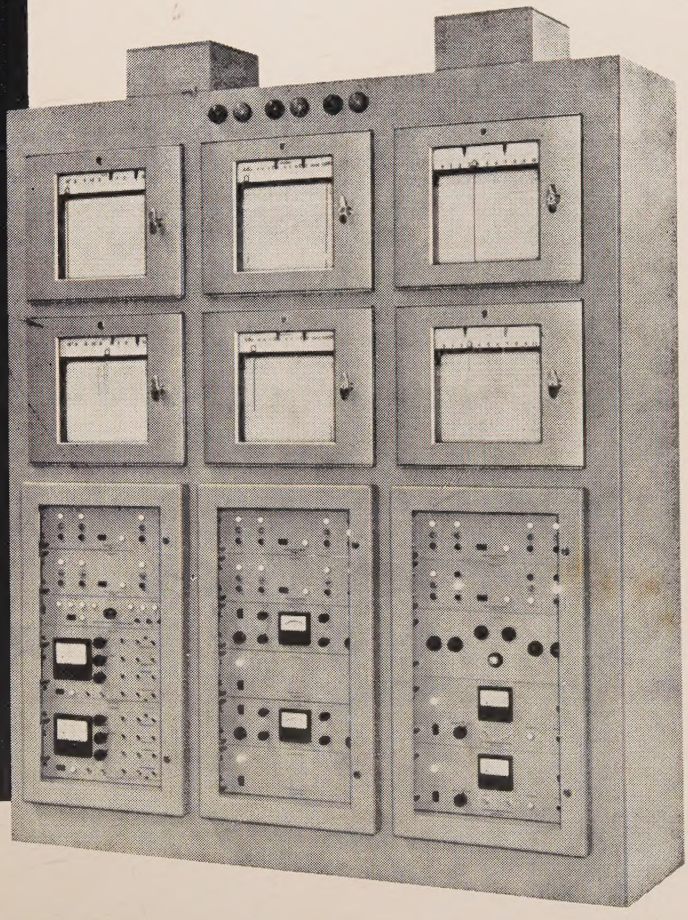

NDO

PHILIPS
Nuclear Equipment

PHILIPS

For further information please apply to one of the following addresses:

N.V. PHILIPS' GLOEILAMPENFABRIEKEN, Scientific Equipment Department, Eindhoven-Holland
RESEARCH & CONTROL INSTRUMENTS LTD., Instrument House, 207/215, King's Cross Road, London WC1
PHILIPS ELECTRONICS INC., Instruments Division, 750, South Fulton Avenue, Mount Vernon N.Y. U.S.A.

E-H

MILLIMICROSECOND PULSE GENERATOR

Ultra fast rise time (2.5 millimicroseconds) and high frequency for advanced solid state, computer and research applications

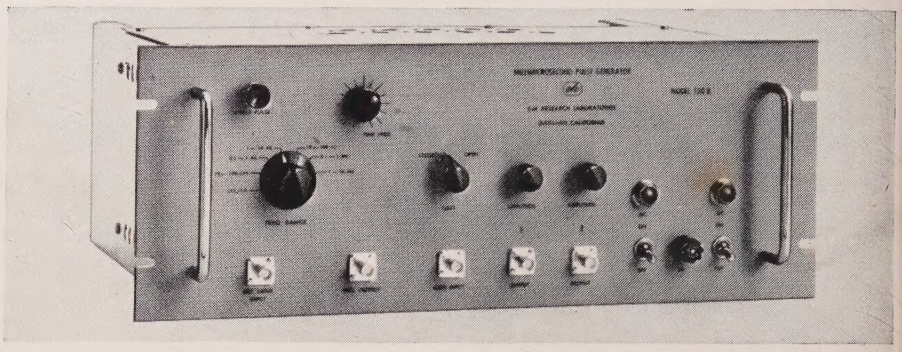

MODEL 120B F.O.B. OAKLAND, CALIF. $1275

The 120B offers unique performance advantages over mercury and competing electronic generators. The 2.5 millimicrosecond rise time feature is ahead of the field and offers a new tool for fast, high resolution work. Two independently variable outputs add to its flexibility, as does the wide range of frequencies provided (10 cps to 10 Megacycles). Available also are an advanced scope triggering pulse and a fast, flexible gating input for complex pulse-time and pulse-amplitude selection.

SPECIFICATIONS

RISE TIME (10% to 90%)
Less than 2.5 millimicroseconds

PULSE WIDTH
2.5 to 25 millimicroseconds

REPETITION RATE (External or Internal)
10 cps to 10 Mc

OUTPUTS
(Two Independent Output Channels)
Amplitude, 0 to −8 volts (also 0 to +8)
Impedance, 93 ohms

TRIGGER OUTPUT
Positive 15 volt pulse

CONNECTORS
All BNC type

TRIGGER ADVANCE
120 millimicroseconds

EXTERNAL DRIVE
Delay, 50 millimicroseconds
Amplitude Required, 3 volts rms

ELECTRONIC GATE
Gating Time, less than 100 millimicroseconds
Amplitude Required, positive 20 volts

E-H

ELECTROMETER AMPLIFIER

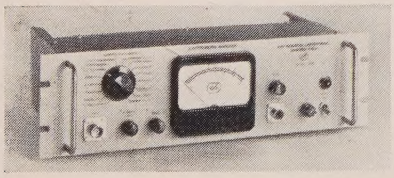

Model 201C f.o.b. Oakland, Calif. $650

The 201C makes *both* DC and AC measurements to 10^{-15} ampere in the low current region. Excellent DC stability, fast response, low noise and high sensitivity make it an outstanding instrument. 16 ranges, 10^{-6} to 3 x 10^{-15} ampere, and response to 40 microseconds give it exceptional flexibility.

E-H

MULTICHANNEL COINCIDENCE UNIT

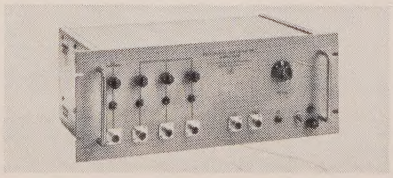

Model 101N f.o.b. Oakland, Calif. $725

Functions as a pulse coincidence-anticoincidence analyzer over 4 channels with resolution of 3 millimicroseconds. Generates two output pulses – a microsecond trigger pulse, and a prompt pulse. Photomultiplier tubes may be tied directly to inputs. Provides exceptional reliability over wide range of input shapes and amplitudes.

E-H

ELECTROMETER MULTIMETER

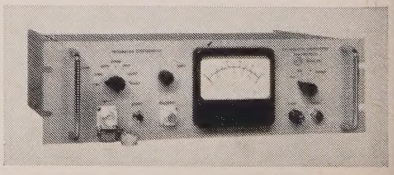

Model No. 215

Excellent stability 30μv/volt line change; high input impedance $10^{15}\Omega$; good sensitivity 200μv; large band pass 5 Kc. Uses – via external R, C, or E: millivoltmeter, 10 mv to 10 v scales, fast response; ammeter, $< 10^{-14}$ amps; ohmmeter, $>10^{16}$ ohms; current integrator, $< 10^{-13}$ coulomb.

E-H instruments are designed to meet the critical requirements of advanced work. Thanks to superior engineering and the finest components, these instruments have a remarkable record for stable performance.

Write or wire E-H for additional information

E-H **E-H RESEARCH LABORATORIES, INC.**
1922 PARK BLVD. • GLENCOURT 2-1314 • OAKLAND 6, CALIFORNIA

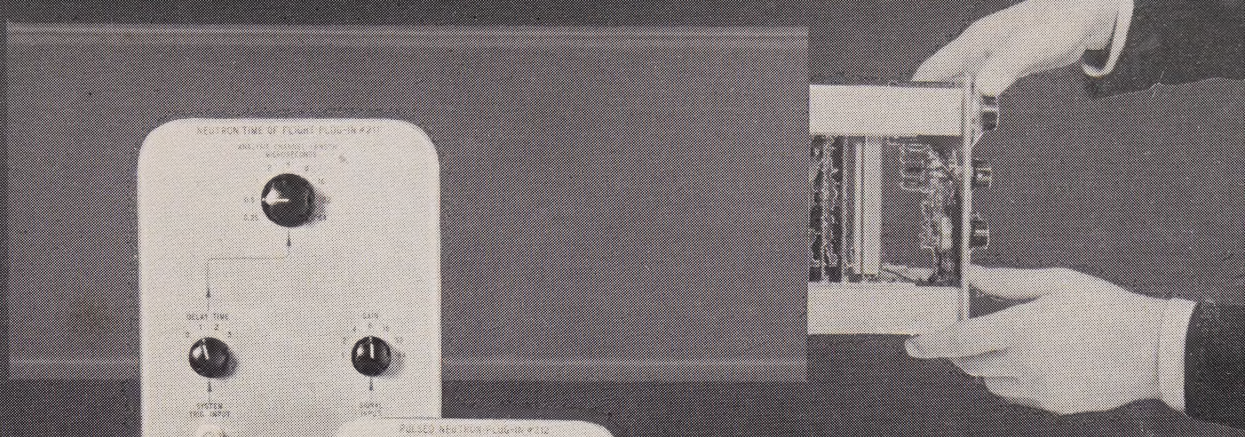

time-of-flight plug-in

pulsed neutron plug-in

PLUG-IN LOGIC

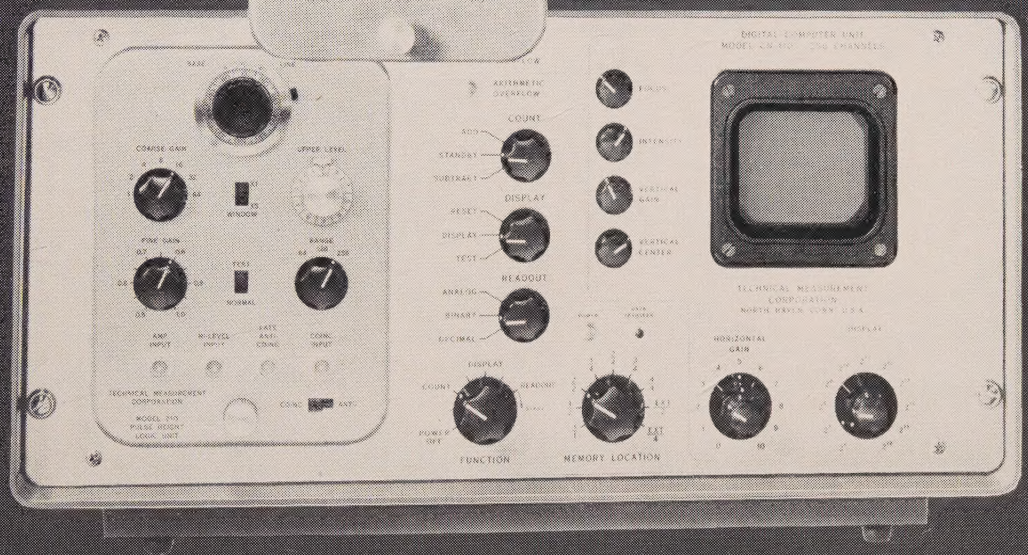

Logic is interchangeable in the TMC Model CN-110 Pulse Analyzer. Into the all-transistor, 30-pound, 256-channel digital computer you can plug Pulse Height Analysis, Pulsed Neutron, Time-of-Flight or special program units. Out of it you can get Analog, Digital or Binary data. You can carry the system and set it up almost anywhere. It is guaranteed for two years.

These instruments and all accessory units are now being delivered. Complete details of design, construction and operation are contained in a new 6-page folder available on request.

220 data handling unit

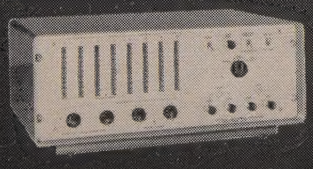

• We have excellent openings for Transistor Circuit Designers •

TMC

TECHNICAL MEASUREMENT CORPORATION

441 WASHINGTON AVENUE, NORTH HAVEN, CONN.

WHAT'S NEW in applied nuclear physics. Well for one thing, we are,

atomium CORPORATION

Many of you in the field have already received corporate and technical announcements from us. We are in the business of designing and constructing systems of high technical content and are actively working in the fields of Low Level Detection, Automatic Nuclear Systems, and Special Medical Instrumentation. ATOMIUM brings together from research laboratories a group of nuclear physicists and instrumentation designers who average more than a decade of experience in experimental nuclear physics and instrument fields. Our specific activities concern the complete engineering of complex nuclear systems.

WHAT ELSE IS NEW . . . Whole Body Counting has been a field of advanced research at a few major laboratories here and abroad. The term "whole body counting" means the detection and measurement of gamma radiation from the whole human body as a single extended source. The radioactivity may have been taken up intentionally as in tracer medicine, or it may consist only of the naturally occurring gamma emitting isotopes found in the human body. For the latter studies a very special low level or controlled background facility ("COBAFAC") is required because the natural radioactivity in standard materials (most shielding materials included) contains the same orders of magnitude of radioactivity as does the normal human. So the general problem requires the subtlest of techniques in all aspects.

The history of the low level whole body counting field begins, as is usually the case in "new" fields, with experiments more than two decades ago when the problem of radium poisoning (in brush-licking dial painters) was brilliantly diagnosed by Harrison Martland, New Jersey Medical Examiner. Applying the available nuclear physics techniques, R. D. Evans made the first geiger counter measurements of radium ingested in humans. These determinations established general techniques (the "one-meter arc measurement", the "closed-background", etc.) and laid the foundations of today's tolerance levels.

About ten years ago, Sievert of Sweden and later Burch and Spiers of England constructed large volume, high pressure gas detectors for the determination of low level gamma radiation in the human body. The program for radium and thorium measurement led workers at Argonne National Laboratory, Div. Radiol. Phys., to the use of scintillation crystals of several inches diameter and specially constructed shielded

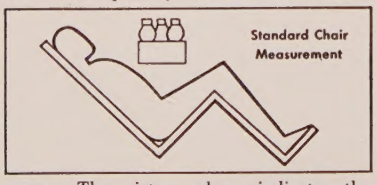

rooms. The picture above indicates the "standard chair" position and crystal. This measurement is made with a large NaI crystal coupled to one or more photomultipliers. During the early 1950's, Los Alamos physicists had developed large volume liquid scintillation counters for their elegant experiments detecting the presence of the neutrino. Subsequently, experimenters modified these highly efficient systems to measure radium burden in dogs (the "K-9 counter") and then natural potassium-40 in normal humans. This sketch illustrates the early form of this liquid scintillation detector. A trough is used to insert the subject

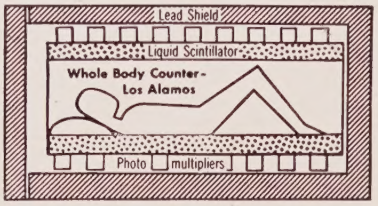

and the liquid scintillator solution is viewed by about 100 photomultipliers. A later version, the Geneva Counter, is a walk-in counter using relatively few 16"D photomultipliers to achieve a moderate energy resolution.

Advances in the technology of large crystals, photomultipliers and multi-channel analyzers have quickened interest so that there are between fifteen and twenty low level facilities operating or under construction.

The requirements of the systems and the state of the art may be summarized. First, of the many possible shielding materials (sugar, wood, water, etc. have been seriously considered) the standard material in use today is iron suitably treated to reduce surface contamination. A significant reduction in the low energy contribution to background is made by the addition of a lining of a few millimeters of lead. Second, the detector should have as high efficiency as possible. The 4π liquid scintillation tank has high geometric efficiency, is insensitive to source distribution, and uses a relatively compact shield. Another efficient system is an assembly of large plastic scintillators shown in this sketch.

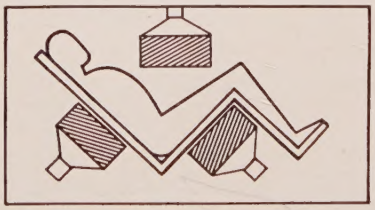

If rapid assays of gross gamma emitters are required, such high efficiency systems (liquid or plastic are the most economical in large sizes) are indicated. Some degree of energy resolution may be obtained with these detectors but they are primarily useful for broad band discrimination. This

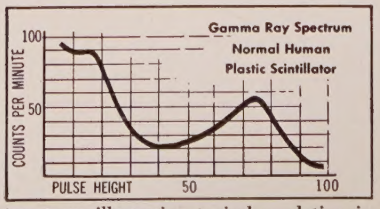

spectrum illustrating typical resolution in liquid or plastic detectors is an early one and thus does not markedly indicate Cs^{137} although the potassium-40 peak is easily distinguished.

atomium CORPORATION

LOW LEVEL GAMMA RAY DETECTION

The single large NaI crystal detector has high stopping power (or "intrinsic efficiency") but is about 40 times less sensitive because of its small solid angle. However, the differential background for any particular gamma ray is low enough that counting times are not prohibitively long. The low geometric efficiency arises from the distance-versus-uncertainty condition requiring use of reproducible geometry ("one-meter arc", "standard chair", etc.) and a shielded room. Similarly in thyroid uptake measurements a distant determination is usually required to minimize sensitivity variations due to uncertainty in the location of the thyroid.

If identification of isotopes is desired, the advantage of the good resolution of the NaI crystal may offset longer counting times. This plot indicates the usefulness of

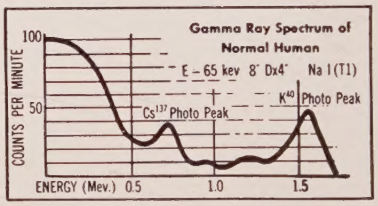

large NaI crystals in energy measurements in vivo. The Cs^{137} peak present in all living subjects has been growing steadily during this decade. Many other spectra of isotopes in vivo have been obtained by the Argonne group experimentalists. Also, the positional sensitivity of the lower efficiency techniques may be useful if localization of the activity is desired. Thus a single large crystal can be used for standard whole body determinations and also positioned or automatically scanned for distribution studies.

Finally, the electronics required for these installations may be as simple as an integral counting scaling system (or at most, several single channel analyzers) for the plastic and liquid scintillators, or as complex as a large multichannel installation for the analysis of isotopes.

Many factors influence the choice of systems. For example, the problems associated with the handling of the inflammable liquid scintillators must be weighed against increased electronic costs of the NaI systems. The sample load must be compared to the degree of analysis desired. A number of uses of these facilities are beginning to emerge: 1) Measurement of normal K^{40} to determine the lean/fat ratio and its relation to physiological conditions. 2) Whole body low level tracer studies in the dynamics of metabolism. 3) Whole body scanning for the localization of isotopes. 4) Radioactivity determinations on large samples of foodstuffs subject to fallout contamination and consumer products in industrial tracer uses.

At ATOMIUM we have designed a number of systems for low level detection combining the best features of past work. If you are considering the usefulness of a low level counting facility in your work, we should be happy to take up the discussion where we leave off here and send you a proposal best suited to your experimental requirements. If you are interested in special nuclear systems, write us at

940 Main Street, Waltham, Massachusetts
TWinbrook 4-6900

★DIGITRON

TYPE DISPLAY

NOW MINIATURISED

FOR INSTANTANEOUS CLOSE-RANGE READOUT

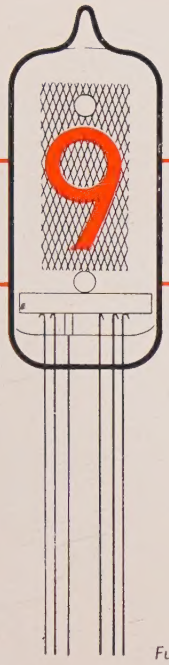

Full Size

THE GR. 10. W

In many digital applications it is often wasteful of valuable equipment space to employ the larger types of numerical indicators. The equipment design may call for a much more personalized type of display such as that required for control consoles, desk equipments, and similar layouts.

It is with these applications in mind that we introduce a newcomer to the DIGITRON range.

Whilst retaining the basic construction of the standard GR.10.G numerical indicator tube, the GR.10.W, being wire ended, can be soldered directly into the circuit and enables the designer to make full use of the display area by mounting these miniatures immediately adjacent to each other. This represents a considerable improvement in the readout facility at close range.

Like previous DIGITRONS, the numerical design of the GR.10.W is "human engineered" to eliminate readout error and again numbers are visible over wide viewing angles.

The miniature side-viewing GR.10.W with its robust construction, vivid presentation and its "no base" facility represents a big step forward in miniature display techniques.

Full Size

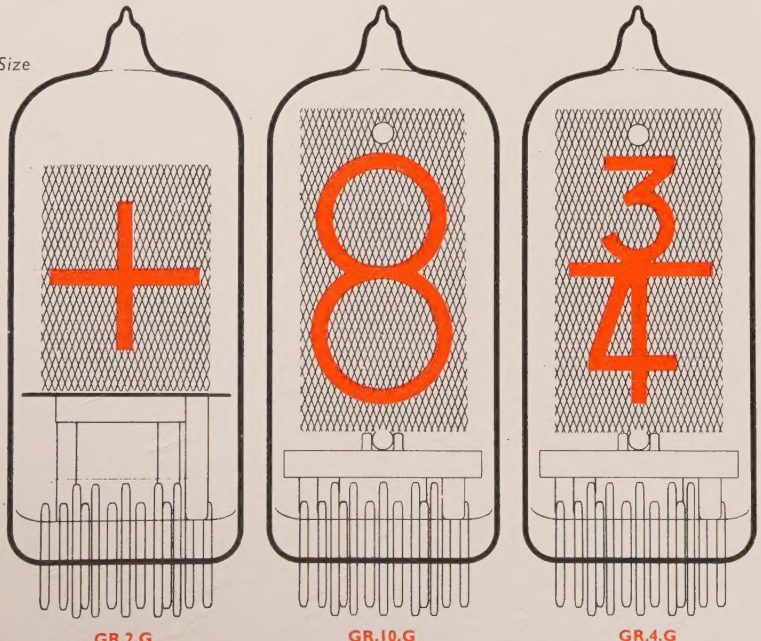

GR.2.G GR.10.G GR.4.G

OTHER SIDE-VIEWING DIGITRONS INCLUDE:

DIGITRON GR.2.G

Designed to display "plus" or "minus", this tube will find many applications in digital equipments requiring unambiguous sign display.

DIGITRON GR.10.G

The original DIGITRON—providing a clear numerical readout up to 50 feet over wide viewing angles. Ideal for audience readout.

DIGITRON GR.4.G

A recent introduction to the DIGITRON range, the GR.4.G displays $\frac{1}{4}$, $\frac{1}{2}$, $\frac{3}{4}$, or 1 in vivid numbers styled for easy readout. Suitable for applications concerned with monetary display.

May we send you full information on the DIGITRON range of display tubes. Write to: TECHNICAL SERVICE DEPT.

ETELCO

TUBE DIVISION

BEESTON, NOTTINGHAM

T E L ENGLAND

★ *Digitron is an Ericsson trade mark*

ETELCO LIMITED · HEAD OFFICE · 22 LINCOLN'S INN FIELDS LONDON W.C.2

Announcing the Eldorado 4100

A Fast, Stable Pulse Height Analyzer

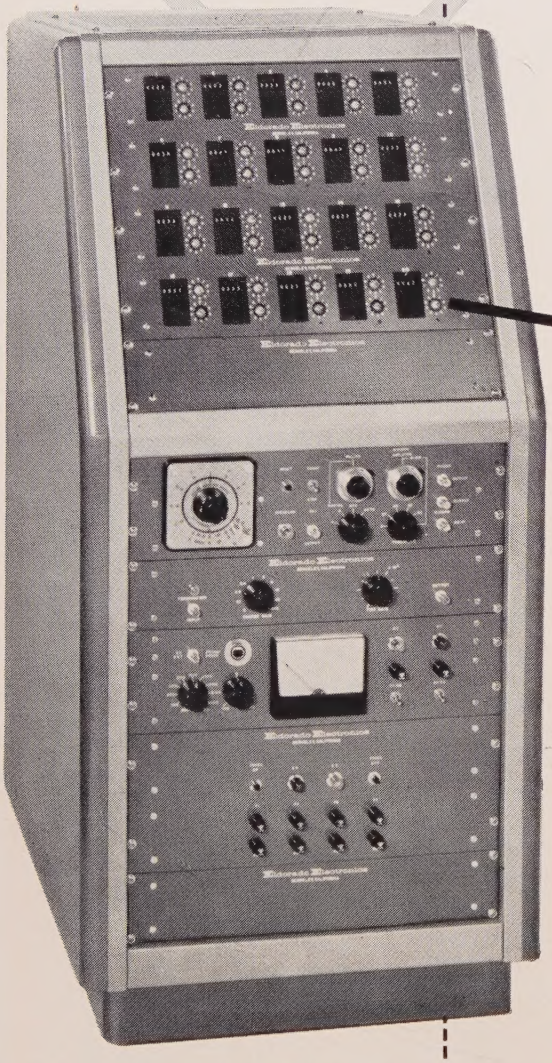

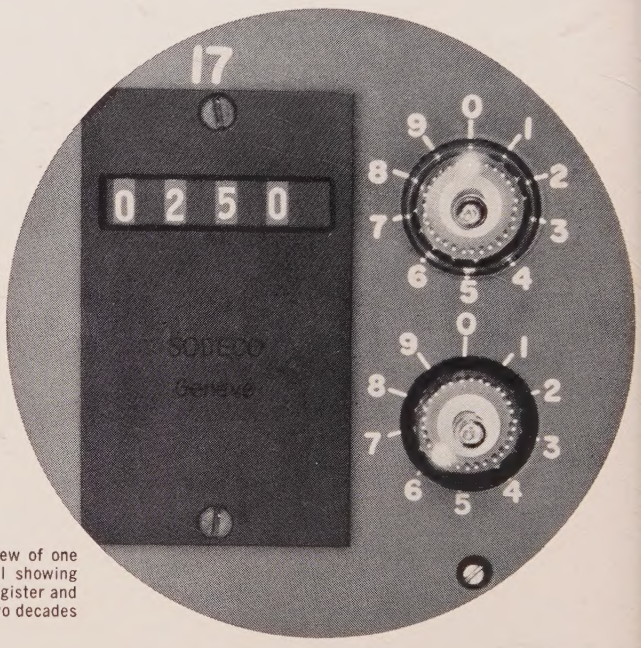

Full size view of one channel showing register and two decades

How Fast?

- Double pulse resolution better than 0.5 microseconds
- Dead time less than 0.1 microseconds
- Average counting rates greater than 10^5 counts per second without baseline distortion or use of temporary storage

How Stable?

- Channel width less than 1% drift per week
- Baseline less than 0.1% shift per week
- Channel triggering level unaffected by changes in input pulse width

For complete details, call your nearby Eldorado Engineering representative or write Dept. H1

Now in production, with 30 day delivery, the 4100 is priced at $8950 f.o.b. Berkeley, California. Shown with optional LA-600 Linear Amplifier and optional High Voltage Power Supply PS-530

BRIEF SPECIFICATIONS

NUMBER OF CHANNELS	20
CHANNEL WIDTH	1.0V NOMINAL
SCALER CAPACITY	10^6 COUNTS/CHANNEL
WINDOW AMPLIFIER INPUT	20V NOMINAL
WINDOW POSITION RANGE	5-105V

Eldorado Electronics

2821 TENTH STREET • BERKELEY 10, CALIFORNIA

Phone THornwall 1-4613

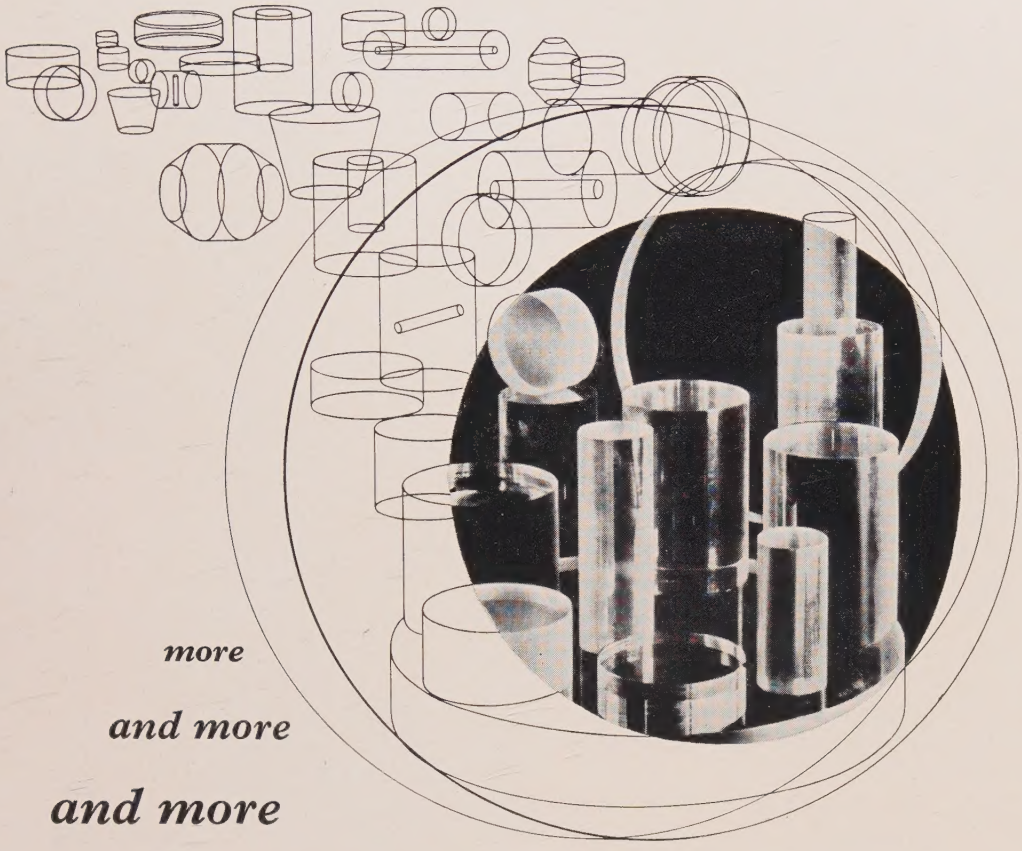

more

and more

and more

Scintillators

Nash & Thompson have now added Sodium Iodide, Caesium Iodide and Neutron Detectors to their extensive range of scintillators.

ORGANIC CRYSTALS. Anthracene, Stilbene, Terphenyl, in discs and cylinders.

PLASTICS. NATON-11 and NATON-136, high sensitivity, high transmission, based on either polyvinyl toluene or polystyrene. Available in discs, cylinders, ingots, foils, and filaments.

LIQUIDS. Ready made, sealed in glass containers to your specification, or in scintipaks

SCINTIPAKS. Accurately mixed dry constituents sealed in polythene envelopes, ready for dissolving in a suitable solvent as required.

CHEMICALS. Scintillation purity for making your own phosphors.

SODIUM IODIDE. Highest resolution, ready canned, in sizes up to 4″ dia × 3″ high, or 5″ dia × 2″ high.

CAESIUM IODIDE. In blocks up to 3″ dia × 3″ high.

Write or telephone for full information

Nash & Thompson LTD

Hook Rise, Tolworth, Surbiton, Surrey. Elmbridge 5252.

JSP 5689

INTERNATIONAL

advertise

YOUR NUCLEAR PRODUCTS IN

sell

YOUR NUCLEAR PRODUCTS

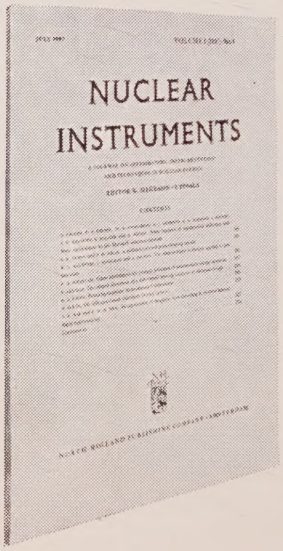

reap

YOUR NUCLEAR SALES
REWARDS

world wide

KEY NUCLEAR MANAGEMENT
NUCLEAR SCIENTISTS
NUCLEAR ENGINEERS
NUCLEAR PRODUCTION
PERSONNEL

SUBSCRIBE TO

you reach

THE WHOLE
NUCLEAR SALES WORLD IN

Entirely international in scope Nuclear Instruments and Methods is the one nuclear scientific journal that has an established subscription clientele throughout the whole world-where-ever nuclear men are at work—they want your nuclear products—they need your nuclear products—advertise in Nuclear Instruments and tell them WHAT – HOW – WHERE they can get your nuclear products

GO INTERNATIONAL WITH YOUR SALES PROGRAM TODAY WRITE

WILLIAM F. BAARS - ADVERTISING MANAGER NORTH-HOLLAND PUBLISHING COMPANY

P.O. BOX 103 – AMSTERDAM, HOLLAND

INTERNATIONAL

COMPACT 100 CHANNEL PULSE HEIGHT ANALYZER

The C.D.C. KICKSORTER

developed by Atomic Energy of Canada and manufactured by Computing Devices of Canada Limited

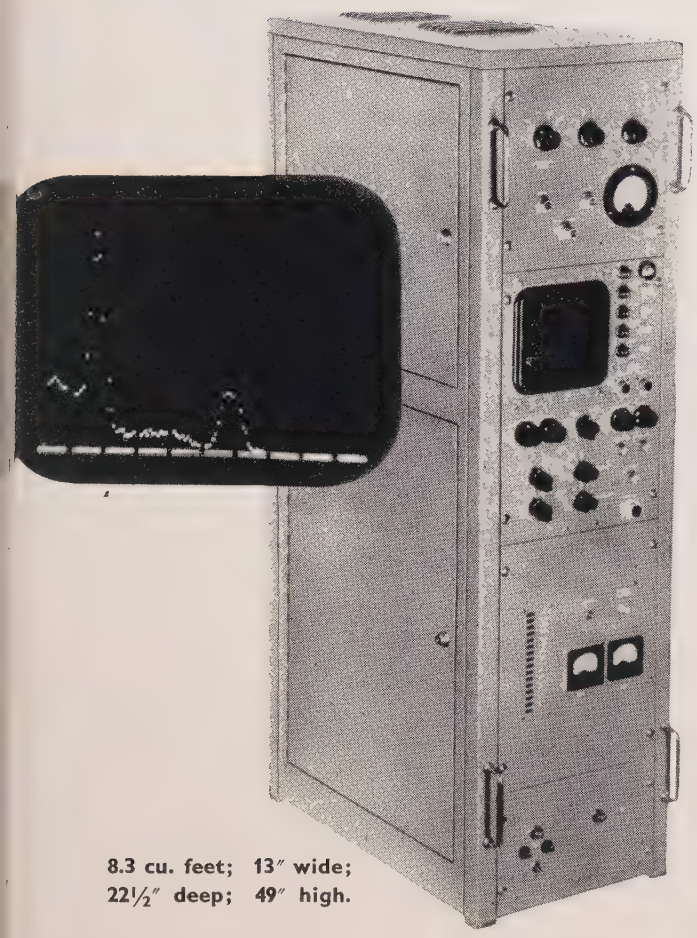

8.3 cu. feet; 13″ wide; 22½″ deep; 49″ high.

88% Transistorized

- Printed Circuitry
- Low Maintenance—High Reliability
- Compact—Semiportable
- Low Power Consumption—120 watts
- No Ventilation or Cooling problems

Highly Versatile

- Oscilloscope display
- Binary manual count readout allows the count on any channel to be displayed in digital form
- Accessory readout devices: photo recording camera, strip chart recorder, punch tape
- Magnetic core memory—65,535 counts can be stored per channel
- Permanent count storage—sixteen magnetic cores for each of the 100 channels

Bendix International

The "Chalk River Kicksorter", recently developed and based on designs and specifications prepared by Atomic Energy of Canada Ltd. is an extremely fast, accurate and versatile instrument.

The "Kicksorter" is designed to span random pulses of various amplitudes and shapes, sort them out according to amplitude into 100 channels, and store a record of the counted pulses in a magnetic core memory. A simple computer with its magnetic core memory and versatile data display system make it possible to observe the pulse amplitude spectrum as it accumulates or after it has accumulated.

In addition to its wide use in gamma spectroscopy, it has many applications in the fields of medical research, neutron time-of-flight studies, radioactive fallout studies, shielding studies, oil well and uranium logging, neutron activation analyses, measuring of radioactivity in humans and other uses.

The analyzer is designed so that information accumulated may be displayed or read out in various ways. Data may be observed on the oscilloscope, or information already accumulated in the memory core may be displayed on the screen, plotted on a strip chart recorder, or printed out in decimal form on an automatic printer.

Since the unit is highly versatile, it can be modified to accommodate most applications which require additional features.

For additional information, wire or write to:

Bendix International

DIVISION OF BENDIX AVIATION CORPORATION

205 E. 42ND ST., NEW YORK 17, N.Y., U.S.A. Cable Address: "BENDIXINT"

Sales Representatives for Great Britain

NUCLEAR ENTERPRISES (G.B.) LTD.

BANKHEAD MEDWAY, SIGHTHILL; EDINBURGH 11, SCOTLAND

NORTH-HOLLAND BOOKS

Paul Ehrenfest

COLLECTED SCIENTIFIC PAPERS

XII + 632 pages

Guilders 45,00 (90s.)

This volume makes widely scattered publications readily available. All Dutch articles appear here in English; the German publications are in the original language.

Sole Agency for U.S.A.:

Interscience Publishers Inc. — New York

NORTH-HOLLAND PUBLISHING COMPANY - AMSTERDAM

FOR SCINTILLATION & PROPORTIONAL COUNTING

Non-overloading Linear Amplifiers

MODELS 108 and 108 p

* GAIN–40,000, continuously variable
* RISE TIME–0.2 microsecond
* ACCEPTS + AND — PULSES

Tremendous Dynamic Range

EXCEEDS 1,000,000 (0.1 mV to 100 V)

Excellent linearity for small pulses in the presence of tremendous overloads that paralyze other amplifiers.
Model 108 P includes precision trigger type Pulse-Height Selector.

Model 413 Mercury relay precision sliding Pulser

The one pulser that fills every need of the Nuclear Physics Laboratory
0 to 100 Volts

10 full scale ranges from 1 mV to 100 volts
Fast rise and exponential decay of 1, 3, 10. 30, and 100 microsec simulate pulses from scintillation, proportional and Geiger counters.
Incorporates both manual control and precision motor drive.
The ideal instrument for precise calibration and test of pulse-height analyzers and other nuclear instrumentation.

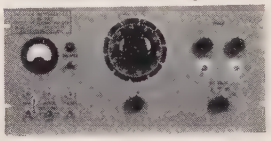

Window widths are determined AUTOMATICALLY, 10 × more ACCURATELY, 40 × FASTER than with conventional pulsers.

Model 108 Amplifier . . . . . $ 545.00
Model 108 P Amplifier (includes pulse-height selector) $ 595.00
Model 413 Precision Sliding Pulser . . . . . $ 630.00
Prices f.o.b. Silver Spring. Md.

RADIATION INSTRUMENT CO.
P.O. BOX 733 SILVERSPRING, MARYLAND, U.S.A.

NORTH-HOLLAND BOOKS

Analytical and Canonical Formalism in Physics

by

ANDRÉ MERCIER

Head of the Department of Theoretical Physics, University of Berne

6 × 9″ VIII + 222 pages Guilders 20.00 (40 s.)

THE CONTENTS

i LAGRANGIAN FORMALISM
ii LAGRANGIAN DENSITY
iii CANONICAL FORMALISM
iv CANONICAL FORM OF ELECTRODYNAMICS
v HAMILTONIAN DENSITIES
vi TRANSFORMATIONS
vii CANONICAL FORMALISM WITH VANISHING JACOBIAN DETERMINANT

Sole Agency for U.S.A.: Interscience Publishers Inc. – New York

NORTH-HOLLAND PUBLISHING COMPANY — AMSTERDAM

RIDL presents

the Complete Line of Nuclear Instrumentation

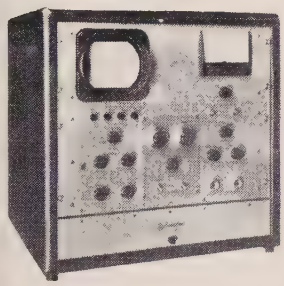

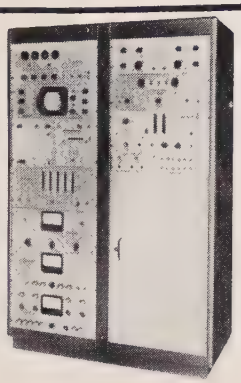

Analyzers Multi-Channel

RIDL offers the most complete line of Multi-Channel Analyzers ever offered by any manufacturer. From 100 channels to 2000 channels – from vacuum tube units to transistorized models, these are all STANDARD items. RIDL Multi-Channel Analyzers are presently in use in all AEC National Laboratories and other major nuclear research centers in the United States and abroad.

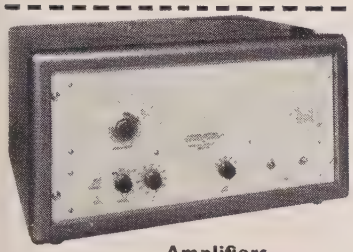

Amplifiers

From basic models to deluxe units with discriminators and high voltage power supplies, RIDL offers an amplifier that will fill your every requirement. Whether you want an Argonne, Brookhaven or Oak Ridge design, these are all manufactured by RIDL.

Scintillation Counters

RIDL offers a full line of scintillation counters designed to fit every requirement from basic probes to deluxe guaranteed resolution models. These units may be used to detect any type of radiation by simply inter-changing crystals.

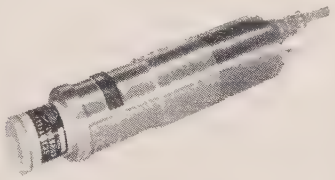

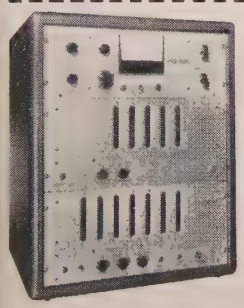

Scalers

RIDL manufactures the most complete line of scalers on the market today. From conventional vacuum tube units to completely transistorized models – from simple utility scalers to fully automated printing scaler systems, these are all STANDARD production items.

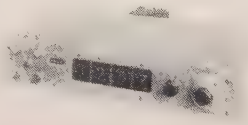

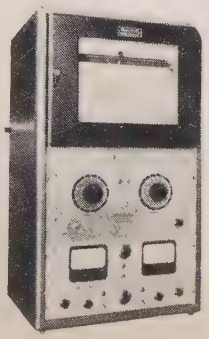

Spectrometers

A complete family of scintillation spectrometers is available from RIDL. From portable models to completely automatic recording systems, RIDL is the recognized leader in the design and manufacture of these units.

ALSO - -

- End Window Counters
- Gas Flow Counters
- Gas Sample Counters
- Cosmic Ray Counters
- PreAmplifiers
- Coincidence/Anti-Coincidence Analyzers
- Single Channel Analyzers
- Count Rate Meters
- Plug-In Counting Units
- Electronic Sweeps
- High Voltage Supplies
- Low Level Counting Systems
- Radiation Monitors
- Printers
- Recorders
- Reactor Control Instruments
- Pulse Generators
- Automatic Sample Changers
- Custom Equipment
- Electronic Timers
- Shields

RIDL is proud to present the most complete line of radiation detecting and measuring equipment ever offered by any manufacturer. From simple end-window Geiger tubes to deluxe guaranteed resolution scintillation detectors—from basic laboratory instruments to completely automated instrument systems, these are all STANDARD production items.

Whatever your radiation laboratory requirement may be, RIDL has the solution. Our staff is always available to answer your inquiries. Write today to Department MB for complete information.

RIDL INC.

Radiation Instrument Development Laboratory, Inc.

5737 South Halsted Street, Chicago 21, Illinois USA TRiangle 3-2345

Representatives in major cities

The place of the Particle Accelerator in Basic Research...

Monoenergetic Neutrons—VII

Since their discovery in 1932, neutrons have been widely used in nuclear bombardment studies. Investigations of excited levels of compound nuclei produced by inelastic collisions with neutrons have enabled physicists to develop models describing these interactions.

Accelerators Gave Control

The early work with neutrons was carried out with radioactive sources. The need for control and precision soon led to the use of particle accelerators as sources of monoenergetic neutrons. Studies were confined to the Mev range from exoergic reactions such as H^2 (d, n) He^3 and H^3 (d, n) He^4. Moderation of these fast neutrons was possible, but monoenergetic sources of slow neutrons could not be provided until the development of the atomic reactor in 1942. The subsequent use of monochromators made homogeneous beams of slow neutrons available.

Much work has been carried out with these thermal-neutron beams in measuring energy levels and spacings but, because of the dimensions of the crystal lattice, the maximum energy is confined to the order of tens of electron volts. The development of mechanical choppers has extended the energy range of monoergic neutrons to the low kev region, but even this method fails above about 20 kev.

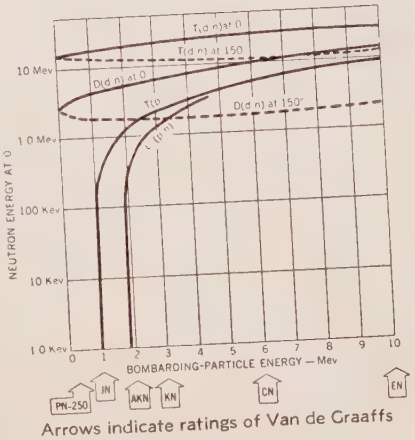

Arrows indicate ratings of Van de Graaffs

Fast Neutrons Needed

The only useful source of monoenergetic neutrons in the high kev range is provided by endoergic reactions of accelerated charged particles with suitable target nuclei. These reactions have threshold energies of the order of a few Mev. At this energy, the neutrons are emitted with the velocity of the compound neucleus. By varying the energy of the incident beam and the angle of observation, any neutron energy from about 30 kev to several Mev can be obtained. An excellent description of the angular-energy relationship has been given by Hanson, Taschek and Williams[1].

The most suitable reactions for monoenergetic-neutron production are H^3 (p, n) He^3 and Li^7 (p, n) Be^7. The former has a threshold of 1.019 Mev and the latter, 1.88 Mev. While the tritium reaction has a broader energy range than the Li^7 reaction, it is difficult to use. The gas must be adsorbed on a suitable metal and care taken to keep the temperature below 100°C. Gas targets have been used but require a thin window between the vacuum system and the gas chamber, producing energy spread in the proton beam. Lithium is a more suitable target material, but above neutron energies of about 600 kev a second neutron group appears.

Variable Monoenergetic Beam Needed

The range of energies available depends on the energy of the incident proton beam, as shown above. The accelerator must have a continuously variable energy if a wide variation of neutron energy is to be obtained.

Neutron energy homogeniety is limited by target thickness, scattering material near the neutron target, and finally, the energy homogeniety of the proton beam. The former are experimental variables. The latter is an inherent property of the accelerator. Monoenergetic beams from the Van de Graaff® have long been considered to be the most suitable for this type of work, and leading nuclear physics laboratories throughout the world are now using Van de Graaffs built by High Voltage Engineering Corporation.

Write for a copy of our new particle-accelerator bulletin.

References.
1. A. D. Hansen, R. F. Taschek, J. H. Williams, Revs. Mod. Phys. 21, 635, 1949.

High Voltage Servicing Company, Ltd.
London, England
High Voltage Engineering (Europa) N.V.
Amersfoort, The Netherlands

HIGH VOLTAGE ENGINEERING CORPORATION
BURLINGTON MASSACHUSETTS

NUCLEAR INSTRUMENTS AND METHODS 6 (1960) 105–125; NORTH-HOLLAND PUBLISHING CO.

THE OAK RIDGE RELATIVISTIC ISOCHRONOUS CYCLOTRON

PART II. MAGNETIC FIELD DESIGN FOR THE ISOCHRONOUS CYCLOTRON†

B. L. COHEN*, H. G. BLOSSER**, E. D. HUDSON, R. S. LORD and R. S. BENDER

*Oak Ridge National Laboratory****, *Oak Ridge, Tennessee*

Received 7 November 1959

The model magnet work and design studies which resulted in the selection of a three-sector azimuthally varying magnetic field with weak spiral are described. A four-sector, tight-spiral field was also considered.

1. Design Requirements

In the early work on azimuthally-varying-field (AVF) cyclotrons, the desired magnetic field was determined from theory, and the principal construction problem was to determine the iron and current configurations to achieve this field. This is a most formidable task, and an unnecessarily restricted one, since all of the theoretical requirements on the field may be satisfied in an infinitely large variety of ways. The approach followed at the Oak Ridge National Laboratory was, therefore, to construct a model with simple iron and current configurations, make measurements and calculations to determine how it fails to satisfy the theroretical requirements, make changes in the model to correct these failures, make new measurements, etc. This turns out to be a rapidly converging process, with the errors decreasing by nearly an order of magnitude on each successive iteration. The theoretical requirements on the magnetic field are:

(1) *Isochronism at all radii,* that is, the time required for a particle to complete a revolution must be equal to a constant independent of radius, namely the period of the radio-frequency (r-f) voltage applied to the dees; at least the phase shifting caused by the differences between these periods must never allow the particle to get out of phase with the r-f voltage by as much as 90 degrees. The condition for isochronism is, to a good approximation, that at radius r the average magnetic field $<B>$ (averaged around a complete turn) is

$$<B> = \frac{B_0\left\{1 + \frac{F}{2N^2}\left(1 + \frac{r}{F}\frac{\mathrm{d}F}{\mathrm{d}r}\right)\right\}}{\sqrt{1-(r/a)^2}} \qquad (1)$$

where F is the "flutter", defined as

$$F = \frac{<B^2> - <B>^2}{<B>^2}. \qquad (2)$$

N is the number of sectors, and a is the cyclotron unit

$$a = \frac{m_0 c^2}{eB_0} \qquad (3)$$

where m_0 and e are the rest mass and charge of the particle being accelerated, B_0 is the field at the center of the cyclotron, and c is the velocity of light.

(2) *Axial stability,* that is, the excursions of the particle in the direction perpendicular to their normal plane of motion must not be so

† This is the second of a series of three articles describing the development and design of a fixed-frequency cyclotron being built to provide variable-energy acceleration of protons to 75 MeV and N^{4+} to 100 MeV. The series was compiled and edited by R. S. Livingston and F. T. Howard.

* Now at the University of Pittsburgh.

** Now at Michigan State University.

*** Operated for the USAEC by Union Carbide Corporation.

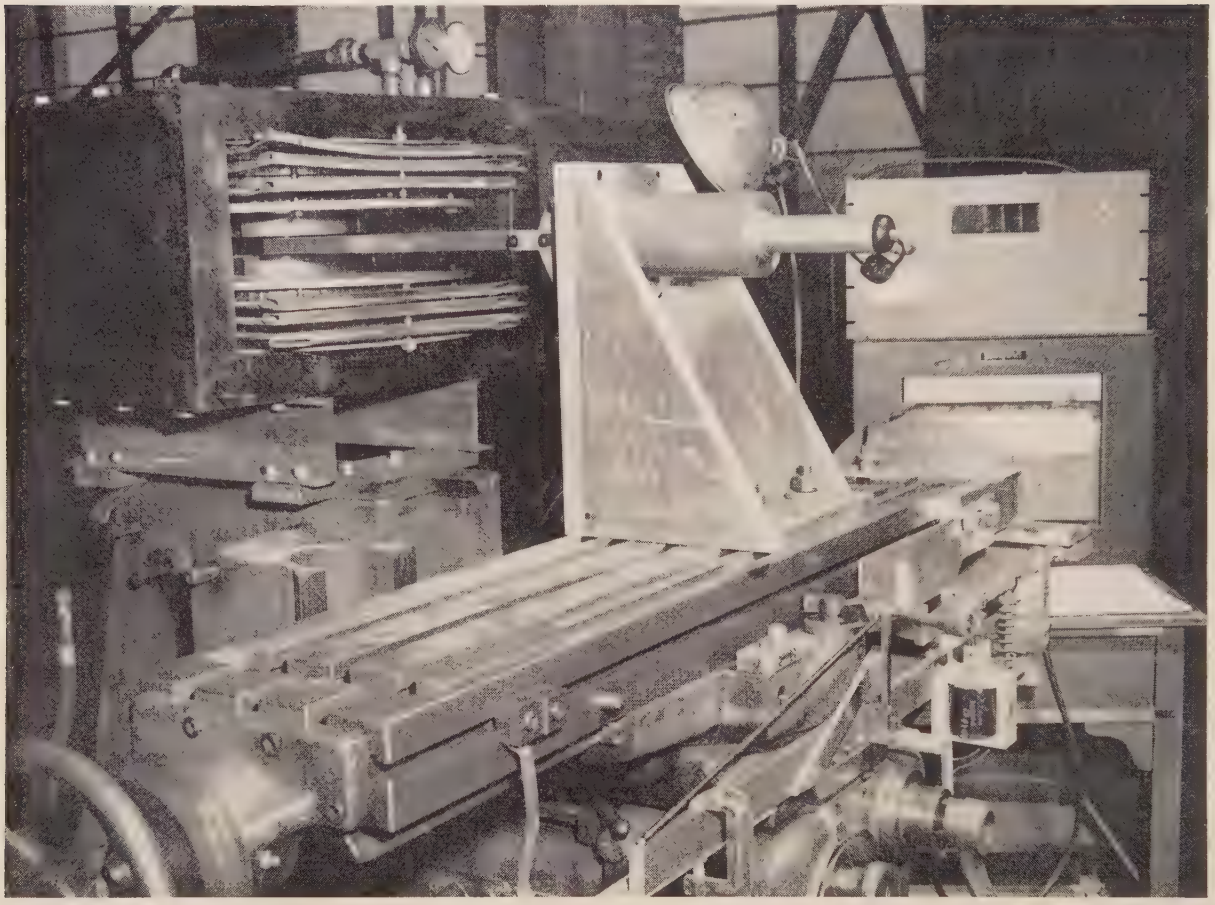

Fig. 1. Model magnet and general arrangement for field measurements.

large that the particles will strike the dees. Since the available aperture in this direction is severely limited, this essentially requires that there be positive axial focusing at all radii. The axial focusing force, F_z, is

$$F_z = -4\pi^2\nu_z^2 Z \tag{4}$$

where the axial oscillation frequency, ν_z, is approximately

$$\nu_z^2 = -\frac{r}{\langle B\rangle}\frac{\mathrm{d}\langle B\rangle}{\mathrm{d}r} + \frac{N^2}{N^2-1}F(1+2\tan^2\alpha) \tag{5}$$

where α is the spiral angle.

(3) *Radial stability*, that is, the radial oscillations must not become unduly large. In practice, when they become larger than some critical size, they begin to increase exponentially, so that the requirement is essentially that the radial oscillation amplitude must not reach this critical size.

As the principal requirement of simplicity of construction, it was decided that the iron configuration be achieved by bolting shims of uniform thickness (shims which can be cut from flat plates) onto the pole bases of the magnet. It was decided that the current configuration might include valley coils and circular trimming coils mounted on the pole faces in addition to the main exciting coils, although an arbitrary upper limit of 500 kW was set on the power consumption of these valley coils.

Since the effectiveness of valley coils increases rapidly with size, they are always designed to use all available space in the valleys. The design of the pole-face windings is determined by the fact that the cyclotron must be capable

of accelerating both protons to 75 MeV and N^{4+} ions to at least 80 MeV, and that these energies must be easily adjustable to any lower values. (It turns out that the range of radio frequency and magnetic field adjustments these variations must be achieved with the circular trimming coils. This determines their minimum design capabilities and, in fact, determines their actual design since the space occupied by these coils is very costly.

Fig. 2. Typical field contours obtained for a four-sector magnet. (Field in kilogauss. No current in valley coils.)

necessary to fulfil these requirements include the adjustments necessary to obtain a large variety of other energetic particles including deuterons up to 40 MeV, alpha particles up to 80 MeV, etc.) The isochronism requirement demands a different average magnetic field at each radius for each final energy of each particle accelerated, and

The parameters of the iron configuration that can be varied to satisfy the theoretical requirements on the magnetic field are: (a) number of sectors, (b) hill gap, (c) valley gap, (d) ratio of hill width to valley width as a function of radius, and (e) amount of spiral as a function of radius.

The axial focusing increases monotonically

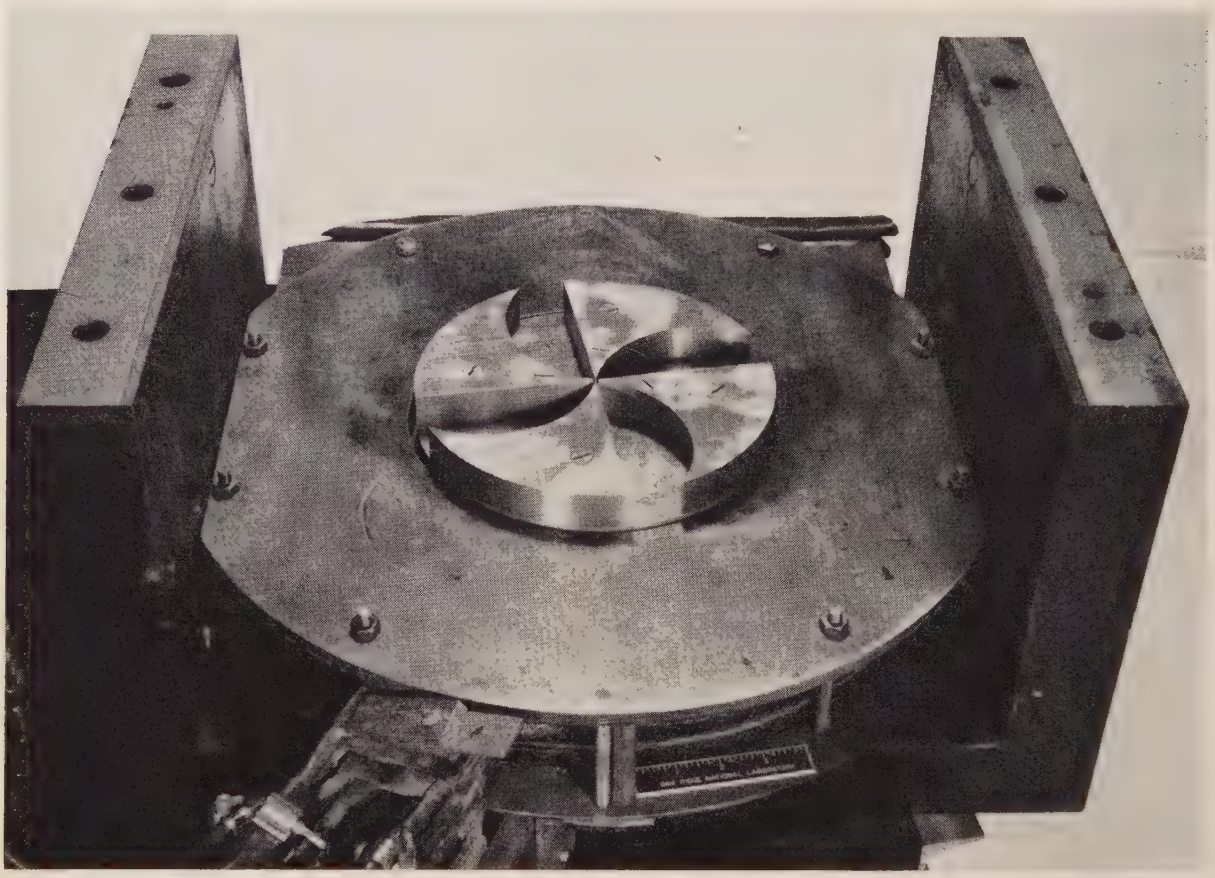

Fig. 3. Lower half of model magnet with four-sector pole tip.

as the valley gap is increased, but when it becomes larger than the distance between neighboring hills, further increases are of little value. In view of this, and as a construction simplification, the valley gap was left as the gap between the pole bases.

A relatively large ratio of hill width to valley width must be used to obtain the necessary magnetic field strengths. Variations of this ratio with radius are used to keep the average field at each radius within a range such that isochronous fields for all particles can be obtained with circular trimming coils of minimum size. Aside from these limitations, the valleys are made as wide as possible so as to allow the use of the largest possible valley coils (these contribute to flutter).

The remaining parameters, the number of sectors N, the hill gap g, and the spiral α, must be chosen by relatively involved compromises. For both N and α the axial and radial stability requirements act in opposite directions, with low N and large α giving increased focusing, but reducing the radial stability. There was good reason to believe that $N = 4$ would give reasonable radial stability, and it was hoped that even $N = 3$ would be sufficiently stable in some cases. Model investigations were made of both three-sector and four-sector magnets. For survey purposes, only two types of spiral were studied: A very weak spiral (actually negligible from the standpoint of radial stability), and the strongest spiral that is useful for axial focusing[1]). The flutter increases as the gap decreases, but as the gap is decreased little space is left for the beam. Thus, the gap is made as large as is con-

[1]) V. Bluemel, J. B. Carroll and P. Stähelin, U. of Ill. Tech. Rept. No. 2, Navy Contract No. 1834 (05).

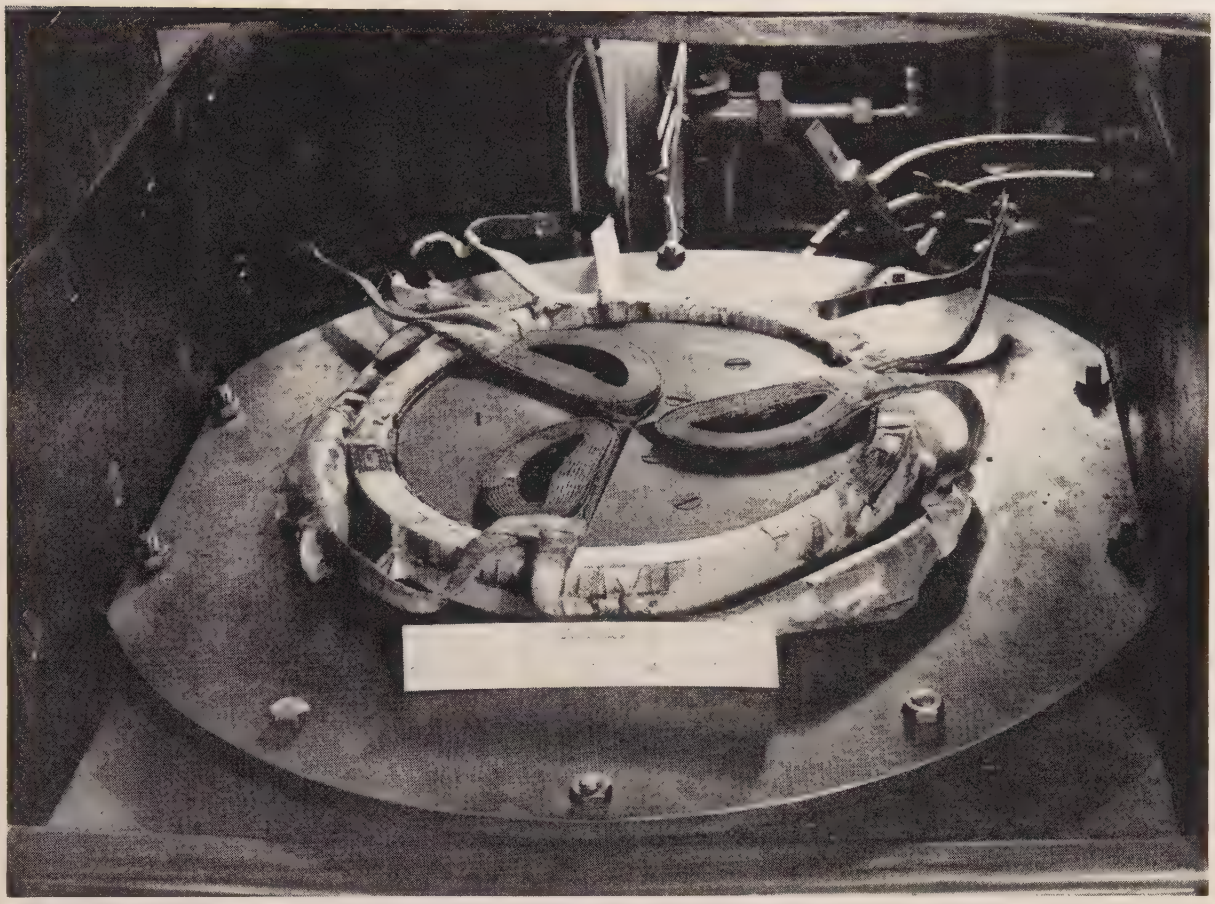

Fig. 4. Three-sector pole tip with valley coils and auxiliary windings.

sistent with obtaining sufficient axial focusing.

It is clear from the above discussion that many of the design parameters can only be determined by model magnet tests. Some of these are:

(1) Size, current capacity, and number of circular trimming coils mounted on the pole faces.

(2) Effectiveness of valley coils in producing flutter.

(3) Ratio of hill width to valley width needed to obtain required average field strengths, and the variation of this ratio with radius necessary to achieve isochronism.

(4) Maximum hill gap capable of producing the necessary axial focusing.

In addition, magnetic field configurations from model magnet tests were very useful in the radial stability calculations and in the axial stability calculations associated with deflection (both to be discussed later, in Part III). Thus, the model magnet test program played the central role in the design of the magnet.

Section 2, below, will describe the model magnets and some of the techniques used in gathering data. Section 3 will then describe the method of analyzing the model magnet data and determining the changes to be made in the subsequent model. The results and conclusions from this work will be given in Section 4.

2. Model Magnet Measurement

Initially, magnetic field configuration studies were made with a $\frac{1}{9}$-scale model magnet. To provide greater accuracy a $\frac{1}{4}$-scale model has recently been used. For additional precise measurements the full-scale magnet is being installed as a temporary test facility to be used until the ORIC building is ready. The electrical characteristics of the three magnets are given

TABLE 1

The electrical characteristics of the ORIC magnets

Magnet	Main Coils			Valley Coils			
	Amps	Turns	kW	Amps	Turns/sector	kW	Total kW
$\frac{1}{9}$-Scale	500	240	45	2900	14	75	120
$\frac{1}{4}$-Scale	2000	144	200	2000	48	216	416
Full-Scale	4000	640	1000	5000	70	750†	1750

† With the acquisition of a separate motor-generator set for the valley coils this power rating has been increased from 500 kW to 750 kW.

in table 1. Each magnet yields a different type of information and requires somewhat different measuring techniques.

To date, most of the model work has been done on the $\frac{1}{9}$-scale model. In it many widely varying configurations were used for exploratory tests of a general nature. The information established with the aid of this model includes the magnetization curve, the gap width, the approximate shape of the pole tips, the number of sectors, direction and magnitudes of forces, and the magnitude of the current required in the valley coils.

The general arrangement for making measurements with the $\frac{1}{9}$-scale model is shown in fig. 1. The measuring system consists of a

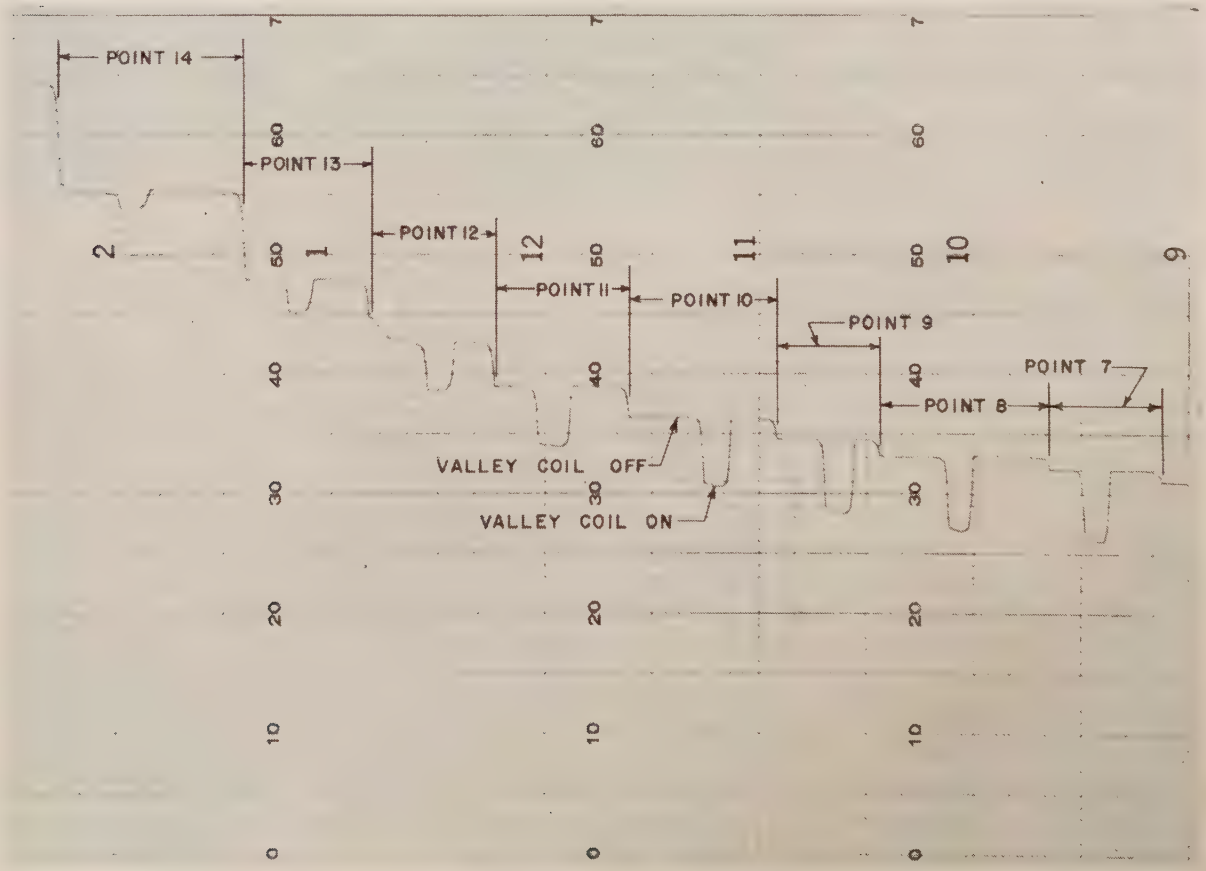

Fig. 5. Typical data showing effect of valley coils.

Rawson rotating-coil fluxmeter feeding a Brown strip-chart recorder. The fluxmeter is moved in rectangular coordinates on a milling machine table which moves in $\frac{1}{4}$-in. steps. The data is recorded on the chart while the fluxmeter is stationary at each point. For speed and convenience the milling machine table is advanced

copper. They were operated at currents up to 2000 amps, pulsed to avoid overheating. Valley coils of this type, along with some auxiliary windings around the pole tips, are shown in fig. 4. Data from these pulsed coils was recorded as shown in fig. 5. The Brown chart runs continuously while the probe is moved from point

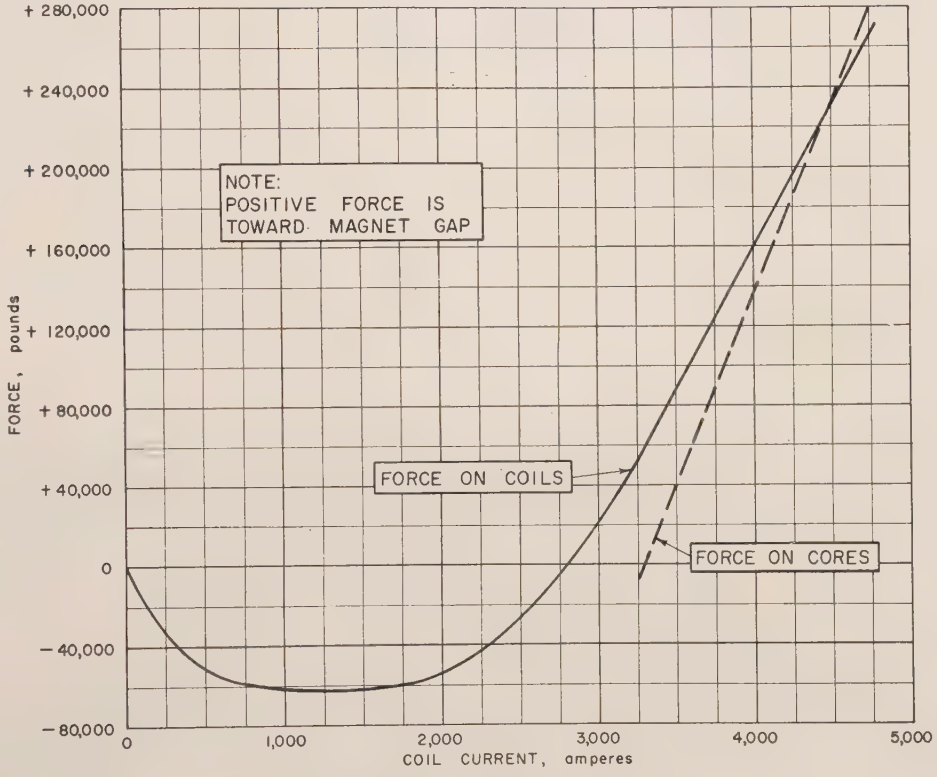

Fig. 6. Forces on coils and cores.

automatically. At each point the position of the probe is recorded on the chart along with the magnet data. The field intensity at each point of the rectangular grid can then be read and manually punched on paper tape for input to the computer.

A typical field contour obtained from a model is shown in fig. 2. The field contours follow the shape of the iron reasonably well except for the central region and near the edge of the pole. A four-sector model with the upper half removed so that the lower pole tips are visible is shown in fig. 3. A similar view of a three-sector magnet is shown in fig. 4.

The first valley coils were made from $\frac{1}{2} \times \frac{1}{16}$

to point, remaining at each position for about 10 sec while the field at that position is recorded. If the probe is over a valley coil when it is pulsed the field contribution appears as a negative pulse on the chart since the main function of the valley coils is to lower the field in this region.

To provide for continuous operation of the model magnet water-cooled valley coils were formed from $\frac{1}{4}$-in. square copper tubing with a $\frac{1}{8}$-in. square hole. They are operated at currents up to 3000 amps, or a current density of 70 000 amps per square inch.

Forces on the coils and the magnet cores are shown in fig. 6. The numbers are for the full-scale

magnet. At low excitation currents the coil forces are away from the median plane, as is the usual case in iron-core magnets. The forces continue to be away from the gap with increasing magnitude until the excitation current reaches 1500 amperes. At the design operating point of 2000 amp the forces have decreased somewhat, but are still away from the gap. However, if the magnet should be connected to a generator that under certain fault conditions could drive the current up to 4000 amp tremenduous forces would be expected in the opposite direction, toward the gap. A similar condition exists for the cores. This reversal of forces is possible because the coils were moved toward the gap to improve the magnet efficiency; the flux distribution at the high fields gives a larger field in the gap than between the yoke and the pole base. This data is presented only to point out that the conventional direction of the forces for an iron core magnet may reverse as magnets are built to operate at higher field intensities. Allowance for this reversal should be incorporated into the mechanical design of the system.

A view of the lower half of the $\frac{1}{4}$-scale model is shown in fig. 7. The two continuous-duty, water-cooled circular trimming coils shown in place on the pole tips are capable of carrying 1000 amperes. The valley coil leads emerge from each valley. These coils are also of $\frac{1}{4}$-in. square copper tubing, with three parallel water circuits in each coil to provide adequate cooling. The $\frac{1}{4}$-scale model was machined to an accuracy of $\pm$ 0.001 in. on all dimensions of the poles. It is expected that data of sufficient accuracy will be obtained from this model to perform calculations on the beam extraction qualities of the field.

Data from the $\frac{1}{4}$-scale model and from the

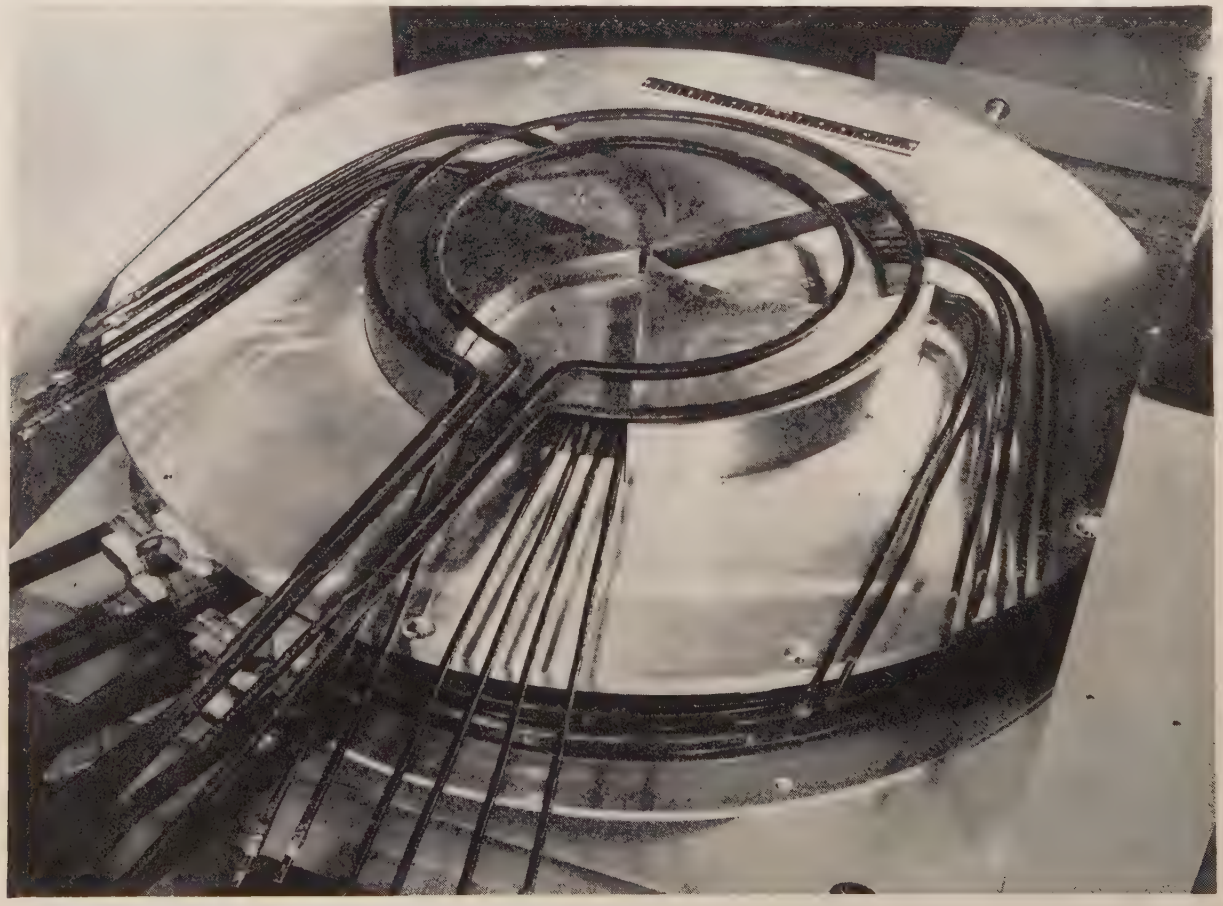

Fig. 7. Lower pole of quarter-scale model magnet, with valley coils and two circular trimming coils.

full-scale magnet will be automatically recorded by the system shown in fig. 8. Hall generators will be used as the field sensing devices, with one located at the center of the magnet as a reference and one moved in azimuthal and radial steps to explore the field. The scanner sequentially selects the input information and feeds it to tests at various magnetic fields from 8 to 22 kilogauss the output voltage stayed within ± 1 part in 10 000 over a 10° C temperature range.

3. Design Study Procedure

The design of the AVF magnet is accomplished by a successive approximation procedure,

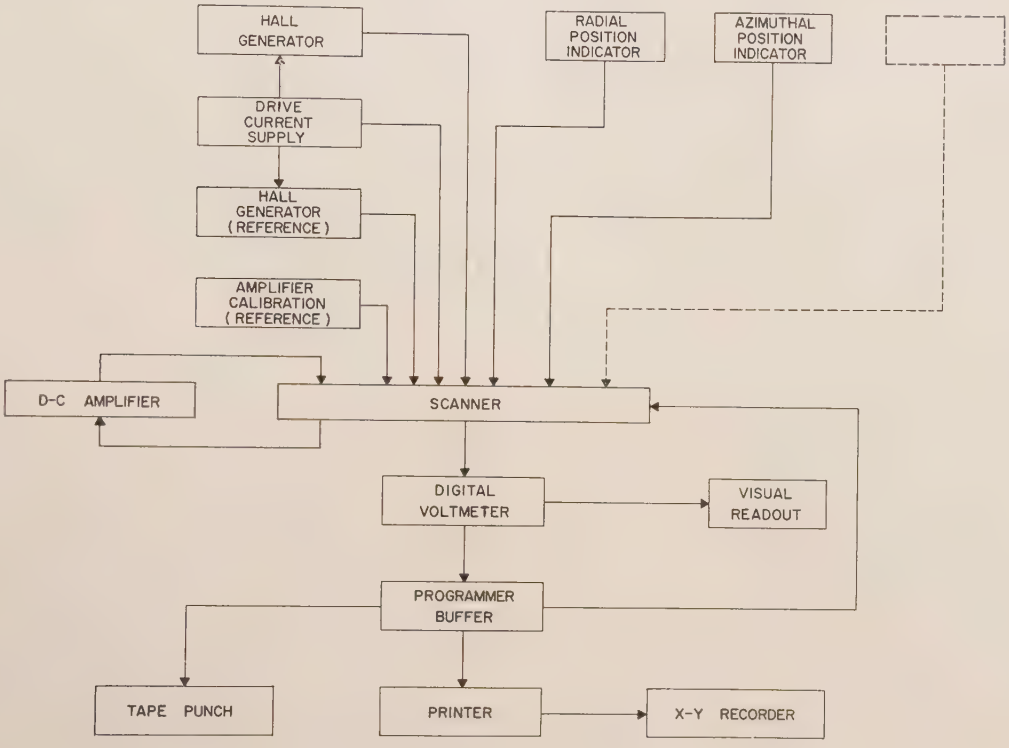

Fig. 8. Data recording system.

the digital voltmeter where it is digitized and then fed to the paper tape punch for input to the digital computer. The data is also recorded by the printer and an analogue plot is made by the X–Y recorder for monitoring purposes.

The Hall generators have a temperature coefficient of output voltage of 0.04 to 0.06% per degree centigrade. This effect can be reduced by the addition of a shunted thermistor in series with the load resistor in the output circuit. The choice of values for the shunt and for the load resistor depends on the desired operating temperature of the Hall generator, on the magnitude of the magnetic field, and on the characteristics of each Hall generator. In as is standard in studies of this type. The magnetic field produced by a given magnet structure is determined (via the model magnet procedure described in the previous section), the orbit properties of this field are calculated, and corrections to the magnet structure are inferred from the orbit properties. The effectiveness of such procedures can vary greatly depending on the acumen with which choices are made in regard to magnet configuration and the subsequent revisions. The situation is complicated by the large number of parameters to be specified by the designer. A semi-empirical model of the field of a given magnet was effectively employed to guide the initial

estimate and to gauge subsequent corrections.

The method is restricted to pole tips of right cylindrical form; for such, the tip geometry is completely prescribed by specification of pole diameter, number of sectors, hill gap, valley gap, angular width of hill as a function of radius, and spiral of the hill as a function of radius. The pole structures being investigated at nearly all laboratories have right cylindrical tips to that the restriction is minor. In addition so the magnet tip parameters, the location and number of ampere-turns of the various coils must be specified to complete the description of the magnet. It is assumed that the yoke is designed on the basis of standard practice, such that the magnetomotive drop in the yoke is small.

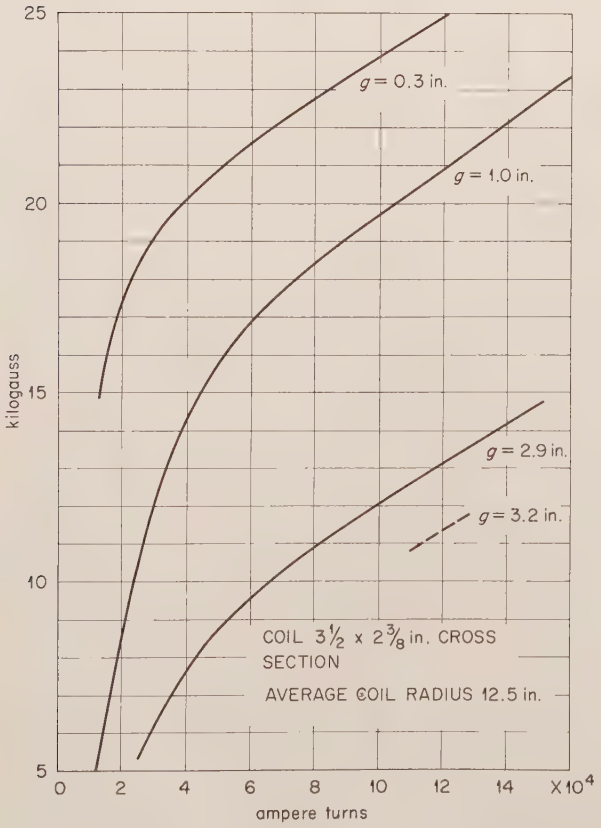

Fig. 9. Magnetization curves for 8.75-in. model.

The analytical model of the field is a linear-edge approximation in which the field is assumed to be constant in hill and valley regions and to vary linearly in fringing regions. If the problem is an initial guess with no previous data available, the magnitude of hill and valley regions is estimated from empirical excitation curves such as those of fig. 9. If the problem is one of gauging corrections to a previous run, the hill and valley magnitudes are set from the previously observed values. The field is assumed to fall off linearly at all edges with $dH/ds = H_{max}/2g$, for ds perpendicular to the field edge, and where H_{max} is taken to be the value of the field in the flat region from which the falloff originated. The falloff is assumed to begin a distance of $0.6\,g$ inside any edge of the magnet structure. Fig. 10 shows the contour map for a typical magnet configuration obtained by the linear-edge approximation. The contours differ

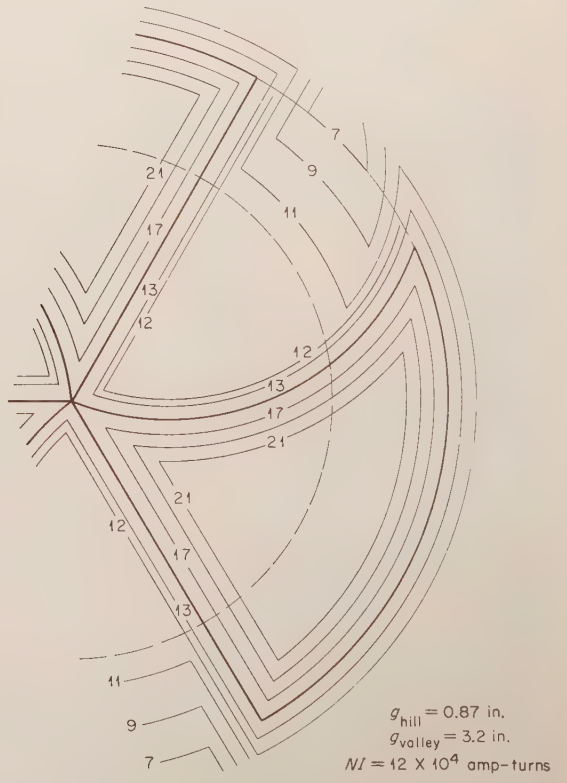

Fig. 10. Contour map from magnetization data, linear-edge approximation.

considerably in detail from typical model magnet contours, as can be noted roughly by comparison with fig. 2, even with allowance for differences in geometry and excitation (in fig. 2

the NI corresponds to 18-kilogauss peak field). In terms of the average properties $< B >$ and F which are of primary concern, the approximation gives good accuracy, as is discussed subsequently. The approximate contour can be calculated in 10 min whereas the measured contour represents approximately a man-month of work.

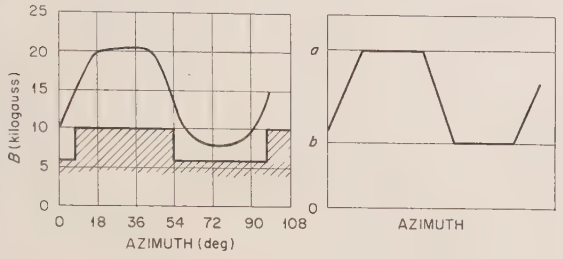

α_1 = RELATIVE WIDTH OF HILL
α_2 = RELATIVE WIDTH OF ONE FRINGING EDGE
$\zeta = \frac{b}{a}$
$\langle B \rangle / a = (\alpha_1 + \alpha_2) + (1 - \alpha_1 - \alpha_2)\,\zeta$
$\langle B^2 \rangle / a^2 = (1 - \alpha_1 - \frac{4}{3}\alpha_2)\,\zeta^2 + \frac{2}{3}\alpha_2\,\zeta + \alpha_1 + \frac{2}{3}\alpha_2$

Fig. 11. Definitions and relationships.

The approximate contour serves the important purpose of yielding a simple algebraic relationship between the magnet structure parameters (hill gap, valley gap, hill width, excitation, radius, etc.) and the $< B >$ and F. If α_1 is defined as the fraction of circumference subtended by the hill region at a given radius, α_2 the fraction subtended by an average fringing edge, and ζ the ratio of hill to valley field strengths, then $< B >$ and $< B^2 >$ are given by the expressions in fig. 11, and F is, of course, simply $(< B^2 > / < B >^2) - 1$. By use of these expressions the $< B >$ and F of new magnet configurations can be quickly computed, and also corrections to parameters of magnets already tested can be computed to accomplish desired changes in $< B >$ and F.

As an example of how the approximation is applied to new, untested magnet configurations, consider the configuration from which fig. 10 is derived. First, by reference to the excitation curves of fig. 9, the hill and valley field strengths are determined, and from this, a contour map such as fig. 10 is plotted. From the contour map, the relative widths of hill and fringing edge are determined by measurement. These values are inserted in the formula for $< B >$ and F. If, for example, we compute at the radius of the dotted curve in fig. 10, the hill measures 47.5 deg and the two fringing edges 14 deg and 16.5 deg, which yield values for α_1 and α_2 of 0.396 and 0.127. The hill field a is 21 kilogauss and the fractional strength of the valley field ζ is 12/21 or 0.572, which gives:

$$\langle B \rangle / a = (0.396 + 0.127) + [1 - (0.396 + 0.127)]\,0.572 = 0.796$$

$$\langle B \rangle = 16.7 \textit{ kilogauss}$$

$$\langle B^2 \rangle / a^2 = (1 - 0.396 - \tfrac{4}{3} \times 0.127)\,(0.572)^2 + \tfrac{2}{3} \times 0.127 \times 0.572 + 0.396 + \tfrac{2}{3} \times 0.127 = 0.671$$

$$F = \frac{\langle B^2 \rangle}{\langle B \rangle^2} - 1 = \frac{0.671}{(0.796)^2} - 1 = 0.058\,.$$

From the actual measurements made subsequently, $< B >$ and F at this radius were found to be 17.3 kilogauss and 0.056, respectively, so that the approximate prediction is in error by about 4% in each case. Calculations of this type are then of great value in estimating the performance of magnet configurations for which previous data are unavailable. The calculations are substantially more acurate than the often used hard-edge approximation in which fringing is neglected and hill and valley fields are assumed to be of uniform strength over their complete respective areas of the poleface.

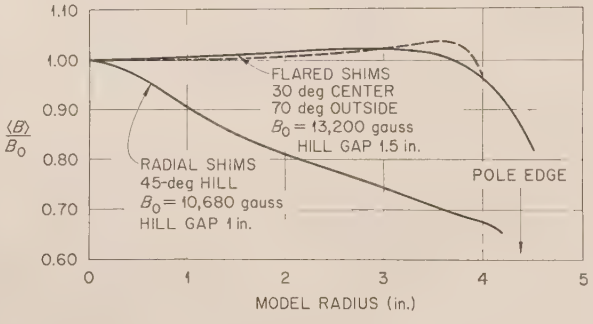

Fig. 12. Typical $\langle B \rangle$ corrections.

The application of the linear-edge approximation to obtain corrections to a previously measured configuration is illustrated in fig. 11. Here the observed field profile at some radius is shown

on the left; a linear edge profile which gives a good fit to the observed profile is picked giving the curve on the right and from this, effective values of α_1, α_2, ζ and a are obtained. Correction terms are calculated by standard inversion of the formulas for $< B >$ and F. If for example, it is desired to correct $< B >$ by a change in the width of the hill α_1, we have

$$\frac{\partial <B>}{\partial \alpha_1} = 1 - \zeta ,$$

and hence,

$$\Delta\alpha_1 = \frac{1}{1-\zeta} \Delta <B> .$$

An actual application of this procedure is shown in fig. 12. For the lower solid curve in the figure, $< B >$ was taken from early model studies at the University of California. Corrections to this were computed, gauged to give the dashed curve in the figure. A set of pole tips with the corrected shape was fabricated and when tested in the model magnet yielded the upper solid curve in fig. 12.

In fig. 13 results of application of the procedure to correction of the flutter are shown. The

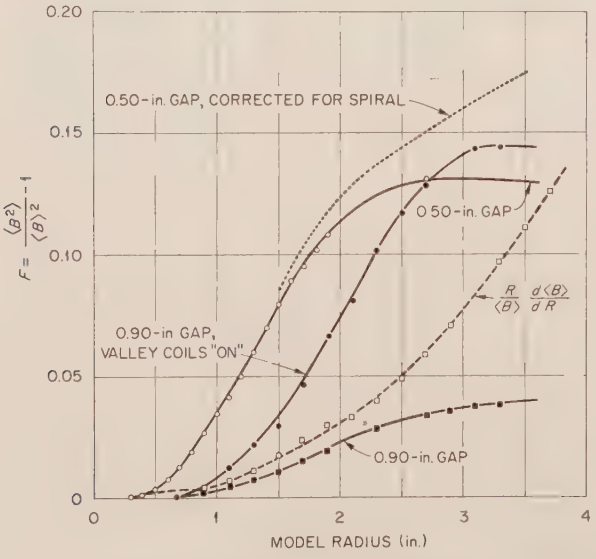

Fig. 13. Typical flutter corrections.

lower solid curve in the figure labeled "0.90-in. gap" is a flutter curve from an early run. It was desired to convert this to a value of 0.11 at 3.5-in. radius† by changing the ζ. Two independent procedures for changing ζ were used; the first increased the hill field by reducing the magnet gap, giving the curve labeled "0.50-in. gap", the second decreased the valley field by means of deexciting coils around the periphery of the valley and gave the curve labeled "0.90-in. gap, valley coils". For the large magnitude of the correction, both curves give values reasonably close to the desired 0.11 at 3.5 inches.

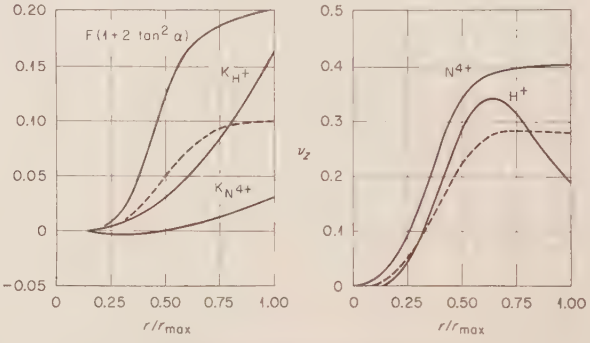

Fig. 14. Schematic axial focusing behavior.

Another interesting feature of magnets with radial (or nearly radial) sectors and right cylindrical tips is illustrated in fig. 13. If the flutter curves are compared with the $(R/< B >)$ $(\mathrm{d} < B > /\mathrm{d}r)$ curve the difference, which is ν_z^2, is seen to go through a maximum at intermediate radii. The behavior is illustrated schematically in fig. 14, the focusing and defocusing terms being given in the left-hand graph and the resultant ν_z on the right-hand graph. The ν_z for H^+ goes through a pronounced maximum and ends at a final value of about 0.2. This intermediate maximum in the ν_z is an inherent property of tips of the type here considered in conjunction with the isochronism requirement. To remove it would require introduction of additional variables such as valley coils with an array of shunts which would vary the valley coil current as a function of radius. The maximum can also be eliminated by proper manipulation of the spiral angle; the fairly tight spirals required appear to be undesirable from the point of view of deflector design.

† An F of 0.11 along with the spiral term and the appropriate $(R/<B>)\,\mathrm{d} <B>/\mathrm{d}r$ gives the desired 0.2 value for ν_z.

The effect of the maximum in the ν_z will be to reduce somewhat the radial stability limit for off-median plane motion due to proximity of the operating point to the Walkinshaw resonance[2]). Radial stability limits in this region are quite large in the first place, however, so that this reduction will probably be of small consequence. This will be explored in detail in a subsequent calculation.

Fig. 14 also shows the effect of change of the accelerated particle assuming an accompanying change in the average field to maintain isochronism. If the focusing term $F\ (1 + 2\tan^2\alpha)$ is left unchanged the solid curve on the right labeled N^{4+} results; the value of about 0.4 which this curve has at 3.5-in. radius is certain to cause difficulty in deflection due to proximity of the Walkinshaw line. If a portion of the focusing force is derived from supplementary coils such as the valley coils, then the focusing force can be reduced to a value, such as shown by the dotted curve on the left, by simply turning off the supplementary coils. For heavy ions a ν_z of the form shown by the dotted curve on the right results, which is more favorable for deflector design. The valley coils are invaluable for proper control over the ν_z as particles are changed.

In the design of the ORIC most of the magnet parameters were fixed on the basis of theoretical and economic considerations as discussed in other sections. After a particular choice of other variables had been made, the techniques here described were used to determine the hill gap and the angular width of the hill as a function of radius to give the proper $< B >$ dependence on radius and the proper focusing at the maximum radius. The method is, however, quite flexible and could be used just as conveniently to fix other design parameters if the conditions of a particular problem made it desirable.

In the preceding discussion it was assumed that orbit properties were determined, for a given field, by the approximate equations (1) and (5). This is purely a question of convenience. When a given magnet has evolved to a point where exact determination of orbit properties (via numerical integration of the equations of motion) is warranted, the exact results are used to fix the corrections $\Delta\nu_z$ and $\Delta< B >$ which are required; these corrections are inserted, and the corrective procedure then procedes just as described.

A comment should also be made as to the effects of coil position. At the field strengths

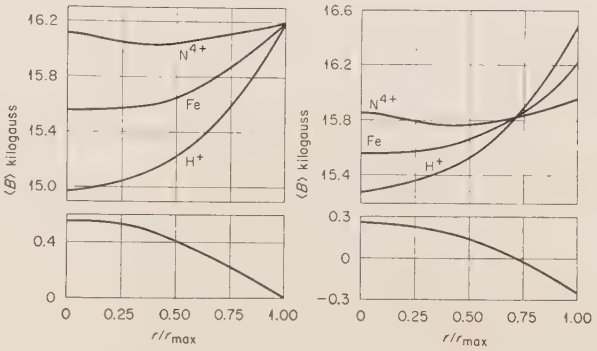

Fig. 15. $<B>$ trimming requirements.

employed in the ORIC such effects are large. It was found that shifting the coils a distance of 1 in. in the model changed by 25% the ampere-turns (and hence power by 50%) required to obtain a given field strength. Thus, curves such as those of fig. 9 are substantially altered, particularly at high excitations, if coils are moved. Care must be exercised to use curves applicable for the particular coil position under consideration.

In addition to the problem of obtaining a proper configuration of the iron and main coils, the multi-particle character of the cyclotron requires that trimming elements be available to shift the field shape to correspond to the different rates of mass increase of various particles. In the upper left sketch of fig. 15 the curves labeled N^{4+} and H^+ are the isochronous $< B >$ values for N^{4+} and H^+ ions of the same final $H\rho$. At small radii the two curves differ by more than a kilogauss. To obtain the necessary adjustment, the main magnet structure is designed to produce a $< B >$ with radial variation corresponding to the curve labeled Fe, and a concentric layer of circular coils mounted on the pole face is used to shift the Fe profile up

[2]) N. M. King and W. Walkinshaw, Nuclear Instruments 2 (1958) 287.

or down as required. These circular trimming coils must produce a maximum field of about 550 gauss with radial variation as shown in the lower left of fig. 15. This trimming field must be

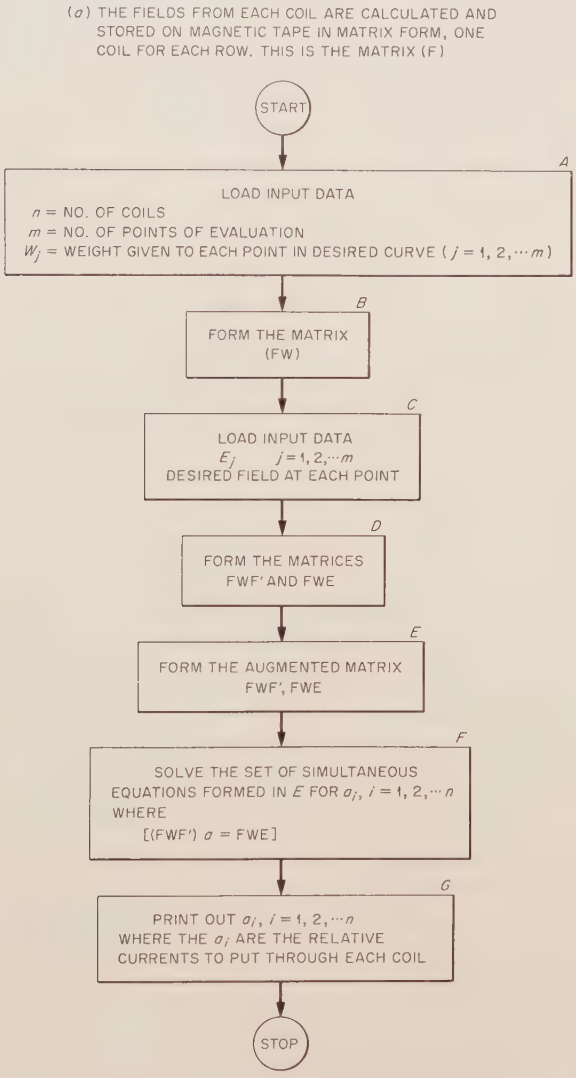
(a) THE FIELDS FROM EACH COIL ARE CALCULATED AND STORED ON MAGNETIC TAPE IN MATRIX FORM, ONE COIL FOR EACH ROW. THIS IS THE MATRIX (F)
START
A
LOAD INPUT DATA
n = NO. OF COILS
m = NO. OF POINTS OF EVALUATION
W_j = WEIGHT GIVEN TO EACH POINT IN DESIRED CURVE ($j = 1, 2, \cdots m$)
B
FORM THE MATRIX (FW)
C
LOAD INPUT DATA
E_j $j = 1, 2, \cdots m$
DESIRED FIELD AT EACH POINT
D
FORM THE MATRICES FWF' AND FWE
E
FORM THE AUGMENTED MATRIX FWF', FWE
F
SOLVE THE SET OF SIMULTANEOUS EQUATIONS FORMED IN E FOR a_i, $i = 1, 2, \cdots n$
WHERE
[(FWF') a = FWE]
G
PRINT OUT a_i, $i = 1, 2, \cdots n$
WHERE THE a_i ARE THE RELATIVE CURRENTS TO PUT THROUGH EACH COIL
STOP

Fig. 16. Circular coil current calculation, outline.

continuously adjustable from "full on" to "full reverse", and in addition substantial changes in shape are required.

The desired corrections can be accomplished by arranging the circular trimming coils in a pancake extending from near the center to the outside of the magnet, with the turns divided into approximately seven separately excited sections. Standard least-square procedures are used to determine the currents in the various sections which give the best fit to the difference between a particular isochronous field and the $< B >$ produced by the magnet at a given excitation. In the computation, it is of course necessary to know the radial dependence of the $< B >$ produced by a given trimming coil. For present purposes, this dependence has been approximately measured by inserting trimming coils in the model magnet. More precise measurements will be made on the full-scale magnet. The least squares computation, in common with nearly all the computations herein described, have been coded for either the Oracle or the IBM 704. Flow sheets, in outline and in detail, of the computer program used in the least squares computation † are given in figs. 16 and 17. The program is a typical example of the many useful programs which have been developed in the course of accelerator design studies at ORNL.

The computation assumes the incremental field produced by a given coil to be a linear function of the coil current. For currents of the order required, the model studies indicate this to be a valid assumption. It is quite possible that situations will be encountered where the assumption breaks down, in which case a non-linear least-squares procedures will be substituted. A routine for this type of calculation has already been worked out and although three to four times longer than the linear routine, the added difficulty is not of major character. For the input to this code, the non-linear relationship between $< B >$ and I for a particular coil would be determined by model measurements in the same fashion as for the linear problem except that measurements would have to be made at a number of different exciting currents.

Application of the fitting procedure to an actual situation is illustrated in fig. 18. In the problem the curve labeled $< B >$ (iron) is an actually observed set of values from a model run. The curve labeled $< B >$ (isochronous) is a calculated curve for nitrogen ions. Best values for the trimming coil currents were computed

† Program written by B. D. Williams.

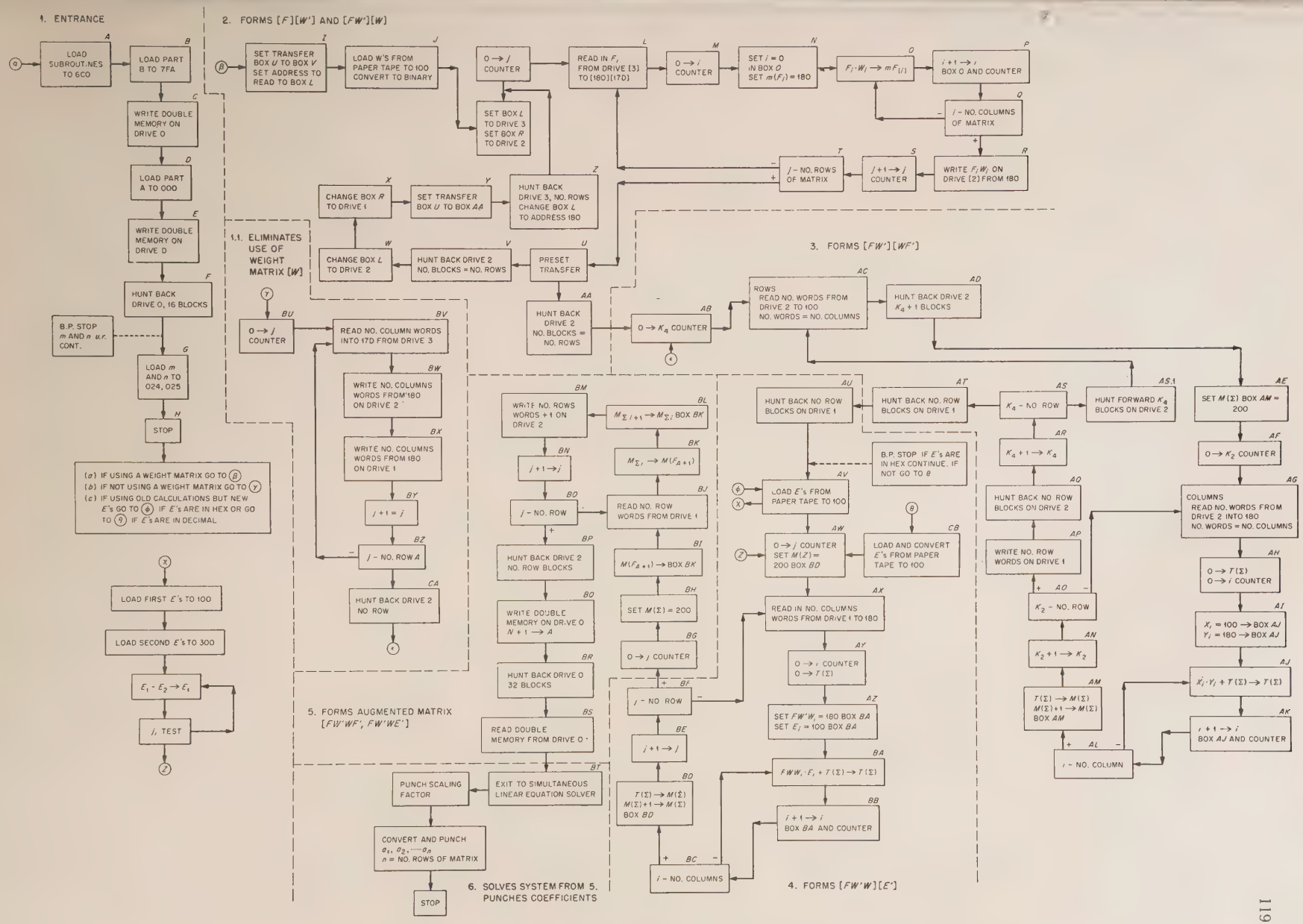
1. ENTRANCE
2. FORMS [F][W'] AND [FW'][W]
3. FORMS [FW'][WF']
4. FORMS [FW'W][E']
5. FORMS AUGMENTED MATRIX [FW'WF', FW'WE']
6. SOLVES SYSTEM FROM 5. PUNCHES COEFFICIENTS
1.1. ELIMINATES USE OF WEIGHT MATRIX [W]
LOAD SUBROUT. NES TO 6C0
LOAD PART B TO 7FA
WRITE DOUBLE MEMORY ON DRIVE 0
LOAD PART A TO 000
WRITE DOUBLE MEMORY ON DRIVE D
HUNT BACK DRIVE 0, 16 BLOCKS
B.P. STOP m AND n u.r. CONT.
LOAD m AND n TO 024, 025
STOP
(α) IF USING A WEIGHT MATRIX GO TO (β)
(b) IF NOT USING A WEIGHT MATRIX GO TO (γ)
(c) IF USING OLD CALCULATIONS BUT NEW E's GO TO (φ) IF E's ARE IN HEX OR GO TO (9) IF E's ARE IN DECIMAL
LOAD FIRST E's TO 100
LOAD SECOND E's TO 300
E1 - E2 → E1
j, TEST
SET TRANSFER BOX U TO BOX V SET ADDRESS TO READ TO BOX L
LOAD W'S FROM PAPER TAPE TO 100 CONVERT TO BINARY
0 → j COUNTER
SET BOX L TO DRIVE 3 SET BOX R TO DRIVE 2
READ IN F, FROM DRIVE [3] TO [180][170]
0 → i COUNTER
SET i = 0 IN BOX O SET m(Fi) = 180
Fi · Wj → mFij
i + 1 → i BOX O AND COUNTER
i - NO. COLUMNS OF MATRIX
WRITE FiWj ON DRIVE [2] FROM 180
j + 1 → j COUNTER
j - NO. ROWS OF MATRIX
HUNT BACK DRIVE 3, NO. ROWS CHANGE BOX L TO ADDRESS 180
SET TRANSFER BOX U TO BOX AA
CHANGE BOX R TO DRIVE 1
CHANGE BOX L TO DRIVE 2
HUNT BACK DRIVE 2 NO. BLOCKS = NO. ROWS
PRESET TRANSFER
HUNT BACK DRIVE 2 NO. BLOCKS = NO. ROWS
0 → Kq COUNTER
ROWS READ NO. WORDS FROM DRIVE 2 TO 100 NO. WORDS = NO. COLUMNS
HUNT BACK DRIVE 2 Kq + 1 BLOCKS
0 → j COUNTER
READ NO. COLUMN WORDS INTO 17D FROM DRIVE 3
WRITE NO. COLUMNS WORDS FROM 180 ON DRIVE 2
WRITE NO. COLUMNS WORDS FROM 180 ON DRIVE 1
j + 1 = j
j - NO. ROW A
HUNT BACK DRIVE 2 NO. ROW
WRITE NO. ROWS WORDS + 1 ON DRIVE 2
MΣ j+1 → MΣ j BOX BK
MΣ j → M(Fq+1)
j + 1 → j
j - NO. ROW
READ NO. ROW WORDS FROM DRIVE 1
HUNT BACK DRIVE 2 NO. ROW BLOCKS
M(Fq+1) → BOX BK
WRITE DOUBLE MEMORY ON DRIVE 0 N + 1 → A
SET M(Σ) = 200
HUNT BACK DRIVE 0 32 BLOCKS
0 → j COUNTER
READ DOUBLE MEMORY FROM DRIVE 0
j - NO. ROW
j + 1 → j
T(Σ) → M(Σ) M(Σ)+1 → M(Σ) BOX BD
i - NO. COLUMNS
HUNT BACK NO. ROW BLOCKS ON DRIVE 1
LOAD E's FROM PAPER TAPE TO 100
0 → j COUNTER SET M(Z) = 200 BOX BD
READ IN NO. COLUMNS WORDS FROM DRIVE 1 TO 180
0 → i COUNTER 0 → T(Σ)
SET FW'Wi = 180 BOX BA SET Ei = 100 BOX BA
FWWi · Ei + T(Σ) → T(Σ)
i + 1 → i BOX BA AND COUNTER
HUNT BACK NO. ROW BLOCKS ON DRIVE 1
B.P. STOP IF E's ARE IN HEX CONTINUE, IF NOT GO TO θ
LOAD AND CONVERT E's FROM PAPER TAPE TO 100
HUNT FORWARD Kq BLOCKS ON DRIVE 2
Kq - NO. ROW
Kq + 1 → Kq
HUNT BACK NO. ROW BLOCKS ON DRIVE 2
WRITE NO. ROW WORDS ON DRIVE 1
K2 - NO. ROW
K2 + 1 → K2
T(Σ) → M(Σ) M(Σ)+1 → M(Σ) BOX AM
i - NO. COLUMN
SET M(Σ) BOX AM = 200
0 → K2 COUNTER
COLUMNS READ NO. WORDS FROM DRIVE 2 INTO 180 NO. WORDS = NO. COLUMNS
0 → T(Σ) 0 → i COUNTER
Xi = 100 → BOX AJ Yi = 180 → BOX AJ
Xi · Yi + T(Σ) → T(Σ)
i + 1 → i BOX AJ AND COUNTER
PUNCH SCALING FACTOR
EXIT TO SIMULTANEOUS LINEAR EQUATION SOLVER
CONVERT AND PUNCH a1, a2, ··· an n = NO. ROWS OF MATRIX
STOP

Fig. 17. Circular coil current calculation, detail.

and the deviation of the resulting field from the desired $< B >$ (isochronous) is plotted on the lower curve, with scale on the right. Radial location of the coils is shown by the arrows along the radius axis. The residual error is quite small and mainly reflects errors in the model

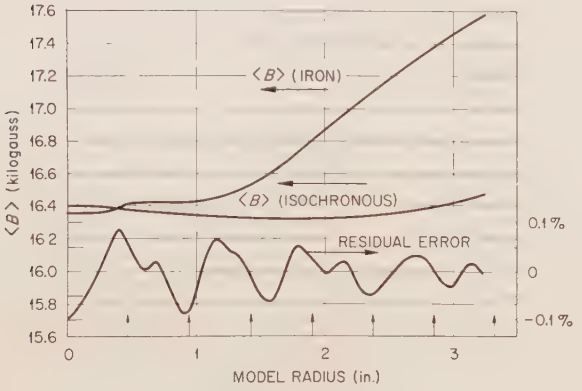

Fig. 18. An example of the accuracy to which $< B >$ can be corrected to isochronous value.

measurements. This is indicated by the lack of correlation between coil location and maxima and minima of the deviation, and has been further substantiated by runs in which analytical contours of form similar to the $< B >$ (iron) were used in place of the $< B >$ (iron). In these latter runs the deviations were a factor of four smaller and showed coherence with the coil location. The trimming procedures are hence of more than sufficient accuracy to meet the requirements. In operation the proper setting of the currents will be computed for every energy of every particle as needed.

The least-squares procedure occasionally gives an undesired result in that adjacent coils will be required to carry large oppositely directed currents which, to a large extent, cancel each other. When such situations arise, one of the pair of coils is removed from the problem and its current is adjusted individually to best fit the required $\Delta < B >$; the remaining coils are then adjusted to fit the remaining difference. The residual error is of course increased by the procedure, but in practice is still found to be small enough for the procedure to resolve the difficulty quite nicely.

In addition to providing a shift in field shape as required for change of particles, the trimming coils must also compensate for changes in field shape due to a shift in saturation effects as the field strength is varied. Measurements of the $< B >$ produced by particular tip configurations were made over wide ranges of field strength. The field shape shifts considerably at reduced fields but also, of course, the range of adjustment required for change of particles narrows rapidly as the field is reduced. The combined behavior requires a trimming coil capacity of 600 gauss for adequate control, which is only slightly greater than the 550 gauss required for change of particles at the maximum field strength.

4. Results and Conclusions

The early model work was directed toward determining the field obtainable from the presently existing magnet† as a function of the magnet gap, the power dissipation, and the positioning of the main exciting coils. From these studies and from other considerations (Sec. 1, above), the design maximum energies were decided upon.

The next series of experiments was directed toward determining the conditions necessary for focusing 75-MeV protons. It was soon found that for hill gaps in the range considered practicable, either a three-sector, weak-spiral (3S-WS) or a four-sector, tight-spiral (4S-TS) configuration would be necessary. These were then investigated for radial stability, first with theoretical fields and later with actual fields obtained from model measurements. As will be described in Part III, both 3S-WS and 4S-TS were found to give sufficient beam stability.

At this point, a series of investigations was undertaken to determine with reasonable accuracy the design parameters for the 3S-WS and 4S-TS cases in order to reach a decision between the two. The principal problems in this

† At this time fabrication of the steel for what was then known as the "48-inch Cyclotron" was already underway. The completed steel pieces for the yoke and poles of the magnet determine the basic dimensions of the newly designed accelerator.

program were in achieving adequate focusing at small radii and at the maximum radius (there is no difficulty at intermediate radii) while still retaining a reasonable hill gap.

The space requirements for the various items that must fit inside the hill gap are:

Pole-face windings	1 in.
Liner structure	$\frac{7}{8}$ in.
R-F voltage breakdown gap (100 kV)	$2\frac{3}{4}$ in.
Dee structure	$\frac{7}{8}$ in.
Total	$5\frac{1}{2}$ in.

It is apparent that to leave a reasonable space for the circulating beam, the hill gap can be no less than $6\frac{1}{2}$ in., and preferably as large as 8 or 9 in.

The problem of achieving adequate focusing at the maximum radius is straightforward. In the 4S-TS case, since the spiral is already maximized and the geometry makes the use of valley coils difficult, the hill gap is the only variable. In the 3S-WS case, the object was to keep the spiral very small. Since sufficient flutter could not be obtained by the iron alone, valley coils were necessary. Setting the power in the valley coils at 500 kW (the arbitrarily determined upper limit) and using as much spiral as seems prudent from stability considerations and compatible with simple valley coil design, we are left again with the hill gap as the only variable. The results of these investigations are shown in the first row of table 2. For focusing

TABLE 2
Maximum magnet gap (in inches) which will permit adequate focusing

	3S-WS	4S-TS	4-sector no spiral
Focusing at large radii	5.8 (7.5) †	9.5	4.3 (6.5) †
Focusing at small radii	9.0	7.0 (7.7) †	6.5 (7.2) †

† Values in parentheses are with 500 kW in valley coils.

at large radii a 7.5-in. gap is well within the limit for the 4S-TS case, adequate for the 3S-WS case if valley coils are used, and is much too large for a four-sector, no-spiral case.

The problem of achieving adequate focusing at small radii proved to be much more complex. Since $< B >$ must increase approximately as r^2 to maintain isochronism while F rises initially

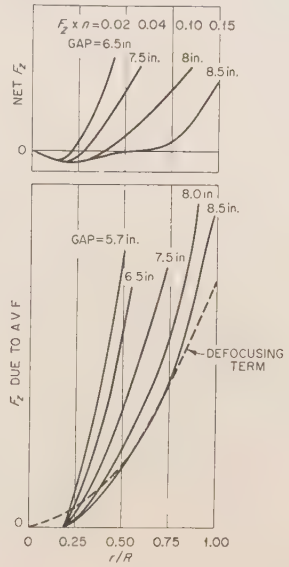

Fig. 19. Focusing in a four-sector, tight-spiral field.

as r^N, the first term in eq. (5) predominates at small radii, giving a net defocusing. The situation in a 4S-TS machine is shown in fig. 19; it is apparent that the difficulty is not easily overcome by decreasing the hill gap. Spiral is completely useless as it rises initially even less rapidly than flutter so that some defocusing seems inevitable. The total defocusing impulse is proportional to the defocusing force times the number of orbit turns; values of this quantity are given at the top of fig. 19 for each gap dimension shown. For comparison the total defocusing impulse in the 86-in. cyclotron is 0.04. Axial defocusing is, of course, the great weakness of all standard cyclotrons. According to fig. 19, the only possibility for reducing it lies in the abandonment of isochronism at small radii; this procedure is, of course, severely limited by the requirement that ions do not get out of phase with the r-f voltage, or equivalently, with a hypothetical ion in an isochronous cyclotron, by more than 90 degrees.

The procedure for investigating nonisochronous magnetic fields was to (1) assume a field shape; (2) calculate the phase as a function of turn number (if it ever gets larger than 90 deg a new field shape must be assumed); (3) calculate the axial forces, both magnetic and electric; and (4) compute the net defocusing impulse as

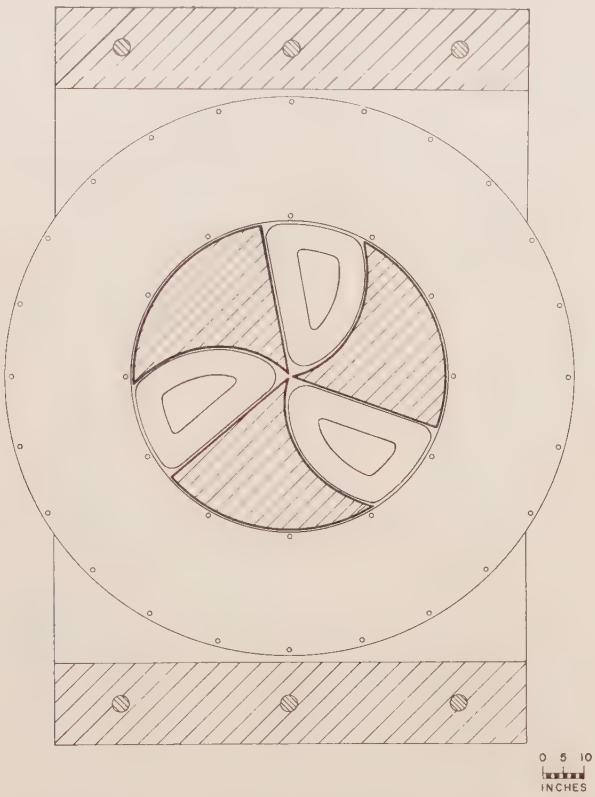

Fig. 20.
Pole configuration of the three-sector, weak-spiral magnet.

defined above. All calculations were numerical and on a turn-by-turn basis, although usually steps of five or even ten turns at a time could be used.

Two approaches were investigated by these calculations; in the first, the magnetic field was lowered in the center in order to shift the phases so as to cause the ions to arrive at the dee gaps after the electric field has passed its maximum (that is, the phase is positive); they thus experience electric phase focusing which, it was hoped, might overcome the magnetic defocusing. The difficulty with this approach is that the magnetic field must eventually reach (and even somewhat exceed) the isochronous field, and to do so, must increase with radius even more rapidly than the isochronous field. This gives magnetic defocusing from the first term of eq. (5), and for all cases studied, this added defocusing was far larger than the electric focusing obtained.

In the second approach, the average magnetic field was made to decrease with increasing radius at small radii, to obtain focusing from the first term in eq. (5). Here again, the magnetic field must eventually reach the isochronous field and to do so must increase even more rapidly than the isochronous field so that an added defocusing is experienced. However, in some cases at least, this field increase could be postponed to radii where the AVF focusing is strong enough to overcome it. To achieve such a long postponement, it is necessary to make the magnetic field larger than the isochronous one at the center of the cyclotron, and let is fall off with radius until it is well below the isochronous field before beginning to increase at radii where the AVF focusing becomes eflective. The phase is thus shifted negative and then back through zero to positive just as in a standard cyclotron. The negative phase during the first several turns causes electric defocusing, but the net defocusing impulse can be substantially reduced relative to that in the corresponding isochronous field. The essential element in determining whether this method works is whether the magnetic field increase can be postponed long enough for the AVF focusing to overcome its effect. This is very sensitive to the hill gap since this determines where the AVF becomes effective. The maximum hill gaps for which this method gives good results are listed in the second row of table 2. For focusing at small radii a 7.5-in. gap is well within the limit for the 3S-WS case, would require valley coils in the 4S-TS case, and would be unsatisfactory for the four-sector no-spiral case.

Actually, these values are also quite sensitive to the dee voltage, since this determines the number of turns required to reach a given radius,

and thus the phase shifting. Increasing the dee voltage, however, requires increasing the required voltage breakdown gap and thus the magnet hill gap, so that some compromise must be reached. While these effects were not investigated in detail, it was determined that a voltage of 400 kV/turn is not far from optimum,

$$\nu_r^2 = 1 + \frac{r}{\langle B \rangle} \frac{\mathrm{d}\langle B \rangle}{\mathrm{d}r}$$

so that at the radius where the magnetic field is flat in changing over from decreasing to increasing with increasing radius, $\nu_r = 1$. The particles spend only a small amount of time near this resonance so that it might be hoped that its

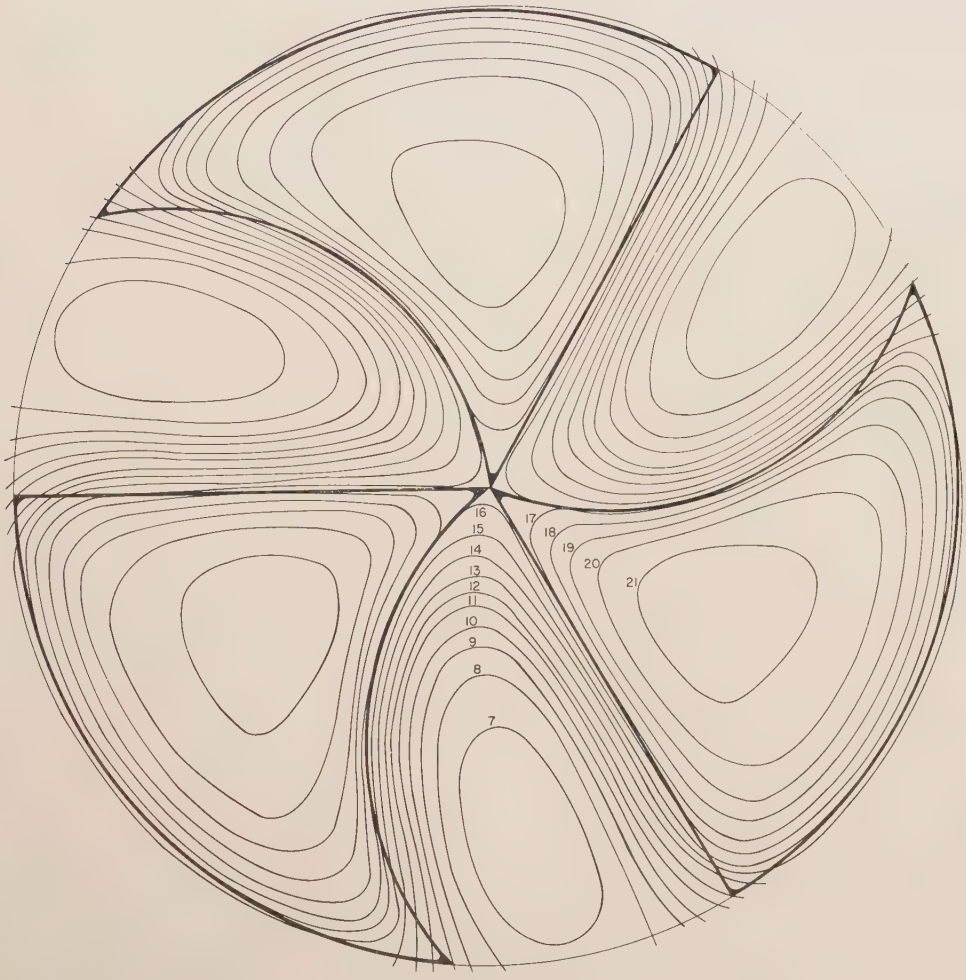

Fig. 21. Field contours of the three-sector, weak spiral magnet. (Field in kilogauss. Sector coils energized.)

and since that voltage is most compatible with other requirements (especially radial stability), it was used in the calculations.

The magnetic field fall-off method introduces still another problem; the ions must pass through a radial oscillation resonance. The radial oscillation frequency is given approximately by

effect may not be catastrophic. However, this point should be carefully investigated before this method of achieving axial focusing is used.

From table 2 it is clear that either a 3S-WS or a 4S-TS cyclotron could be built with about a $7\frac{1}{2}$-in. hill gap; this corresponds to 2 in. of beam space, which is considered relatively adequate. In the 3S-WS case, valley coils

would be needed, but the situation at small radii is much more favorable than in the 4S-TS. In the latter, a rather intricate and delicately balanced field shape must be obtained, an advantage would seem to easily justify the addition of valley coils.

As a result of all these investigations, it had become abundantly clear that a very high

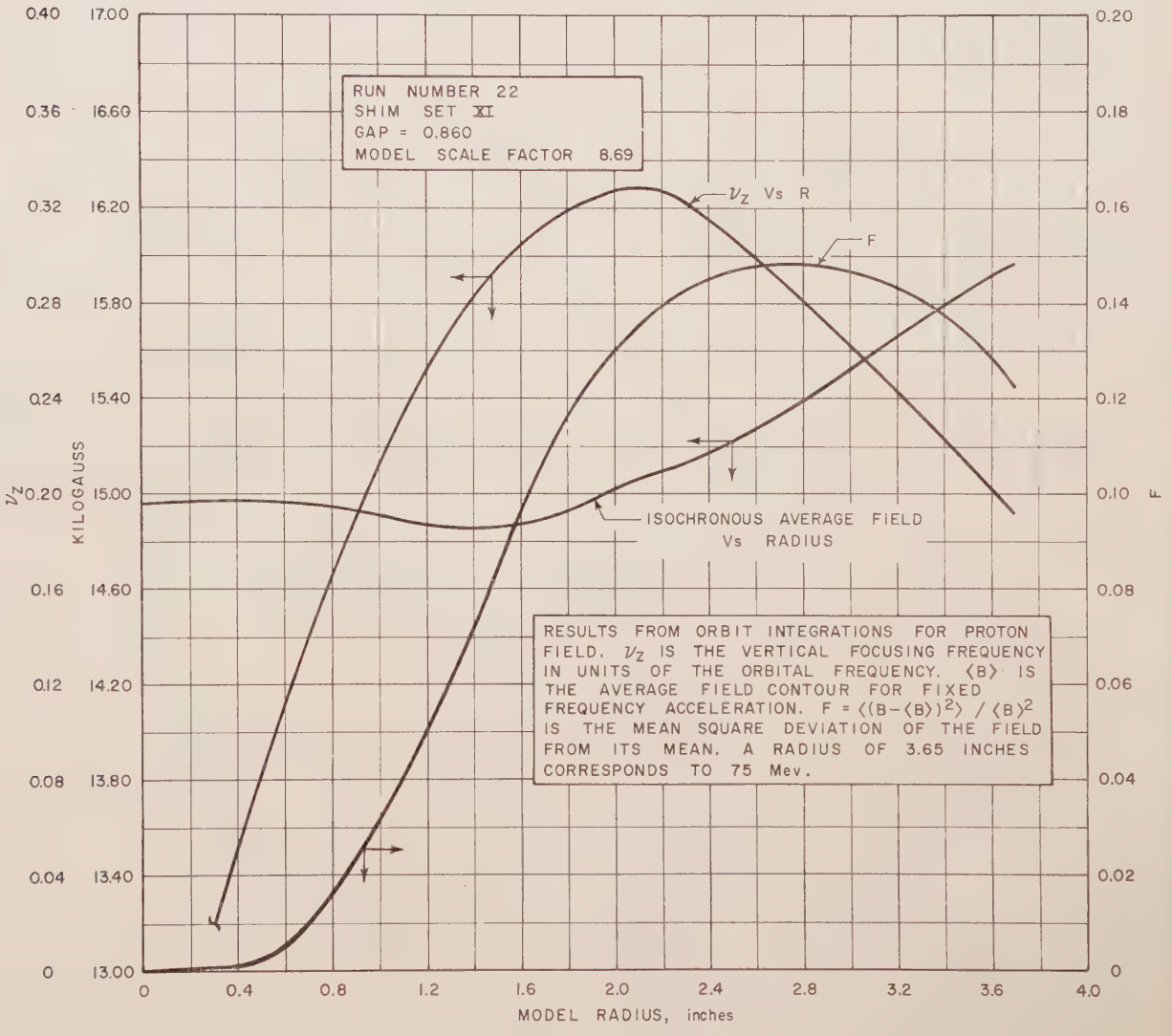

Fig. 22. Net focusing for 75-MeV protons.

integral resonance for radial oscillations must be passed through, and there is still a moderate defocusing impulse during the first several turns. In the 3S-WS case the situation is so overdesigned at small radii with a $7\frac{1}{2}$-in. hill gap that, it turns out, even an isochronous magnetic field gives no defocusing and, of course, avoids the other above-mentioned difficulties. The premium should be placed on hill-gap space; practically every difficulty in the design can readily be overcome by reducing this gap. At this time, therefore, careful consideration was given to the fact that, in all of the design that had been considered, about $\frac{2}{3}$ of the gap ($4\frac{1}{2}$ in.) is being used for the r-f system. This situation is difficult to change as long as a dee structure is

used; thus, consideration was given to the use of resonant cavities placed in the valleys. This would allow the gap to be reduced sufficiently for a four-sector machine with no spiral to give good focusing at all radii (table 2). Such a machine would, of course, be ideal from the standpoint of radial stability.

It was finally decided, however, in view of the fact that the 3S-WS machine with a $7\frac{1}{2}$-in. hill gap appeared to be completely feasible and was in a relatively advanced state of design, that it would not be profitable to undertake the numerous new engineering problems that would be introduced by so radical a change in design. Therefore, the 3S-WS design was adopted. The shape of the poles and the magnetic field contour are shown in figs. 20 and 21. The average field, flutter, and net focusing as a function of radius are shown for 75-MeV protons in fig. 22 and for 90-MeV N^{4+} ions in fig. 23.

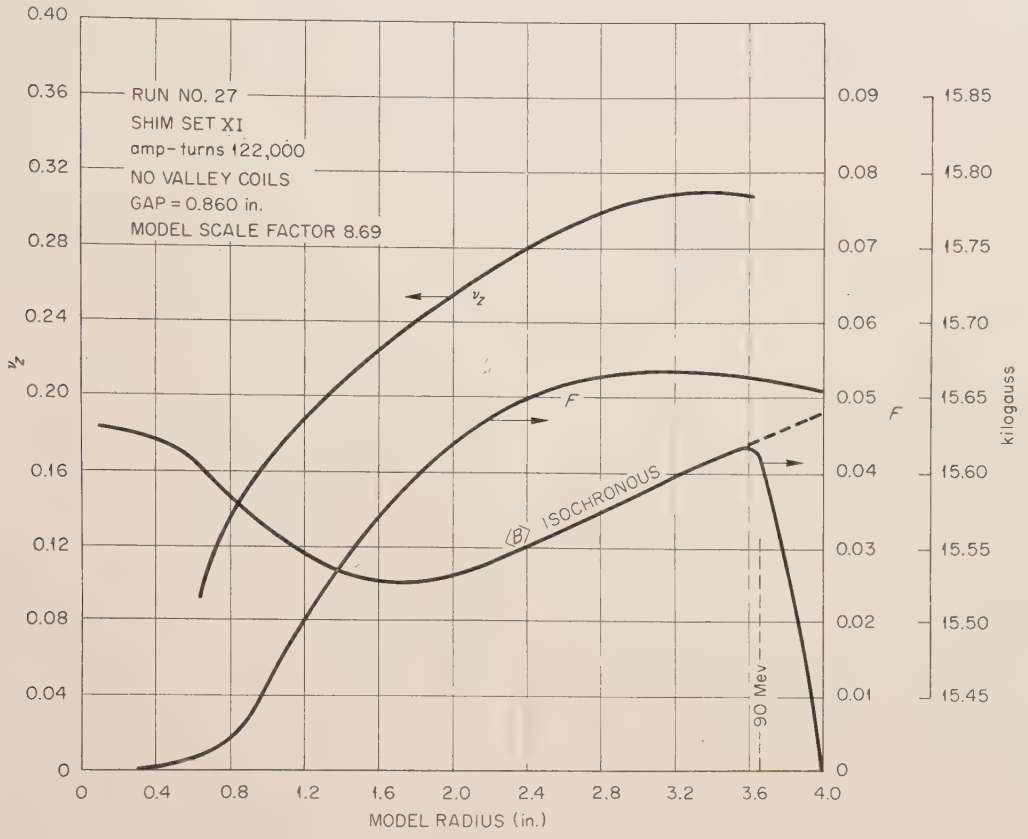

Fig. 23. Net focusing for 90-MeV N^{4+} ions.

As this manuscript is being prepared for publication, preliminary measurements are being made with the $\frac{1}{4}$-scale model magnet. Measurements from this model will be used to verify and extend the information on the orbit and focusing properties of the cyclotron previously explored on the $\frac{1}{9}$-scale model. The more precise data expected from the $\frac{1}{4}$-scale model will be used in designing a resonant deflection system, using techniques to be described in Part III of this article.

NUCLEAR INSTRUMENTS AND METHODS 6 (1960) 126–156; NORTH-HOLLAND PUBLISHING CO.

LES LENTILLES QUADRUPOLAIRES MAGNETIQUES (I)

PIERRE GRIVET et ALBERT SEPTIER†

Laboratoire d'Electronique et Radioélectricité de la Faculté des Sciences de Paris

B.P. No. 9, Fontenay-aux-Roses (Seine)

Reçu le 19 mai 1959

In the first part we recall the physical properties of quadrupole lenses.

Integration of the equations of motion is possible if the characteristic function of the transverse gradient is represented by simple mathematical models i.e. rectangular or bell shaped models.

We give the formulae of the main elements of a lens and of a system of two crossed lenses.

The second part is devoted to measures of field and gradient on typical magnetic lenses for CERN's 50 MeV linear proton accelerator, i.e. determination of the various components of field and transverse gradient inside the lens and in the leakage fields, calculation of equivalent lengths relative to the transverse field and to the gradient and correction of the variations of these equivalent lengths in the useful space.

Measurements made with very high intensities on saturated lenses show that the poles do not saturate and thus the field configuration is not disturbed. The measuring instruments used are described in detail and results are given in graphical form.

INTRODUCTION

1. Applications actuelles des lentilles quadrupolaires

1.1. LES LENTILLES QUADRUPOLAIRES DANS LE SYNCHROTRON A PROTONS DU CERN

Le groupe du synchrotron à protons, utilisera des lentilles quadrupolaires magnétiques dans deux buts bien distincts:

1.1.1. A l'injection, pour adapter au mieux l'émittance de la source (constituée ici par l'orifice de sortie de l'accélérateur linéaire de 50 MeV) et l'acceptance du synchrotron[1]). On recherche le rendement unité dans cette opération en tenant compte de l'action des déflecteurs. Une étude au premier ordre des propriétés optiques devra être complétée d'une estimation puis d'une correction poussée des aberrations, celles-ci provoquant une perte de particules difficile à évaluer. Le dispositif se compose en principe de deux groupes de 2 lentilles quadrupolaires magnétiques, fonctionnat en régime statique††. Dans chaque groupe, les centres des lentilles seront distants de 0.50 m et la distance focale globale pourra varier de 1 à 3.5 m environ.

1.1.2. Tout au long de l'anneau, des paires de lentilles régulièrement disposées permettront de compenser, durant le cycle d'accélération, les perturbations provoquées par les variations de l'indice n des aimants (ou plus exactement de compenser la valeur de ces variations intégrée sur un tour) et de traverser plus facilement la zone de l'énergie de transition. On peut ainsi éviter pratiquement les zones d'instabilité et les oscillations qui provoqueraient la destruction du faisceau. Ces lentilles, fonctionnant en impulsions, selon une loi de courant liée directement aux variations de n, sont beaucoup plus importantes que les précédentes, puisqu'agissant sur des particules plus rapides, mais le même soin doit être apporté dans la réalisation du champ,

†† Cet article résulte du travail effectué depuis 1953 par les deux auteurs, au sein du "Proton synchrotron Group du CERN". Ils sont heureux de remercier les members de ce groupe, MM. J. B. Adams, H. G. Hereward et P. Lapostolle avec qui ils ont eu des discussions fructueuses.

† Par opposition au régime d'impulsion qui peut être envisagé aussi dans ce type d'application pour réduire l'échauffement moyen.

[1]) H. G. Hereward, K. Johnsen et P. Lapostolle, Problems of Injection. CERN Symposium 1956, part I, p. 179–191;

P. Lapostolle, Nouveau schéma de déflection, CERN, PS/PL 5 (1955) non publié.

en particulier sur les bords, pour ne pas imposer de nouvelles perturbations au faisceau. L'étude du profil à donner aux pôles a été déterminée par voie analogique[2]).

Mais l'intérêt des lentilles quadrupolaires dépasse de beaucoup ce premier cadre. Nous envisagerons rapidement les autres applications possibles, pour lesquelles les résultats de l'étude qui va suivre conservent leur valeur.

1.2. LES LENTILLES QUADRUPOLAIRES DANS LES ACCELERATEURS

1.2.1. Focalisation des faisceaux émergents

On pourra les utiliser pour focaliser le faisceau émergent sur une cible, afin d'y accroître la densité de courant; il s'agit alors de systèmes optiques simples, qu'on peut calculer à l'aide des lois de l'optique classique.

L'astigmatisme des lentilles est particulièrement utile pour former l'image d'une source ronde sur la fente d'entrée d'un analyseur.

On pourra aussi constituer à l'aide d'un très grand nombre de lentilles faibles à convergence alternée, un dispositif de canalisation permettant de guider sur une grande distance des particules de très haute énergie, en particulier des mésons μ[3]).

1.2.2. Focalisation dans les accélérateurs linéaires

La focalisation par grilles entraîne une forte perte de particules. On a songé à introduire des quadrupôles dans les tubes de glissement. Pour des énergies supérieures à 10 MeV, les tubes sont longs et la force défocalisante est relativement faible: des gradients de quelques webers par mètre suffisent et on pourra utiliser des quadrupôles magnétiques en régime statique, des aimants permanents par exemple.

Vers les faibles énergies au contraire, les tubes sont très courts et les forces défocalisantes beaucoup plus fortes: on ne pourra atteindre les convergences nécessaires qu'en alimentant les quadrupôles magnétiques en impulsions de courant, solution qui, étudiée au CERN par P. Lapostolle, sera appliquée entre 0.5 et 10 MeV, dans la première cavité de l'accélérateur linéaire.

1.3. LES LENTILLES QUADRUPOLAIRES DANS D'AUTRES DOMAINES

1.3.1. Action sur les dipôles

Les lentilles quadrupolaires permettront de focaliser toute particule douée d'un moment magnétique ou électrique en appliquant la proposition initiale de R. Vauthier[4]). Certaines molécules possèdent un moment dipolaire électrique; d'autres l'acquièrent lorsqu'elles sont placées dans un champ électrique. Une lentille quadrupolaire suffisamment longue permettra de séparer des molécules d'énergies thermiques différentes sortant d'une source convenable, et de les focaliser en un point. Un jet de molécules d'ammoniac de moment donné peut ainsi être concentré dans une cavité résonnante pour l'obtention d'un oscillateur, ou d'un amplificateur du type "Maser".

1.3.2. Sources d'ions polarisés

La même idée peut être transposée dans le domaine magnétique: la lentille polarise tout d'abord des atomes d'hydrogène puis canalise jusqu'à une chambre d'ionisation à faisceau électronique les atomes ayant une polarisation donnée, en éliminant les atomes indésirables. On obtient ainsi directement une source de protons polarisés de forte intensité, pouvant servir dans tous les types d'accélérateurs. Une source de ce type est en voie de réalisation au CERN[5]).

1.3.3. Séparation des ions

Des lentilles quadrupolaires magnétiques à fonctionnement statique peuvent permettre la séparation d'isotopes légers; nous le verrons à la fin de cette étude. Mais des lentilles électriques excitées en H.F. (de 5 à 15 MHz) sont utilisées effectivement pour filtrer des masses[6]); les ions

[2]) Van der Meer, The Design of Quadrupole lenses for the proton synchrotron, CERN-PS/MM 31 (1957).

[3]) A. Citron et H. Øverås, On a focusing channel for collecting μ mesons from π-μ-decay in flight, CERN-SC 27/3/57.

[4]) R. Vauthier, Un dispositif pour focaliser les particules neutres-C.R. **228** (1949) 1113.

[5]) R. Keller, Projet d'une source d'ions polarisés, CERN-SC/57-30 (1957).

[6]) W. Paul et M. Raether, Das elektrische Massenfilter, Zeit. für Phys. **140** (1955) 262–273.

injectés à très faible énergie (200 à 400 volts) traversent des zones alternativement convergentes et divergentes. A chaque masse M correspondra une seule fréquence f du champ H.F. conduisant à des trajectoires stables. Avec une lentille suffisamment longue et des courants très faibles, le pouvoir séparateur peut facilement dépasser 100.

1.3.4. Obtention de systèmes de révolution

L'association de lentilles quadrupolaires conduit à des systèmes très astigmatiques. En choisissant bien les excitations, on peut faire l'image d'un point donné en un autre point, mais en général les grandissements linéaires diffèrent dans les deux plans de symétrie radiaux.

On a cherché s'il était possible d'obtenir un système optique équivalent à un système de révolution: il faut que les convergences et les foyers soient les mêmes dans les deux plans.

Avec deux lentilles identiques nous avons déterminé ici un point de fonctionnement possible, et montré qu'on pouvait faire des images de bonne qualité en microscopie électronique, mais le système a alors ses foyers immergés. La distance focale ets de l'ordre de 3 à 5% de la longueur d'une lentille.

Il serait très intéressant de déterminer un système de révolution formé de plusieurs lentilles fortes ayant ses foyers à l'extérieur: la version électrostatique pourrait être utilisée pour la focalisation des faisceaux issus de sources d'ions, car les tensions à appliquer seraient très faibles, et les lentilles quadrupolaires pourraient travailler avec des ouvertures plus fortes et des aberrations plus faibles que les lentilles classiques utilisées jusqu'ici dans ce but.

2. Différents types de lentilles

Le mode d'excitation des pôles, électrique ou magnétique, permet de distinguer deux catégories de lentilles, dont les limites vers les hautes énergies sont très différentes.

2.1. LENTILLES ELECTROSTATIQUES

De construction simple, et très légères si on les compare aux lentilles magnétiques, elles sont un outil commode pour la focalisation de particules d'énergie relativement basse, inférieure à 10 ou 20 MeV. Les phénomènes de claquages limitent en effet les différences de potentiel entre électrodes voisines à 50 keV environ, et, bien que la convergence soit proportionnelle à la longueur de la lentille, nous verrons qu'on ne peut accroître trop la valeur de ce paramètre sans perdre une grande partie des particules à focaliser. Un fonctionnement en impulsions de tension très courtes (de l'ordre de la microseconde) permettrait d'accroître encore la tension par un facteur 2 au moins, donc la convergence. Ce mode de fonctionnement pulsé pourrait être envisagé pour des faisceaux d'électrons issus d'accélérateurs linéaires.

Ces lentilles doivent être placées dans l'enceinte à vide, ce qui est parfois un désavantage. Mais leur maniement facile et leur fonctionnement insensible à la masse des particules, permettent de les utiliser comme modèle pour l'étude des propriétés d'un système optique complexe. Il suffit de le réaliser à petite échelle et d'y injecter des particules chargées de faible énergie. Une similitude convenable permet ensuite de revenir au système original.

2.2. LENTILLES MAGNETIQUES

Beaucoup plus encombrantes que les précédentes, elles offrent l'immense avantage d'être encore efficaces jusqu'aux plus hautes énergies actuellement réalisées. Il suffit de les dimensionner de façon convenable.

Pour une construction et des particules d'énergie données, la convergence est limitée par les phénomènes de saturation de la carcasse magnétique. Nous verrons qu'il est pratiquement impossible de saturer les pôles eux-mêmes: ceux-ci restant des surfaces équipotentielles magnétiques. Les propriétés optiques resteront donc semblables à elles-mêmes, si on conserve la même relation entre l'excitation de la lentille et l'énergie des particules injectées, ce qui nous a permis l'étude directe de ces propriétés (en particulier des aberrations) à l'aide de faisceaux d'ions de faible énergie. Avec ces lentilles il est même possible de simuler des particules légères

de haute énergie en utilisant des ions lourds de basse énergie, puisque seule la quantité de mouvement intervient dans les équations du mouvement.

3. But du travail

En résumé, l'étude entreprise dans notre laboratoire sous l'impulsion du groupe du proton synchrotron du CERN a eu pour but:

– la réalisation pratique de lentilles relativement faibles destinées à l'adaptation du faisceau à l'injection dans le synchrotron;

– la détermination précise de la répartition des composantes du champ magnétique, aussi bien dans la zone centrale où on s'efforce d'obtenir la distribution théorique à gradient radial constant dans une région la plus étendue possible, que dans les champs de fuite des extrémités où apparaissent des perturbations provoquant des aberrations;

– de déterminer l'influence possible de la saturation sur la topographie du champ dans la zone utile;

– la détermination des propriétés optiques au premier ordre d'un système de deux lentilles;

– la mesure des aberrations par un procédé direct, en utilisant des faisceaux ioniques sur un banc d'optique spécialement construit et adapté à ce genre d'étude;

– enfin, la correction de ces aberrations, dont la présence se traduit par une perte de particules.

Nous donnerons en outre les résultats des calculs d'aberrations effectués concurremment aux expériences à l'aide de machines électroniques.

PREMIERE PARTIE

PROPRIETES OPTIQUES AU PREMIER ORDRE

Nous résumerons ici les résultats essentiels de cette théorie classique, auxquels nous aurons recours très souvent dans la suite.

1. Expression du potentiel et des champs

Dans l'hypothèse où les électrodes matérialisent des surfaces équipotentielles, la répartition cherchée du champ est obtenue grâce à quatre électrodes de longueur l disposées parallèlement à l'axe Oz et dont la méridienne, dans un plan XOY normal à Oz est une hyperbole équilatère (fig. 1a) d'équation $XY = \pm \frac{1}{2} a^2$ ou $x^2 - y^2 = \pm a^2$.

Les quatre hyperboles sont tangentes à un cercle de rayon a, que nous appellerons "cercle de gorge". Il faut en réalité se limiter à des segments d'hyperbole (fig. 1b) de largeur D telle que la répartition idéale subsiste sensiblement dans l'espace utile: $X, Y \leqslant a$.

Les pôles opposés sont Nord ou Sud dans le cas magnétique, et correspondent à des potentiels scalaires $\pm \psi_1$. Lorsqu'on est suffisamment loin des extrémités, le champ est purement transversal: il se réduit à B_X dans le plan YOz, à B_Y dans le plan XOz; il est purement radial: B_x et B_y dans les autres plans de symétrie xOz et yOz. Dans tout ce qui suit, on convient de désigner le plan XOz par la dénomination

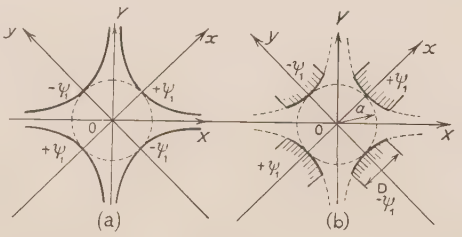

Fig. 1

"plan convergent" et YOz par celle de "plan divergent", pour des particules positives incidentes.

Le potentiel scalaire ψ en un point quelconque M de l'espace utile est donné par une expression de la forme[6a])

[6a]) M. Y. Bernard, Lentilles électrostatiques permettant la focalisation des particules de grande énergie—Répartition des champs, C.R. **236** (1953) 185–187.

$$\psi(X,Y,z) =$$

$$\frac{2\psi_1}{a^2} = \left[-XY\cdot k(z) + \frac{1}{12}XY(X^2+Y^2)\frac{\mathrm{d}^2k}{\mathrm{d}z^2} + \cdots\right].$$

La fonction $k(z)$ est égale à l'unité dans la zone centrale éloignée des extrémités ($k(0) = 1$), mais n'est pas représentée par une fonction analytique simple dans la zone des champs de fuites.

Le potentiel ψ_1 est relié de façon simple au nombre d'ampèretours nI relatifs à un pôle, dans le cas où l'on peut attribuer une perméabilité infinie à l'acier doux.

$$\psi_1 = nI\,.$$

De l'expression $\boldsymbol{B} = -\mu_0\, grad\, \psi$, on tire l'expression des composantes du champ; si on s'en tient au terme fondamental de ψ:

$$B_x = \frac{2\mu_0 n\dot{I}}{a^2}\,Y\cdot k(z)\,, \qquad B_y = \frac{2\mu_0 n\dot{I}}{a^2}\,X\cdot k(z)$$

$$B_{(z)} = \frac{2\mu_0 n\dot{I}}{a^2}\,XY\,\frac{\mathrm{d}k(z)}{\mathrm{d}z}\,.$$

Le gradient radial du champ transversal est alors

$$K(z) = \frac{\partial BX}{\partial Y} = \frac{\partial BY}{\partial X} = \frac{2\mu_0 n\dot{I}}{a^2}\,k(z)$$

où encore $K(z) = K(0)\cdot k(z)$ avec

$$K(0) = \frac{2\mu_0 nI}{a^2} \qquad \text{et} \qquad k(0) = 1\,.$$

$K(0)$ représente le gradient dans la zone centrale (on suppose la lentille assez longue pour que la répartition idéale existe sur une certaine longueur au voisinage de $z = 0$).

La fonction $k(z)$ est la "fonction caractéristique" de la lentille.

Remarque:

Dans le cas électrique, on aurait les mêmes expressions, en remplaçant $\mu_0 nI$ par Φ_1, potentiel de l'électrode positive, et ψ par Φ, potentiel en un point. La fonction $k(z)$ serait inchangée.

2. Equations du mouvement au premier ordre

On part de l'équation fondamentale

$$m\frac{\mathrm{d}\boldsymbol{v}}{\mathrm{d}t} = e\,(\boldsymbol{v}\wedge\boldsymbol{B})$$

où $\boldsymbol{v}$ est la vitesse, m la masse de la particule, e sa charge et $\boldsymbol{B}$ le vecteur induction. On utilise également l'intégrale première de la force vive

$$\tfrac{1}{2}mv^2 = e\Phi_0\,.$$

On peut négliger la correction relativiste, ce qui est encore justifié pour des protons de $\Phi_0 = 50$ MeV. On considère en première approximation que la vitesse est purement longitudinale:

$$v = \frac{\mathrm{d}z}{\mathrm{d}t} = \sqrt{\frac{2e\Phi_0}{m}} \qquad \text{où} \qquad \frac{\mathrm{d}.}{\mathrm{d}t} = \sqrt{\frac{2e}{m}\Phi_0}\,\frac{\mathrm{d}.}{\mathrm{d}z}$$

ce qui revient à négliger les termes en $\mathrm{d}X/\mathrm{d}t$ et $\mathrm{d}Y/\mathrm{d}t$ c'est-à-dire l'inclinaison sur l'axe Oz du vecteur vitesse $\boldsymbol{v}$.

On suppose au premier ordre que l'induction B est purement transversale et proportionnelle à la distance à l'axe: on néglige ici les termes non linéaires, du type de ceux qui apparaissent dans les champs de fuite, et dus en particulier à la présence de la composante B_z parallèle à Oz.

On arrive alors aux équations des trajectoires dans les plans de symétrie XOz et YOz:

$$\frac{\mathrm{d}^2X}{\mathrm{d}z^2} + \beta^2\cdot k(z)\cdot X = 0$$

$$\frac{\mathrm{d}^2Y}{\mathrm{d}z^2} - \beta^2\cdot k(z)\cdot Y = 0$$

où β est un facteur caractéristique de l'excitation des lentilles

$$\beta^2 = K(0)\cdot\frac{e}{mv}$$

où

$$\beta^2 = \frac{\mu_0 n\dot{I}}{a^2}\cdot\sqrt{\frac{2e}{m\Phi_0}}$$

pour des particules relativistes on aurait

$$\beta^2 = \frac{\mu_0 n\dot{I}}{a^2}\sqrt{\frac{2e}{m_0\Phi_0(1+\frac{1}{2}\varepsilon)}}$$

avec

$$\varepsilon = \frac{e\Phi_0}{m_0c^2} = \frac{\text{énergie cinétique}}{\text{énergie au repos}}\,.$$

On aboutit donc à un système simple d'équations non couplées. Nous verrons dans la quatrième partie qu'il n'est plus de même au 3ème ordre

Remarque:

On obtient des équations de mouvement identiques dans une lentille électrique, à condition de faire subir aux axes de coordonnées une

rotation de $+\frac{1}{4}\pi$: OX et OY sont remplacés par Ox et Oy.

Dans ce cas le facteur caractéristique est donné par

$$\beta^2 = \frac{1}{a^2}\frac{\Phi_1}{\Phi_0}$$

pour les faibles énergies et

$$\beta^2 = \frac{1}{a^2}\frac{\Phi_1\,(1+\varepsilon)}{\Phi_0\,(1+\frac{1}{2}\varepsilon)}$$

pour des particules relativistes.

3. Trajectoires, éléments cardinaux d'une lentille

3.1. INTEGRATION DES EQUATIONS: MODELE RECTANGULAIRE

On peut intégrer les équations du mouvement. dans les plans OX et OY, si on connaît $k(z)$ Cette fonction ayant une expression analytique complexe[6b]), il faut avoir recours à des modèles plus simples.

$k(z)$ représente en effet, à un facteur près, la répartition du champ transversal B_r sur des parallèles à Oz; celle-ci a l'aspect représenté fig. 2 pour une lentille suffisamment longue:

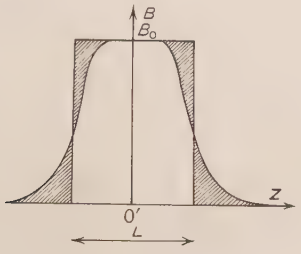

$$\int_{-\infty}^{+\infty} B\cdot \mathrm{d}z = B_0 L.$$

Fig. 2. Modèle rectangulaire.

deux demi-cloches séparées par un plateau central où $B_r = B_0$. La solution la plus simple consiste à considérer une lentille fictive équivalente à la lentille réelle et ayant les propriétés suivantes: le champ B_r est nul de $-\infty$ à $-\frac{1}{2}L$ et de $+\frac{1}{2}L$ à $+\infty$; il est égal à B_0 de $-\frac{1}{2}L$ à $+\frac{1}{2}L$. La fonction champ $B(z)$ est alors un rectangle de hauteur B_0 et de longueur L telle que son aire soit égale à celle de la courbe réelle (fig. 2).

$$S = \int_{-\infty}^{+\infty} B\,\mathrm{d}z = B_0\,L\,.$$

C'est le "modèle rectangulaire".

[6b]) M. Y. Bernard, La focalisation forte dans les accélérateurs linéaires d'ions, Ann. de Phys. Paris **9** (1954) 633.

La longueur L, comme nous le verrons, est légèrement supérieure à la longueur mécanique l des pôles. L sera appelée "longueur efficace" de la lentille.

On a alors, puisque $k(z) = 1$ dans tout l'espace occupé par la lentille et $k(z) = 0$ en dehors:

$$\frac{\mathrm{d}^2X}{\mathrm{d}z^2} + \beta^2 X = 0$$

$$\frac{\mathrm{d}^2Y}{\mathrm{d}z^2} - \beta^2 Y = 0$$

et

$$X = A\cos\beta z + B\sin\beta z$$

$$Y = C\,\mathrm{ch}\,\beta z + D\,\mathrm{sh}\,\beta z$$

A, B, C et D sont déterminées grâce aux conditions initiales, l'origine des z étant maintenant dans le plan d'entrée.

Si on considère un faisceau incident parallèle, on détermine facilement les éléments cardinaux définis à partir des rayons extérieurs à la lentille (fig. 3). Dans le plan convergent XOz (fig. 3a)

$$f'_X = \overline{H'_X F'_X} = \frac{1}{\beta\sin\beta L}\,; \qquad Z_{F'X} = \frac{L}{2} + \frac{\cos\beta L}{\beta\sin\beta L}$$

et

$$Z_{H'X} = \frac{L}{2} - \frac{1-\cos\beta L}{\beta\sin\beta L}$$

Dans le plan divergent OY (fig. 3b)

$$f'_Y = \overline{H'_Y F'_Y} = -\frac{1}{\beta\,\mathrm{sh}\,\beta L}\,; \qquad Z_{F'Y} = \frac{L}{2} - \frac{\mathrm{ch}\,\beta L}{\beta\,\mathrm{sh}\,\beta L}$$

et

$$Z_{H'Y} = \frac{L}{2} - \frac{\mathrm{ch}\,\beta L - 1}{\beta\,\mathrm{sh}\,\beta L}\,.$$

Une lentille seule transforme un faisceau incident de révolution en un faisceau à section elliptique s'appuyant sur une focale réelle et une focale virtuelle.

Dans le cas où le facteur (βL) est très petit, on peut écrire

$$\sin\beta L = \mathrm{sh}\,\beta L = \beta L\,, \qquad \cos\beta L = 1 - \tfrac{1}{2}(\beta L)^2$$

et

$$\mathrm{ch}\,\beta L = 1 + \tfrac{1}{2}(\beta L)^2\,.$$

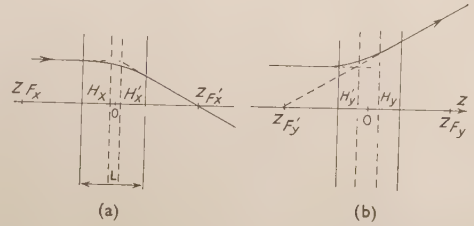

Fig. 3. (a) Plan convergent XOz. (b) Plan divergent YOz.

On a alors l'approximation des lentilles faibles

$$f'_X = -f'_Y = 1/\beta^2 L \qquad \text{et} \qquad Z_{H'_X} = Z_{H'_Y} = 0\,.$$

Les plans principaux sont confondus au centre, et on peut remplacer la lentille épaisse par une lentille mince.

3.2. MODELE ANALYTIQUE PLUS EVOLUE

On peut encore intégrer les équations du mouvement à l'aide d'un procédé plus évolué: on considère (fig. 4) que:

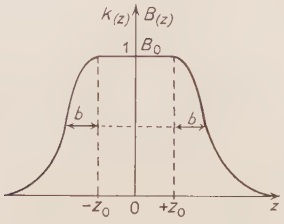

Fig. 4. Modèle évolué.

$$k(z) = 0 \qquad \text{pour} \quad -z_0 \leqslant z \leqslant +z_0$$

$$k(z) = \frac{1}{1 + \left(\dfrac{z + z_0}{b}\right)^2} \qquad \text{pour} \quad -\infty < z \leqslant -z_0$$

$$k(z) = \frac{1}{1 + \left(\dfrac{z - z_0}{b}\right)^2} \qquad \text{pour} \quad z_0 \leqslant z < +\infty$$

b est la largeur à mi-hauteur des demi-cloches ainsi définies; on détermine z_0 et b en conservant l'égalité des aires des courbes expérimentale et théorique, et en les faisant coïncider au mieux dans les zones où B varie le plus vite. Si on pose:

$$\omega_1^2 = 1 + \beta^2 b^2 \quad \text{et} \quad \omega_2^2 = 1 - \beta^2 b^2$$

on arrive aux expressions suivantes, après intégration dans les trois domaines successifs et raccordement des trajectoires en $z = -z_0$ et $z = +z_0$.

$$\frac{1}{\beta f'_X} = \sin \beta z_0 \left[\frac{\sin^2 \omega_1 \tfrac{1}{2}\pi}{\omega_1^2} + \frac{\cos^2 \omega_1 \tfrac{1}{2}\pi}{1 - \omega_1^2}\right] - \frac{a}{b}\frac{\sin \omega_1 \pi}{\omega_1} \cos 2\beta z_0$$

$$\frac{1}{\beta f'_Y} = -\operatorname{sh} \beta z_0 \left[\frac{\sin^2 \omega_2 \tfrac{1}{2}\pi}{\omega_2^2} + \frac{\cos^2 \omega_2 \tfrac{1}{2}\pi}{1 - \omega_2^2}\right] - \frac{a}{b}\frac{\sin \omega_2 \pi}{\omega_2} \operatorname{ch} 2\beta z_0$$

$$z_{F'_X} = 2z_0 + f'_X \left[\beta a \sin 2\beta z_0 \left(\frac{1}{\omega_1^2} - \frac{1}{1 - \omega_1^2}\right) \frac{b \sin \omega_1 \pi}{2a} - \cos 2\beta z_0 \cdot \cos \omega_1 \pi\right]$$

$$z_{F'_Y} = 2z_0 + f'_Y \left[-\beta a \operatorname{sh} 2\beta z_0 \left(\frac{1}{\omega_2^2} - \frac{1}{1 - \omega_2^2}\right) \frac{b \sin \omega_2 \pi}{2a} - \operatorname{ch} 2\beta z_0 \cdot \cos \omega_2 \pi\right].$$

4. Eléments cardinaux d'un doublet

Nous appellerons "doublet" un système optique épais formé par deux lentilles croisées de même axe Oz, séparées par un espace sans champ. Le plan convergent XOz de la première coïncide avec le plan divergent de la seconde, et réciproquement. Le plan XOz sera donc le plan "convergent-divergent" (C–D) du doublet, et le plan YOz, le plan "divergent-convergent" (D–C).

Nous n'envisagerons ici que le cas où les deux lentilles sont identiques: elles sont caractérisées par une même longueur efficace L; seuls les facteurs caractéristiques β peuvent différer: β_1 pour la première, β_2 pour la seconde.

Le système peut être schématisé par deux répartitions de champs rectangulaires Q_1 et Q_2 de longueur L séparées par une distance D (fig. 5). On nomme X_0 X'_0 Y_0 Y'_0 les conditions initiales à l'entrée de la première lentille X_1 X'_1 Y_1 Y'_1 les valeurs correspondantes à la sortie,

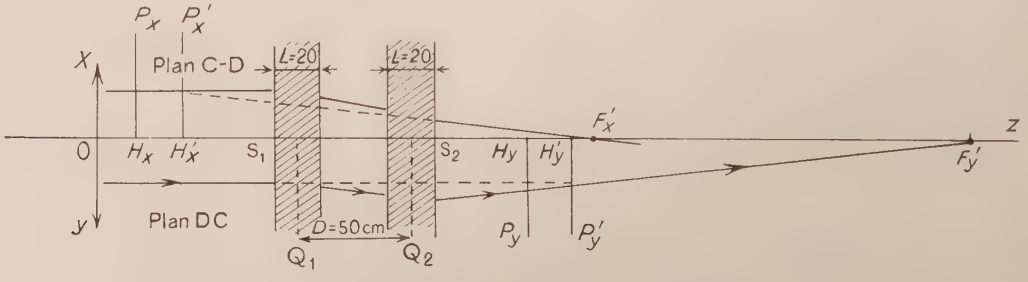

Fig. 5

etc. On arrive ainsi à $X_3\ X'_3\ Y_3\ Y'_3$ à la sortie de la seconde.

Les équations d'un rayon à la sortie de Q_1 sont données par:

$$X_1 = X_0 \cos \beta_1 L + \frac{X'_0}{\beta_1} \sin \beta_1 L$$

$$X'_1 = -\beta_1 X_0 \sin \beta_1 L + X'_0 \cos \beta_1 L$$

$$Y_1 = Y_0 \operatorname{ch} \beta_1 L + \frac{Y'_0}{\beta_1} \operatorname{sh} \beta_1 L$$

$$Y'_1 = \beta_1 Y_0 \operatorname{sh} \beta_1 L + Y'_0 \operatorname{ch} \beta_1 L$$

qu'on peut représenter par l'expression

$$\begin{pmatrix} X_1 \\ X'_1 \end{pmatrix} = \begin{pmatrix} \cos \beta_1 L & \frac{1}{\beta_1} \operatorname{sh} \beta_1 L \\ -\beta_1 \sin \beta_1 L & \cos \beta_1 L \end{pmatrix} \begin{pmatrix} X_0 \\ X'_0 \end{pmatrix} = \begin{pmatrix} A_1 & B_1 \\ C_1 & A_1 \end{pmatrix} \begin{pmatrix} X_0 \\ X'_0 \end{pmatrix}$$

$$\begin{pmatrix} Y_1 \\ Y'_1 \end{pmatrix} = \begin{pmatrix} \operatorname{ch} \beta_1 L & \frac{1}{\beta_1} \operatorname{sh} \beta_1 L \\ +\beta_1 \operatorname{sh} \beta_1 L & \operatorname{ch} \beta_1 L \end{pmatrix} \begin{pmatrix} Y_0 \\ Y'_0 \end{pmatrix} = \begin{pmatrix} D_1 & E_1 \\ F_1 & D_1 \end{pmatrix} \begin{pmatrix} Y_0 \\ Y'_0 \end{pmatrix}.$$

La matrice de transfert relative à l'espace de glissement de longueur $(D - L)$ situé entre les lentilles s'écrit:

$$\begin{pmatrix} 1 & D - L \\ 0 & 1 \end{pmatrix}.$$

D'où finalement, en attribuant l'indice 2 aux grandeurs correspondantes de Q_2:

$$\begin{pmatrix} X_3 \\ X'_3 \end{pmatrix} = \begin{pmatrix} D_2 & E_2 \\ F_2 & D_2 \end{pmatrix} \begin{pmatrix} 1 & D - L \\ 0 & 1 \end{pmatrix} \begin{pmatrix} A_1 & B_1 \\ C_1 & A_1 \end{pmatrix} \begin{pmatrix} X_0 \\ X'_0 \end{pmatrix}$$

$$\begin{pmatrix} Y_3 \\ Y'_3 \end{pmatrix} = \begin{pmatrix} A_2 & B_2 \\ C_2 & A_2 \end{pmatrix} \begin{pmatrix} 1 & D - L \\ 0 & 1 \end{pmatrix} \begin{pmatrix} D_1 & E_1 \\ F_1 & D_1 \end{pmatrix} \begin{pmatrix} Y_0 \\ Y'_0 \end{pmatrix}.$$

Dans le cas d'un rayon incident parallèle à l'axe $X'_0\ Y'_0 = 0$. On peut calculer les distances focales (fig. 5).

$$\overline{H'_X F'_X} = -\frac{X_0}{X'_3} \quad \text{et} \quad \overline{H'_Y F'_Y} = -\frac{Y_0}{Y'_3}$$

d'où:

$$-\frac{1}{\overline{H'_X F'_X}} = F_2 (A_1 + (D - L) C_1) + D_2 C_1 = \frac{1}{\overline{H_X F_X}}$$

$$-\frac{1}{\overline{H'_Y F'_Y}} = C_2 (D_1 + (D - L) F_1) + A_2 F_1 = \frac{1}{\overline{H_Y F_Y}}.$$

Les distances focales objet et image sont égales dans chaque plan, mais différentes d'un plan à l'autre, sauf si $(\beta_1 L) = (\beta_2 L)$. Dans ce cas on a alors

$$\overline{H'_X F'_X} = \overline{H'_Y F'_Y} = -\overline{H_X F_X} = -\overline{H_Y F_Y}$$

et

$$\frac{1}{\overline{H'_X F'_X}} = -\beta \left[\cos \beta L \cdot \operatorname{sh} \beta L - \sin \beta L \cdot \operatorname{ch} \beta L - \beta (D - L) \sin \beta L \cdot \operatorname{sh} \beta L\right].$$

La position des foyers est donnée par

$$\overline{S_2 F'_X} = -\frac{X_3}{X'_3} = X_3 \overline{H'_X F'_X} \text{ et } \overline{S_2 F'_Y} = Y_3 \overline{H'_Y F'_Y}$$

soit:

$$\overline{S_2 F'_X} = [D_2 (A_1 + (D - L) C_1) + E_2 C_1] \overline{H'_X F'_X}$$

$$\overline{S_2 F'_Y} = [A_2 (D_1 + (D - L) F_1) + B_2 F_1] \overline{H'_Y F'_Y}$$

$$\overline{S_1 F_X} = [A_1 (D_2 + (D - L) F_2) + B_1 F_2] \overline{H_X F_X}$$

$$\overline{S_1 F_Y} = [D_1 (A_2 + (D - L) C_2) + E_1 C_2] \overline{H_Y F_Y}.$$

Pour deux lentilles identiques, on a la relation

$$\overline{S_2 F'_X} = -\overline{S_1 F_Y} \quad \text{et} \quad \overline{S_2 F'_Y} = -\overline{S_1 F_X}.$$

Si on considère un point source situé sur l'axe à distance finie, il aura en général deux images différentes dans les plans XOz et YOz, chaque image étant constituée par deux lignes focales. La focale du plan C — D sera nommée "première focale" et celle du plan D — C "seconde focale". Suivant la position du point source par rapport à la lentille et la valeur des excitations, elles peuvent être réelles ou virtuelles. L'utilisation normale d'un doublet conduit à des focales réelles (fig. 6).

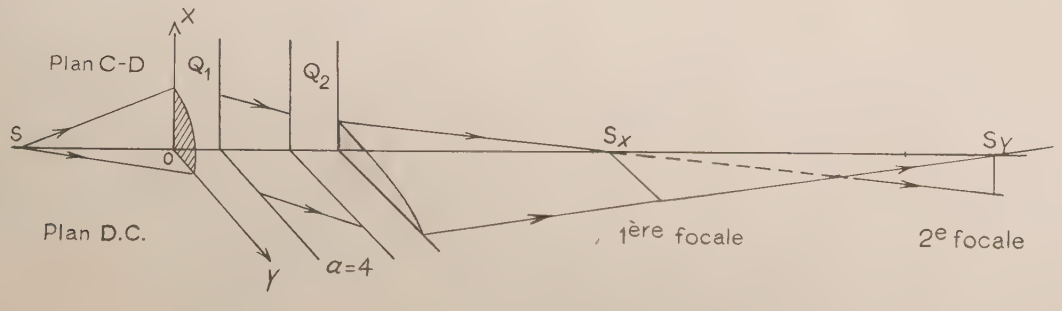

Fig. 6

Les deux focales peuvent se rejoindre pour certains couples de valeurs de $(\beta_1 L)$ et $(\beta_2 L)$, la position de l'objet étant fixée. Si les deux lentilles sont identiques, il existera également une valeur de (βL) permettant d'amener les deux focales dans le même plan image. Objet et image occupent alors des positions telles que

$x_1 x'_1 = f_1 f'_1$ dans le plan OX

$x_2 x'_2 = f_2 f'_2$ dans le plan OY (voir fig. 7)

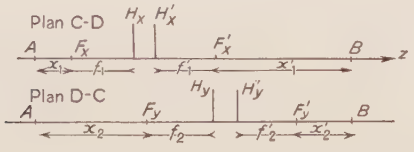

Fig. 7

avec $x_1 = x'_2$ et $x_2 = x'_1$ dans le cas des lentilles identiques. Mais les grandissements restant différents dans les deux plans, car la position des plans principaux est différente.

Les distances focales peuvent être infinies; dans le plan zOX par exemple

$$H'_X F'_X = \infty \text{ si } \beta_2 L \cdot \operatorname{th} \beta_2 L = \frac{\beta_1 L \cdot \operatorname{tg} \beta_1 L}{1 - \beta_1 (D - L) \operatorname{tg} \beta_1 L}.$$

Si l'objet est à l'infini, le doublet est alors afocal dans l'un ou l'autre plan, pour $(\beta_1 L)^2 = 0.5$ ou $(\beta_2 L)^2 = 0.5$.

On conçoit que dans le cas général le calcul des éléments optiques d'un doublet destiné à remplir une fonction donnée soit excessivement longs, et, bien que l'approximation des lentilles faibles ne soit valable que pour de très petites valeurs de (βL) les utilisateurs effectuent souvent les calculs en utilisant les formules simplifiées. Chaque lentille est remplacée par une lentille mince située au centre de la lentille réelle, et de distance focale $f_X = -f_Y = 1/\beta^2 L = f$. Pour deux lentilles minces distantes de D, on aurait alors:

$$\frac{1}{F_X} = \frac{1}{f_{1X}} + \frac{1}{f_{2Y}} - \frac{D}{f_{1X} f_{2Y}} = \frac{1}{f_1} - \frac{1}{f_2} + \frac{D}{f_1 f_2}$$

$$\frac{1}{F_Y} = \frac{1}{f_{1Y}} + \frac{1}{f_{2X}} - \frac{D}{f_{1Y} f_{2X}} = -\frac{1}{f_1} + \frac{1}{f_2} + \frac{D}{f_1 f_2}.$$

Si les deux lentilles sont identiques

$$\frac{1}{F_X} = \frac{1}{F_Y} = \frac{D}{f^2}.$$

On obtient bien un doublet convergent dans les deux plans, grâce à l'écartement D de deux lentilles divergente et convergente de même force.

On peut obtenir une meilleure approximation en supposant les plans principaux confondus au centre, mais les distances focales données par leur expression exacte en $\sin \beta L$ et $\operatorname{sh} \beta L$.

Nous verrons plus loin que le modèle rectangulaire (et les formules auxquelles il conduit) fournit des résultats très proches de la réalité.

DEUXIEME PARTIE

MESURES MAGNETIQUES

1. Réalisation des lentilles magnétiques

1.1. DESCRIPTION

Le schéma de la section des pièces polaires par un plan perpendiculaire à l'axe est donné sur la figure 1 avec les notations utilisées dans la suite.

1.1.1. Excitations prévues

La donnée initiale est ici le cercle de gorge, de rayon a, qui définit la zone utilisable pour le faisceau. Le cercle de gorge prévu à l'origine, pour l'application particulière envisagée (adaptation injecteur-synchrotron), avait un rayon $a = 4$ cm.

Dans notre cas particulier, pour des protons de 50 MeV, on a $e/m_0 \approx 10^8$ M.K.S. et $e\Phi_0/2m_0c^2 \approx 2.6 \times 10^{-2}$. On peut donc négliger ce terme dans l'expression du facteur caractéristique β^2, qu'on écrira simplement

$$\beta^2 = \frac{\mu_0 n I}{a^2} \sqrt{\frac{2e}{m_0 \Phi_0}}.$$

La distance focale f d'une lentille est donnée approximativement par

$$\frac{1}{f} = \beta \sin \beta L$$

dans le plan convergent. L est la "longueur efficace" de la lentille. Il suffit de savoir qu'elle est voisine de la longueur l des pièces polaires et reliée par la relation empirique $L \neq l + a$.

Pour obtenir: $2 > f > 0.8$ m, avec, $a = 4$ cm, $L = 0.2$ m, et des protons de 50 MeV, il faut pouvoir disposer d'environ

$$1700 < nI < 5000 \quad A.\text{t par pôle}.$$

Les valeurs remarquables du champ magnétique et de son gradient $K(0)$ sont alors: gradient:

$$2.60 < K(0) < 8 \quad \text{weber}/m^3$$

induction sur le cercle de gorge:

$$0.104 < B_a < 0.32 \text{ weber}/m^2 .$$

Nous avons étudié une autre réalisation caractérisée par $a = 6$ cm et $L = 0.2$ m il faut alors multiplier les valeurs précédentes par le facteur $(6/4)^2 = 2.25$, d'où:

$$3825 < nI < 11\,250 \; A.\text{t}.$$

$$0.234 < B_a < 0.72 \; Wb/m^2 .$$

Ces valeurs sont relativement faibles pour $f = 2$ m, et aisées à obtenir: elles n'entraînent ni échauffement prononcé, ni saturation. Mais pour $f \approx 0.8$ m il faudrait prendre des précautions pour éviter la saturation de la carcasse et, à priori, des pièces polaires. C'est là que ses effets seraient les plus nuisibles: elle amènerait des distorsions notables dans la répartition du champ; une saturation de la carcasse n'agirait que sur la loi de variation de B en fonction de l'intensité I du courant d'excitation, ce qui n'est pas en général préjudiciable, sauf dans la "compensation" des variations de n dans le synchrotron. Dans cette application particulière, le champ et le gradient doivent avoir à un instant donné une valeur définie en relation avec celle qui existe simultanément dans les aimants; le plus simple, pour assurer cette concordance, est d'avoir des lentilles de compensation qui aient même loi champ-courant que les aimants, ou à défaut une loi linéaire.

Nous verrons dans la suite que la saturation se produit toujours loin des pôles, contrairement à ce qui se produit pour les lentilles magnétiques à symétrie de révolution, pour lesquelles une bonne construction amène à saturer d'abord les pôles[7,8]).

1.1.2. Choix des pièces polaires[9])

En principe, la distribution de champ à gradient radial constant et égal dans toutes les directions ne peut être obtenue qu'avec des pièces polaires hyperboliques. Mais des études à la cuve rhéographique nous ont montré que le remplacement de l'hyperbole théorique par un cercle convenable n'introduisait aucune différence appréciable dans la région intéressante, intérieure au cercle de gorge. D'autre part, pour éviter que le gradient ne varie dans différentes directions radiales, il faut donner une largeur D suffisante aux pièces polaires, de l'ordre de $2a$ au moins, si on veut que l'approximation reste très bonne dans tout le cercle de gorge. Si on se contente de $D = 1.1\ a$, une distorsion importante apparaît pour $X, Y \geqslant 0.8\ a$.

Dans nos premières lentilles, que nous nommerons Q_1 et Q_2, pour $a = 4$ cm, les pièces polaires sont des portions de cylindre circulaire de rayon $R = 1.15\ a = 4.6$ cm et d'épaisseur 4 cm; elles sont vissées sur des supports parallélépipédiques de largeur $D = 10$ cm $= 2.5\ a$, fixés à demeure sur la carcasse magnétique. Cette disposition permet un changement rapide des pôles sans avoir à démonter la lentille. L'hyperbole théorique $XY = 8$ cm^2 est remplacée ainsi par un cercle tangent en son sommet A, et la recoupant en des points B et C (fig. 8) sans que l'écart Δ entre les deux courbes dépasse 0.25 mm, soit $\Delta/a = 6.2 \times 10^{-3}$; cette approximation est valable jusqu'à des points d'abscisse $X, Y = 5$ cm.

[7]) G. Liebmann, The Effect of Pole Piece Saturation in magnetic Electron lens, Proc. Phys. Soc. (London) B **66** (1953) 448–458.

[8]) P. Durandeau et Ch. Fert, Lentilles électroniques magnétiques, Revue d'Optique **36**, No. 5 (1957) 206–234.

[9]) A. Septier, Réalisation pratique d'une lentille quadrupolaire magnétique pour particules de très haute énergie, C.R. **243** (1956) 132–135;

A. Septier, CERN-PS/Sp 12 (1955) non publié.

Nous avons utilisé une deuxième série de pièces polaires fixées sur les mêmes supports (lentilles Q'_1 et Q'_2), avec $a = 6$ cm et $R = 6.9$ cm; l'épaisseur des pôles n'est plus que de 2 cm. Dans ce cas le rayon R_0 de la zone utile, qui reste égal à 4 cm, ne représente plus que $R_0 = \frac{2}{3} a$; la diminution de largeur des pièces polaires ($D = \frac{4}{3} a$) ne se fera pas sentir à l'intérieur de la zone utile. Nos mesures de champ vérifieront le bien fondé de ces hypothèses de départ.

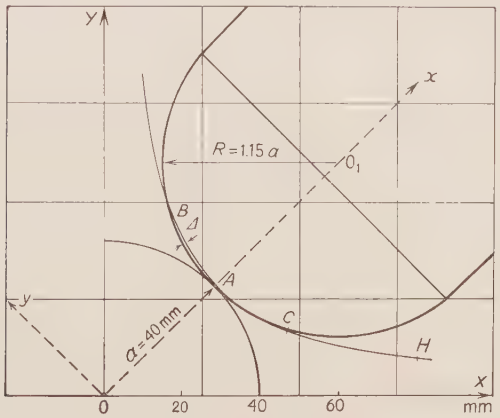

Fig. 8

1.1.3. Caractéristiques mécaniques et électriques

Les lentilles construites à l'échelle 1 ont les caractéristiques suivantes:

Rayon du cercle de gorge $a = 4$ cm, ou $a = 6$ cm;

Rayon des pièces polaires $R = 1.15\, a$;

Longueur des pièces polaires $l = 15$ cm;

Carcasse magnétique carrée: côté extérieur, 48 cm, épaisseur 6 cm;

Supports des pièces polaires: largeur, $D = 10$ cm, profondeur 10 cm;

Entrefer minimum entre 2 pôles adjacents, 29.6 mm;

Quatre bobines à section trapézoïdale de $n = 627$ spires, en fil méplat de 2×4 mm, dépassant de 12 cm environ aux extrémités;

Résistance des 4 bobines en série: 4.25 ohm à 20° C;

Une des lentilles est représentée dans la fig. 9.

Les pôles et les supports de pièces polaires sont en fer Armco, la carcasse en acier doux (C < 0.15%, Si < 0.2%, Mn ≈ 0.3%) type AFNOR XC 10 F†.

A l'origine, les lentilles étaient munies d'un circuit de refroidissement par eau; il était formé de plaques de laiton entourant les bobines, et refroidies par une circulation d'eau dans des tubes de cuivre soudés sur les bords des plaques. Le dispositif s'est avéré inutile en régime normal.

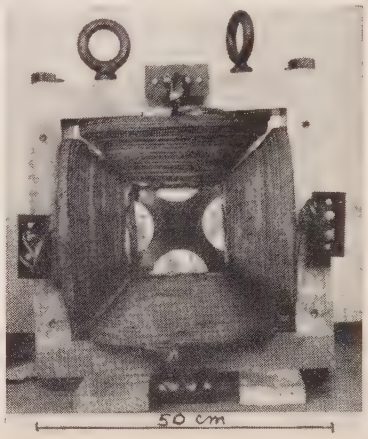

Fig. 9

1.2. ECHAUFFEMENT EN SERVICE CONTINU

Pour une distance focale de 2 mètres, le courant d'excitation serait de 3 ampères environ dans Q_1, Q_2 et de 7 ampères dans Q'_1 Q'_2.

La mesure de l'échauffement a été effectuée en marche continue avec $I = 10$ A. La température était mesurée en deux points A et B (fig. 10) entre bobine et carcasse, et entre deux spires de la surface non refroidie d'une bobine, grâce à deux thermocouples. Les courbes de la fig. 11 montrent la montée de température en ces points, au cours du temps, lorsque la circulation d'eau fonctionne (débit 3 l/min) et lorsqu'elle est coupée.

Sans refroidissement forcé, l'équilibre thermique est atteint au bout de 8 heures; la carcasse

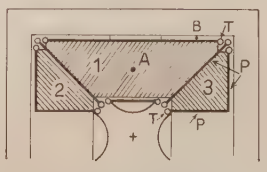

Fig. 10. Bobines 2 et 3 coupées. Bobine 1 vue par dessus. A et B = Thermocouples. T = Tubes. P = Plaques de Cuivre.

† Définition de l'Association Française de Normalisation, 23 rue N.D. des Victoires, Paris.

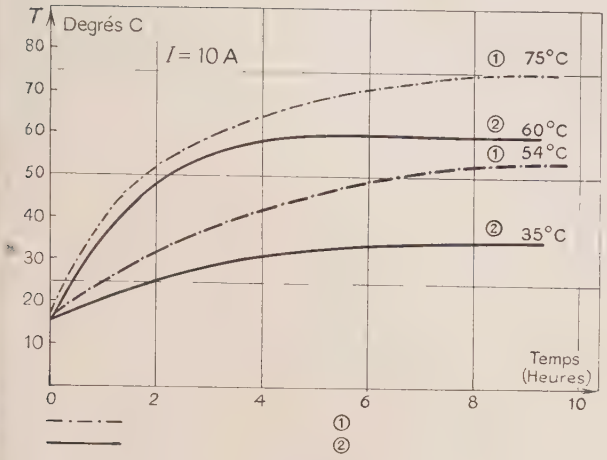

Fig. 11

—·—·— Sans circulation d'eau. ——— Avec circulation d'eau. (1) Surface des enroulements. (2) Carcasse magnétique.

magnétique a alors une température de 54° C et celle du centre des bobinages doit être voisine de 100° C. Les bobines imprégnées au vernis bakélite peuvent supporter des températures de 180° C: le circuit de refroidissement peut donc être supprimé sur ce type de lentille.

La résistance des bobines passe de 4.25 ohms à 5 ohms dans ces conditions de fonctionnement.

D'autre part la carcasse et les supports des pôles ayant des coefficients λ de dilatation linéaire voisins, l'accroissement des côtés de l'entrefer est très faible: il s'agit d'un phénomène différentiel. Pour $\Delta t \approx 35°$ C et $\lambda = 10^{-5}$, on a $\Delta a/a \approx 0.35 \times 10^{-3}$, soit $\Delta a < 1.5 \times 10^{-2}$ mm, ce qui est inférieur aux tolérances mécaniques de fabrication ($\Delta a = 2.5 \times 10^{-2}$ mm).

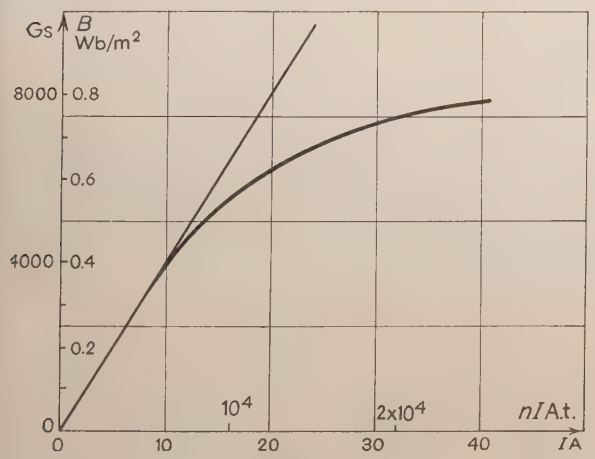

Fig. 12

1.3 CARACTERISTIQUE CHAMP-COURANT

Le champ magnétique B mesuré dans le plan radial passant par le centre de la lentille Q_1 varie en fonction de I comme l'indique la figure 12, pour un point P situé sur OX à 4 cm de l'axe ($X = a$).

La caractéristique est parfaitement linéaire jusqu'à $I = 9$ A; pour $I = 20$ A, l'écart entre le champ mesuré et le champ théorique est de l'ordre de 15%; pour $I = 33$ A, on observe seulement $B_a = 0.75$ web/m² au lieu de $B_a = 1.32$ web/m² que donnerait la loi linéaire du début; il y a donc une importante saturation. Pour $I = 0$, le champ rémanent varie de 12 à 16×10^{-4} web/m², d'une expérience à l'autre, sans prendre de précaution spéciale (démagnétisation, etc.).

1.4. SATURATION DU CIRCUIT MAGNETIQUE

Pour simplifier la construction des bobines, les supports des pièces polaires ont une section constante: $S = 150$ cm², entre les pôles et la carcasse.

Le flux a tout d'abord été estimé dans l'étude préliminaire en utilisant les formules empiriques de Hubbard[10]), dans différentes sections; puis il a été mesuré sur la lentille. Nous donnons les résultats comparés de cette étude:

1.4.1. Estimation du flux

Le flux ψ traversant les supports des pièces polaires de Q_1 a été calculé dans trois plans de section droite (fig. 13). On trouve:

$$\psi_{A(\text{weber})} \simeq 330 \times 10^{-4} B_a \ (\text{web}/m^2)$$

$$\psi_{B(\text{weber})} \simeq 385 \times 10^{-4} B_a \ (\text{web}/m^2)$$

$$\psi_{C(\text{weber})} \simeq 390 \times 10^{-4} B_a \ (\text{web}/m^2) \ .$$

Pour $B_a = 0.32$ web/m², on aurait $\psi_C \approx 1.28 \times 10^{-2}$ web c'est-à-dire une induction moyenne dans le fer, $B_m \approx 0.85$ web/m².

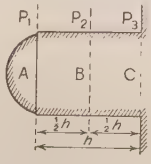

Fig. 13

Dans la lentille Q'_1 ($a = 6$ cm), la valeur de ψ_C est sensiblement la même: $\psi_C \approx 400 \times 10^{-4} B_a$, mais il faut un champ B_a plus grand. Pour $B_a = 0.72$ web/m², on aurait une induction dans le fer de $B_m \approx 1.92$ web/m² ce qui est encore possible avec le fer Armco.

1.4.2. Mesure du flux

Pour comparer la réalité aux prévisions précédentes et déterminer les limites d'utilisation de la carcasse, le flux ψ et la densité B_m ont été mesurés en différents points du circuit magnétique de Q_1 à l'aide de spires collées sur le fer et d'un fluxmètre intégrateur à galvanomètre asservi[11]), pour différentes intensités de fonctionnement. Le courant magnétisant était établi durant un temps très court, pour éviter un échauffement trop grand aux fortes intensités; il était mesuré grâce à une résistance étalon de 10^{-3} ohms, et d'un millivoltmètre de précision, puis coupé; chaque spire était reliée successivement au fluxmètre. Cet appareil dispose de plusieurs sensibilités allant de 10^{-6} web/volt à 10^{-2} web/volt (soit 10^2 maxw/volt à 10^6 maxw/volt). La tension de sortie est lue sur un voltmètre à lampes.

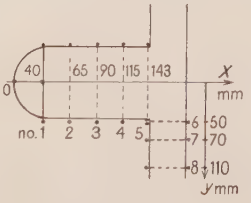

Fig. 14

La figure 14 indique l'emplacement des 8 spires de mesure sur l'un des supports de pièces polaires et sur la carcasse. La section du fer est de 150 cm² pour les spires No. 1 à 5 et 90 cm² pour les spires suivantes. Les résultats relatifs à ψ sont donnés figure 15 pour $I_1 = 6$ A (courbe 1) et $I_2 = 33$ A (courbe 2), ce qui correspond respectivement à $nI_1 = 3762$ et $nI_2 \neq 20\,700$ A.t. par pôle. Le rapport ψ_2/ψ_1 est pratiquement constant en tous points, et B_m ne dépasse pas 2.2 web/m² dans le fer Armco au voisinage de la carcasse pour $I_2 = 33$ A. La saturation n'est donc pas atteinte dans les supports des pôles.

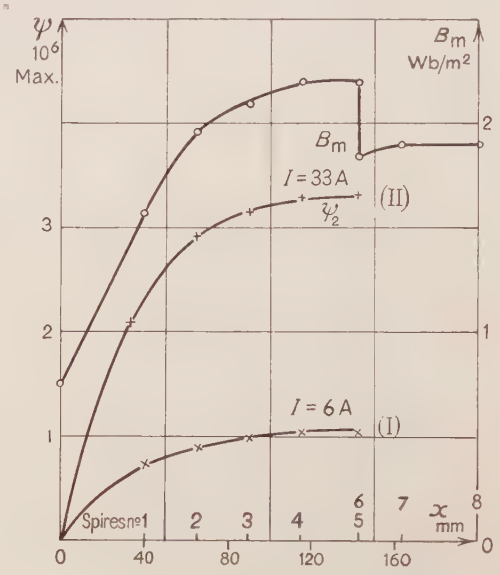

Fig. 15

Dans la carcasse par contre, on a $B_m \neq 1.9$ web/m². L'acier doux est alors pratiquement saturé, ce qui explique la difficulté d'obtenir de très fortes valeurs de B_a dans l'entrefer.

Contre la carcasse, on a $\psi_{max} \approx 440 \times 10^{-4} B_a$ web/m²; d'autres mesures, effectuées sur une lentille de forme différente, (et que nous décrivons plus loin) confirment que les formules empiriques citées plus haut conduisent à des résultats trop optimistes (10 à 20% selon les cas).

2. Topographie des champs

2.1. METHODES DE MESURE

2.1.1. Composantes intéressantes

Dans une lentille quadrupolaire infiniment longue, le champ B_r est purement transversal. Suivant OX n'existe que la composante B_Y et réciproquement (fig. 16). Si on ne considère que la grandeur de $|B|$ la distribution est de révolution autour de l'axe Oz, sauf pour $r > a$, où apparaissent les perturbations dues à la largeur finie des pièces polaires.

Mais dans une lentille de longueur finie, des effets de bout se produisent et jouent un rôle

[10]) E. L. Hubbard, Design of strong focusing magnets for linear Accelerators, U.C.R.L. Eng. Note DV-7, 4111–4163 (1953).

[11]) M. Sauzade, Sur la réalisation d'un fluxmètre électronique photoélectrique, C.R. **246** (1958) 272–730.

d'autant plus important que la lentille est plus courte. Dans les champs de fuite apparaît une composante parallèle à Oz: B_z. La connaissance de B_z est nécessaire pour le calcul:

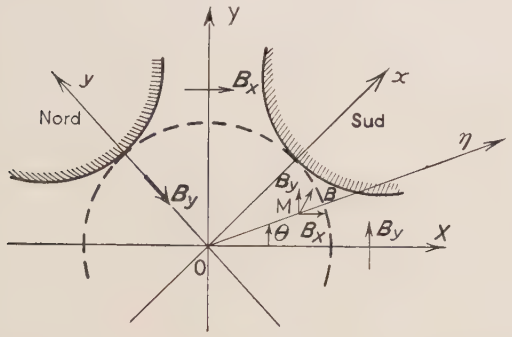

Fig. 16

– de l'effet du champ de fuite, que l'on peut considérer comme un défaut particulier aux lentilles quadrupolaires,

– des aberrations proprement dites.

Nous avons donc cherché à mesurer

B_r et son gradient k, dans les plans OX, OY, Ox et Oy

B_z en différents points de l'espace utile.

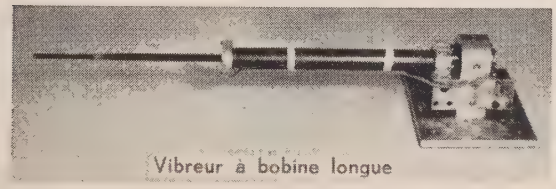

Fig. 17 (a)

On peut déterminer B_r grâce à une bobine courte tournante dont l'axe de rotation est parallèle à Oz, disposition différente de celle

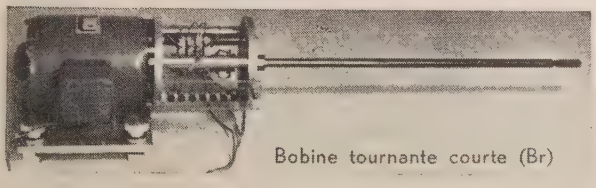

Fig. 17 (c)

adoptée pour les mesures sur les maquettes d'électroaimants du synchrotron dont les entrefers sont accessibles latéralement.

Ici, on ne peut donc pas utiliser deux bobines voisines montées sur le même arbre tournant pour d'éterminer le gradient radial k. C'est pourquoi nous avons mis au point un dispositif spécial à bobine courte vibrant transversalement. Un autre système à bobine longue vibrant parallèlement à Oz nous a permis de mesurer B_z.

Pour ces mesures, l'axe de la lentille, placée sur un support de bois orientable est vertical; les appareils de mesure sont portés par un plateau de fraiseuse orientable et déplaçable dans trois directions perpendiculaires. La figure 17 groupe la photographie des divers appareils, que nous allons décrire.

2.1.2. Composante transversale B_r: bobine tournante

La bobine courte de 5 mm de diamètre, et 5 mm de long, fixée à l'extrémité d'un axe isolant est entraînée à 1500 tours-minute par un moteur synchrone triphasé. Les balais sont en carbo-argent† et frottent sur des bagues en argent, ce qui ramène les parasites de balais à un niveau inférieur à 0.01 mV. Une des extrémités de la bobine est reliée à la masse du

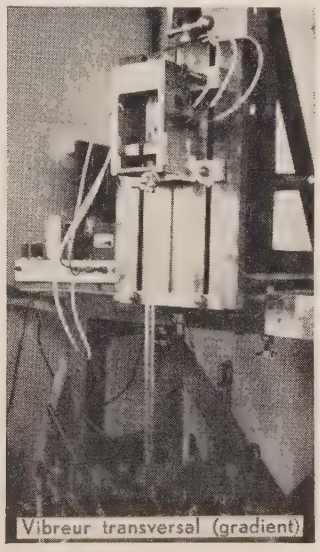

Fig. 17 (b)

montage. L'axe tournant formé par un tube de bakélite de 5 mm de diamètre, traverse trois paliers graphités fixés dans un manchon rigide

† Produit de la Société "Le Carbone Lorraine".

de laiton, et il est raccordé à l'arbre moteur par un flector de Klégécell. Après centrage de la bobine et des paliers, aucune perturbation gênante due aux vibrations n'a été enregistrée.

La sensibilité de la bobine était de 7 volt par web/m² soit 7×10^{-4} volt/gauss, pour une fréquence $f_0 = 25$ Hz.

Sur l'axe de la lentille subsiste un signal parasite v_1 parfaitement sinusoidal de fréquence double de celle du signal fondamental. Son amplitude est rigoureusement proportionnelle au gradient radial, tant que celui-ci reste constant. On peut le vérifier en montant en opposition deux bobines identiques juxtaposées, alignées sur l'axe de rotation, et en les déplaçant suivant une direction radiale Or, au voisinage du plan $z = 0$: le signal principal à $f_0 = 25$ Hz est nul.

(a) Centrage au moyen de v_1. La présence de v_1, permet un alignement rigoureux de l'axe Oz et du déplacement vertical de la sonde tournante: v_1 est de l'ordre de 10^{-2} volt sur l'axe pour $I = 4$ A dans Q_1. Un déplacement latéral inférieur à 5×10^{-2} mm déforme la sinusoïde observée à l'oscillographe, en lui superposant le fondamental v_0.

(b) Mesures avec v_0. Pour les mesures, v_1 et les termes supérieurs sont éliminés par filtrage, grâce à un filtre passe-bas ayant une fréquence de coupure à 37 Hz; la sensibilité de la bobine est abaissée à 6 volt·web^{-1}·m^{-2} et v_1 est divisé par 100.

La reproductibilité des mesures avec cet appareillage est meilleure que 1%, l'intensité du courant dans la lentille étant lue sur un appareil de classe 0.2.

Nous décrirons plus loin un autre type de bobine tournante qui fournit directement un signal proportionnel à l'intégrale

$$I = \int_{-\infty}^{+\infty} B_r \, dz \, .$$

2.1.3. Mesure du gradient transversal[12])

Soit une bobine courte M d'axe parallèle à OY, vibrant dans une direction radiale OX (fig. 18) avec un mouvement:

$$\xi = x_0 \cos \omega t \, .$$

Si x_0 est petit, on obtiendra un signal fondamental V_0 de la forme:

$$V_0 = k x_0 B' \cos \omega t$$

proportionnel à x_0 et au gradient $B' = \partial B_Y / \partial X$.

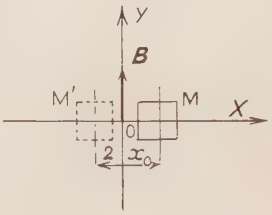

Fig. 18

Nous avons utilisé une bobine portée par l'extrémité libre d'une tige de plexiglas parallèle à Oz, donc verticale, l'autre extrémité étant rigidement fixée. La tige, longue de 500 mm, de section rectangulaire (15 × 5 mm) porte, fixés à 10 cm du point fixe, deux disques d'acier doux, qui font face à deux petits électroaimants E_1 et E_2 (fig. 19). Si on alimente ceux-ci avec des

Fig. 19

courants alternatifs de fréquence quelconque, en opposition de phase dans les deux bobines, la tige vibre. Pour une fréquence égale à l'une des fréquences propres de la tige, il y a résonance et on a des amplitudes importantes avec une puissance d'excitation relativement faible.

La fréquence fondamentale étant trop faible, nous utilisons le partiel d'ordre 2 pour lequel $f_0 = 85$ Hz. L'amplitude est alors réglable de

[12]) A. Septier, Mesure des gradients et des champs dans une lentille quadrupolaire, CERN-PS/Sp 8 (1955)non publié.

$2x_0 = 0$ à $2x_0 = 2.5$ mm, en faisant varier l'excitation des électroaimants.

Ces électroaimants sont alimentés par deux lampes montées en pushpull fonctionnant en classe B. La fréquence d'attraction est alors égale à celle du courant. Grâce à l'excitation symétrique, l'attraction constante due au courant continu qui traverse E_1 et E_2 est nulle, et le mouvement de la bobine (et par suite le signal induit) est parfaitement sinusoïdal.

Pour des mesures absolues de gradient, il est possible de déterminer l'amplitude x_0 du mouvement avec précision grâce à un miroir fixé en bout de tige et un dispositif optique amplificateur. Cette mesure absolue permet d'étalonner la tension fournie par un cristal piézo-électrique qui presse contre la tige au voisinage du point fixe où les amplitudes sont faibles. Il fournit une tension V qui sert en service normal à mesurer x_0, d'après la courbe $x_0 = f(V)$ établie une fois pour toutes.

Ce système de contrôle permet de vérifier qu'à excitation constante, la tension de sortie de la bobine est parfaitement constante; alors il n'existe pas de vibrations parasites.

Pour rendre x_0 aussi stable que possible malgré une variation accidentelle du courant d'excitation des électroaimants, on peut mettre à profit la tension V fournie par le cristal. Celle-ci

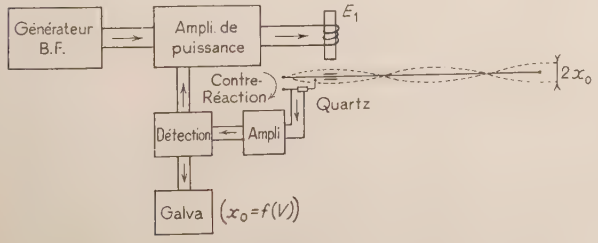

Fig. 20

amplifiée, puis détectée, est envoyée sur la grille de la première lampe de l'amplificateur de puissance alimentant E_1 et E_2, qui est une lampe à pente variable (6SK7). Le schéma de l'ensemble des alimentations est donné (fig. 20)†.

Pour $x_0 = 1$ mm, $f_0 = 85$ Hz; la sensibilité est de $v = 10^{-3}$ volt pour 1 web/m^3, $v = 10^{-5}$ volt par gauss·cm^{-1}. Un préamplificateur de gain 100†† permet la mesure commode de gradients de quelques 10^{-2} web/m^3 (quelques gauss/cm).

2.1.4. Mesure de la composante longitudinale B_z

Un solénoïde d'axe parallèle à Oz, vibrant longitudinalement, et tel que ses extrémités A et B soient respectivement dans des zones où $(B_z)_A \neq 0$ et $(B_z)_B = 0$ (fig. 21) donne un signal v proportionnel à B_z au point A[13]).

$v = (n\pi a^2\omega)\, z_0 \cos \omega t \cdot (B_z)_A +$ termes supérieurs, avec

$n =$ nombre de tours par unité de longueur,

$a =$ rayon des spires

$\omega = 2\pi f_0$, f_0 étant la fréquence de vibration, et z_0, amplitude du mouvement.

Nous avons utilisé une bobine longue de 300 mm à spires jointives, bobinée sur un tube de verre de 5 mm de diamètre. Cette bobine, fixée dans un tube T_1 de bakélite (fig. 22) vibre à la fréquence $f_0 = 50$ Hz grâce à un moteur électrodynamique M analogue à celui d'un haut-parleur. Le tube de bakélite support est fixé à une extrémité sur l'axe moteur de M, et suspendu par 3 ressorts R formant palier vibrant sans amortissement dans un tube rigide T_2 qui

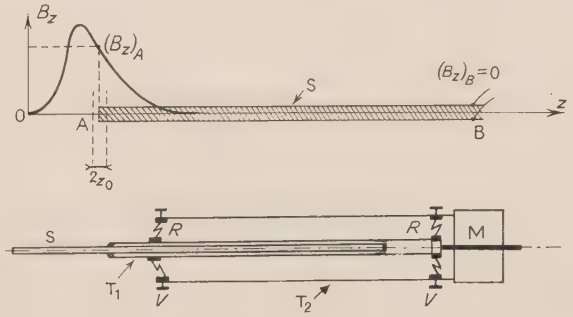

Fig. 21 et 22

l'entoure. Des vis de centrage V permettent d'aligner l'axe du solénoïde et celui du vibreur.

Le signal, après traversée d'un amplificateur de gain 100 et d'un filtre passe-bas qui élimine au mieux les composantes parasites de fréquence supérieure à 50 Hz atteint 3 volt·web^{-1}·m^{-2}.

† Cet appareil a été réalisé par A. Hampikian.

†† Préamplificateur type GM 4574 Philips.

[13]) P. Gautier, Méthode d'induction pour l'étude de la topographie du champ sur l'axe d'une lentile électronique magnétique puissante, J. Phys. Rad. **15** (1954) 684–691.

Alors que les bobines tournantes sont des instruments robustes, il est à remarquer que la mise au point de la bobine vibrante est délicate malgré sa position verticale: une légère dissymétrie dans la tension des ressorts constituant les paliers fait apparaître un signal parasite de fréquence multiple de celle du fondamental, même lorsque l'ensemble est bien centré. Un léger excentrage provoque en plus une vibration parasite transversale à la fréquence du fondamental; le signal parasite proportionnel au gradient du champ transversal est important dans toute la zone centrale de la lentille, et peut masquer la variation de B_z.

Cette vibration transversale peut être éliminée grâce à un réglage soigneux des vis de centrage, mais elle peut réapparaître après quelques heures de fonctionnement: un nouveau réglage est alors nécessaire. En prenant soin de vérifier l'étalonnage avant et après chaque série de mesures, les résultats sont reproductibles à 1% dans les régions où B_z prend de fortes valeurs, 3 à 5% lorsqu'on se rapproche de la zone centrale où B_z s'annule.

2.2. CHAMP TRANSVERSAL[14,15])

2.2.1. Répartition radiale du champ dans la zone centrale de la lentille

Champ. Définissons dans le plan $z = 0$, un double système d'axes rectangulaires (fig. 16) situés dans les plans de symétrie radiaux de la lentille:

– axes OX et OY dans les entrefers,

– axes Ox et Oy dans le fer, tels que OX, $Ox = \frac{1}{4}\pi$.

L'espace utile est limité par le cercle de gorge de rayon a. Dans la lentille Q_1, $a = 4$ cm et dans Q'_1, $a = 6$ cm, mais les deux lentilles ne sont pas homothétiques, puisque les supports de pièces polaires restent identiques (fig. 23). La répartition transverse de B_X est donnée pour Q_1 sur la figure 24 pour différentes intensités, y compris $I = 0$ qui donne le champ rémanent, suivant OY. La variation est parfaitement linéaire jusqu'à $Y = 3$ cm, avec un gradient $(K)_{Q_1} \neq 0.01$ wb·m^{-3}·A^{-1}. Une légère diminution du gradient se manifeste pour $I \geqslant 10$ A, due à la saturation (mais les courbes restent des droites), et pour $Y > 3$ cm. Le champ passe par un maximum pour X, $Y \neq 6.2$ cm.

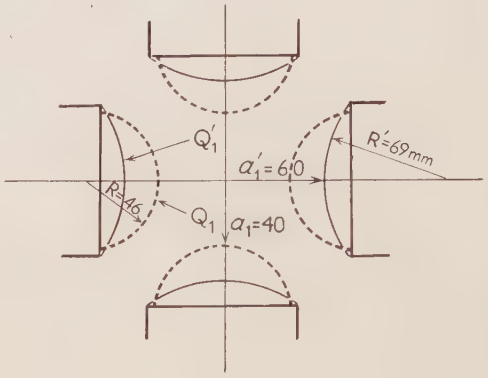

Fig. 23

Dans les directions Ox et Oy, la variation du

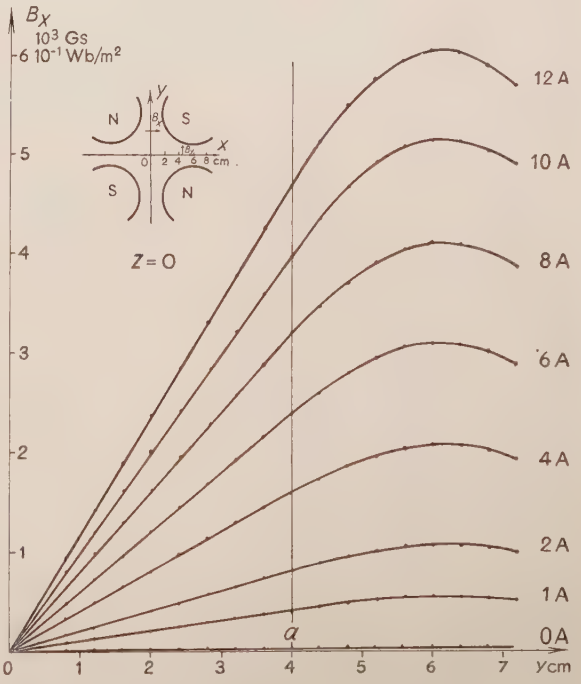

Fig. 24

† Nous avons utilisé un moteur fabriqué par la firme suisse Dreyfus-Graf.

[14]) A. Septier, Répartition du champ dans la première maquette de lentille quadrupolaire, CERN-PS/Sp 13 (1955) non publié.;

Mesures effectuées sur le deuxième modèle de lentille quadrupolaire, CERN-PS/Sp 16 (1956) non publié.

[15]) A. Septier, Etude des champs de fuite d'une lentille quadrupolaire magnétique, C.R. **243** (1956) 1026–1029.

champ est identique ; les courbes représentatives se confondent avec les précédentes jusqu'à $x, y = a$.

La fig. 25 est relative à Q'_1: on y a porté les points expérimentaux relatifs à OX et Ox pour $I = 4$ A: toutes les courbes sont confondues jusqu'à $X, x = 45$ mm $= \frac{3}{4}a$, avec une droite de pente $(K)_{Q'_1} = 0.0177$ web/m^3, ce qui correspond bien à

$$(K)_{Q_1}/(K)_{Q'_1} = \left(\frac{(a)_{Q'_1}}{(a)_{Q_1}}\right)^2 .$$

Pour $X, x > \frac{3}{4}a$, un léger écart se manifeste entre les deux répartitions, le champ étant légèrement plus faible sur Ox, Oy. Cette dissymétrie est due à l'influence des angles des

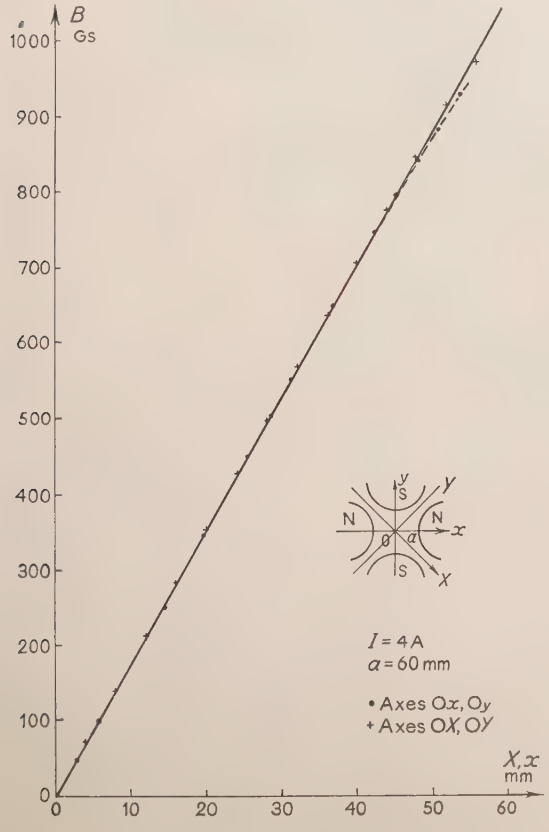

Fig. 25

supports des pièces polaires: un accroissement du champ sur OX, OY entraîne automatiquement une diminution sur Ox, Oy au voisinage du fer.

Gradient $\partial B/\partial r$. Les variations des gradients $K_X = \partial B_Y/\partial X$, et $K_x = \partial B_x/\partial x$, sont mises en évidence sur les courbes de la figure 26 relatives à Q_1' et obtenues à l'aide du vibreur à bobine

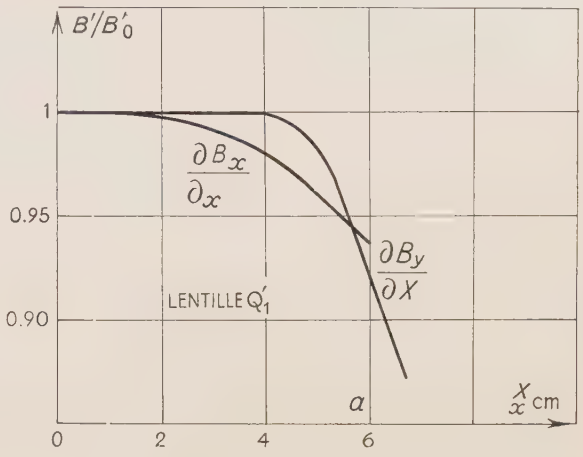

Fig. 26

courte: cette méthode de mesure permet de déceler très facilement les faibles variations qui se manifestent dans la répartition du champ transversal.

2.2.2. Répartition du champ transversal en suivant des parallèles à l'axe optique

Pour $r < \frac{1}{2}a$, l'allure des courbes $B = f(z)$ est la même dans tous les plans radiaux, mais pour $r > \frac{1}{2}a$ ces courbes commencent à différer sensiblement, suivant qu'on les relève dans les plans OX, OY ou dans les plans Ox, Oy.

Si $r < \frac{1}{2}a$, elles présentent un plateau central de l'ordre de 7 cm dans Q_1, 3 à 4 cm dans Q'_1, puis le champ transversal décroît et s'annule pratiquement à 24 cm du centre (figure 27). Pour $r > \frac{1}{2}a$, le plateau central s'allonge à mesure qu'on s'éloigne de l'axe suivant OX et OY; suivant Ox et Oy les bords du plateau se relèvent et, au voisinage du fer on obtient des pointes très marquées (fig. 28, relative à Q_1). Le champ transversal peut atteindre sur le fer une valeur double de celle qu'il a en $z = 0$. L'effet est encore plus visible si on se reporte aux courbes donnant $B_r = f(r)$ dans les plans OX et Ox pour différentes valeurs de z (fig. 29, Q_1) et aux répartitions du gradient (fig. 30, Q_1).

Les pertubations sont dues à un "effet de

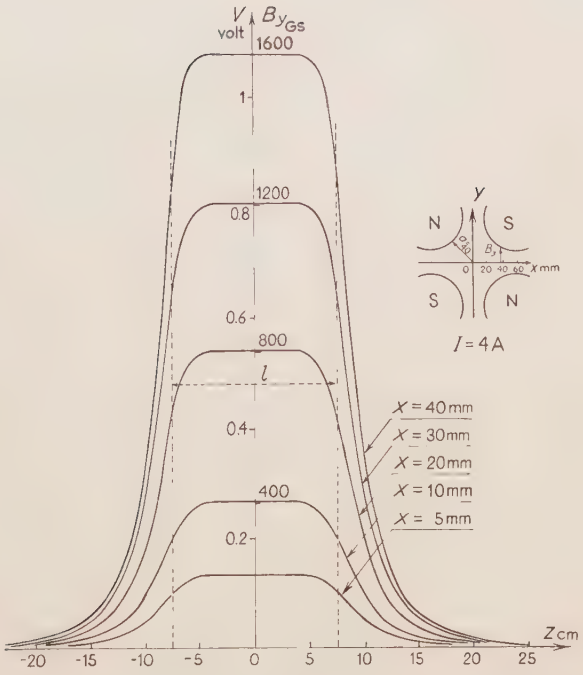

Fig. 27

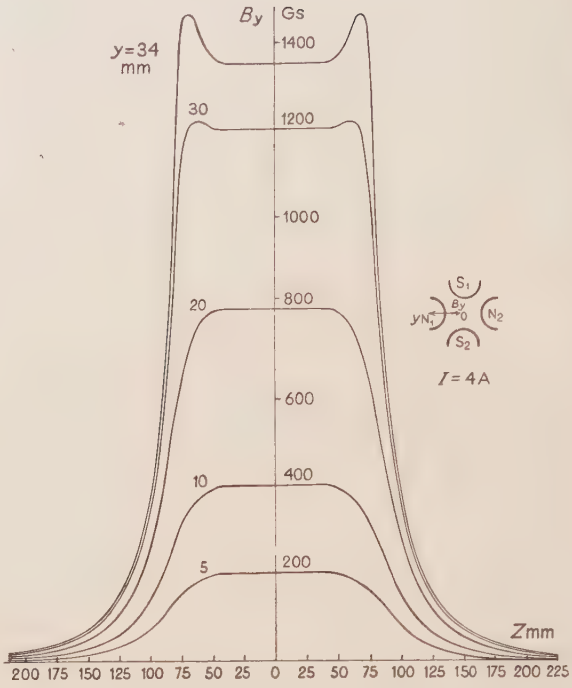

Fig. 28

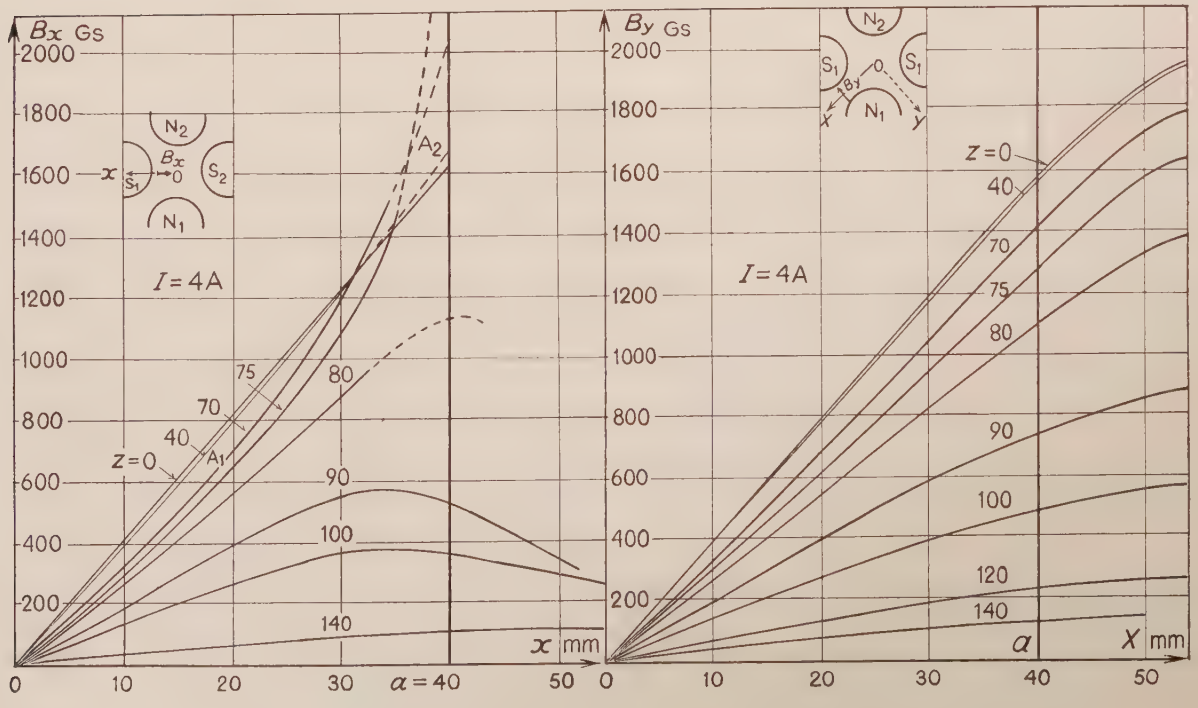

Fig. 29

pointe" au voisinage de l'angle vif de l'extrémité des pièces polaires. Elles sont maximum dans les plans Ox et Oy, mais la figure 29 montre qu'elles se manifestent encore suivant OX et OY.

surface du fer en extrapolant les courbes de la figure 29 puisque

$$\int_0^a B\,dx = \mu_0 nI = \int_0^a B_0\,dx$$

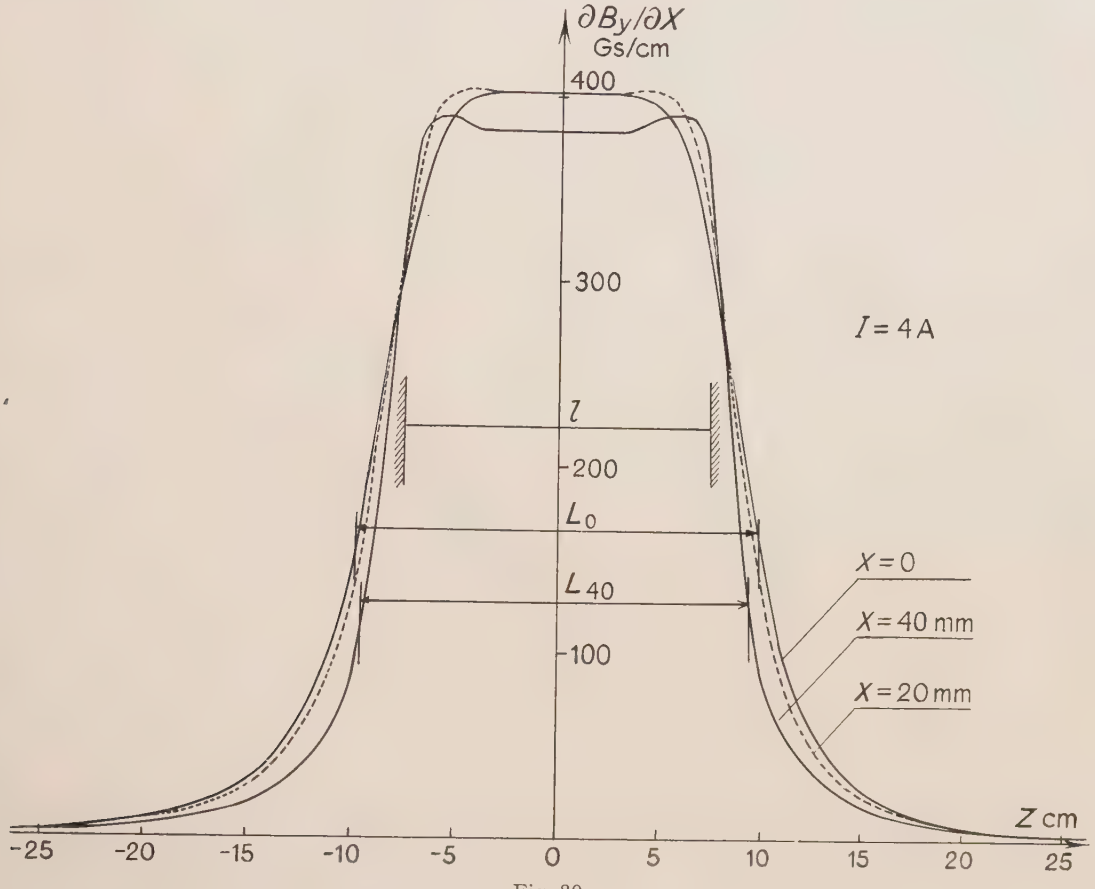

Fig. 30

Donnons quelques valeurs typiques tirées de la figure 29. Suivant OX et OY, jusqu'à $z = 40$ mm, les courbes restent des droites jusqu'à $X, Y = a$. Mais pour $70 < z < 80$ mm, la pente des courbes se relève après $X, Y = \frac{1}{2}a$ avant de décroître pour $X, Y = a$. Pour $z = 70$ mm, $k = 0.0365$ web/m³ pour $X = \frac{3}{2}$ et $k = 0.039$ web/m³ pour $X = a$. Dans les plans Ox et Oy, jusqu'à $x, y = \frac{1}{2}a$, les courbes sont confondues avec les précédentes. Mais pour $\frac{1}{2}a < x, y < a$, elles deviennent très différentes: en $z = 70$, on a $k = 0.0365$ web/m³ près de l'axe et 0.08 web/m³ à $0.8\,a$ de l'axe; en $z = 75$ mm, on a respectivement $k = 0.029$ et 0.10 web/m³. On peut déterminer le champ transverse à la B_0 désignant la valeur en $z = 0$. Pour $z = 70$, on a donc sur le fer B_a de l'ordre de 0.2 web/m², au lieu de 0.16 en $z = 0$, lorsque $I = 4$ A.

Le remplacement des angles vifs par des arrondis de rayon 5 mm, ou par des pans coupés à 45° de 5 mm d'épaisseur n'amène aucune amélioration sensible (figure 31).

Les figures 32 et 33 sont relatives à la lentille Q'_1.

2.2.3. Influence de la deuxième lentille Q_2

Un système convergent comprend deux lentilles juxtaposées Q_1 et Q_2 croisées de même axe (face à un pôle sud de Q_1, on trouve un pôle N de Q_2 et réciproquement). On peut

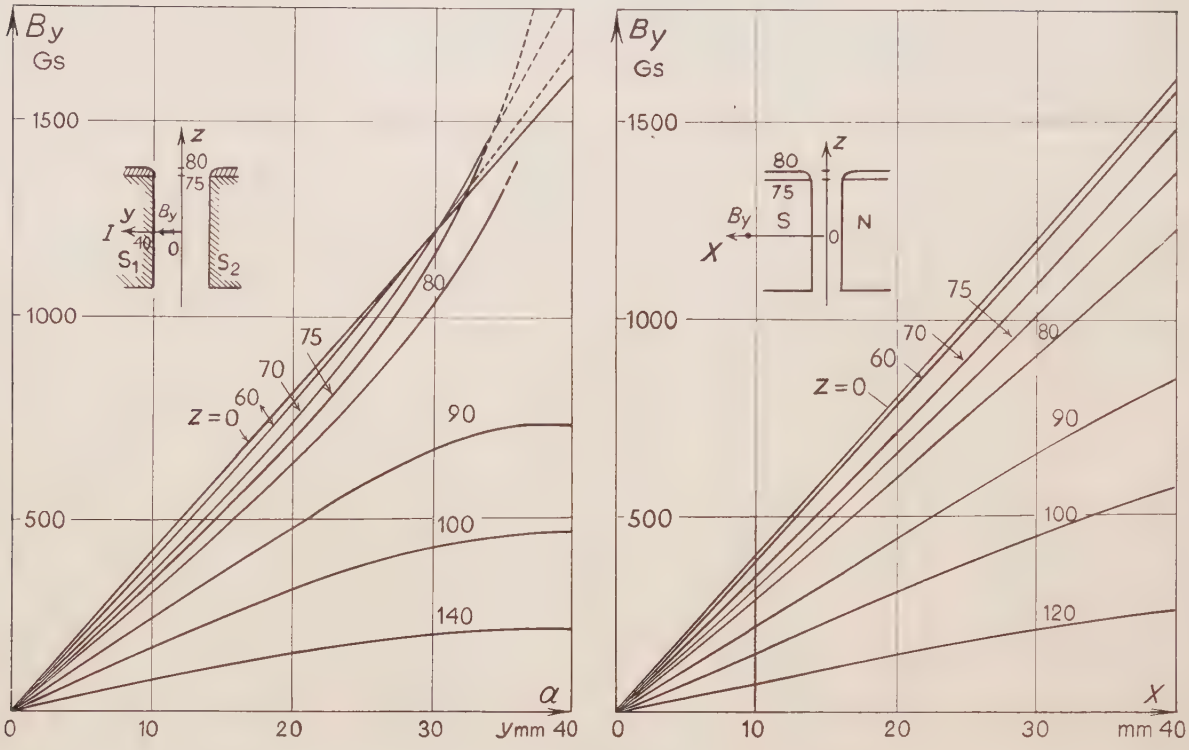

Fig. 31

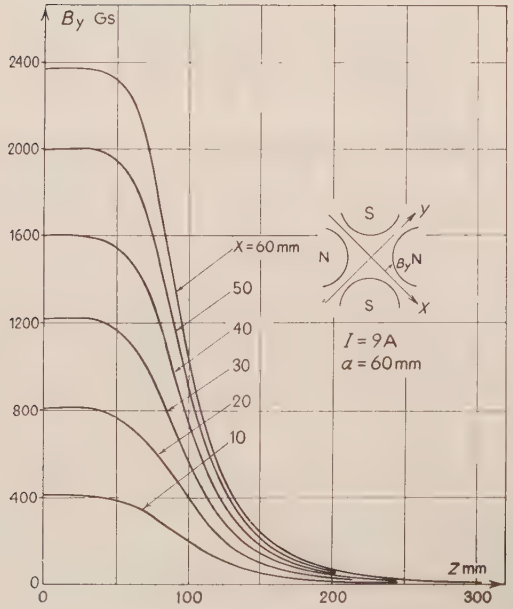

Fig. 32

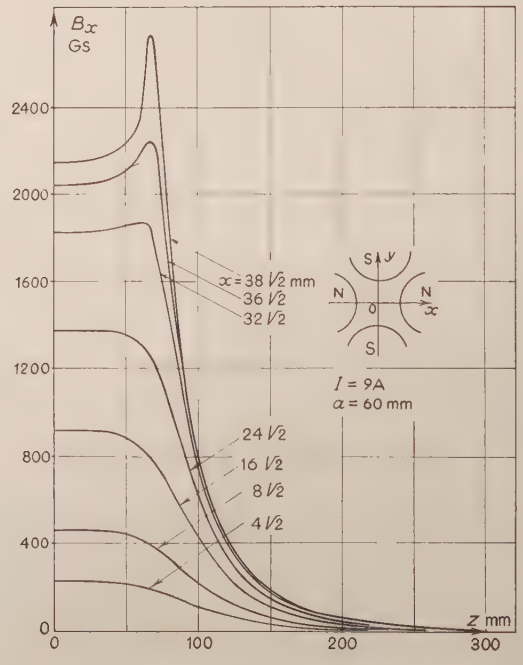

Fig. 33

simuler économiquement l'influence de Q_2 sur le champ de Q_1 en approchant progressivement de Q_1 seule une plaque d'acier doux P suffisamment épaisse représentant l'équipotentielle magnétique $\psi = 0$, située à mi-chemin des deux

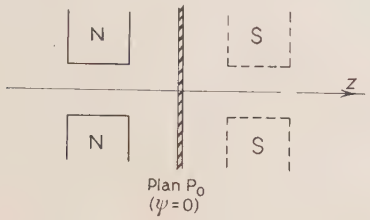

Fig. 34

lentilles dans le cas réel. Un trou de diamètre 12 mm permet le passage de la sonde de mesure dans la plaque à 20 mm de l'axe (figure 34). La figure 35 montre l'influence de P sur le champ transversal pour 3 distances de la plaque au centre de Q_1: $D = 22.5$, 20.5 et 16 cm. Pour $D = 22.5$, aucune modification car le champ de fuite est négligeable à cette distance. Mais pour $D = 16$ cm, la répartition est modifiée: B devient nul sur P (on peut noter une légère pénétration dans le trou de passage de la sonde), et il y a un léger relèvement de la valeur du champ au centre.

Donc, pour une distance entre lentilles supérieure à 45 cm, on pourra considérer comme indépendantes les répartitions de Q_1 et Q_2.

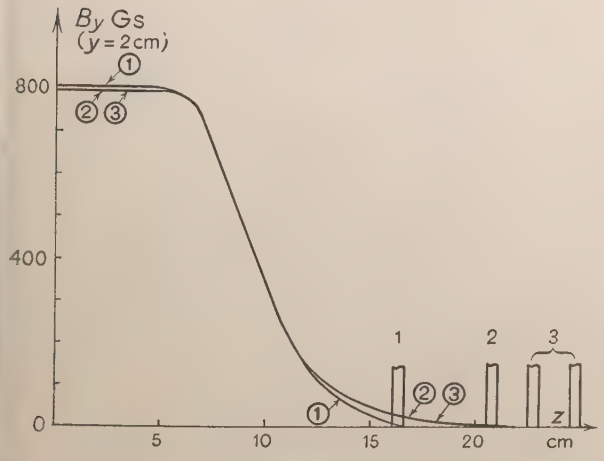

Fig. 35

2.3. COMPOSANTE LONGITUDINALE B_z

2.3.1. Résultats

Par raison de symétrie, B_z est nulle dans les plans OX et OY, ainsi que dans la zone centrale où B_r reste constant, en vertu de la loi div $\boldsymbol{B} = 0$. Les valeurs de B_z ont été mesurées sur des parallèles à Oz; la position de ces droites est déterminée en coordonnées x et y mesurées le long des axes de symétrie médians. La figure 36 donne les valeurs de B_z dans le plan Ox de Q_1, face à un pôle sud, pour différentes valeurs de x. On obtient des courbes en cloche dissymétriques dont le maximum se situe entre $z = 75$ et $z = 85$ mm. Pour $x = a = 40$ mm, il serait situé en $z = 75$ mm, sur l'angle de la pièce

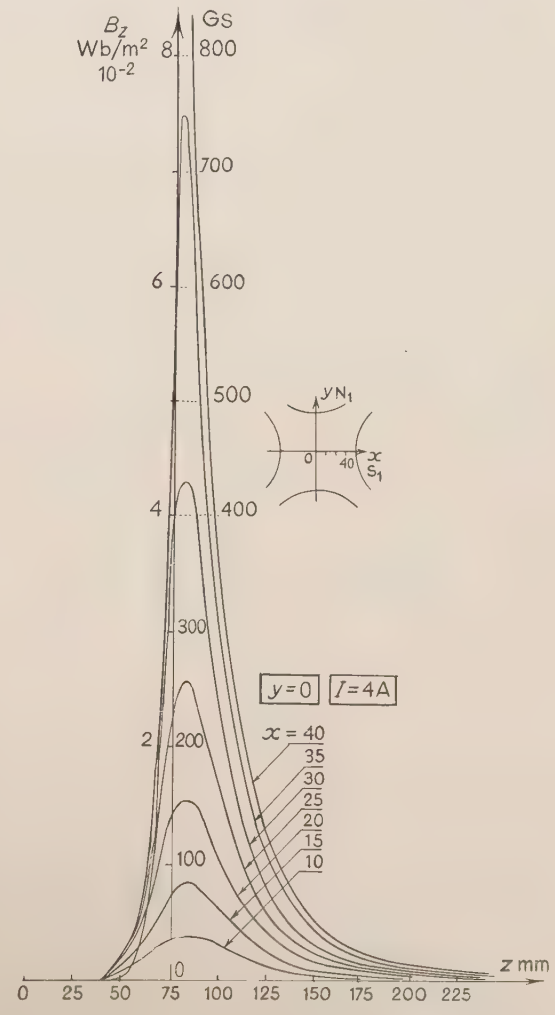

Fig. 36

polaire, où il dépasse 0.2 web/m² (avec $I = 4$ A). B_z est nulle sur l'axe, et encore très faible pour $x = \frac{1}{2}a$. Sa variation radiale, pour différentes valeurs de z est donnée figure 37, dans le plan Oy, face à un pôle nord. On note une légère dissymétrie entre pôles nord et pôles sud, les valeurs de B_z étant légèrement supérieures au voisinage des pôles nord. Nous n'avons pas trouvé d'explication à cet effet, la construction mécanique étant très précise et parfaitement symétrique.

La figure 38 donne les valeurs de B_z dans le plan Ox de Q'_1: les courbes sont plus larges que celles de Q_1.

2.3.2. Comparaison avec la théorie

A partir des répartitions de B_z, on peut calculer l'intégrale

$$L_1 = \int_0^\infty B_z \, dz .$$

mesurée en web/m (ou en gauss × cm), et comparer sa valeur à celle que fournit le calcul.

On a en effet au premier ordre la relation

$$L_1 = \frac{2\mu_0 n I}{a^2} XY \int_0^\infty \frac{dk(z)}{dz} dz$$

$$L_1 = K(0)\, XY = K(0)\, \tfrac{1}{2}x^2 \text{ sur } Ox .$$

Pour $I = 4$ A, on a $K(0) = 0.04$ web/m³. Les valeurs de L_1 mesurées au planimètre, et de L_1 calculées, sont portées figure 39 pour la lentille Q_1. Dans deux lentilles différentes, ayant même gradient radial, on doit retrouver les mêmes de L_1: c'est ce qu'on vérifie sur la figure 40 où on a porté les points expérimentaux relatifs à Q_1 pour $I = 4$ A et à Q'_1 avec $I = 9$ A.

La courbe obtenue est bien une parabole. La figure 41 est une carte à lignes de niveaux donnant la répartition de L_1 dans l'entrefer de Q_1. On peut y noter une légère dissymétrie entre les pôles nord et sud.

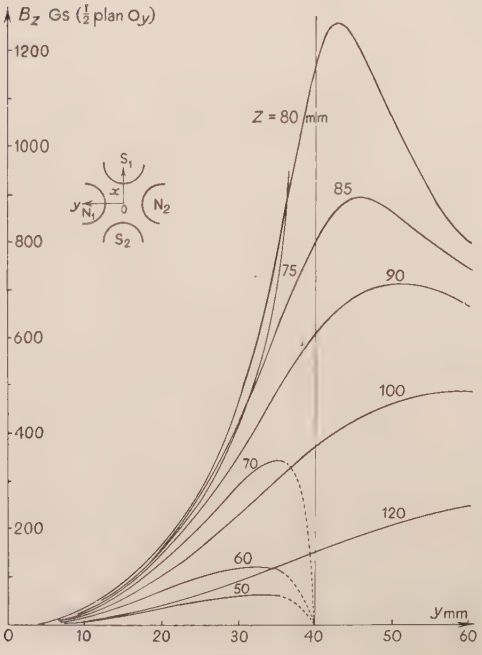

Fig. 37

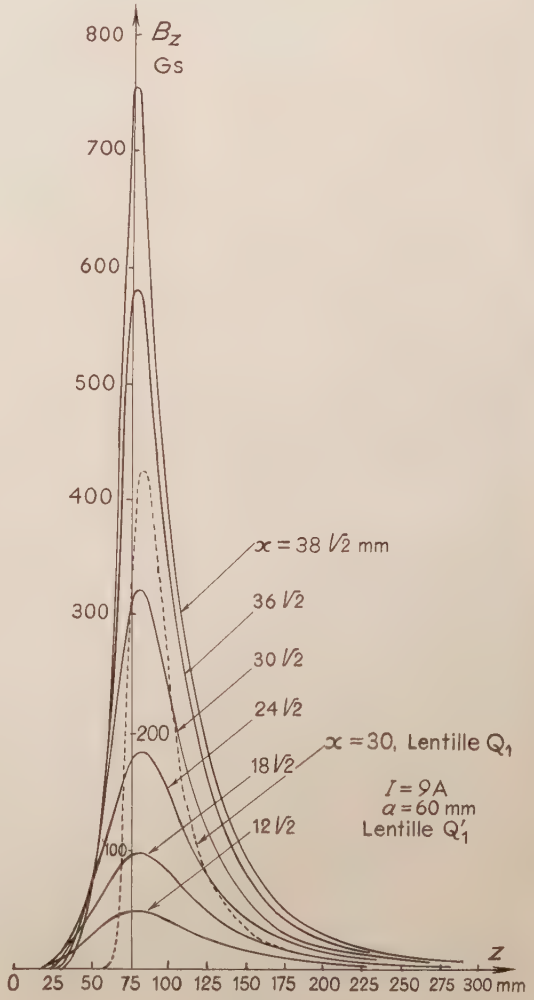

Fig. 38

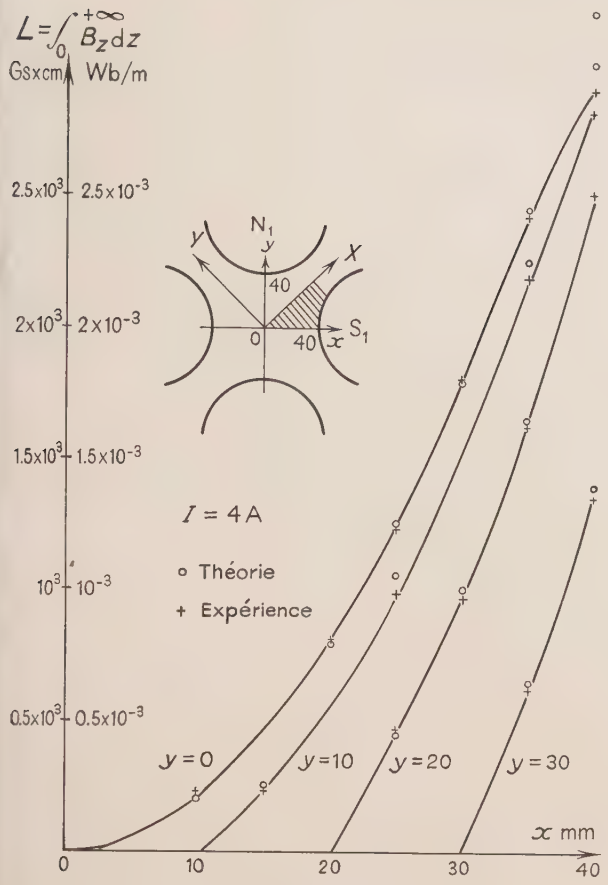

Fig. 39

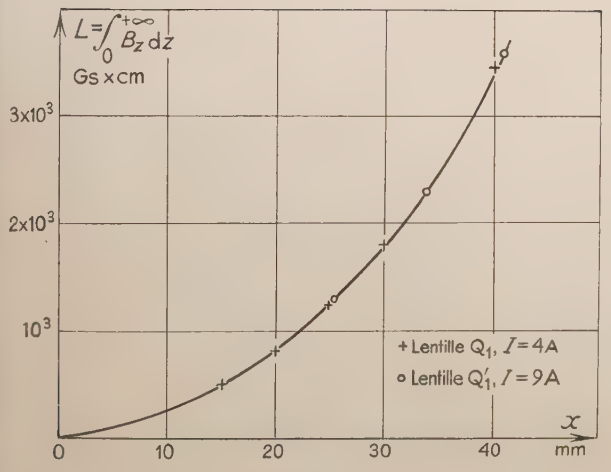

Fig. 40

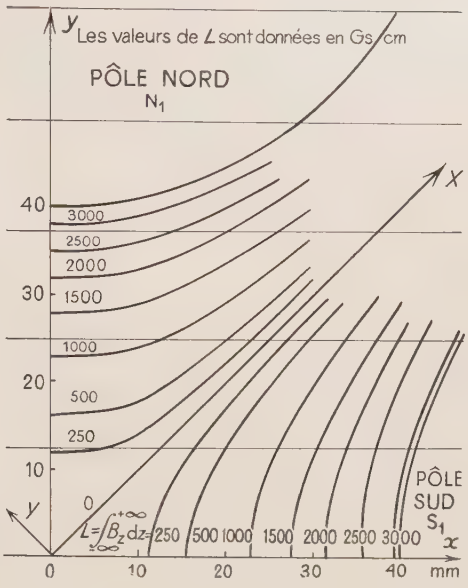

Fig. 41

3. Longueur efficace de la lentille [16])

3.1. DEFINITIONS

3.1.1. Moyenne sur le gradient L_G

A partir des courbes donnant $K(z)$ on peut définir une longueur efficace L_G de la lentille idéale équivalente, dite "longueur efficace" du gradient

$$L_G = \frac{1}{K(0)} \int_{-\infty}^{+\infty} K(z)\, dz\,.$$

3.1.2. Moyenne sur le champ L_C

Avec l'approximation du modèle rectangulaire, on peut considérer sur des parallèles à Oz des répartitions de champ radial également rectangulaires. Si B_0 désigne le champ en $z = 0$, on peut définir une longueur efficace L_C "du champ".

$$L_C = \frac{1}{B_0} \int_{-\infty}^{+\infty} B(r)\, dz\,.$$

On peut montrer[17]) qu'on a la relation

$$L_G = L_C + \frac{B(r)}{(\partial B/\partial r)_r} \frac{\partial L_C}{\partial r}$$

[16]) A. Septier, Etude de la longueur efficace d'une lentille quadrupolaire magnétique et de ses variations dans l'entrefer, C.R. **243** (1956) 1297–1300;
CERN-PS/Sp 14 (1956) non publié;
CERN-PS/Sp 15 (1956) non publié.

[17]) M. G. N. Hine, Effects of Systematic Magnet and Momentum Errors, CERN-PS/MGNH — Note 17 (1956) non publié.

où r désigne la distance à l'axe, soit, en première approximation

$$L_G = L_C + r\frac{\partial L_C}{\partial r}$$

et on n'aura $L_G = L_C$ que si $\partial L_C/\partial r = 0$, ou si $r = 0$ (axe de la lentille). Dans ce cas on posera :

$$L_G = L_C = L_0 .$$

3.2. MESURE DIRECTE DE LA MOYENNE L_C

Les valeurs de L_G et L_C peuvent être calculées à partir des répartitions longitudinales de $K(z)$ ou de $B_r(z)$, après intégration graphique.

Pour L_C il existe un moyen simple d'en suivre les variations dans toute la zone utile. Une bobine longue et étroite de section rectangulaire, ayant ses deux extrémités A et B en dehors du champ (fig. 42), et tournant autour d'un axe parallèle à Oz donnera un signal proportionnel à l'intégrale

$$I = \int_{-\infty}^{+\infty} B\, dz$$

d'où

$$L_C = AI .$$

La constante A est déterminée si on connaît L_C en un point de l'entrefer, par une mesure à l'aide de la bobine tournante courte, et la variation radiale de B_0.

Nous avons réalisé une bobine de ce type, formée de 12 spires de fil de 0.1 mm bobinées à fond de gorge dans deux rainures parallèles ménagées dans une tige de plexiglas longue de 700 mm et de diamètre 20 mm. Le moteur, le collecteur et le système de déplacement sont identiques à ceux de la sonde à bobine courte. La tige de plexiglas est guidée sur une certaine longueur par un tube de laiton fixe muni de paliers graphités. La disposition verticale durant les mesures permet seule une rotation sans vibrations parasites, si la tige est bien rectiligne. Le signal produit à 25 Hz comporte également une composante parasite à 50 Hz qu'un filtrage soigné permet d'éliminer.

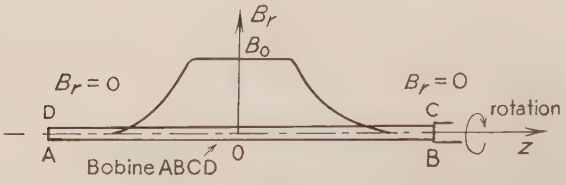

Fig. 42

3.3. VARIATIONS DE L_C DANS L'ENTREFER

3.3.1. Lentille Q_1

A une intensité donnée, la longueur L_C décroît légèrement lorsqu'on s'éloigne de l'axe et cette décroissance est la même dans toutes les directions radiales, Cette décroissance atteint 1% pour $r = \frac{2}{3}a$ et 2.5% environ pour $r = a = 4$ cm. La valeur de L_C sur l'axe est $L_0 = 195 \pm 0.5$ mm, soit $L_0 = l + 1.1\,a$.

On voit que L_0 est nettement supérieure à la longueur mécanique l de la lentille, et l'écart $(L_0 - l)/l$, atteint 30%. La figure 43 montre la

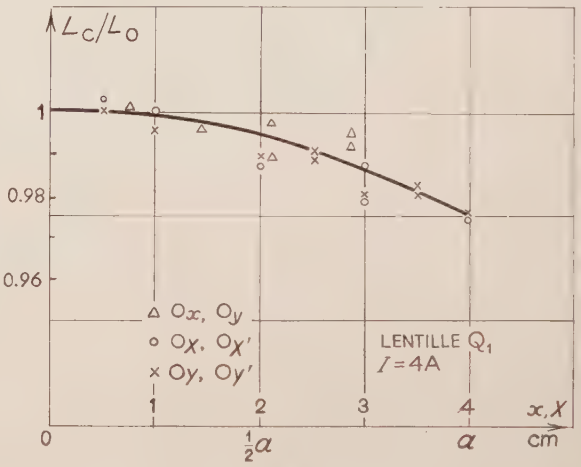

Fig. 43

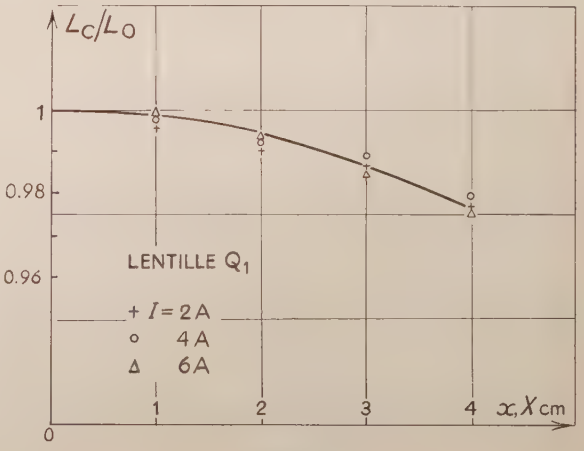

Fig. 44

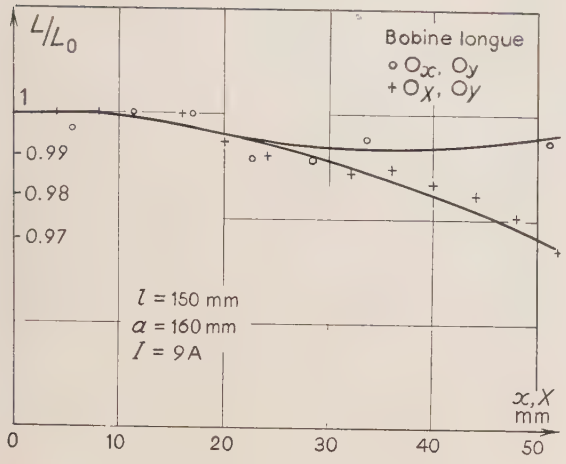

Fig. 45

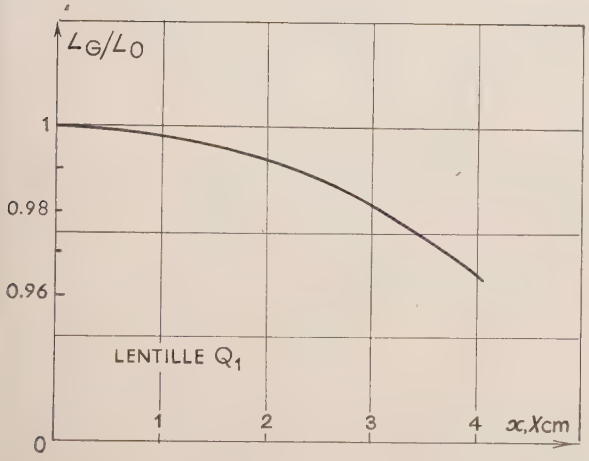

Fig. 46

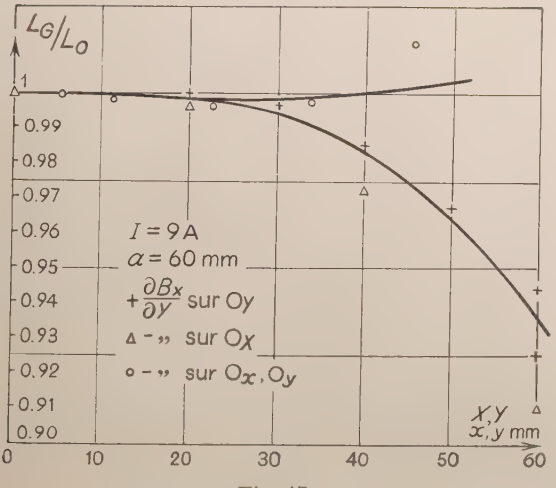

Fig. 47

variation de L_C/L_0 en fonction de la distance à l'axe; la courbe tracée est une courbe moyenne, les points expérimentaux se plaçant dans une zone d'épaisseur 1.5 à 2%.

Cette loi de variation reste la même lorsque l'intensité I varie (fig. 44).

3.3.2. Lentille Q'_1

L_0 est de l'ordre de 207 mm, d'où $L_0 \neq l + 0.95\,a$. Les variations de L_C ne sont plus identiques dans les plans OX, OY d'une part et Ox, Oy d'autre part, si on calcule L_C avec les vraies valeurs de B_0 en $z = 0$; le fléchissement du gradient face aux pôles se traduit par des valeurs de B_0 inférieures aux valeurs théoriques, et par une remontée apparente de L_C (fig. 45). Mais si on calcule L_C à partir des valeurs théoriques de B_0 (ce qui traduit mieux les propriétés réelles de convergence de la lentille), les deux courbes sont pratiquement confondues, avec une décroissance $\Delta L/L$ de 3% à 50 mm de l'axe, et cette courbe commune est confondue avec celle de Q_1 si on utilise des coordonnées réduites, avec a pour unité d'abscisses; il y aura donc avantage à utiliser une lentille à gros trous, pour un faisceau de taille donnée.

3.4. COMPARAISON DE L_C ET L_G

3.4.1. Lentille Q_1

Les mesures de L_G au vibreur ont été effectuées seulement dans OX et OY pour les gradients de B_X et B_Y:

Plans OX $B_Y \neq 0$ $K_1 = \partial B_Y/\partial X$

OY $B_Y = 0$ $K'_1 = \partial B_Y/\partial X$.

Plans OY $B_X \neq 0$ $K_2 = \partial B_X/\partial Y$

OX $B_X = 0$ $K'_2 = \partial B_X/\partial Y$.

Les mesures permettent de vérifier que $K_1 = K'_1 = K_2 = K'_2$ et que la décroissance de L_G est légèrement plus rapide que celle de L_C (fig. 46): $\Delta L_G/L_0$ atteint 3.5% pour $r = a$, mais reste inférieure à 1% pour $r = \frac{1}{2}\,a$.

3.4.2. Lentille Q'_1

Le même phénomène se manifeste (fig. 47), la décroissance atteignant 5 à 5.5% pour $r = a$.

La relation théorique entre L_C et L_G est vérifiée à la précision des mesures près (1% environ) sur les valeurs de L_C et L_G.

3.5. CORRECTION DES VARIATIONS DE L_C

Physiquement la décroissance de L_C lorsqu'on s'éloigne de l'axe entraîne une décroissance de la convergence de la lentille (supposée mesurée

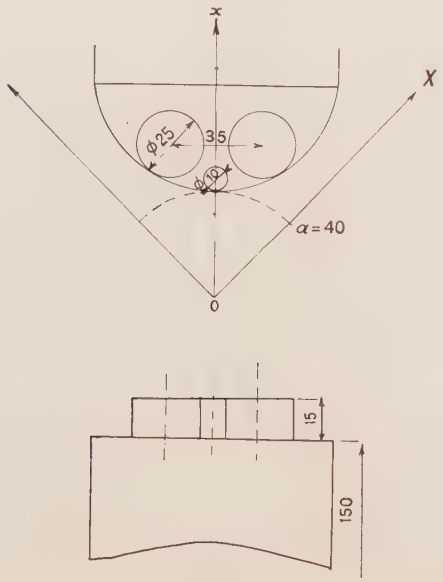

Fig. 48

pour un pinceau de rayons cheminant initialement à la distance r de l'axe) c'est-à-dire, en langage optique, une aberration d'ouverture négative, de signe opposé à celui de l'aberration d'ouverture des autres lentilles convergentes utilisées en optique corpusculaire.

Si on se préoccupe de réduire l'aberration d'ouverture, il faut réduire ou annuler la variation de L. Il suffit de raisonner sur L_C car si $\Delta L_B = 0$, on aura partout $L_C = L_G = L_0$. Nous avons cherché empiriquement un moyen d'accroître L_C sur les bords, sans changer la valeur de L_0 au centre; la difficulté est de réaliser une correction identique dans toutes les directions radiales.

Cette correction a pu être effectivement réalisée sur Q_1 en accroissant localement la longueur des pièces polaires par l'addition de masselottes de fer doux convenablement disposées. A chaque modification l'exploration de l'espace central à l'aide de la bobine longue renseignait sur l'efficacité de la correction. Le système de masselottes fournissant la correction suivant les quatre plans radiaux de symétrie (on peut alors supposer que la correction est effectuée dans les autres directions) est représenté fig. 48: il s'agit pour chaque pièce polaire de trois cylindres de fer doux de 15 mm de hauteur et de diamètres 25 mm pour les pièces latérales, 10 mm pour la pièce centrale.

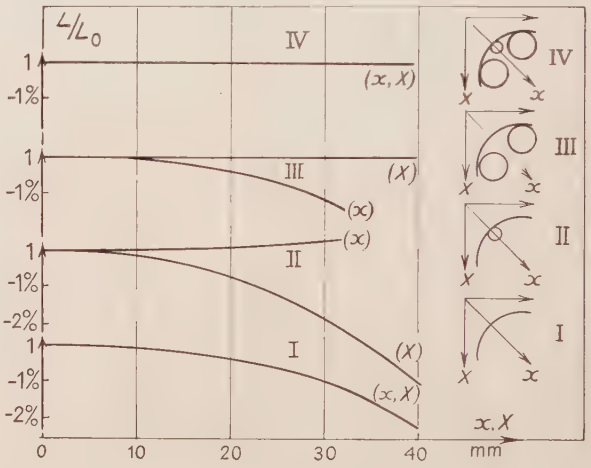

Fig. 49

Leurs actions respectives sont représentées fig. 49; en 49_I, on retrouve la courbe $L/L_0 = f(r)$ de la lentille non corrigée; en 49_{II}, l'action de la masselotte centrale dédouble la courbe: le plan Ox est sur-corrigé, tandis que la décroissance est accrue suivant OX; en 49_{III}, dédoublement inverse, dû aux pièces latérales. Enfin en 49_{IV}, action conjuguée de toutes les pièces; on a $L = L_0$ dans tout l'espace utile.

Nous avons vérifié que l'addition des masselottes n'influait pas sur la répartition du champ en $z = 0$. Par contre la répartition du champ B_z est perturbée, surtout dans le plan Ox: le raccordement des lignes de champ sur la pièce polaire et la masselotte centrale devient compliquée, et la courbe donnant B_z présente deux maxima successifs (figure 50). L'influence des correcteurs commence à se manifester pour $x \geqslant \frac{1}{2} a$. L'aire des courbes reste pratiquement inchangée: on peut supposer que l'action globale

de B_z restera la même et que le terme d'aberration provoqué par cette composante parasite sera inchangé par la correction.

Cette méthode de correction nécessite la présence aux extrémités des pièces polaires d'un espace libre qui ne soit pas recouvert par les enroulements: elle est possible pour les lentilles où l'excitation est faible.

On peut songer à remplacer l'action des masselottes latérales par une modification du profil des pièces polaires en réduisant les entre-

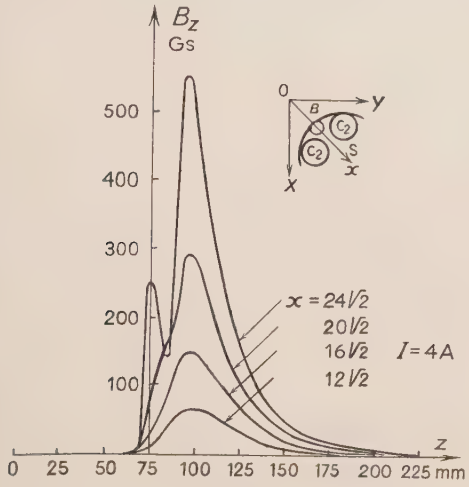

Fig. 50

fers latéraux; on accroît le champ, et par suite la longueur L_C calculée à partir du champ théorique à gradient constant. C'est la solution adoptée en particulier pour les lentilles quadrupolaires de compensation placées entre les unités du synchrotron[2]). Mais on ne peut effectuer par ce procédé la correction suivant Ox, Oy. L'étude des aberrations nous montrera que la non correction de L suivant Ox, Oy conduit en réalité à une aberration d'ouverture plus faible.

4. Influence du rétrécissement des pièces polaires et de la saturation sur la topographie du champ dans la zone utile[18])

4.1. FORME DES PÔLES UTILISES

Sur la carcasse magnétique carrée de Q_1 nous avons monté 4 pièces polaires trapézoïdales, spécialement étudiées pour obtenir des gradients intenses tout en retardant au maximum l'apparition de la saturation†. Leur forme et leurs dimensions sont indiquées figure 51a; leur longueur est de 88 mm, puis passe à 108 mm, pour diminuer l'induction moyenne; dans le même but, la largeur des pôles, à l'origine de $D = 44$ mm $= 1.1\,a$, passe progressivement à $D = 100$ mm $= 2.5\,a$. Chaque pôle a une méri-

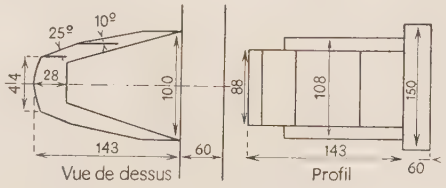

(a) Fig. 51 (b)

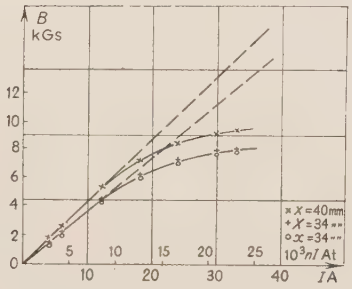

Fig. 52

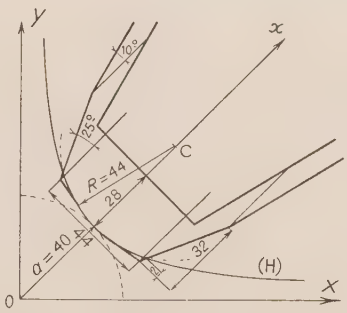

Fig. 53

dienne formée d'un arc de cercle de rayon $R = 44$ mm $= 1.1\,a$, prolongé par deux segments de droites tangentes (figure 51b), situées à l'extérieur de l'hyperbole théorique afin de compenser le rétrécissement des pôles. Ce

† Le projet de ces modifications a été proposé par MM. M. Morpurgo et A. Citron, de la division du Synchrocyclotron du CERN.

[18]) A. Septier, Influence de la saturation sur la topographie du champ dans une lentille quadrupolaire magnétique, CERN-SC/Sp 1 (1958) non publié.

rétrécissement est ici nécessaire pour loger le maximum d'ampères-tours magnétisants. Les bobines comportent 695 spires, grâce à l'addition de petites bobines de 68 spires placées au voisinage du cercle de gorge.

4.2. CARACTERISTIQUE CHAMP-COURANT

En $X = a = 40$ mm, la courbe $B = f(I)$ est donnée fig. 52; dans la zone linéaire de la caractéristique, le gradient mesuré est de 1.09 web·m^{-3}·A^{-1}, en bon accord avec la valeur théorique.

On peut comparer cette courbe à celle de Q_1 (fig. 12). Pour $nI = 20\,700$ A.T., on aurait ici $B_a = 0.91$ web/m^2, au lieu de $B_a = 0.75$ web/m^2. Notons toutefois que pour cette valeur de nI la convergence de Q_1 serait supérieure à celle de la nouvelle lentille Q_3, car la longueur efficace de Q_3 est très inférieure à celle de Q_1 (135 mm au lieu de 195 mm), le rapport des facteurs caractéristiques $(\beta L)_{Q_1}/(\beta L)_{Q_3}$ est de l'ordre de 1.3 en faveur de Q_1.

4.3. TOPOGRAPHIE DU CHAMP, LONGUEUR EFFICACE L_C

Dans le plan $z = 0$ on obtient pour différentes intensités, les courbes de la figure 54; malgré la saturation les répartitions radiales restent identiques: après une zone linéaire, le champ croît plus rapidement que la droite théorique jusqu'en $X = \frac{2}{3}a$, puis décroît ensuite en recoupant cette droite vers $X = a$. Dans les plans Ox, Oy, les valeurs de B sont toujours en dessous de la droite théorique: il existe une légère dissymétrie suivant les directions radiales. Les mesures de gradient le confirmeront.

Suivant des parallèles à Oz, on obtient par exemple les courbes de la figure 55. Ces courbes ont permis d'obtenir les valeurs de la longueur efficace L_C. Celle-ci est de 135 mm sur l'axe, et varie lorsqu'on s'en éloigne selon les courbes de la figure 56: les variations sont différentes suivant OX et Ox. Les courbes en trait continu correspondent aux valeurs de L_C obtenues à l'aide des valeurs réelles de B_0, tandis que pour les courbes en trait discontinu on a utilisé les valeurs théoriques de B_0.

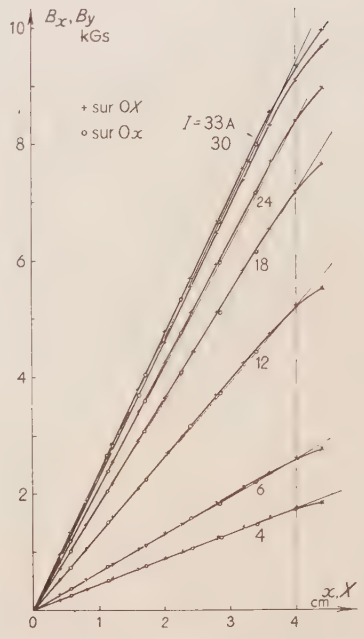

Fig. 54

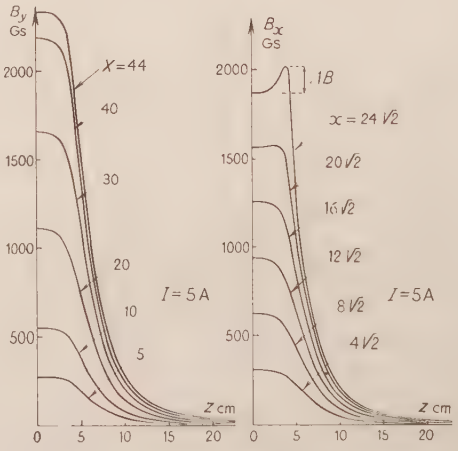

Fig. 55

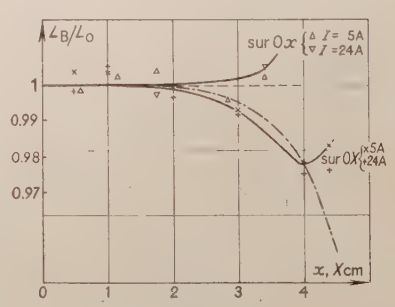

Fig. 56

4.4. TOPOGRAPHIE DU GRADIENT, LONGUEUR EFFICACE L_G

Les mesures du gradient radial B', beaucoup plus sensibles aux inhomogénies que les mesures de champ, conduisent dans le plan $z = 0$ aux courbes de la figure 57. Suivant OX, on voit que le gradient, d'abord constant près de l'axe, croît lentement, passe par un maximum peu accusé,

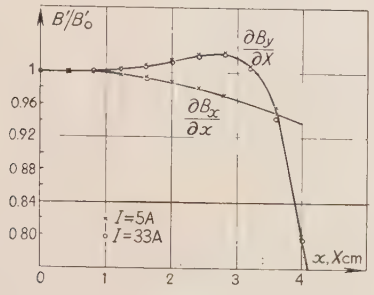

Fig. 57

($\Delta B'/B'_0 \approx 2\%$) vers $X = \frac{2}{3}a$, puis décroît ensuite très rapidement; l'écart $\Delta B'/B'_0$ atteint 25%, pour $X = a$. Dans la direction Ox, la décroissance est constante, mais ne dépasse pas 6% sur le sommet des pôles.

La zone pour laquelle $\Delta B'/B'_0$ reste inférieure à 5% dans toutes les directions s'étend donc jusqu'à $r = 0.9\,a$; sans les surépaisseurs latérales des pôles, la chute de B' serait beaucoup plus rapide dans les directions OX, OY.

La longueur efficace L_G a été calculée à l'aide des répartitions $K(z)$ de B', semblables à celles de la figure 58. Elle coïncide avec L_C sur l'axe; ses variations suivant OX et Ox sont différentes: elles sont données figure 59, où les courbes en trait plein sont obtenues à partir des valeurs réelles de B'_0. Suivant OX, on peut ici vérifier la relation donnée plus haut entre L_C et L_G: on a bien en effet $L_C = L_G$ lorsque $dL_C/dX = 0$.

4.5. INFLUENCE DE LA SATURATION

Quelle que soit l'intensité I, la topographie du champ reste la même. Les mesures du gradient effectuées à la saturation le confirment: les points correspondant à $I = 33$ A se placent bien sur la courbe de la figure 57 avec $I = 5$ A.

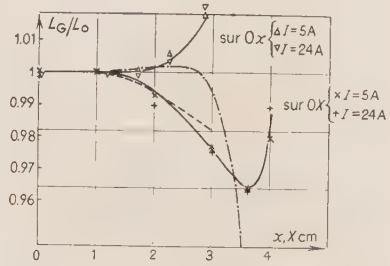

Fig. 59

L'exploration de la répartition du flux ψ dans les pièces polaires en fournit l'explication.

Nous avons mesuré ψ dans les pièces polaires et la carcasse par la méthode décrite pour Q_1. Les résultats relatifs à ψ sont portés figure 56 pour $I = 33$ A. Les raccordements des courbes au voisinage de la discontinuité de longueur de la pièce polaire, puis de la carcasse, montrent qu'une partie des lignes de champ préfère se fermer dans l'air. Le point T de la figure 60 correspond au flux qui traverse effectivement la carcasse et qui devrait traverser la

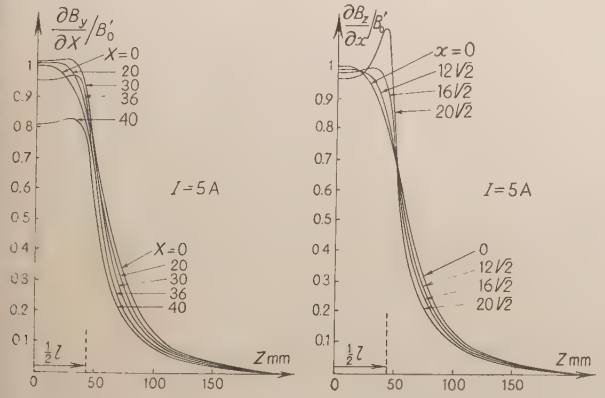

Fig. 58

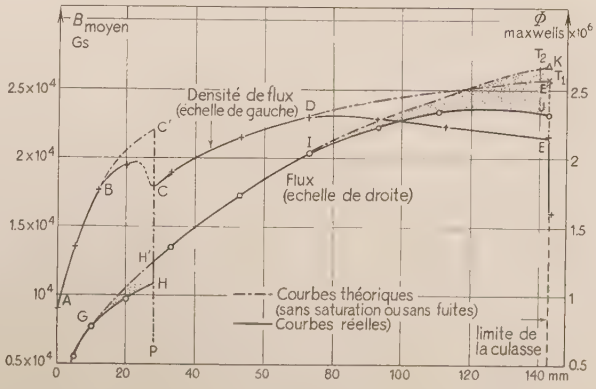

Fig. 60

base de la pièce polaire s'il n'y avait pas saturation.

L'induction moyenne atteint $E_m = 2.3$ web/m² à 6 cm environ de la carcasse, ce qui entraîne la saturation de cette zone. Dans la carcasse, B_m est plus faible que pour Q_1: $B_m = 1.55$ web/m², et cette carcasse n'est pas saturée; la limitation est due ici aux pièces polaires qui sont en acier doux et non en Armco. Des pièces polaires plus courtes seraient plus avantageuses mais la diminution devrait dépasser 50%, ce qui ne permettrait plus de loger un nombre suffisant de spires. L'emploi du fer Armco permettrait de faire croître légèrement B_a, qui est de 0.94 web/m². Il semble que la valeur $B_a = 1$ web/m², soit une limite difficile à atteindre.

La figure 61 montre les variations de ψ telles qu'on peut les obtenir à l'aide des formules empiriques citées plus haut; l'écart avec la réalité est faible près du pôle, mais devient ensuite très grand.

Les mesures montrent que la saturation, même pour des pièces à section variable croissante, se produit loin des pôles. Dans les entrefers latéraux, l'induction locale B_m ne dépasse pas 2 web/m²; nous l'avons vérifié à

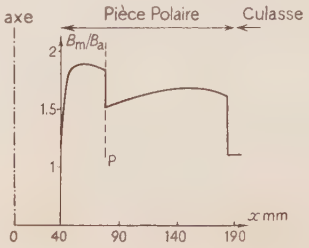

Fig. 61

l'aide de spires de faible dimension collées sur les angles en regard des pôles N et S: aucune saturation locale ne s'y produit. Par suite, la surface des pôles reste une surface équipotentielle magnétique: les défauts des lentilles resteront les mêmes, quelle que soit l'excitation, ce qui permet leur étude à champ faible.

NUCLEAR INSTRUMENTS AND METHODS 6 (1960) 157–163; NORTH-HOLLAND PUBLISHING CO.

THE SPHERICAL CONDENSER AS A HIGH TRANSMISSION PARTICLE SPECTROMETER

I. POINT SOURCE

R. H. RITCHIE, J. S. CHEKA and R. D. BIRKHOFF

Health Physics Division, Oak Ridge National Laboratory†, Oak Ridge, Tennessee

Received 9 September 1959

The inverse square electric field between two concentric charged spheres provides a focussing of charged particles which leave a point source on the inner sphere. An analysis of the transmission, resolution, and line profile shape which may be obtained with a spectrometer utilizing this focussing has been carried out analytically and graphically. It is found that the fractional transmission T is related to the resolution $\delta_{\frac{1}{2}}$ (the fractional energy spread at half the maximum transmission) according to $T = \sqrt{\delta_{\frac{1}{2}}}$. Transmissions as high as 25% are obtainable at 6% energy resolution with such a device.

1. Introduction

Electrostatic focussing beta-ray spectrometers have been little used until the present time[1]). Devices constructed from concentric spherical conductors seem to offer much promise in applications where high transmission is important, because of their two dimensional focussing property. Purcell[2]) has considered an application in which focussing occurs inside a spherical sector after field-free flight of particles from the source to the spectrometer. Allison and Weyl[3]) have constructed a spherical electrostatic spectrometer, primarily intended for heavy particle analysis, in which the source is located in the electric field of the device. Siegbahn[4]) has expressed the opinion that such devices will become more frequently used in the future because both the ratio of transmission to resolution and the transmission itself may be made very high.

It is the purpose of Parts I and II of this paper to analyze the performance of a spherical electrostatic analyzer in which the source is located on the surface of the inner sphere and where particles emitted from the source after energy analysis emerge into a field-free region where post-acceleration and detection may occur. Fig. 1 shows how such a device might appear in cross section[5]). Several representative

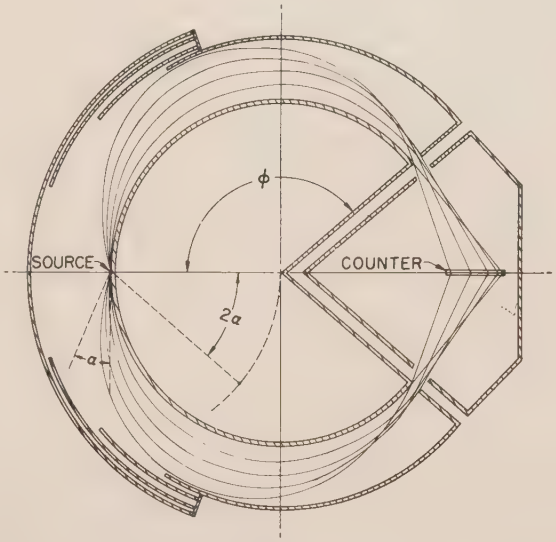

Fig. 1

† Operated by Union Carbide Corporation for the U.S. Atomic Energy Commission.

[1]) K. Siegbahn, Beta- and Gamma-Ray Spectroscopy (North-Holland Publishing Company, Amsterdam, 1955).

[2]) E. M. Purcell, Phys. Rev. **54** (1938) 818.

[3]) S. K. Allison and P. Weyl, Personal communication (1954) to K. Siegbahn, reported in Beta- and Gamma-Ray Spectroscopy (North-Holland Publishing Co., Amsterdam, 1955) p. 90.

[4]) K. Siegbahn, op. cit.

[5]) This device has been called the "Keplertron", for obvious reasons.

trajectories are shown. The electric field is adjusted so that monoenergetic particles, emitted tangent to the inner sphere, will follow the surface of the inner sphere, i.e., have circular trajectories, until they emerge from the spectrometer into a field-free region after having gone through a central angle ϕ. Particles making (initially) an angle α with the tangent plane follow elliptical paths as shown. As the angle α is increased the radial displacement of the trace from the inner sphere at the fixed angle ϕ ($> \frac{1}{2}\pi$) increases until a maximum is reached, whereupon the trace begins to return as α increases still further. Finally, for still larger α the trace reaches the inner sphere. If one plots $n(r)$, the number of traces per unit radial interval which have radial displacement r, at a given value of ϕ for an isotropic distribution of velocities from the source point, one finds that as long as ϕ is $> \frac{1}{2}\pi$ there is a value of r at which n becomes infinite. In the small-angle approximation discussed below, n is proportional to $1/\sqrt{r_m - r}$, where r_m is the maximum radius attained by a trace at the angle ϕ. This "bunching" of trajectories at the central angle ϕ suggests the introduction of an annular slit at this position in order to give the arrangement energy selectivity without sacrificing transmission. A counter placed along the line joining the source and center of the spheres intercepts the trajectories after they emerge from the region between the spheres. The counter enclosure is shown as separated from the spheres to indicate that a post-accelerating voltage may be applied between the spheres and the enclosure. Anti-scatter baffles are shown schematically in fig. 1. These may be accurately located on equipotentials of the electric field. Only non-relativistic particles will be considered in the present discussion of this device.

Part II of this paper will consider the effect of the finite size of the source; the present study is restricted to particles emerging from a point located on the inner sphere and on the axis of the instrument. It is assumed that the detector is large enough so that all particles emerging from the slit will be detected.

2. Trace Equation

Fig. 2 shows a schematic representation of a section through the spherical condenser. The velocity vector $\boldsymbol{v}$ of a non-relativistic particle of kinetic energy $E = \frac{1}{2}mv^2$ emitted from a point on the inner sphere and on the axis of symmetry is assumed to make an angle α with a tangent plane perpendicular to this axis. The differential equation and solution of the orbit may be readily shown to be[6])

$$\frac{d^2}{d\phi^2}\left(\frac{1}{r}\right) + \left(\frac{1}{r}\right) - \frac{mk}{l^2} = 0 \tag{1}$$

$$\frac{1}{r} = \frac{mk}{l^2} + A \sin\phi + B \cos\phi \tag{2}$$

where k is the force constant obtained from eq. (3) which equates m times the centripetal acceleration to the electrostatic force for a particle leaving the source with $\alpha = 0$ and an energy $E_0 = \frac{1}{2}m v_0^2$ such that it executes a circular orbit with $r = r_m$;

$$\frac{mv_0^2}{r_m} = \frac{k}{r_m^2}. \tag{3}$$

The parameter l is the angular momentum given by

$$l = mvr_m \cos\alpha. \tag{4}$$

The value of mk/l^2 is then

$$\frac{mk}{l^2} = \frac{1}{(1+\delta)\, r_m \cos^2\alpha} \tag{5}$$

where the energy parameter δ given by

$$\delta = \frac{E}{E_0} - 1 \tag{6}$$

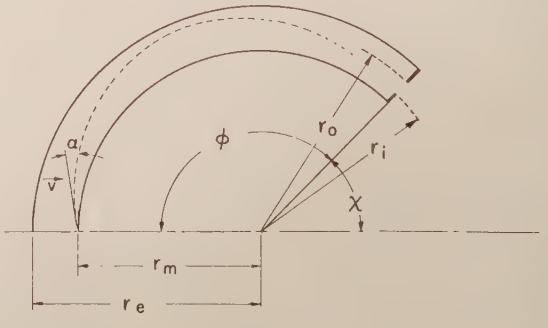

Fig. 2

[6]) For example, see H. Goldstein, Classical Mechanics (Addison-Wesley Press, Inc., Cambridge, Mass., 1951) p. 76.

has been introduced. The parameter A is obtained from elementary considerations in three steps. By inspection, the relationships

$$(\dot{r})_{\phi=0} = v \sin\alpha$$
$$(\dot{\phi})_{\phi=0} = \frac{v\cos\alpha}{r_m} \tag{7}$$

may be seen to hold. Secondly $(dr/d\phi)_{\phi=0}$ may be obtained from eq. (2). This value of $(dr/d\phi)_{\phi=0}$ may then be equated to the ratio $(\dot{r})_{\phi=0}$ and $(\dot{\phi})_{\phi=0}$ given in eqs. (7) and the result solved for A to yield

$$A = -\frac{\tan\alpha}{r_m}. \tag{8}$$

The parameter B is obtained from eq. (2) evaluated when $\phi = 0$ and $r = r_m$.

$$B = \frac{1}{r_m}\left[1 - \frac{1}{(1+\delta)\cos^2\alpha}\right]. \tag{9}$$

A substitution of eqs. (5), (8), and (9) into (2) yields the orbit equation in terms of parameters useful in calculations of transmission and resolution.

$$\frac{r}{r_m} = \frac{\cos^2\alpha}{\frac{1}{1+\delta}(1-\cos\phi) + \cos\alpha\cos(\phi+\alpha)}. \tag{10}$$

In terms of V_0, the potential difference applied between the spheres,

$$E_0 = \frac{V_0 r_e}{2(r_e - r_m)}. \tag{11}$$

One supposes that at the angle ϕ there exists an annular gap with inner and outer radii r_1 and r_0, respectively. These radii will be chosen so as to optimize the transmission profile, $T(\delta)$, defined below, for the spectrometer.

If the spectrometer accepts traces in the range $\alpha_1 \leqslant \alpha \leqslant \alpha_2$ at the energy δ, the transmission $T(\delta)$ is found from

$$dT(\delta) = \tfrac{1}{2}\cos\alpha\, d\alpha$$

or

$$T(\delta) = \tfrac{1}{2}(\sin\alpha_2 - \sin\alpha_1) \tag{12}$$

where $T(\delta)$ is normalized to unit isotropic emission from the source point.

There will in general be traces which would be transmitted by the gap except that they intercept the outer or inner sphere. The assumption is made in Parts I and II of this article that no electron striking either the inner or outer spheres can reach the detector by scattering on the spheres nor can it give rise to secondary electrons which might reach the detector. Also if a particle emerges from the source with $\alpha < 0$, one assumes that it enters the surface of the inner sphere and does not re-emerge.

3. Transmission, Resolution and Line Profile in Small Angle Approximation

It is illuminating and valuable for computational purposes to expand eq. (10) under the assumption that $\pi - \phi \equiv \chi \ll 1$. Letting $r/r_m = 1 + \varepsilon$ and assuming that α is an infinitesimal of the same order of magnitude as χ but that δ is of the order χ^2 one finds

$$\varepsilon = \chi\alpha - 2\alpha^2 + 2\delta. \tag{13}$$

This may be rewritten in terms of the dimensionless variables $e = \varepsilon/\chi^2$, $a = \alpha/\chi$, and $d = \delta/\chi^2$ as follows

$$e = a - 2a^2 + 2d. \tag{14}$$

The solid lines of fig. 3 show d versus a for various values of e plotted from this equation. An inspection of this figure is very helpful in establishing the effect of variations of the radii of the inner and outer gaps on the line profile exhibited by the spectrometer.

If the gap system accepts particles in the range of angles $\alpha_1 \leqslant \alpha \leqslant \alpha_2$, the transmission is given by the small angle approximation to eq. (12)

$$T = \tfrac{1}{2}(\alpha_2 - \alpha_1) = \tfrac{1}{2}\chi(a_2 - a_1) \tag{15}$$

to the same order of accuracy used in obtaining eqs. (13) and (14).

In order to see how the outer sphere interception varies with α and δ, one returns to the complete trace equation (eq. (10)) and expands for $\phi = \tfrac{1}{2}\pi - \theta$, where $\theta \ll 1$. One finds that to the same order of approximation as was employed before,

$$d = e - \frac{1}{\chi}a \tag{16}$$

showing that θ drops out of the equation to this

order. A term proportional to a^2 has been neglected compared with $(1/\chi)\,a$ since $\chi \ll 1$.

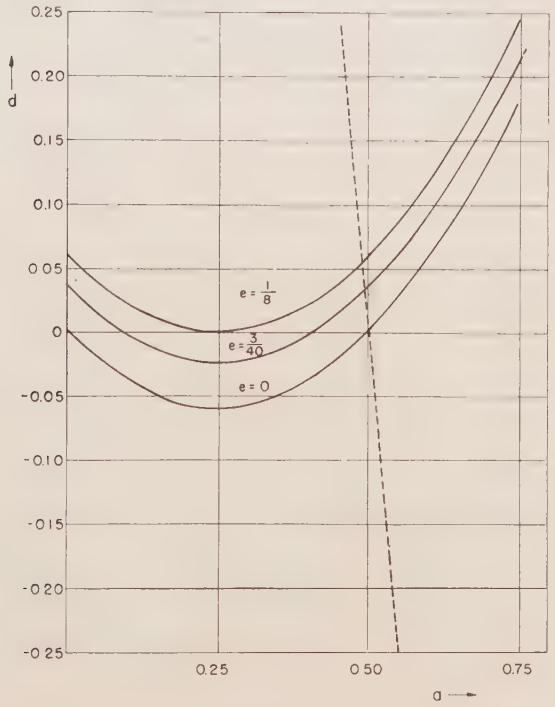

Fig. 3

The radius of the outer sphere is set to just pass the trace with $\delta = 0$ at its maximum

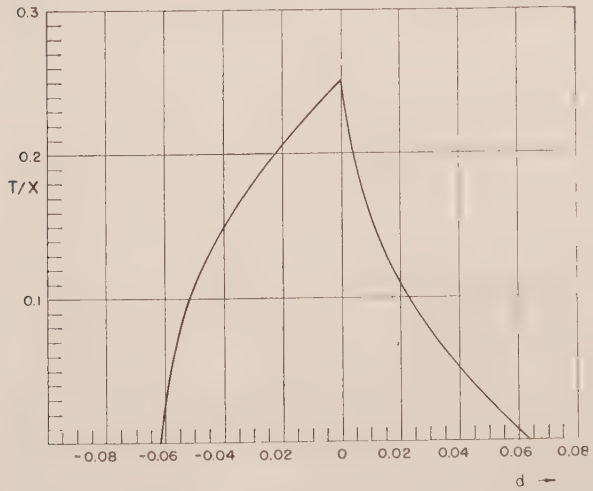

Fig. 4

radial distance from the center. This distance is found by first obtaining α_{max}, the take-off angle for which the trace just touches the inner sphere after the central angle ϕ. By setting $\delta = 0$ and $r = r_m$ in the general trace equation (10) the value of α_{max} is easily found to be $\frac{1}{2}\chi$. Then from eq. (16) the radius of the outer sphere is found to be $e_e = a_e/\chi = \alpha_{max}/\chi^2 = \frac{1}{2}\chi$.

Finally eq. (16) may be written for a trace intersection with the outer sphere ($e = e_e$)

$$d = e_e - \frac{a}{\chi} = -\frac{1}{\chi}(a - \tfrac{1}{2})\,. \qquad (17)$$

This relation is plotted as the dotted line in fig. 3 for $\chi = 0.2$ and for $\alpha_e = \varepsilon_e = 0.1$.

Considerations important in the choice of r_i and r_o are that the curve of transmission (T) versus energy (δ) should: (1) be as large as possible at $\delta = 0$; (2) decrease rapidly as δ increases in either the positive or negative directions; and (3) be as symmetric as possible with respect to δ.

The transmission versus energy characteristic of this device is easy to visualize from fig. 3. At a given value of d, the length of the total intercept parallel to the a axis lying in the region bounded by the lines e_i, e_o, and by vertical lines passing through the points $a = 0$ and $a = 0.5$, is proportional to the transmission at that value of d. The dotted line representing the intercept of a trace with the outer sphere is so steep (for $\chi \ll 1$) that we take it to be vertical.

One sees that all three of the desiderata mentioned above are satisfied reasonably well if one takes $e_i = 0$ and $e_o = \frac{1}{8}$. If one takes $e_i = 0$ and $e_o = \frac{3}{40}$, for example, the maximum transmission decreases and is shifted to negative values of δ. If one takes $e_i = \frac{3}{40}$ and $e_o = \frac{1}{8}$, the maximum transmission decreases also but does not shift in energy: however, the transmission curve develops a tail in the region of positive δ and hence becomes skewed in this region. We shall assume, then, both in Part I and Part II of this paper that the gap extends from $e = 0$ to $e = \frac{1}{8}$. The equation for $T(\delta)$ is easy to write down for this case and is given by

$$T(d) = \tfrac{1}{4}\chi\sqrt{1 + 16d} \quad 0 > d \geqslant -\tfrac{1}{16} \qquad (18)$$

$$= \tfrac{1}{4}\chi\,(1 - 4\sqrt{d}) \quad \tfrac{1}{16} \geqslant d > 0 \qquad (19)$$

$$= 0 \qquad \tfrac{1}{16} \leqslant |\,d\,|\,. \qquad (20)$$

A plot of T/χ versus d is shown in fig. 4. It is easy to show that the width of this curve at half height is $d_{\frac{1}{2}} = \frac{1}{16}$ while the total width is $\frac{1}{8}$.

Then one may write the following relation for T_0, the transmission of the spherical condenser at $\delta = 0$, and $\delta_{\frac{1}{2}}$, the width of the line profile at half height (the energy resolution):

$$T_0 = \sqrt{\delta_{\frac{1}{2}}} . \tag{21}$$

4. Transmission, Resolution and Line Profile for Large Angles $\chi \approx 1$

A graphical analysis was carried out for angles $\chi \approx 1$. In order to construct the trajectories graphically, use is made of the fact that the total energy (kinetic plus potential) of a particle in an inverse square field is proportional to the length of the major axis of the ellipse. For a major axis of fixed length (monoenergetic particles), with one focus at the center of the spheres, the other focus must lie on a circle which has the source as its center and which passes through the center of the spheres. For a take-off angle α, the included angle between the source-center line and the source-focus line will be 2α as shown in fig. 1. The ellipses are drawn as follows: fix the ends of a fine wire at the foci; place a pencil in the loop at the source position (vertex of the angle 2α); move the pencil, constrained by the wire, to trace out the ellipse. A set of ellipses for various angles α is thus obtained corresponding to the trajectories of monoenergetic particles. The transmission of the apparatus is then

$$T_0 = \tfrac{1}{2} \sin \alpha_{\max} \tag{22}$$

where $\alpha_{\max}$ is again the angle for which the trace just touches the inner sphere after the central angle ϕ. As before, the annular slit edges are chosen to lie at the inner sphere and at the maximum radius attained by a trace at ϕ.

The value for $\alpha_{\max}$ is easily found from the general trace equation (10) by setting $\delta = 0$ and $r/r_m = 1$. One finds

$$\alpha_{\max} = \tfrac{1}{2}(\pi - \phi) \tag{23}$$

and so the maximum transmission under these conditions is

$$T_0 = \tfrac{1}{2} \cos \tfrac{1}{2}\phi . \tag{24}$$

The width of the slit is found from the value of α at which the trace has its maximum radius at ϕ for $\delta = 0$

$$\tan \alpha_{\max \text{ displ}} = \tfrac{1}{2} \cot \tfrac{1}{2}\phi . \tag{25}$$

A substitution of this value of α into eq. (10) for $\delta = 0$ yields r_0, the radius of the outer slit edge.

Trajectories of particles were drawn for $\delta \neq 0$ in a way similar to that described above except that the foci are located at the center of the spheres and on a circle about the source but not passing through the center (not shown). Fig. 5 shows a typical diagram for $\phi = 120°$ with α plotted on the abscissa and δ plotted on the ordinate. Curves of trace intercepts for various slit radii at the angle ϕ are given (the parabolic curves). The nearly straight lines represent trace intercepts with the outer sphere for $r_e = 40.7$, 43.0 and 45.3 cm.

Fig. 6 shows T versus δ curves for $r_0 = 34.3$ cm, and for $r_i = 30.2$ cm, (curve A) 32.2 cm

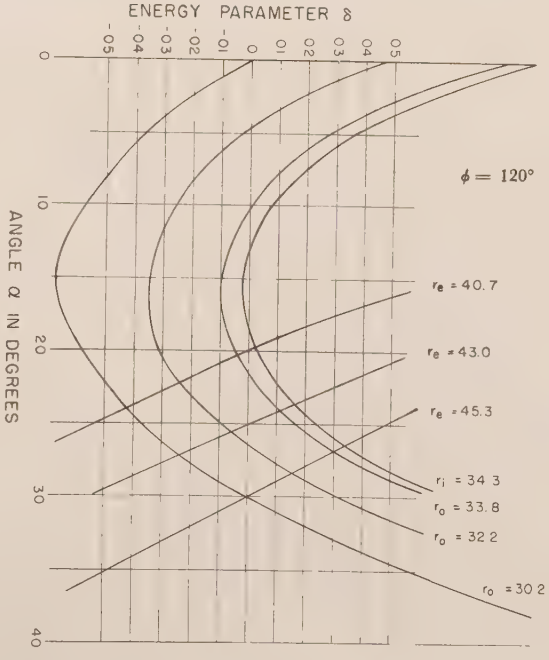

Fig. 5

(curve B) and 33.8 cm (curve C). One sees that even when the gap has its full width (curve A) there is a perceptible but not large effect due to outer sphere interception by particle paths. As

the gap is made smaller (curves B and C) the main peak of the curve becomes narrower but an undesirable tail develops for $\delta > 0$. One concludes that if high resolution is desired, a value of ϕ

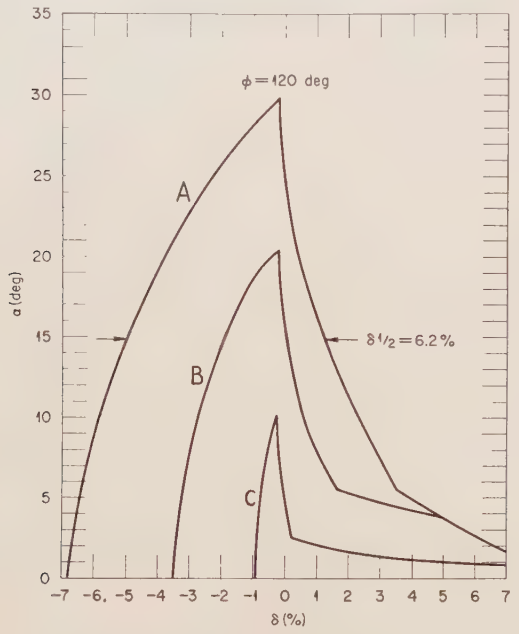

Fig. 6

near 180° should be chosen rather than a narrowing of the slits at a smaller value of ϕ.

Fig. 7 shows a plot of T_0 and $\delta_{\frac{1}{2}}$ versus ϕ for ϕ in the range 120° — 180°. The relation $T_0 = \sqrt{\delta_{\frac{1}{2}}}$ is valid to a good approximation over this whole range of ϕ.

The performance of this spectrometer may be contrasted favorably with the Purcell[2]) type which had a transmission of about one per cent at an energy resolution of 0.2%, and the more recent versions of the Purcell instrument by Browne *et al.*[7]) where $T = 0.025\%$ and $\delta_{\frac{1}{2}} = 0.2\%$ and Kobayshi[8]) where $T = 3.4\%$, and $\delta_{\frac{1}{2}} = 1.3\%$. Allison and Weyl[3]) have built a spectrometer with $\phi \approx 180°$, which has a T of 0.4% and $\delta = 1.2\%$. Frankel and Nelson[9]) have given T versus $\delta_{\frac{1}{2}}$ relations for a number of spectrographs which generally are of the form

$$T = A\sqrt{\delta_{\frac{1}{2}}} \tag{26}$$

where A is a constant ≥ 1. For point sources, then, the performances of these devices are thus comparable with the spherical condenser spectrometer. However, the latter instrument should enable one to operate at the very large transmission of 25% at $\delta_{\frac{1}{2}} = 6\%$ which is a momentum resolution of 3%, and should be very useful where high transmission is important.

As mentioned above, one assumes that after passing through the slit into the field-free region, the traces are straight lines which come back to the counter on the axis at a distance τ

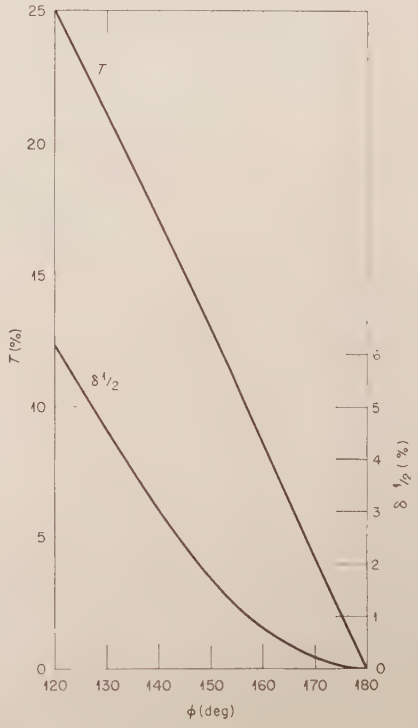

Fig. 7

(in units of the inner sphere radius) from the center of the spheres, where

$$\tau = \frac{\cos^2 \alpha}{1 - \cos \phi - \cos^2 \alpha} \tag{27}$$

[7]) C. P. Browne, D. S. Craig and R. M. Williamson, Rev. Sci. Inst. 22 (1951) 952.

[8]) Y. Kobayshi, J. Phys. Soc. Japan 8 (1953) 440.

[9]) S. F. Frankel and E. C. Nelson, Preliminary Report on Beta Spectrometer Design Investigation (Unpublished, June, 1948). Referred to in USAEC-NYO-912, "Design of Double Focussing Beta-Ray Spectroscope and Application to Internal Conversion in Cu-64", by G. W. Hinman.

when $\delta = 0$. A post accelerating voltage may be placed across the gap between the conical surfaces where the trajectories emerge from the deflecting field.

The spectrometer may be useful as a low energy X-ray spectrometer using a photoelectric radiator at the source position. X-rays moving to the left in fig. 1, from the center to the radiator eject photoelectrons having an angular distribution peaked in the lateral direction (i.e., into the angular aperture of the spectrometer). Thus the spectrometer is ideally suited to detecting these electrons.

NUCLEAR INSTRUMENTS AND METHODS 6 (1960) 164–168; NORTH-HOLLAND PUBLISHING CO.

THE INPUT STAGE OF A TRANSISTOR PULSE AMPLIFIER

A. W. PRYOR

Australian Atomic Energy Commission, Lucas Heights, Sutherland, N.S.W., Australia

Received 26 September 1959

The input signal of a linear amplifier for nuclear detectors is in the form of a charge released in very short time. Under these circumstances a transistor input stage behaves very differently from a valve input stage both in the shaping of the pulse and in the noise conditions. An experimental and semi-theoretical account of the performance of typical R.F. transistors is presented.

1. Introduction

It has been shown[1]) that for transistor amplifying stages the common-emitter configuration gives the best gain-bandwidth product. However, when the common-emitter stage is used as the input stage of an amplifier which is fed by the current pulses coming from a detector of nuclear particles, such as a scintillation counter, proportional counter or fission counter, the behaviour of the stage, both in the shaping of the pulse and in the noise conditions, is quite different from that encountered in valve amplifiers.

2. The Shaping of the Input Pulse

Suppose the detector releases a charge dQ on the passage of a nuclear particle. It will be assumed initially that this charge is released as a current impulse in an infinitely short time.

Now, if

C_d = the capacitance of the detector and its associated cable

C_i = the input capacitance of the amplifier; then

$dQ/(C_i+C_d)$ = the magnitude of the voltage step at the input of the amplifier.

Now for a valve amplifier the input resistance is very large so that, for all practical purposes, a true voltage step is produced at the input, and, in most cases, this voltage step is amplified in a few stages and then differentiated with a selected differentiation time to produce pulses with exponential decays. The factors influencing the choice of differentiation times are given in Elmore and Sands[2]).

Now in the case of the common-emitter transistor input stage two differences occur.

(1) The input capacitance is very much greater than for a valve. The input capacitance equals the emitter diffusion capacitance, C_e. Moreover, C_e is proportional to the emitter current I_e.

(2) The input resistance is comparatively low being set by the emitter diffusion resitance R_e which is inversely proportional to the emitter current I_e.

The input circuit of the transistor is given in fig. 1 in which r'_{bb} = the base spreading resistance which is a physical resistance and is usually small enough to be neglected. Well known[1,3]) formulae exist for R_e and C_e.

Fig. 1. Input circuit of transistor.

[1]) Hunter, Handbook of Semiconductor Electronics (McGraw Hill, 1956).

[2]) Elmore and Sands, Electronics (McGraw Hill, 1949).

[3]) Evans, Fundamental Properties of Transistors (Heywood and Co., 1957).

These are:

$R_e = kT/qI_e$

$C_e = (q/2kT)\ (W^2/D)\ I_e$

k = Boltzman's constant

T = Temp. in degrees K

q = electronic charge

W = thickness of base

D = diffusion constant for minority carriers in the base.

The product R_eC_e is determined by the cut-off frequency in the common-emitter configuration.

If

h_{fe} = the current gain in common emitter

f_α = the cut-off frequency in common base

then

$f_\alpha/h_{fe} = 1/2R_eC_e$.

In the operation of the common-emitter stage the input charge dQ is deposited on C_d and C_e in parallel. A fraction of dQ, given by

$$dQ_B = \frac{C_e}{C_e + C_d} dQ \qquad (1)$$

is deposited on the base. When this charge is available in the base then current can flow in the collector. But the charge dQ_B diffuses out of the base with a time constant, T_D given by

$$T_D = R_e\,(C_e + C_d)\,. \qquad (2)$$

Therefore, the collector current rises, almost instantaneously, to a value I_{cp} which is proportional to dQ_B and then decays with time constant T_D.

This behaviour may be observed by connecting the transistor as shown in fig. 2. The pulse generator feeds a current impulse into the base

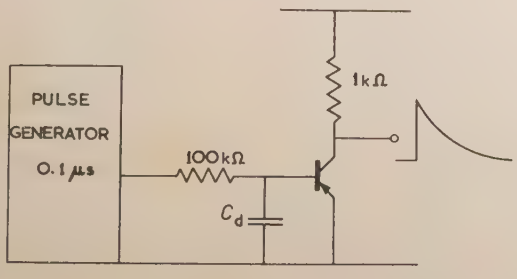

Fig. 2. Current impulse applied to transistor.

of the transistor. For a typical Philips type 0C44 transistor

$$I_{cp} = K\,dQ_B$$

where $K = 33 \times 10^9$ mA/coulomb.

It should be noted that K is independent of I_e although, seeing C_e is increased as I_e increases, dQ_B is increased as C_e becomes greater than C_d. Sparkers and Beaufay[4]), when discussing the operation of the transistor as a charge-controlled device, give a formula

$$\frac{dQ_B}{I_e} = \frac{1.215}{2\pi f_\alpha} \qquad (3)$$

which agrees well with the results obtained experimentally.

The rise time of the current pulse at the collector is very short even for an audio transistor, being limited only by the effects of collector capacitance and of base resistance r'_{bb}. The decay time constant, T_D, depends on the cut-off frequency of the transistor. For a Philips type 0C44, for which $f_\alpha = 12$ Mc/s. T_D varies from about 3 to 10 μs depending on the value of C_d and I_e. With a Philco type SB102 transitor, for which $f_\alpha = 50$ Mc/s, values of T_D below 1 μs were normally encountered.

It is seen that differentiation of the input voltage step occurs at the input. If it is desired to introduce a controlled differentiation later in the amplifier then, to avoid underswing of the pulse, the differentiation time T_D must be lengthened to at least 20 times greater than the differentiation time to be introduced later; in a practical case T_D may have to be increased to 50 μs or more. This may be done by adding an external capacitor from base to earth but this is undesirable as it decreases the gain and the signal-to-noise ratio. Goulding[5]) describes an amplifier in which this is done. T_D may be varied, with little effect on gain or signal-to-noise ratio, by introducing an external resistance from base to earth. For an 0C44 transistor it is feasible (with $C_d = 100$ pF) to vary T_D between about 1 and 4 μs, and for a SB102 transistor, between about 0.2 and 0.7 μs.

So far, only current impulses have been considered. If the input consists of a current

[4]) Sparkes and Beaufay, Proc. I.R.E. 45, No. 12 (1957) 1740.

[5]) Goulding, I.R.E. Trans on Nucl. Sc. (Aug. 1958) p. 38.

pulse for which the width $W \ll T_D$ then the only effect is that the rise time of the collector pulse is equal to W. If, however, $W \gg T_D$ then the collector current pulse is simply an amplified version of the input current pulse into the base. This might be the case, if, for example, a proportional counter with an ion collection time of several microseconds were used in conjunction with an SB102 input transistor.

3. Noise

It is generally thought that the transistor input stage is not as good as the valve input stage in signal-to-noise ratio. This is, regrettably, quite true under most conditions, but the difference is usually not very great and under some circumstances (when C_d equals several hundred pF) the transistor may even be better than the valve.

Elmore and Sands[2]) give the best way of describing and the best way of measuring the noise performance of a pulse amplifier for nuclear detectors. The best way of describing the noise is in terms of the equivalent input noise charge, Q_n, because a nuclear detector releases as the input signal a certain charge. The best way of measuring Q_n is by plotting out the pulse height distribution resulting from the amplification of an input pulse which is of similar magnitude to the input noise voltage. The equipment for doing this is shown in fig. 3. The transistor is "emitter-biased" from a positive supply. This is perhaps the best method of biasing common-emitter amplifiers and has the advantage in this case of allowing independent control of emitter current, collector voltage and external base resistance. If V_n is the standard deviation of the Gaussian distribution of input signal and noise, then the r.m.s. equivalent noise charge is given by

$$q_n = V_n C_d$$

and the most probable value by

$$Q_n = 0.67\, q_n\,.$$

[6]) Terman, Radio Engineers Handbook (McGraw Hill, 1943).

[7]) Jones, I.R.E. Nat. Conv. Rec. (1957) Part 9, p. 78.

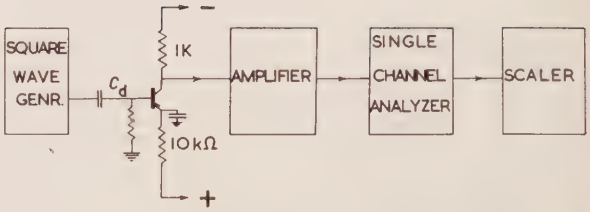

Fig. 3. Method of measurement of equivalent noise charge Q_n.

If I_{nc} is the equivalent shot noise current in the collector junction then, in accordance with the usual theory,

$$I_{nc}^2 \propto I_e$$

Jones[7]) has shown that, for the surface barrier transistors he tested, this expression holds for values of I_e between 30 microamps and 5 mA.

Now the equivalent noise charge on the base capacitance C_e will be proportional to I_e as shown in eq. (3); and Q_n, the total equivalent noise charge on $C_e + C_d$, will be related to the equivalent noise charge on C_e alone by eq. (1). Hence we have:

$$Q_n^2 = \text{const.} \times I_e \left(\frac{C_e + C_d}{C_e}\right)^2 .$$

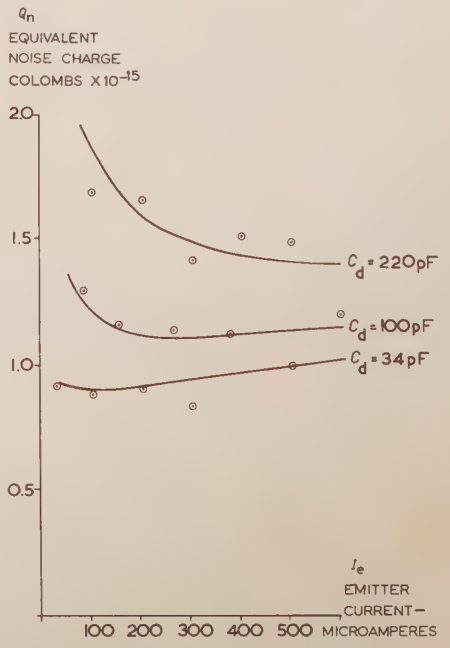

Fig. 4. Experimental results of noise measurements on SB102 transistor together with theoretical curves drawn according to eq. (4). Ordinate Q_n, Equivalent noise charge (coulombs $\times$ 10^{-15}). Abscissae I_e, Emitter Current (mA).

Table 1

	Philco Type SB102	Philips Type 0C44 (1)	Philips Type 0C44 (2)
Current gain	38	44	197
Emitter diffusion cap. C_d (pF with I_e in mA)	$340\ I_e$	$404\ I_e$	$800\ I_e$
Constant K_1 arising from noise at base	0.57×10^{-30}	1.40×10^{-30}	1.34×10^{-30}
Constant K_2 arising from shot noise at the collector, I_e in mA, C_d and C_e in pF	4.7×10^{-36}	4.5×10^{-36}	2.4×10^{-36}

If a constant term is added to describe the contribution from shot noise in the base current and from thermal noise in R_e, then we have, as a plausible expression for Q_n,

$$Q_n^2 = K_1 + K_2 \left(\frac{C_e + C_d}{I_e}\right)^2 \qquad (4)$$

seeing that C_e is proportional to I_e.

This is very similar to the equation given by Elmore and Sands[2]) for the Q_n of a valve amplifier. They give the equation:

$$Q_n^2 = A_1 + A_2 (C_i + C_d)^2 R_s$$

where A_1 is the term describing input resistance noise and grid current shot noise, and the second term describes the plate current shot noise. C_i is the input capacitance and R_s the equivalent shot noise resistance which is equal to $3/g_m$ for a triode[6]). If, in the case of the transistor, C_e is substituted for C_i, and it is remembered that g_m is proportional to I_e, then eq. (4) results.

It is possible to select values for the two constants, K_1 and K_2 in eq. (4) which will give a convincing fit to the experimental values of Q_n.

Observed values for three transistors are given in table 1.

In fig. 4 the observed values of Q_n for the SB102 transistor are shown in conjunction with the theoretical curves eq. (4) using the two constants given in the table.

Measurements on a good quality commercial valve amplifier gave the result,

$$Q_n^2 = 70 \times 10^{-36} (C_d + C_i)^2$$

where $C_i = 20$ pF.

The following practical conclusions may be drawn:

(i) When C_d is small (say, 10 to 30 pF) a valve amplifier is substantially better than a transistor amplifier. When C_d is intermediate (say, 100 to 200 pF) the two are much the same. When C_d is large (say, above 300 pF) then the transistor amplifier has the advantage. This is illustrated in table 2.

Table 2

C_d (pF)	Q_n for valve amplifier	Min. value of Q_n for transistor amplifier (SB102)
10	0.25×10^{-15}	0.79×10^{-15}
33	0.44	0.88
100	1.00	1.10
330	2.92	1.62

(ii) A simple differentiation of eq. (4) (remembering that C_e is proportional to I_e) shows that Q_n has a minimum when $C_e = C_d$. Little is lost by operating above this value but, particularly when C_d is large, operating at too low a value of I_e may cause an appreciable loss in signal-to-noise ratio. For the transistors tested a value of I_e of 200 to 300 μA seems suitable under most circumstances.

(iii) The SB102 transistor (besides having a greater sensitivity and shorter differentiation time—see eqs. (2) and (3)) had a lower noise value by about 3 dB than either of the 0C44 transistors. The two 0C44 transistors had much the same value of Q_n although the values of h_{fe} differed greatly (the lower value of the constant K_2, for the second transistor, being offset by the higher value of C_e).

Further experiments enabled the following additional conclusions to be drawn:

(i) The noise charge Q_n decreases slightly with increasing collector voltage, as shown in fig. 5.

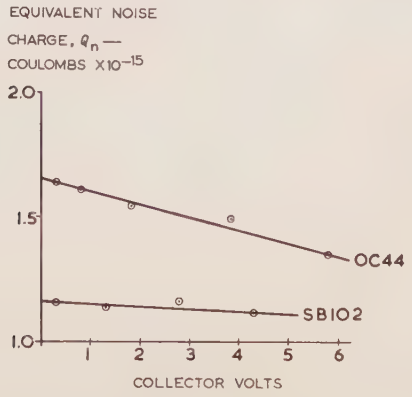

Fig. 5. Noise as a function of collector voltage for two transistors, $I_e = 100\ \mu A$; $C_d = 100$ pF. Ordinate Q_n, Equivalent noise charge (coulombs $\times 10^{-15}$). Abscissae: Collector (volts).

(ii) When connected in the common collector configuration or when two common-emitter stages were arranged with feedback so as to have a high input impedance, the values of Q_n were similar to those obtained with the simple common emitter stage.

4. Operation of Final Amplifier

An amplifier for use with a fission counter for reactor flux measurements was designed and built in accordance with the preceding data. The input stage consisted of an SB102 transistor biased as shown in fig. 3 with $I_e = 500\ \mu A$, $V_e = -3$ V. This was followed by three "feedback-pairs" of the circuit shown in fig. 6. The performance of this amplifier was:

Gain $= 3 \times 10^{12}$ volts per coulomb

Integration time $= 0.08\ \mu s$

Differentiation time $= 0.3\ \mu s$

Noise charge, Q_n, $= 1.4 \times 10^{-15}$ coulombs with $C_d = 220$ pF $= 4\,400$ ion pairs.

This amplifier fed into a transistor discriminator and scaler and performed satisfactorily at count rates up to several hundred thousand per second.

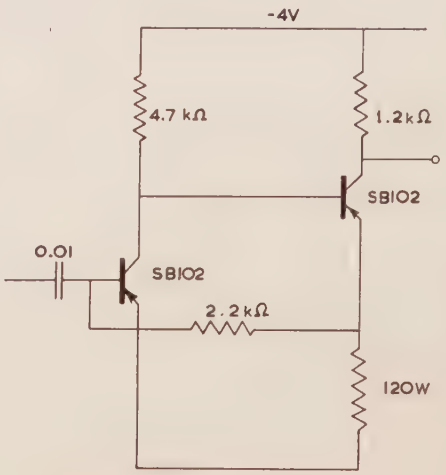

Fig. 6. Transistor amplifying stage.

5. Conclusion

The transistor input stage differs from the valve input stage in several important ways: chief among these are:

(i) Differentiation occurs at the input. The gain and decay time constant are given in eqs. (1), (2) and (3) above.

(ii) The noise of the transistor input stage is significantly greater than that of a valve input stage when the detector capacitance is small, but may be equal or even less when the detector capacitance is large. There is an optimum value of emitter current.

(iii) When the detector capacitance is quite large (e.g. when using a fission counter on several metres of cable to explore a reactor) then the transistor input stage is particularly valuable.

Acknowledgments

The work described in this paper was carried out at the Australian Atomic Energy Commission Research Establishment, Lucas Heights, Sydney and published with permission of the Chief Scientist.

NUCLEAR INSTRUMENTS AND METHODS 6 (1960) 169–175; NORTH-HOLLAND PUBLISHING CO.

EIN MODULATOR FÜR DAS SYNCHROZYKLOTRON BONN MIT FERROELEKTRISCHER KERAMIK

HANNO BRÜCKMANN

Institut für Strahlen- und Kernphysik der Universität Bonn

Eingegangen am 9. August 1959

The frequency modulation system for the university of Bonn 190 cm synchrocyclotron is described. The unusual feature of this system is the use of Ba-Sr-TiO_3 sinterceramic capacitors for the variable capacity. 4.3% frequency modulation is obtained at 11 Mc/s with 24 capacitors (0.6 mm thick and 11 mm dia, mounted in xylene) each controlled by a low frequency modulating voltage up to 1400 volts. Design problems, concerning heat transfer and breakdown are discussed.

The main advantage of this system is that many modulating wave-shapes and repetition rates are possible.

1. Einleitung

Bisher wurden für die Frequenzmodulation bei einem Synchrozyklotron nur rotierende Kondensatoren oder andere Spezialkonstruktionen verwendet, die jedoch alle darauf beruhen, dass eine Kapazität durch geeignete mechanische Bewegung geändert wird.

Grundsätzlich gibt es noch weitere Wege, ohne mechanisch bewegte Teile die Eigenfrequenz eines Schwingkreises zu verändern: erstens ist dies möglich mittels geeigneter Reaktanzröhren-Schaltungen, zweitens durch Vormagnetisierung eines Ferritkernes und drittens durch Vorpolarisation eines Dielektrikums.

Diese dritte Möglichkeit wurde untersucht und es gelang, ferroelektrische Ba-Sr-TiO_3-Mischkristalle für die Frequenzmodulation in einem Hochfrequenzsystem mit grosser Blindleistung zu verwenden.

Das Bonner Synchrozyklotron (190 cm Poldurchmesser, 31 MeV-Deuteronen oder 62 MeV-He-Ionen) benötigt einen Frequenzhub von 4.3%, die mittlere Umlauffrequenz der Teilchen beträgt ca. 11 MHz.

2. Das Hochfrequenzsystem

Abb. 1 zeigt schematisch den frequenzbestimmenden Schwingkreis. Innerhalb der Vakuumkammer bilden das "Dee" und das "Gegen-Dee" die beiden Beschleunigungselektroden. Das Dee ist mit dem Innenleiter der konzentrischen Lecherleitung verbunden. Als Vakuumabschluss dient ein ringförmiger Steatit-Isolator S, sodass sich der Teil B der Lecherleitung vollkommen in Luft befindet. Das System wird durch einen Sender in Gitterbasis-Schaltung erregt.

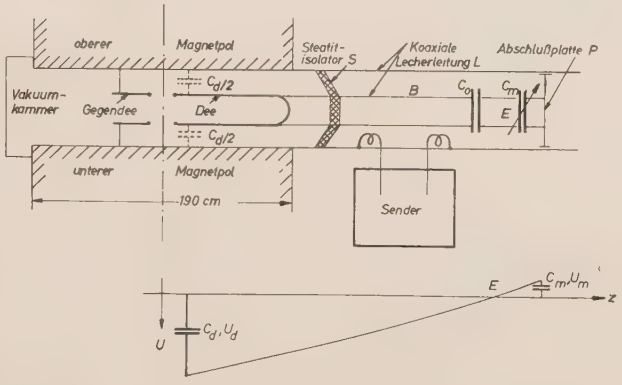

Abb. 1. Hochfrequenzsystem des Bonner Synchrozyklotrons (Schematisch).

Der Trennkondensator C_0 bietet die Möglichkeit, der Hochfrequenz-Beschleunigungsspannung noch eine Gleichspannung zu überlagern. Das Ende der Leitung L ist über die veränderbare Modulatorkapazität C_M und die Abschlussplatte P kurzgeschlossen. Die Eigenfrequenz des Syste-

mes lässt sich durch Verschieben der Platte P an die Magnetfelstärke anpassen.

Eine Abschätzung für die Blindleistung an der Dee-Kapazität ergibt mit 11 MHz Grundfrequenz, 550 pF Dee-Kapazität und 10 kV_{Sp} Dee-Spannung einen Wert von 2×10^6 VA.

Die Frequenzmodulation muss durch Änderung der Eigenfrequenz erreicht werden. Ohne

3. Das ferroelektrische Material

Infolge der zu erwartenden Hf-Wirkleistung benötigt man mindestens ein Materialvolumen von 1 cm^3. Aus diesem Grund kommt vorläufig nur Sinterkeramik in frage. Eigene Versuche, brauchbares Material herzustellen, haben bisher noch nicht zu reproduzierbaren Ergebnissen geführt. Daher wird zur Zeit in dem Modulator

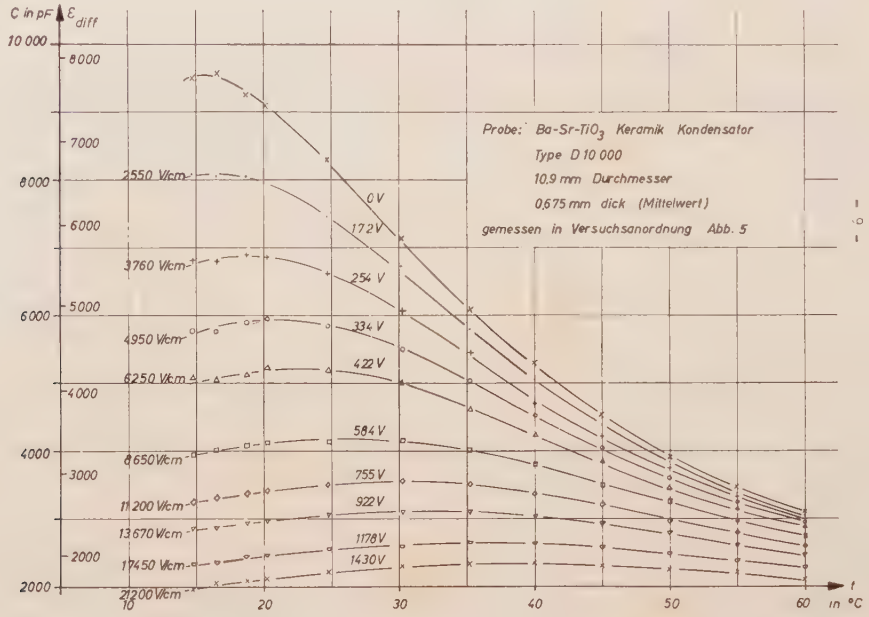

Abb. 2. Dieelektrische Konstante als Funktion von Temperatur und Steuerfeldstärke.

Berücksichtigung von Verlusten gilt für einen aus Kapazitäten und Induktivitäten aufgebauten Schwingkreis

$$\frac{d\omega}{\omega} = \frac{1}{2}\frac{dN_e}{N_e}$$

(ω Eigenfrequenz, $N_e = \Sigma i\, \omega \cdot C_i \cdot ({}_cU_i)^2$ Blindleistung in den Kapazitäten).

Mit oben angeführten Werten und der Annahme, dass die Modulator-Kapazität um einen Faktor 3 verändert werden kann, ist dann in dem Modulationssystem eine mittlere Blindleistung von 3×10^5 VA zu erwarten.

Von Bedeutung ist ausserdem noch die Grössenordnung des Hochfrequenzstromes, der über den Innenleiter und somit auch über die Modulatorkapazität fliessen muss. Mit den oben angegebenen Werten erhält man 400 A_{Sp}.

die Ba-Sr-TiO_3-Sinterkeramik D 10 000 der Fa. Stettner, Lauf, verwendet.

Die Messergebnisse für Temperatur- und Feldabhängigkeit der Dielektrizitätskonstanten zeigt Abb. 2. ε_{diff} hat die Bedeutung von $d\vartheta/d\boldsymbol{E}$. Die Messfrequenz betrug 10 bis 30 kHz. Als Steuerspannung wurde Gleichspannung verwendet. Die Messprobe war vorher schon längere Zeit in einem Modulatormodell unter Hochfrequenzbeslastung verwendet worden und hatte angelötete Kontaktfahnen entsprechend Abb. 3. Die beobachteten Hystereseerscheinungen für Temperatur und Steuerfeldstärke sind in Abb. 2 nicht berücksichtigt. Die Curietemperatur für dieses Material liegt bei 16° C.

Für Versuchszwecke liessen sich noch Steuerfeldstärken bis 35 000 V/cm anwenden. Im

Dauerbetrieb sind jedoch nur ca. 23 000 V/cm zulässig, ohne dass infolge von Durchschlägen die Betriebssicherheit beeinträchtigt wird.

Messungen des Verlustfaktors mit einem

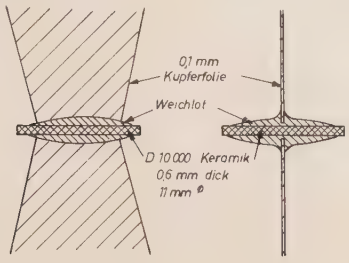

Abb. 3. Plättchen mit Stromzuführungfahnen.

Substitutionsverfahren zeigten im Gebiet von 100 kHz bis 10 MHz folgendes Verhalten: Zwischen 1 und 10 MHz treten Resonanzstellen auf. An diesen Stellen wächst der Verlustfaktor durch Anlegen einer Steuerfeldstärke (5000 V/cm) um einen Faktor 10–20. Der Absolutwert lässt sich durch die Halterung und den umgebenden Stoff beeinflussen. Bei 10 MHz wurden an einer Probe mit angelöteten Stromzuführungsfahnen in Öl folgende Werte gemessen: $\operatorname{tg}\delta = 0.9\%$ bei 17° C, $\operatorname{tg}\delta = 0.25\%$ bei 30° C und $\operatorname{tg}\delta = 0.1\%$ bei 45° C (alle Werte für Steuerspannung 0 Volt).

Im Gebiet der Resonanzstellen lässt sich das Material wohl kaum für Modulationszwecke bei grosser Blindleistung verwenden. Unterhalb der Curietemperatur treten die Hysteresseerscheinungen stark hervor. Aus diesem Grunde sollte das Material unter Berücksichtigung der Temperaturabhängigkeit des Verlustfaktors zwischen 20 und 30° C verwendet werden.

4. Der Aufbau des Modulators

An einem Modell des Zyklotron-Hochfrequenzsystems wurden die günstigsten Betriebsbedingungen und die Grenzbelastungen eines Plättchens (11 mm Durchmesser, 0.6 mm Dicke) experimentell ermittelt.

Folgende Gesichtspunkte sind für die Entwicklung eines Modulators mit ferroelektrischer Keramik von besonderer Bedeutung:

(a) Ableitung der entstehenden Verlustwärme

(b) Zuführung der Hochfrequenzströme

(c) Zuführung und Isolation für die Steuerspannung

(d) mechanische Beanspruchung der Keramik durch die Halterung

(e) eine gute Betriebssicherheit sollte trotz Aufbau aus vielen Einzelplättchen erhalten bleiben.

Für die Ableitung der Verlustwärme wurden die Möglichkeiten: Wärmekontakt mit einem festen Stoff, Sieden einer umgebenden, stehenden Flüssigkeit und Wärmeableitung durch eine umgebende, strömende Flüssigkeit geprüft.

Nur die Wärmeableitung durch eine strömende Flüssigkeit führte zu zufriedenstellenden Ergebnissen. Es wird mit Natrium getrocknetes und anschliessend destilliertes Xylol als Kühlflüssigkeit verwendet.

Eine Störung verursachten mikroskopische Verunreinigungen in dem Xylol. An den Rändern der Plättchen-Versilberung bzw. -Verzinnung entstehen besonders hohe Feldstärken. Diese Stellen wirken wie Elektrofilter. Alle Verunreinigungen werden an diesen Randzonen aufgesammelt. Nach einiger Zeit ist dann an einer solchen Stelle die Strömung bzw. Kühlung an der Plättchenoberfläche nicht mehr ausreichend. Es zündet eine Entladung, die dann nach kurzer Zeit zum Durchschlag führt.

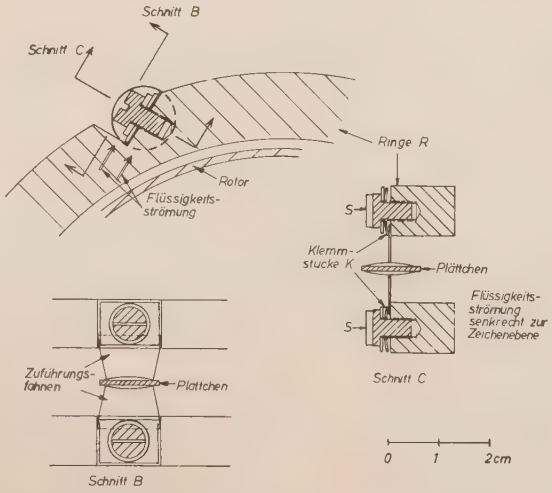

Abb. 4. Aufhängung eines einzelnen Plättchens.

Dieser Störeffekt lässt sich mit der besonders grossen Dielektrizitätskonstanten und dem ne-

gativen Temperaturkoeffizienten erklären. Ist in der an die Versilberung angrenzenden Randzone keine oder zu geringe Wärmeableitung möglich, führt dies zu einem instabilen Zustand. Die Feldstärke steigt dann bis zur Durchtung eine Temperaturerhöhung gegenüber der Umgebung und die Steuerfeldstärke führt zum Durchschlag an der betreffenden Randstelle. Dieser Effekt ist in dieser Form nur bei Ferroelektrika und hoher Belastung zu erwarten und

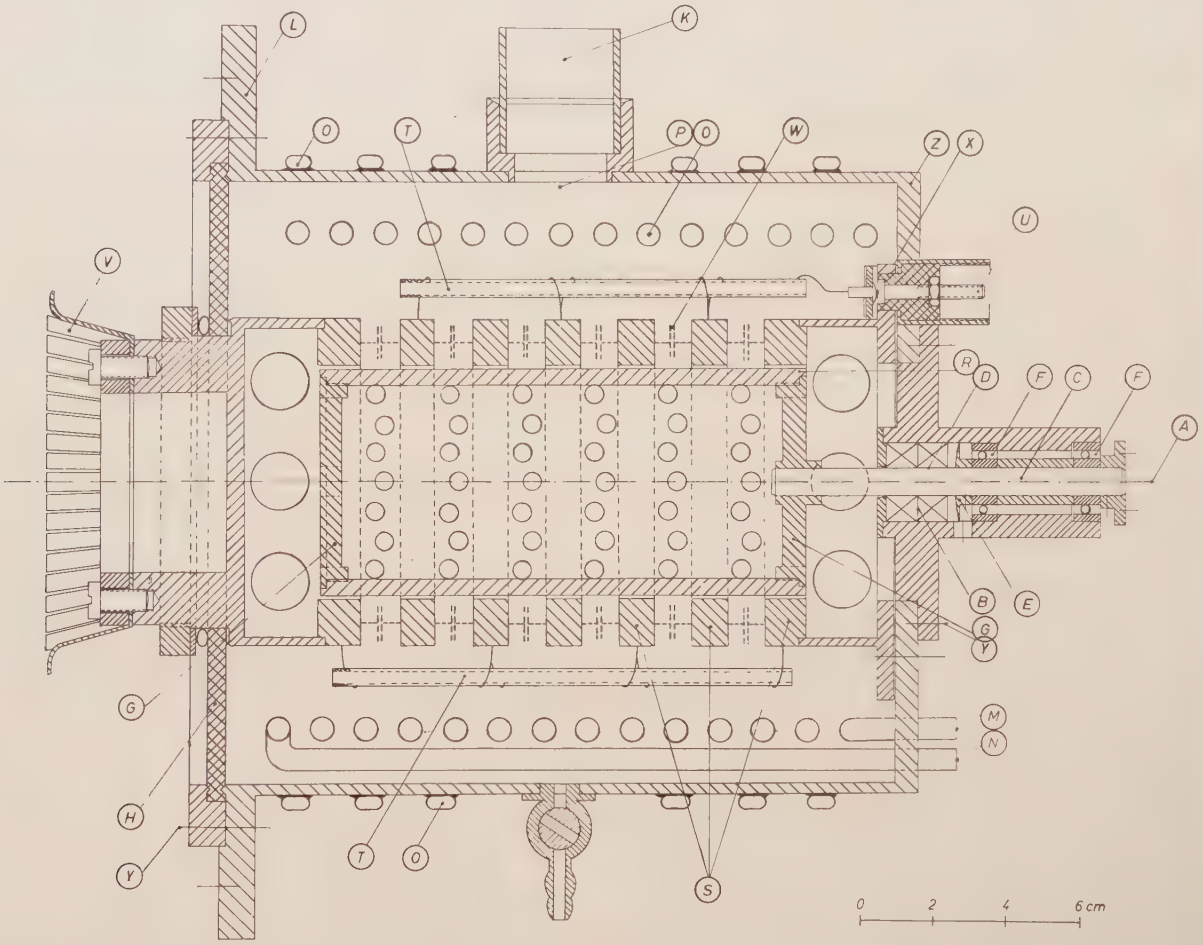

Abb. 5. Schnitt durch den Betriebsmodulator. C, geschliffene und polierte Stahlwelle; E, Schleuderring; F, Kugellager; K, Ausdehnungsvolumen; L, Flansch für Anschluss an Platte P aus Abb. 1; M, N, Kühlwasserzu- und -ablauf; P, Thermometer; U, Koaxial-Stecker für Steuerspannungsanschluss; V, Anschlussfedern für Übergang zu dem Innenleiter der Lecherleitung; W, Ferroelektrische Kapazitäten (Schaltung siehe Abb. 6); X, Federnder Kontakt für Steuerspannungszuleitung, Y, Schrauben für die Befestigung des Innenteils in dem Gehäuse; Z, Gehäuse.

bruchsfeldstärke. Es bilden sich in dieser Randzone Oberflächenentladungen und innere Durchschläge.

Diese Zonen sind besonders empfindlich, wenn gleichzeitig eine hohe Hochfrequenzbelastung (grosse Hf-Verlustleistung pro Volumenelement) und eine hohe Steuerspannung an dem Plättchen anliegen. In diesem Falle verursacht die Hochfrequenzverlustleister verursachte erhebliche Schwierigkeiten bei der Entwicklung des Modulators.

Deshalb muss besonders darauf geachtet werden, dass innerhalb der Flüssigkeit durch Abrieb an Lagern oder einer Pumpe keine Fremdkörper entstehen, und dass die Strömungsgeschwindigkeit an der Plättchenoberfläche genügend gross ist.

Die Stromzuführungsfahnen für die Zuleitung

der Hf-Ströme wurden, wie in Abb. 3 skizziert, (siehe auch Abb. 11) rechtwinklig stumpf auf die verzinnten Plättchen aufgelötet. Andere Ausführungen haben stets Unsymmetrien an

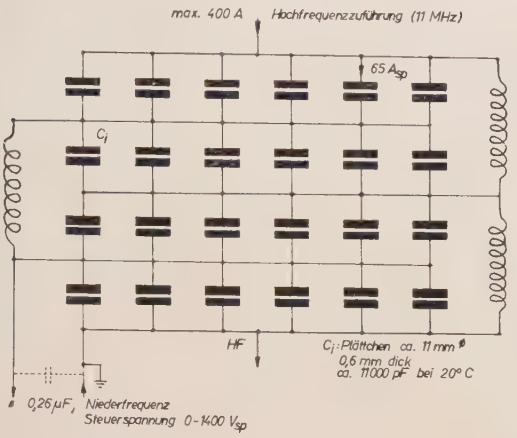

Abb. 6. Elektrische Schaltung für 24 Plättchen.

der Randzone und führten deshalb leichter zu oben beschriebener Störung.

Abb. 4 zeigt die Aufhängung eines einzelnen Plättchens. Es wurde dafür gesorgt, dass die Zuführungsfahnen keine Zugbeanspruchung auf das Plättchen übertragen können. Die Flüssigkeitsströmung wird durch die Zuführungsfahnen nur wenig beeinflusst. Als Pumpe wurde ein System entwickelt, bei dem die Möglichkeit zur Bildung von mechanischem Abrieb weitgehendst ausgeschlossen wird. Ausserdem sollte dieses Pumpsystem gewährleisten, dass alle Keramikoberflächen auf der gleichen Temperatur gehalten werden, damit sich die Hf-Spannungen gleichmässig auf alle Plättchen verteilen.

Abb. 5 zeigt einen Schnitt durch den ganzen Modulator. Die Symmetrie- und Rotor-Achse (A) liegt im Betriebszustand waagerecht. Der Rotor wird von einem Asynchronmotor von 1500 U/min über eine biegsame Welle angetrieben. Er ist innerhalb der Flüssigkeit nicht mehr gelagert. In der flüssigkeitsdichten Durchführung (D) werden Teflonsimmerringe (B) verwendet. Der Rotor selbst (R) ist aus Teflon hergestellt, damit die Parallelkapazitäten zwischen den Ringen (S) möglichst klein werden. An den beiden Enden des Rotors ist je ein axial zur Mitte förderndes Flügelrad (G) eingebaut. Die Ringe (S) sind auf drei geschliffenen Keramikstäben festgeklemmt. Mit diesen Stäben lässt sich ein sehr stabiler Aufbau des ganzen Innensystems erreichen.

Als Abschluss für die Flüssigkeit an der Seite der koaxialen Leitung dient eine Teflonscheibe (H).

Das ganze Gehäuse und alle metallischen Innenteile sind elektrolytisch versilbert.

Aus dem Xylol wird die Verlustwärme über die Kühlspiralen (O) an den Wasserkühlkreislauf abgegeben.

Das ganze Gehäuse lässt sich leicht in den Innenteil (Abb. 10) und den Aussenmantel mit Kühlschlange und Rotor teilen. Für das Auswechseln eines Plättchen benötigt man einschliesslich Ab- und Anbau des Modulators am Zyklotron etwa 15 Minuten. Obwohl das Gehäuse für 54 Plättchen konstruiert ist, werden zur Zeit nur 24 Stück verwendet. Abb. 6 zeigt die Schaltung. Als Drosseln (T in Abb. 5) werden Widerstandsdrähte verwendet, um alle unter Mitwirkung der Drosseln zustande kommenden Eigenfrequenzen möglichst stark zu dämpfen. Diese Drähte wurden auf Teflon-Gewindestangen aufgewickelt.

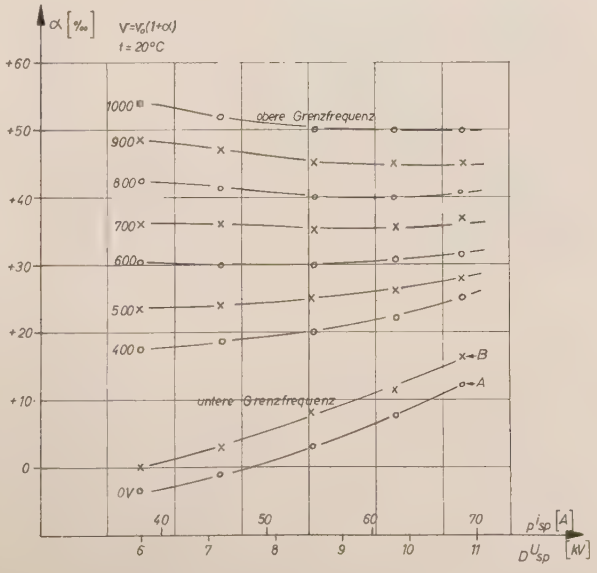

Abb. 7. Eigenfrequenz in Abhängigkeit von der Deespannung. Parameter: Steuerspannung. A statisch für Steuerspannung 0 Volt. B dynamisch, untere Grenzfrequenz.

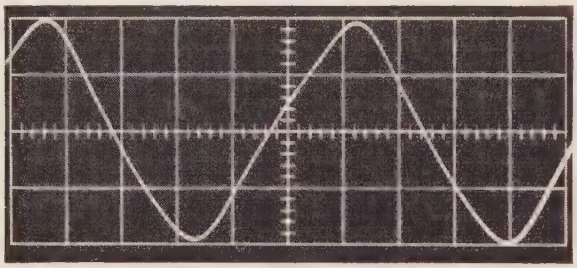

Abb. 8. Verlauf der Steuerspannung. Frequenz 750 Hz. Effektivwert der Spannung 850 Volt.

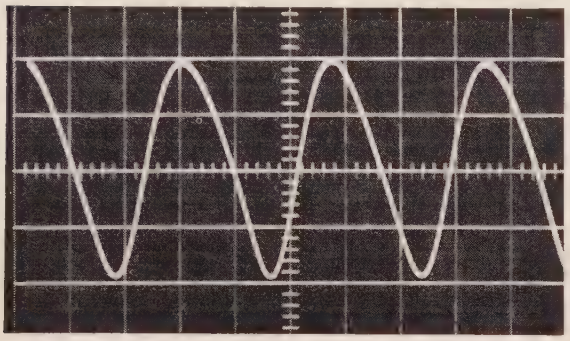

Abb. 9. Frequenzverlauf. Wiederholungsfrequenz 1500 Hz. Frequenzhub 4.3% bei 7.8 KV_{sp} Deespannung und 22° C Betriebstemperatur. (Seit Messung der Kurven aus Abb. 7 wurden einige Plättchen und die Drosseln ausgewechselt).

Für die Steuerspannung wirkt der Modulator wie eine kapazitive Belastung von 0.26 μF. Als Steuerspannungsquelle wird zur Zeit ein rotierender, drehzahlregelbarer Mittelfrequenzgenerator mit annähernd sinusförmigem Spannungsverlauf (Abb. 8) benutzt.

Im Anfang führten Überschläge in der Vakuumkammer am Dee zum Durchschlag von Plättchen. Nach Einbau einer zweiten Überspannungsüberwachung mit Gasentladungsableitern unmittelbar am Modulator trat diese Art der Störung nicht mehr auf.

5. Betriebsergebnisse

In Abb. 7 ist die Eigenfrequenz als Funktion der Deespannung dargestellt. Auf der Ordinate ist die relative Verstimmung gegenüber einer Festfrequenz (10.48 MHz) aufgetragen. Als Parameter ist die Steuerspannung gewählt.

Kurve A zeigt die Eigenfrequenz für Steuerspannung O im statischen Fall. Kurve B zeigt die tiefste Frequenz, die im dynamischen Betrieb erreicht wird. Der Unterschied von 0.5% ist auf Relaxationserscheinungen mit grossen Zeitkonstanten zurückzuführen.

Der Anstieg der Kurve A mit zunehmender Deespannung ist mit einer Erhöhung der mittleren Temperatur in der Keramik zu erklären.

Die obere Grenzfrequenz ändert sich bei 1000 V_{eff} Steuerspannung nur noch wenig. Ein Vergleich mit Abb. 2 zeigt, dass sich ε_{diff} bei 1430 V Gleichspannung im Temperaturbereich von 35–40° C ebenfalls kaum mit der Temperatur ändert. Temperaturschwankungen der Kühlflüssigkeit bewirken infolgedessen im wesentlichen nur eine Änderung der unteren Grenzfrequenz. Die Frequenz entspricht dem Ende einer Beschleunigungsperiode. Ist der Frequenzhub etwas grösser als unbedingt notwendig, kann der Modulator ohne automatische Temperaturregelung betrieben werden.

Zur Veranschaulichung der Hochfrequenzbe-

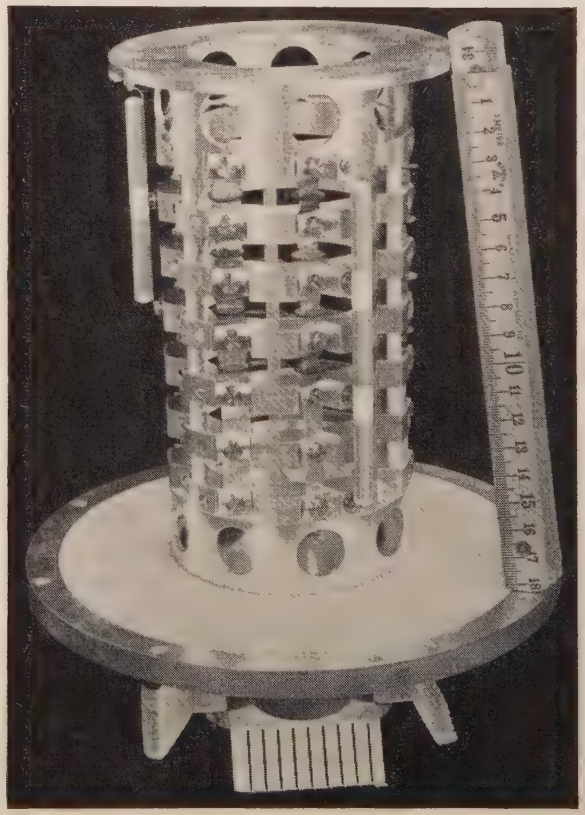

Abb. 10. Der Innenteil des Modulators bestückt mit 24 Plättchen.

lastung ist in Abb. 7 noch der maximale Hochfrequenzstrom durch ein Plättchen eingezeichnet. Bei 10 kV Deespannung werden in ca. 1 cm^3 Keramikmaterial (24 Plättchen) etwa 1000 Watt Hochfrequenzleistung in Wärme umgesetzt.

Infolge von Alterungserscheinungen ändern sich die elektrischen Eigenschaften des ferroelektrischen Materials im Laufe der Zeit geringfügig.

In Abb. 8 wird noch der Verlauf der Steuerspannung gezeigt, und in Abb. 9 ist der entsprechende Frequenzverlauf dargestellt. Zu berücksichtigen ist, dass durch die Symmetrie der ferroelektrischen Eigenschaften eine Frequenzverdopplung auftritt.

Zusammenfassend kann gesagt werden, dass sich ferroelektrische Ba-Sr-Keramik als "elektrisch steuerbare Kondensatoren" für die Frequenzmodulation in dem Hochfrequenzsystem für das 30 MeV Synchrozyklotron Bonn verwenden lassen.

Infolge der vielseitigen Anforderungen ist die Lösung des Problems auch von der technologischen und technischen Seite her recht verwickelt. Die Betriebserfahrungen haben jedoch gezeigt, dass sich mit 24 Plättchen bis zu einer Deespannung von 10 kV der notwendige Frequenzhub betriebssicher erreichen lässt. (Steuerspannung 1100 V.)

In den letzten sieben Monaten arbeitete der Modulator vollkommen einwandfrei, es liess sich mit dem Zyklotron ein Strahlstrom von 10 μAmpère (Deuteronen) erreichen. In dieser Zeit war weder ein Austausch von Plättchen, noch von anderen Modulatorbauelementen not-wendig.

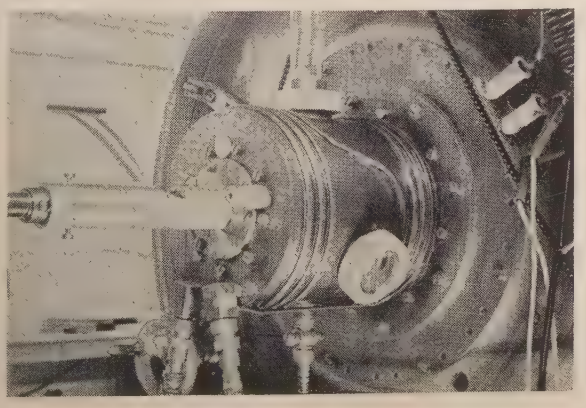

Abb. 11. Der Modulator am Zyklotron angebaut.

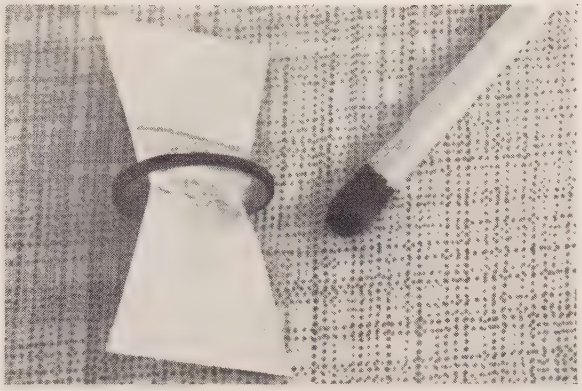

Abb. 12. Ein einzelnes Plättchen mit angelöteten Stromzuführungsfahnen. Als Grössenvergleich daneben ein Streichholz.

Im Gegensatz zu den sonst verwendeten mechanischen Modulatoren ist es möglich, während des Betriebes des Synchrozyklotrons sowohl die Wiederholungsfrequenz als auch den Frequenzhub zu veränderen. Mit Hilfe geeigneter elektronischer Steuerspannungsgeräte würden sich auch fast beliebige Frequenzprogramme einstellen lassen. Versuche in dieser Richtung sind in Vorbereitung.

An dieser Stelle möchte ich Herrn Professor Dr. W. Riezler für die Förderung dieser Arbeit meinen besonderen Dank aussprechen. Ferner danke ich allen Migliedern unseres Institutes, die bei Messungen und Experimenten geholfen haben und dem Bundesministerium für Atomkernenergie und Wasserwirtschaft für die Bereitstellung von Mitteln für den Bau der benötigten Geräte.

Literatur

Herbert Sachse, Ferroelektrika (Verlag Springer 1956) enthält 278 Literaturangaben.

Helen D. Megaw, Ferroelektricity in Crystals, (Methuen and Co., Ltd., London 1957).

The Harvard University 95 Inch Cyclotron, (Department of Physics, Havard University Cambridge, Mass., July 1950).

F. A. Heyn, Das Synchrozyklotron in Amsterdam, Philips Technische Rundschau 12 (1951) 245.

NUCLEAR INSTRUMENTS AND METHODS 6 (1960) 176–178; NORTH-HOLLAND PUBLISHING CO.

A TWO-DIMENSIONAL PULSE-HEIGHT ANALYSER

A. E. LITHERLAND and D. A. BROMLEY

Chalk River Laboratories, Ontario, Canada

Received 20 October 1959

A method is described whereby a 120-channel pulse-height analyser can be converted into three forty-channel pulse-height analysers. This is accomplished by adding three voltage pedestals of different height to the input pulses. The method has been successfully used in a study of the $N^{14}(He^3p\gamma)O^{16}$ reaction.

1. Introduction

Many measurements in nuclear spectroscopy involve the recording of a pulse-height spectrum that is in coincidence with a portion of another pulse-height spectrum. For example, in the recent study[1]) of the complex gamma-ray decay schemes from states in O^{16} formed by the reaction $N^{14}(He^3,p)O^{16}$ a 5-inch diameter by 4-inch long NaI(Tl) crystal and a 1-inch diameter by $\frac{1}{16}$-inch thick CsI(Tl) crystal were used in coincidence. Many 120-channel pulse-height spectra from one crystal were taken in coincidence with a narrow range of pulse heights in the second crystal. Since each coincidence spectrum took approximately one hour it is obvious that a device for simultaneously recording several such pulse-height spectra would be of great value†. Consequently additional circuits were devised which converted the 120-channel analyser then available into a two-dimensional analyser. When combined with the 120-channel analyser these circuits permitted, for example, the simultaneous recording and visual presentation of three separate 40-channel spectra in coincidence with three different and independent voltage gates. This was accomplished by adding voltage pedestals of a characteristic amplitude to the linear input pulses from one detector when they occurred in coincidence with a pulse in any one of three voltage gates set on the spectrum from the other detector.

Several two-dimensional analysers[2,3]) have been described in the literature recently which are considerably more advanced than the one described in this communication. However, the pedestal insertion method is simple to apply and has the advantage of visual presentation of the coincidence spectra both during and after the experiment. The circuits to be described have been used successfully[1]) in the measurement of gamma-ray spectra in coincidence with protons from the reaction $N^{14}(He^3,p)O^{16}$.

2. Operation of the Circuits

A block diagram of a typical experimental set-up is shown in fig. 1. The pulses from two scintillation counters A and B are amplified by linear amplifiers and analysed by single-channel analysers. Three single-channel analysers select portions of the pulse spectrum from crystal A. The output pulses from the single-channel analysers are then put in slow, $2\tau = 2\,\mu$sec, coincidence with a pulse from a "Fast Coincidence Unit", which requires that there are pulses from the crystals A and B in fast,

† Such a device is often referred to as an XYZ analyser[2]) or a coincidence sorter. In this note it will be referred to as a two-dimensional pulse-height analyser or more briefly a two-dimensional analyser.

[1]) D. A. Bromley, H. E. Gove, J. A. Kuehner, A. E Litherland and E. Almqvist, Phys. Rev. **114** (1959) 758.

[2]) L. Grodzins, A/Conf. 15/P/647 U.S.A. Second United Nations International Conference on the Peaceful Uses of Atomic Energy.

[3]) Multichannel Pulse-Height Analysers, Edited by H. W. Koch and R. W. Johnstone, Nuclear Science Series, Report Number 20, National Academy of Sciences, Washington, D.C., U.S.A. (1957)

$2\tau = 40$ nsec, coincidence[4]). The outputs from the three coincidence units are then applied to the three inputs, 1, 2 and 3, of the Pedestal Insertion Gate to be described below. It is necessary for the successful operation of the Pedestal Insertion Gate that the spectrum of pulses from crystal B be limited to a certain range of pulse heights. This is accomplished quite simply as shown in the lower half of fig. 1. A wide voltage window is set by the single-channel analyser and the output pulses put in slow, $2\tau \approx 2\ \mu$sec, coincidence with the pulses from the fast coincidence unit. The output pulses then open the Pedestal Free Gate[5]) which passes the portion of the spectrum from

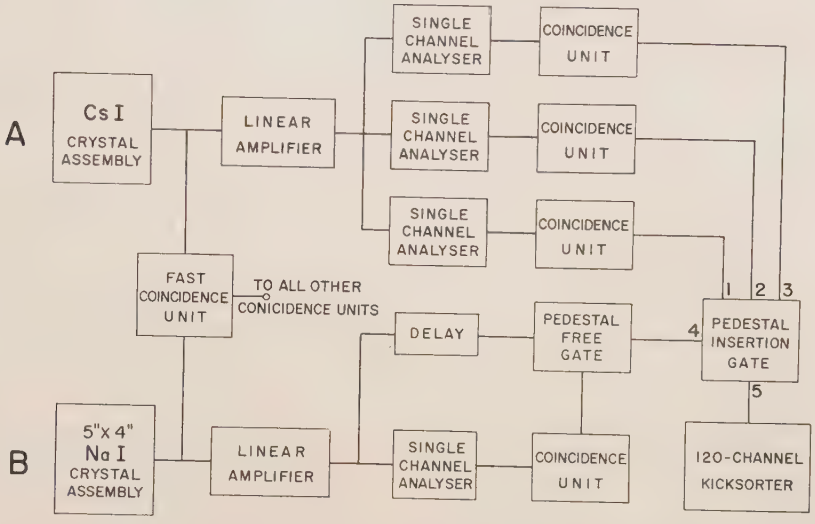

Fig. 1. A block diagram of the circuits used to display three 40-channel spectra on a 120-channel kicksorter.

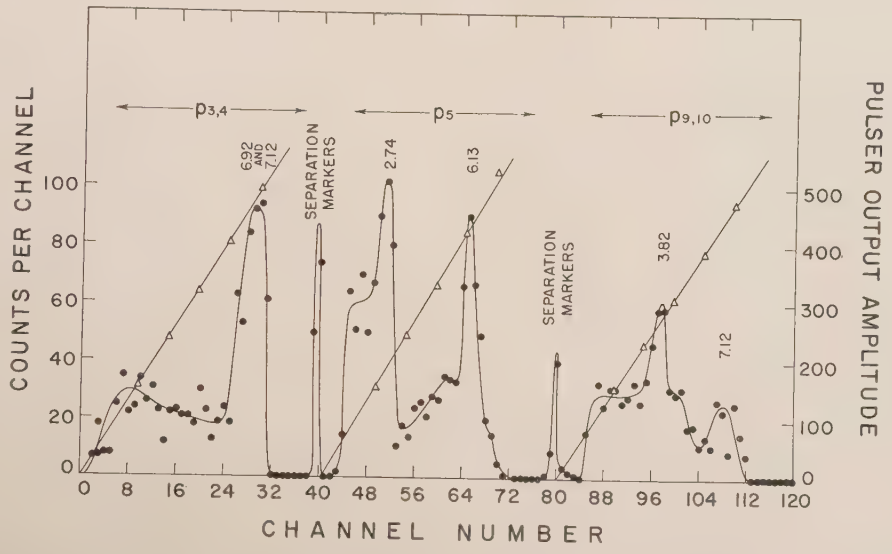

Fig. 2. Three 40-channel spectra displayed simultaneously on a 120-channel kicksorter. The spectra shown are gamma-ray pulse spectra in coincidence with proton groups from the reaction $N^{14}(He^3,p\gamma)O^{16}$. The energies in MeV of the principal gamma-rays are shown.

[4]) R. E. Bell, R. Graham and H. E. Petch, Can. J. Phys. **30** (1952) 35.

[5]) R. L. Clarke and A. J. Ferguson (unpublished).

crystal B selected by the single-channel analyser. This pulse spectrum is then applied to input number 4 of the Pedestal Insertion Gate.

A pulse at, for example, input 2 to the Pedestal Insertion Gate triggers one of three univibrators which produces a rectangular output of adjustable width. This pulse then cuts off one of three pentodes to produce a pedestal of the same width and of height determined by the quiescent current through the pentode. The currents through the three pentodes are adjusted to produce pedestals of three different heights corresponding to the three different inputs 1, 2 and 3.

Addition of the pedestal to the appropriate pulse entering input 4 occurs in the common anode load of the pedestal forming pentode and a second linear-amplifier pentode stage which passes the pulse from input 4. The summed output is then mixed in a common cathode load of three cathode followers and applied to the 120-channel kicksorter. Pulses which enter the Pedestal Insertion Gate from crystal B which are not in coincidence with pulses at inputs 1, 2 and 3 are eliminated from the 120-channel spectrum by using backbias. The pedestal heights are adjusted to divide the 120 channels into three groups of 40 channels. The range of pulses analysed from crystal B is limited to 40 channels by means ot the single-channel analyser as described earlier. This ensures that pulses larger than the range of interest are not recorded in the next higher spectrum. The effective dead time of the system is that of the multichannel analyser which for the spectra shown in fig. 2 to be discussed below was approximately 4 milliseconds.

An example of the use of the two-dimensional analyser described above is shown in fig. 2. In this example three single-channel analysers were set on the proton groups, P_3 and P_4, P_5, P_9 and P_{10} from the reaction $N^{14}(He^3,p)O^{16}$, corresponding to the formation of O^{16} in its third and fourth unresolved excited states, its fifth excited state and its ninth and tenth unresolved excited states. These excited states are at 6.92, 7.12, 8.87, 10.94 and 11.06 MeV respectively. Gamma-radiation spectra in coincidence with these three proton channels, and therefore associated with the decay of the corresponding levels in O^{16}, were displayed simultaneously on a 120-channel kicksorter. A discussion of these measurements has been published[1]).

A pulse generator has been used to examine the linearity of the system with the results shown in fig. 2. In the absence of any pulse arriving at the linear input 4 of fig. 1, as a result of the finite resolving time of the coincidence circuits used, the system produces three groups of pulses corresponding to the pedestals alone. These peaks are called separation markers in fig. 2 where the separation marker corresponding to the lowest pedestal has been back-biased just below the analyser threshold and the higher two markers appear in channels 40 and 80 respectively. This feature provides a convenient method of splitting the kicksorter display into its appropriate sections.

Additional uses for the two-dimensional analyser described above suggest themselves readily.

1. Spectra taken with adjacent voltage gates, one set upon a particular peak and the other immediately above it, can be taken simultaneously and then subtracted to eliminate background contributions to the pulse spectrum in coincidence with the pulses corresponding to the peak.

2. The spectrum from a single detector can be displayed sequentially in three repetitions at any interval such that appreciable losses are not made by the kicksorter. This eliminates the time interval normally required for reading out of spectra until after three have been accumulated.

3. Spectra from three detectors can be recorded simultaneously.

NUCLEAR INSTRUMENTS AND METHODS 6 (1960) 179–182; NORTH-HOLLAND PUBLISHING CO.

ANGULAR SELECTIVITY OF A GEIGER TELESCOPE ARRANGEMENT FOR COSMIC RAY AIR SHOWERS

W. M. LAYSON†, J. MALOS and D. D. MILLAR

The F.B.S. Falkiner Nuclear Research and Adolph Basser Computing Laboratories, School of Physics††, The University of Sydney

Received 21 September 1959

An arrangement of geiger telescopes for the selection of vertical air showers has been investigated. The arrangement shows little selectivity in responding to near-vertical showers. The experimental results are in good agreement with the calculated angular selectivity. The arrangement is, therefore, not likely to be of great value in looking for anisotropy in the high energy primary cosmic radiation.

1. Introduction

The search for possible anisotropies in the directions of arrival of the high energy cosmic rays which give rise to the extensive air showers has led to the application of several methods for determining experimentally the directions of incidence of such showers. Fast electronic measurements of the arrival times of shower particles at rapid response detectors distributed in a horizontal array have been used by Bassi, Clark and Rossi[1]). Cloud chamber photographs giving the directions of the air shower particles in high density regions of the shower have been used by Rothwell, Wade and Goodings[2]). Neither method can be said to be either simple or inexpensive. On the other hand Shen and Singer[3]) have proposed the use of a particularly simple arrangement of geiger counter telescopes in coincidence and have claimed for such an arrangement a high selectivity in detecting air showers arriving from the near-vertical direction. If such an arrangement could be shown to be effective in selecting showers falling within a narrow solid angle of acceptance then it would no doubt find wide application in the search for sidereal variations in the intensity of extensive air showers.

The present paper describes an experiment which has been carried out to test the response of such a geiger telescope arrangement, using it in conjunction with the Sydney air shower apparatus[4]). This apparatus consists of an array of scintillation counters, from the response of which may be obtained the size, the location of the core and the direction of incidence of each shower recorded. No marked selectivity for vertical showers was exhibited by the telescope arrangement. This is in agreement with calculations which have been made, and which are discussed in 4.

2. Experimental Apparatus

Three geiger counter telescopes were located at the vertices of a triangle of side approximately 3 m. Each telescope consisted of two geiger counters parallel to each other and with vertical separation of 22.5 cm. The counters were each of length 65 cm and diameter 3.2 cm. For a single particle to be recorded by a telescope its maximum angle to the vertical projected on the plane perpendicular to the counter axes is $\bar{\theta}_0 = 8°$. The apparatus is triggered by a

† Present address: Department of Physics, Massachusetts Inst. of Technology, Cambridge, Mass., U.S.A.

††Also supported by the Nuclear Research Foundation within the University of Sydney.

[1]) P. Bassi, G. Clark and B. Rossi, Phys. Rev. **92** (1953) 441.

[2]) P. Rothwell, B. Wade and A. Goodings, Proc. Phys. Soc. A **69** (1956) 902.

[3]) K. Y. Shen and S. F. Singer, Phys. Rev. **106** (1957) 555.

[4]) M. H. Brenman, D. D Millar and C. S. Wallace, Nature **182** (1958) 405.

fourfold coincidence provided by at least one air shower "particle" (electron or photon) traversing each of four scintillation counters. The areas of the scintillators were 0.23 m² and they were situated at the corners of a rectangle of dimensions 26 m by 31 m, inside which was the triangular array of telescopes as shown in fig. 1. With such a triggering array it is estimated that

Fig. 1. Plan view of the apparatus showing the position of the three geiger telescopes relative to the four triggering scintillators. (Dimensions in metres.)

more than 95 per cent of all showers of size greater than 4×10^5 particles whose cores fall within the rectangle are detected. Only those showers are considered here which set off all six of the geiger counters.

3. Experimental Results

During a period of two months discontinuous running 190 events were recorded at an average rate of 0.42 ± 0.03 hr^{-1}. The histogram of fig. 2 shows the distribution of the sizes of

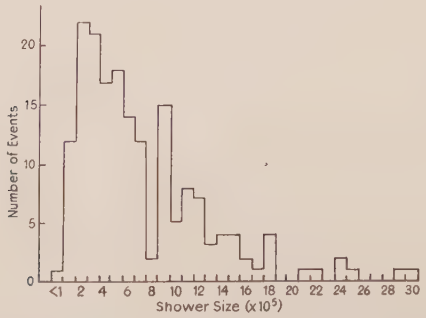

Fig. 2. The frequency of showers of different sizes setting off the four scintillators and three telescopes.

these 190 showers. The size of each shower has been determined from the response of the whole air shower array of nine scintillators. The sharp cut-off for showers of size less than 10^5 particles produced by this arrangement of geigers and scintillators is clearly seen.

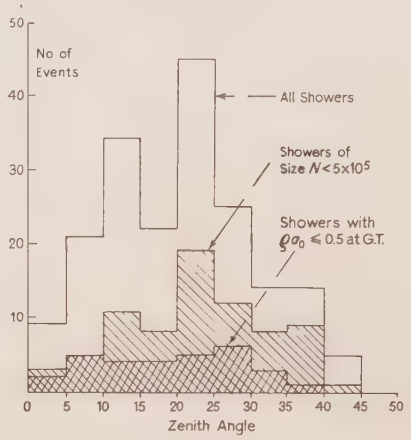

Fig. 3. The frequency of showers of different zenith angles setting off the arrangement. Also shown are the zenith angle distributions for small showers, and for showers of low particle density at the location of the geiger telescopes.

The direction of incidence of each of these 190 showers was also determined to within $\pm 4°$, by the fast timing method from the delays between the pulses from the four triggering scintillators. Fig. 3 shows the zenith angle distribution of these showers. It will be observed that there is no marked preference for near-vertical showers. The projected zenith angle for each shower in the vertical plane perpendicular to the axes of the telescopes was also determined. It was found that 62 per cent of the showers had projected angle greater than the "acceptance angle" of the telescopes, $\bar{\theta}_0 = 8°$, rather than 10 per cent as suggested by Shen and Singer.

4. Discussion

The apparatus then shows little preference for showers whose projected angles are less than 8°. To see why this should be, the expected response of the telescopes has been calculated on the assumption that all the shower particles travel in a direction parallel to the shower axis, as in the calculation of Shen and Singer.

The counting rate C_6 is given by the following integral:

$$C_6 = \int_0^\infty \int_0^{2\pi} \int_0^{\frac{1}{2}\pi} \frac{9K}{2\pi} \rho^{-2.4} f(\rho, a'(\theta,\phi)) \cos^8\theta \sin\theta \, d\theta \, d\phi \, d\rho ,$$

ρ is the density in particles/m². θ is the zenith angle, ϕ the azimuth angle. K is the constant in the frequency of density spectrum ($N(\rho)\,\mathrm{d}\rho = K\rho^{-2.4}\,\mathrm{d}\rho$). $9/2\pi$ is a normalization factor and $f(\rho,a')$ is a probability function given below, which depends upon the particle density and a variable area $a'(\theta,\phi)$. $a'(\theta,\phi)$ is the area which must be traversed by a particle travelling at angle (θ,ϕ) if it is to fire both counters of a telescope. a_0 is the geometrical area of a single counter. The counting rate must include the probability of all types of coincidence and therefore:

$$f(\rho,a') = \begin{cases} [(1-\mathrm{e}^{-\rho a'}) + (1-\mathrm{e}^{-\rho(a_0-a')})^2\,\mathrm{e}^{-\rho a'}]^3 & 0 \leqslant \theta \leqslant \theta_m \\ [1-\mathrm{e}^{-\rho a_0}]^6 & \theta_m \leqslant \theta \leqslant \tfrac{1}{2}\pi \end{cases}$$

θ_m is the maximum angle for which three-fold coincidence of particles is sufficient to fire six counters. This calculation differs from that of Shen and Singer in the use of the $\cos^8\theta$ distribution, the recognition of the area variation with θ and ϕ, the inclusion of a solid angle term, $\sin\theta$. Of these, the last factor is the one which plays the main role in reducing the predicted angular selectivity of the apparatus.

The results of the calculation are given in table 1. They have been made for a counter telescope of 8° half-angle and of 12.7°, the former corresponding to the Sydney telescopes, the latter to those used by McCusker, Page and Reid[5]). R_v is the counting rate for three vertical telescopes and R_h is the rate for the telescopes lying on their sides in a horizontal plane. F_v and F_h are the fractions of showers recorded with the two arrangements which have projected zenith angles less than θ_0.

The values of F_v may be compared with the experimental values. Experimentally we find 38 per cent to be compared with the predicted value of 40 per cent. McCusker *et al.* obtain 55 per cent to be compared with 57.5 per cent predicted.

A further calculation was carried out for the case where in each counter telescope a third counter was inserted, parallel to the other two and mid-way between them. The nine-fold coincidence rate was then calculated as for the six-fold rate and here a large contribution to the rate must be taken into account which arises from showers in which one particle may traverse two adjacent counters of a telescope and a second particle traverses the third counter. The calculated nine-fold rate was only 15 per cent lower than the six-fold rate, a result not inconsistent with the experimental result of Shen and Singer.

Table 1

The calculated responses of 3 geiger telescopes in coincidence of half-angle 8° and 12.7°.

θ_0	R_v	F_v	R_h	F_h
8°	$0.35\,Ka_0^{1.4}$	40 %	$0.31\,Ka_0^{1.4}$	32%
12.7°	$0.37\,Ka_0^{1.4}$	57.5%	$0.31\,Ka_0^{1.4}$	49%

R_v and R_h are the expected counting rates for vertical and horizontal telescopes. F_v and F_h are the corresponding calculated fractions of recorded showers having projected zenith angle less than the half-angle of the telescopes.

The above calculations are incomplete in that we have ignored the triggering requirement that four scintillation counters must be set off in coincidence as well as the six, or nine, geiger counters in order that the shower be recorded. The sample of showers which we are recording experimentally is consequently different from the sample which would be detected by an arrangement of three geiger telescopes alone, for which the above calculations were carried out. The counting rate of the vertical telescope arrangement is given in table 1 as $0.35\,Ka_0^{1.4}$ where a_0 is the area of a geiger counter. Using the value of K given by Murdoch[6]) the predicted rate is 1.0 hr^{-1}, to be compared with our experimental rate of coincidences between the telescopes and the four scintillators of 0.42 hr^{-1}. Sixty per cent of the showers capable of setting off the telescopes alone have failed to set off the four scintillators as well. These showers are presumably, therefore, small showers whose cores fall close to the telescopes or large showers

[5]) C. B. A. McCusker, D. E. Page and R. J. Reid, Phys. Rev., in press.

[6]) H. S. Murdoch, Nuclear Physics **8** (1958) 157.

falling farther away, for which the probability of setting off the four scintillators is less than 1. In fig. 3 the zenith angle distributions are given for small showers and for showers whose calculated density of particles at the telescopes was less than 0.5 particles per geiger counter area. There is no evidence of any strong increase of selectivity for vertical showers for either the small showers or the showers of low particle density.

5. Conclusion

It has been shown experimentally that an arrangement of vertical geiger telescopes as proposed by Shen and Singer shows little angular selectivity in selecting preferentially extensive air showers of cosmic rays whose directions of incidence fall within the solid angle of the telescopes.

A calculation has been carried out which predicts the selectivity of such an arrangement, and which gives good agreement with the experimental value observed.

Acknowledgements

The authors wish to thank the other members of the Sydney air shower group for assistance in the running of the apparatus and, particularly, Mr. C. S. Wallace and Dr. M. H. Brennan for valuable discussions. Thanks are also due to Professor H. Messel and the Nuclear Research Foundation for the provision of the experimental facilities. One of us (W. M. L.) carried out this work under a grant from the United States Educational Foundation in Australia.

NUCLEAR INSTRUMENTS AND METHODS 6 (1960) 183–186; NORTH-HOLLAND PUBLISHING CO.

ON THE EFFECT OF TOTAL REFLECTION ON THE OPTIMUM DIMENSIONS OF COLLIMATORS FOR NEUTRON CRYSTAL SPECTROMETERS AND DIFFRACTOMETERS

P. SZABÓ

Central Research Institute for Physics, Budapest

Received 8 October 1959

In developing further the considerations of a previous paper[4]), presently we examine the effect that is exercised by the total reflection developing at the walls of primary collimators used in neutron diffractometers and crystal spectrometers on the optimum dimensions of such collimators. The formulae for computation of the intensity transmitted by a single total reflection are given. It is shown that as to the intensity thus transmitted (similarly to the case of direct transmission treated in ref.[4])) there is an optimum in the dimensions of the collimator which in cases of practical interest is found to be the same as that determined for direct transmission.

1. Introduction

In connection with neutron diffractometers and cyrstal spectrometers containing Soller type collimators[1]) the attainable resolving power[2]) as well as the problem of the suitable sequence of angular divergences if three collimators are applied in a diffractometer[3]) have been discussed in the literature.

In a recent paper[4]) the author has discussed how the primary collimator dimensions have to be chosen in order to obtain the maximum transmitted intensity, having been already determined the angular divergence adequate for the resolving power to be obtained.

It is known that the total reflection developing at the collimator plates made of an appropriate material considerably increases the intensity of the beam transmitted by collimators. In the following, in addition to the considerations of ref.[4]), this effect will be discussed in connection with the calculation of optimum collimator dimensions.

2. Initial Assumptions

It is obvious that an ideal collimator plate would (a) have a critical angle for total reflection δ equal to the required horizontal angular divergence and (b) reflect truly all the neutrons incident at an angle below δ.

Technically it would be extremely difficult to realise condition (b). On the other hand, conditon (a) is not satisfied for crystal spectrometers where the required horizontal angular divergence may be only 1′ or 2′, because the critical angle for total reflection on the available collimator materials (primarily on steel) is about 10′[5]). Therefore the realization of condition (b) must not even be allowed in the case of these substances since, in the case, the multiple reflections would also greatly contribute to the neutron transmission so that the angular divergence of the transmitted beam could not be reduced below δ.

Consequently, in the following we shall restrict our considerations to the virtually most important case where the effect of multiple reflections may be neglected and only that of single total reflection will be taken into account. Mutatis mutandis, however, our calculations

[1]) W. Soller, Phys. Rev. **24** (1924) 158.

[2]) V. L. Sailor, H. L. Foote, Jr., H. H. Landon and R. E. Wood, Rev. Sci. Instr. **27** (1956) 26.

[3]) G. Caglioti, A Paoletti and F. P. Ricci, Nuclear Instruments **3** (1958) 223.

[4]) P. Szabó, Nuclear Instruments **5** (1959) 184.

[5]) A critical angle smaller at will could be achieved if an element of negative scattering amplitude were alloyed in a suitable proportion e.g. to the steel, since the index of refraction and thus δ, too, is determined by the average scattering amplitude. The alloying of Mn in an appreciable proportion which comes into consideration at first rate for this purpose owing to its scattering properties, would involve difficult metallurgical problems. It seems it would be highly interesting to deal with them.

can be readily applied also to account for multiple reflections.

Our other initial assumptions are the same as those used in ref.[4]). Thus we omit to make them known now and only we add a single little observation as follows. It has been mentioned in section 2 of ref.[4]) that in order to obtain the required resolving power it is sufficient as a rule to preset the horizontal angular divergence α since the vertical angular divergence of the beam is usually kept below the allowed margin (which is much greater than α) by the dimensions of the reactor channel. Thus no presetting of the vertical angular divergence of the collimator $\beta \equiv \text{arctg}\ (h/l)$ is required. We may now add that our present considerations as well as those in ref.[4]) will hold even if this restriction is not imposed by the reactor channel, but in the latter case we have to set in our optimum calculations a lower limit for the value of the collimator length l considered variable (that is an upper limit for the value of the corresponding number n of collimating channels). This does not, however, affect our results.

The predominant part of our symbols corresponds to those used in ref.[4]). Here we give the definitions only of the newly occurring ones. All the old symbols are to be found collected at the end of ref.[4]), and the new ones at the end of this paper.

3. Calculation of the Intensity Due to Total Reflection

Total reflection may occur on the (vertical) collimator plates as well as on the (horizontal) "spacers" placed in between. We consider first intensity $I_{\text{refl.}}$ due to total reflection on the vertical plates, then intensity $I'_{\text{refl.}}$ due to that on the horizontal walls. (Intensity means here the same ratio as in section 2 of ref.[4]).) The fact of the reflection actually not being total will be taken into account subsequently by a reducing efficiency factor ε.

The horizontal cross section of the reactor channel and that of one (m^{th}) of the collimating channels is shown in fig. 1. In fig. 2, on the other hand, is seen a vertical cross section of the channel and collimator inclined at an angle φ to the collimator axis.

In fig. 1 the straight lines lying parallel to and between the pair of parallel straights subtending an angle φ with the axis, illustrate the projection on a horizontal plane of the beam incident at azimuth φ and polar angle ϑ, that is at angle $\psi \equiv \vartheta - \frac{1}{2}\pi$ corresponding to the latter, and transmitted by the collimator in consequence of total reflection on one of the collimator plates. This projection cuts a $l \operatorname{tg} \varphi$ long straight stretch (denoted on fig. 1 by a question mark) on the surface of neutron source.

The intensity incident at "unit" solid angle about this direction φ, ψ and transmitted by total reflection in the above said manner, is proportional to the product of this beam width $l \operatorname{tg} \varphi$ and the beam height denoted in fig. 2 by A and exactly defined in ref.[4]). In consequence of single reflection also such neutrons can be transmitted through the collimator which strike the collimator plate at an angle of incidence larger than the horizontal angular divergence α but smaller than arctg $(2 \operatorname{tg} \alpha)$. It is obvious that in this case the beam width will be $l \operatorname{tg} \alpha$, independently of the direction of the rays in the beam, instead of the width $l \operatorname{tg} \varphi$ denoted by the question mark in fig. 1.

The intensity thus transmitted is consequently given by the following sum made over the total number n of collimating channels:

$$I_{\text{refl.}} = \sum_{m=1}^{n} 4l \left\{ \int_0^{\phi_1} \int_0^{\beta} \operatorname{tg} \varphi \cdot A\ (\varphi,\psi) \cdot \cos \psi \, \mathrm{d}\varphi \, \mathrm{d}\psi + \right. \\ \left. + \int_{\phi_1}^{\phi_2} \int_0^{\beta} \operatorname{tg} \alpha \cdot A\ (\varphi,\psi) \cdot \cos \psi \, \mathrm{d}\varphi \, \mathrm{d}\psi \right\}. \tag{1}$$

Here and below, in the double integrals, the limits of integration with respect to φ are given at the first symbol for integration, and the limits with respect to ψ at the second one.

The meaning of the limits of integration with respect to φ: that the lowest of the quantities

$$\gamma'_{\text{m}},\ \delta \quad \text{and} \quad \left\{ \begin{matrix} \alpha \\ \text{arctg}\ (2 \operatorname{tg} \alpha) \end{matrix} \right\}$$

has to be substituted for $\left\{ \begin{matrix} \phi_1 \\ \phi_2 \end{matrix} \right\}$.

The integrals in (1) can be reduced to the

types of integral given in section 3 of ref. [4]) and thus they can be obtained in the form of closed expressions consisting of elementary functions. Instead of that, however, considering that within the limits of integration only very low values of φ and ψ are involved, we can introduce (as in ref.[4])) such a simplification which is

Hence for $\beta > \gamma' > \gamma''$

$$I_{\text{refl.}} = 6h\alpha[s-(n-1)v] \left\{ \frac{\frac{e-h}{2} - \frac{e^2-h^2}{4h} + \frac{(e-h)^2}{8h}}{L - \frac{s-(n-1)v}{\alpha n}} + \frac{(e+h)^2}{8hL} \right\} \qquad (1'a)$$

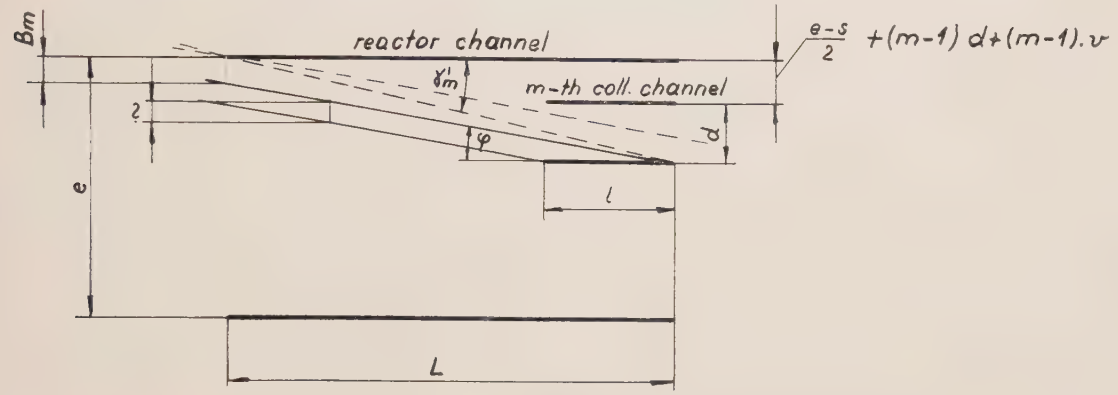

Fig. 1

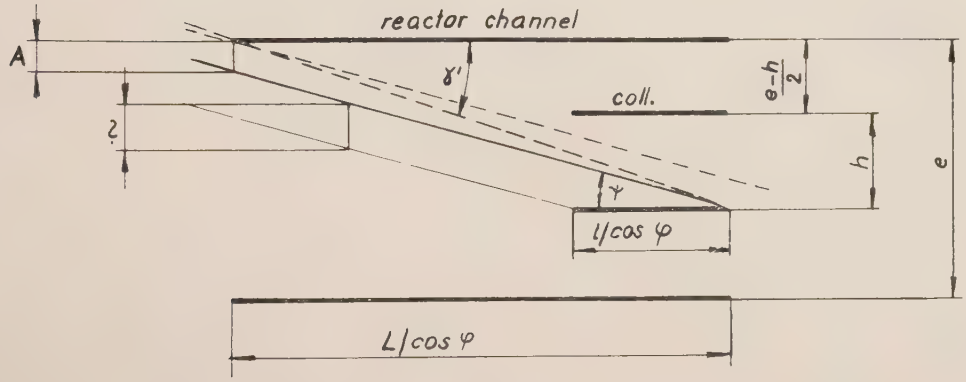

Fig. 2

highly significant from the point of view of numerical computation, as it is shown in ref.[4]). This consists in setting equal the occurring cosines to l and the sines and tangents to their arguments.

Furthermore if we restrict our treatment to the practically most important case when $\phi_2 = 2\alpha$ (and consequently $\phi_1 = \alpha$) then, making use of the proper relations of ref.[4]) we have instead of (1) the following expression:

$$I_{\text{refl.}} = 4nlh \left\{ \int_0^{\alpha} \int_0^{\beta} \varphi \left(1 - \frac{\psi}{\beta}\right) f(\psi)\, d\varphi\, d\psi + \right. \\ \left. + \alpha \int_{\alpha}^{2\alpha} \int_0^{\beta} \left(1 - \frac{\psi}{\beta}\right) f(\psi)\, d\varphi\, d\psi \right\}. \qquad (1')$$

and for $\beta \approx h\ l < \gamma' < \gamma''$

$$I_{\text{refl.}} = 3h^2\alpha^2 n\,. \qquad (1'b)$$

The calculation of the intensity contributed by total reflection on the horizontal walls is illustrated in fig. 2. In that the straight lines lying parallel to and between the pair of straights at angle ψ to the horizontal plane show the beam incident on one of the spacer plates at angle φ, ψ and transmitted by the collimator due to total reflection, as projected on a polar coordinate plane with azimuth angle φ. This projection cuts a $(l/\cos\varphi)$ tg ψ long straight

stretch (denoted on fig. 2 by a question mark) on the surface of neutron source. The intensity incident at "unit" solid angle about this direction φ, ψ and transmitted by total reflection in the above said manner, is proportional to the product of this beam height $(l/\cos\varphi)\ \mathrm{tg}\ \psi$ and the beam width denoted in fig. 1 by B_m and exactly defined in ref.[4]).

Thus the intensity due to total reflection on the horizontal walls is given by

$$I'_{\mathrm{refl.}} = \sum_{m=1}^{n} 4l \int_0^{\alpha}\int_0^{\Psi} \frac{\mathrm{tg}\ \psi}{\cos\varphi} B_\mathrm{m}(\varphi)\cdot\cos\psi\ \mathrm{d}\varphi\ \mathrm{d}\psi\ . \qquad (2)$$

Ψ denotes here the lowest value of quantities δ, γ' and β. $I'_{\mathrm{refl.}}$ can be also reduced to the types of integral given in section 3 of ref.[4]) and thus it can be also obtained in the form of closed expression consisting of elementary functions.

Now, making use once more of above approximation based upon the low limits of integration, we have

$$I'_{\mathrm{refl.}} = \sum_{m=1}^{n} 4ld \int_0^{\alpha}\int_0^{\Psi} \psi\left(1-\frac{\varphi}{\alpha}\right) f_\mathrm{m}(\varphi)\ \mathrm{d}\varphi\ \mathrm{d}\psi\ . \qquad (2')$$

In the practically most interesting case when $\alpha < \gamma'_\mathrm{m} < \gamma''_\mathrm{m}$ and $\Psi = \delta$, (2′) turns into

$$I'_{\mathrm{refl.}} = 4nld \int_0^{\alpha}\int_0^{\delta} \psi\left(1-\frac{\varphi}{\alpha}\right) \mathrm{d}\varphi\ \mathrm{d}\psi = \frac{[s-(n-1)\,v]^2}{n}\,\delta^2\ . \qquad (2'')$$

4. Conclusions

Upon closer investigation of above expressions it turns out that in all cases of practical interest $I'_{\mathrm{refl.}} \ll I_{\mathrm{refl.}}$. $(I'_{\mathrm{refl.}}/I_{\mathrm{refl.}} < 0.01.)$ Thus $I'_{\mathrm{refl.}}$ virtually does not contribute to the intensity transmitted.

The total intensity transmitted by the collimator is given by the sum of the intensity transmitted directly I (dealt with in ref.[4])) and that transmitted by total reflection. With the assumptions in section 2 and owing to the value of $I'_{\mathrm{refl.}}$ being negligible the intensity transmitted by total reflection is equal to $\varepsilon I_{\mathrm{refl.}}$. Thus the total intensity is $I + \varepsilon I_{\mathrm{refl.}}$. The length l and the corresponding number n of collimating channels for a collimator of given angular divergence and overall cross section has to be chosen in the way to obtain the maximum of this sum.

It is easy to show that similarly to the intensity I dealt with in ref.[4]), $I_{\mathrm{refl.}}$ as a function of n (i.e. of l) does also have a maximum. Now we still show that in the case of practically almost exclusive interest when $I_{\mathrm{refl.}}$ is given by equation (1′), $I_{\mathrm{refl.}} = 3I$, thus the total intensity is $I + \varepsilon I_{\mathrm{refl.}} = (1 + 3\varepsilon)\, I$. That means that the maximum of total intensity is at the same value of n (i.e. of l) as that of I, consequently the optimum dimensions of the collimator are equal to those computed by taking into account direct transmission only according to ref.[4]).

Proof. In this case in equation (11) of ref.[4]) $f_\mathrm{m}(\varphi) = 1$ and we may write this equation as follows:

$$I = 4qn \int_0^{\alpha}\int_0^{\beta}\left(1-\frac{\varphi}{\alpha}\right)\left(1-\frac{\psi}{\beta}\right) f(\psi)\ \mathrm{d}\varphi\ \mathrm{d}\psi = 2h\,[s-(n-1)\,v]\,\alpha\int_0^{\beta}\left(1-\frac{\psi}{\beta}\right) f(\psi)\ \mathrm{d}\psi\ . \qquad (3)$$

And the expression for $I_{\mathrm{refl.}}$ in equation (1′) may be transformed into

$$I_{\mathrm{refl.}} = 6h\,[s-(n-1)\,v]\,\alpha\int_0^{\beta}\left(1-\frac{\psi}{\beta}\right) f(\psi)\ \mathrm{d}\psi\ . \qquad (1'')$$

Thus in fact $I_{\mathrm{refl.}} = 3I$.

Symbols

Here only such symbols are given which were not used in ref.[4]). The symbols given in ref.[4]) are used in the present paper in unchanged sense.

$I_{\mathrm{refl.}}$ intensity of single total reflection on the vertical walls

$I'_{\mathrm{refl.}}$ intensity of single total reflection on the horizontal walls

δ critical angle for total reflection

ε efficiency of total reflection

ϕ_1 the lowest value of quantities γ'_m, δ and α

ϕ_2 the lowest value of quantities γ'_m, δ and arctg (2 tg α)

Ψ the lowest value of quantities γ', δ and β

NUCLEAR INSTRUMENTS AND METHODS 6 (1960) 187–192; NORTH-HOLLAND PUBLISHING CO.

A FAST COINCIDENCE UNIT OF VARIABLE RESOLVING TIME

J. B. GARG

The Physical Laboratories, the University, Manchester, England

Received 1 October 1959

A fast coincidence unit of variable resolving time in the range 0–100 ns is described. The unit is designed to accept pulses of either polarity and uses fast discriminators in order to select the amplitude of the input pulses.

1. Introduction

A coincidence unit of variable resolving time forms an important tool in the study of nuclear physics. A number of coincidence units of such type are available commercially but their resolving times are in the range (0.1 μs–few μs). The coincidence circuits whose resolving times are in the nanosecond range are usually designed for fixed values of time resolution[1–4]). However, in nuclear physics experiments quite often the necessity arises when a coincidence circuit having the resolving time in the nanosecond range together with the possibility of varying it within reasonable limits would offer much greater utility.

Another important need in fast coincidence circuits is the possibility of selecting the amplitude of the input pulses.

The present circuit described here is one which satisfies these requirements. The resolving time of this unit can be varied continuously from 1 ns to 100 ns, with a maximum uncertainty of

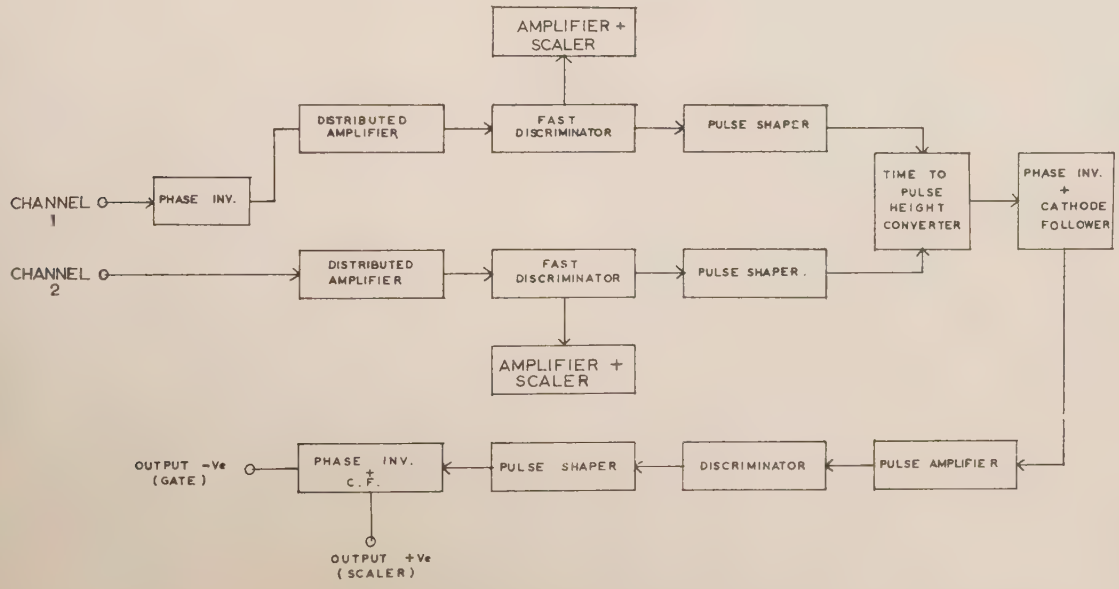

Fig. 1. Schematic block diagram of the coincidence unit.

[1]) J. Fischer and J. Marshall, Rev. Sci. Instr. **23** (1952) 417.
[2]) R. E. Bell, R. L. Graham and H. E. Petch, Canad. J. Phys. **30** (1952) 35.
[3]) D. H. White and G. W. Hutchinson, Nuclear Instruments **1** (1957) 331.
[4]) K. Skarsvåg, Nuclear Instruments **3** (1958) 336.

$\pm$ 1 ns for all settings. Moreover this unit is designed to accept pulses of either polarity of amplitude greater than 0.25 volt and gives a coincidence output pulse of about 60 volt of both polarities, which can be used to operate a gate and a scaler.

2. Principle

In principle this coincidence unit is quite simple and its main features are quite similar to circuits developed by many pioneer workers in this field. However, this present circuit incorporates additional facilities as stated above and, therefore, it was felt necessary to describe it in some detail.

Fig. 1 shows the schematic block diagram of the coincidence unit. The distributed amplifiers used are Hewlett Packard model A and B. The model A gives an output of the same polarity as the input pulse and model B gives an output of the opposite polarity. Hence a single stage phase inverter unit has been built and was used before one of the amplifiers depending upon the polarity of the input pulses chosen. The positive pulses from these amplifiers trigger the following fast discriminator circuits and thus ensures the possibility of amplitude selection of the input pulses. The $-Ve$ pulses at the output of the discriminators are applied to a pulse forming circuit which produces rectangular pulses of fixed duration and amplitude. These pulses in turn are applied to a time to pulse height converter circuit of a conventional type. The coincidence output pulse is amplified by a standard pulse amplifier of gain 10 and is then fed to a discriminator circuit whose bias determines the resolving time of the coincidence unit. The $-Ve$ pulse at the output of this discriminator is used to produce a $+Ve$ and a $-Ve$ pulse of fixed amplitude and duration which can be used for gating and coincidence counting purposes.

3. Circuit Details

Figs. 2 and 3 show the circuit details of the coincidence unit. The various parts are as follows:

3.1. FAST DISCRIMINATOR

This consists of valves V_{2A}, V_{2B} and V_3. It has been designed to accept $+Ve$ pulses of amplitude variable from 2.5 to 25 volt, though the output from the amplifiers reaches a saturation value at about 10 volt. Initially the V_{2B} is in a conducting state and the grid of V_{2A} is maintained at a cut off bias. When a $+Ve$ pulse of proper amplitude depending upon the bias setting of the discriminator is applied at the grid of V_{2A}, this valve starts conducting and a fast trigger action is obtained. The valve V_3 is used in order to increase the speed of this trigger action. In order to limit the output pulse amplitude, the germanium diodes 0A85 are used which clamp the valves for any further rise of the voltages at the anodes.

3.2. LIMITER AND PULSE FORMING CIRCUIT

The limiter circuit consists of a single valve V_4 which is a sharp cut off pentode. Initially this valve is in a conducting state with an anode current of about 13 mA. When a $-Ve$ pulse of amplitude greater than 2.5 volt is applied at its grid, the valve is completely driven to cut off and thus produces a $+Ve$ pulse of about 4.0 volt in its anode load which consists of a 330 Ω inpedence delay cable of delay equal to 50 ns. This pulse is rectangular in shape and of duration 100 ns with fast rise and decay times. A germanium diode is used to eliminate any $-Ve$ undershoot of the pulse.

3.3. COINCIDENCE STAGE

This consists of a single valve V_5 which is a gated beam valve 6BN6 operated at voltages $V_p = V_{g2} = 50$ volt and $V_{g1} = V_{g3} = -3$ volt. The characteristic of this valve is that no anode current flows unless the two control grids are driven positive simultaneously. Hence when the two pulses are applied at its two grids respectively, the anode current flows over a time proportional to the time of overlap of these pulses. This anode current charges the stray capacity of the anode in parallel with an anode load of 100 kΩ which gives an integrating time constant of about 1 μs. Thus the amplitude of

the coincident pulse is proportional to the relative time delay between the two pulses. If the relative delay between the two pulses is zero the output pulse is of maximum amplitude and if the relative delay of the two input pulses is greater than 100 ns, there is no output pulse. This output pulse is amplified and fed to the coincidence resolving time selector.

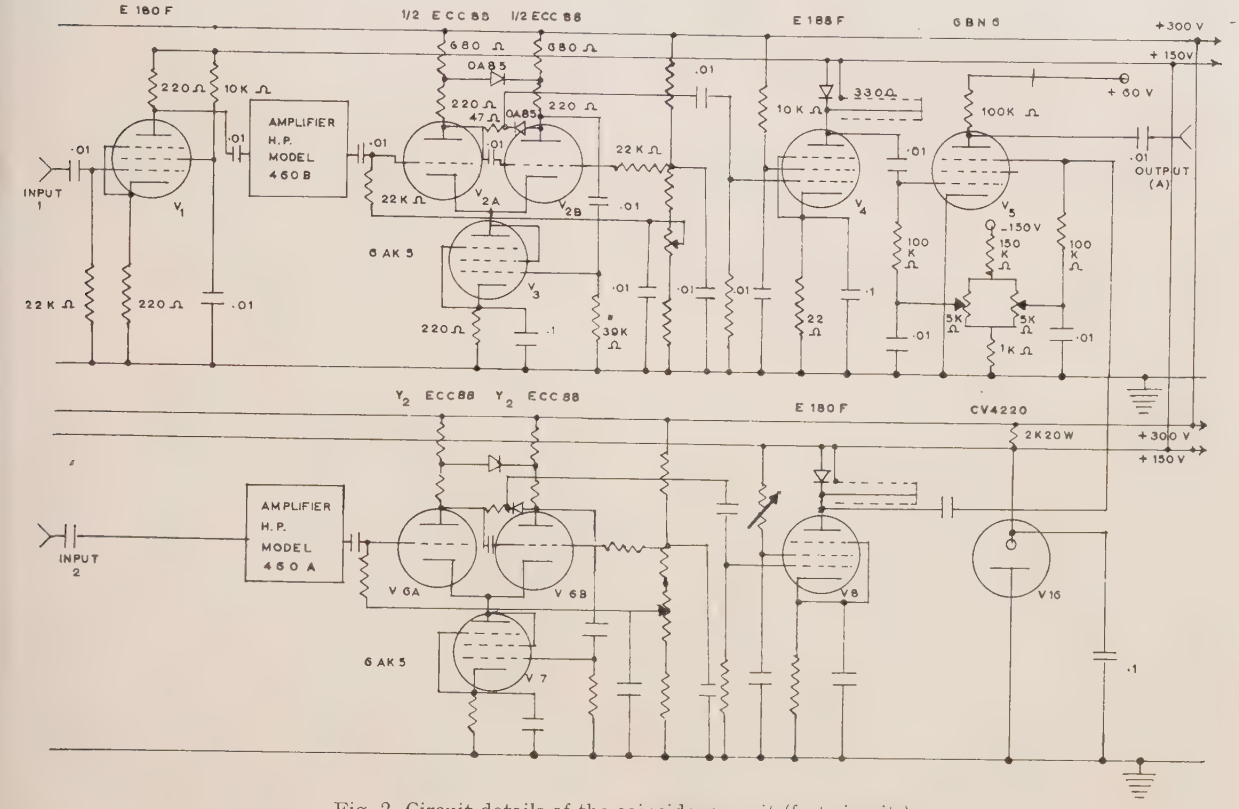

Fig. 2. Circuit details of the coincidence unit (fast circuits).

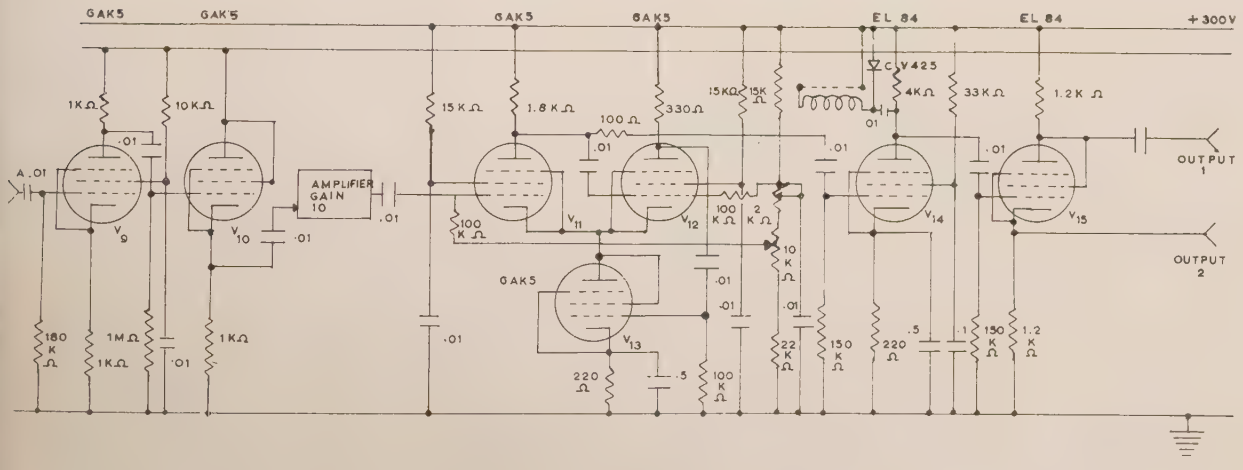

Fig. 3. Circuit details of the coincidence unit (slow circuits).

3.4. COINCIDENCE RESOLVING TIME SELECTOR

This is a discriminator circuit of conventional type consisting of valves V_{11}, V_{12} and V_{13}. The discriminator bias can be adjusted from few

volts to about 40 volt. When a coincidence pulse of proper amplitude depending upon the bias setting of the discriminator is applied, it triggers the discriminator and produces a — *Ve* pulse at the anode of V_{11}. This pulse in turn is applied to a pulse forming circuit.

3.5. SECOND LIMITER AND PULSE FORMING CIRCUIT

The output pulse from the coincidence time selector has a fixed amplitude but variable duration depending upon the amplitude of the input pulse and bias setting of the discriminator. However, in order to be able to operate satisfactorily a gating circuit or a scaler it is essential to have the coincident output pulse of fixed amplitude and duration. Hence it was found necessary to use a limiter and pulse forming circuit after the coincidence resolving time selector. This consists of a single valve V_{14}. Initially this valve is in the conducting state with an anode current of about 30 mA. When a — *Ve* pulse from the previous stage is applied at its grid, it is driven to cut off and thus produces a + *Ve* pulse of about 60 volts amplitude and of a duration fixed by the length of the delay cable connected at its anode. In the present case this was a cable of 5 μs time duration and of characteristic impedence of 4 kΩ.

As the gating circuit of the pulse amplitude analyser used in this laboratory operates by a — *Ve* pulse of amplitude between 25 and 100 volt it was found necessary to use a phase inverter unit following the pulse shaper circuit. This consists of a valve V_{15}. The — *Ve* pulse from the anode of this valve is used as a gating pulse and the + *Ve* output pulse from its cathode is used for scaling purposes.

An output pulse from each channel fast discriminator is suitably amplified to operate standard scalers in order to obtain the counting rates in each channel.

4. Performance

The coincidence unit has been tested with pulses from a mercury relay pulse generator having a sharp rise time and rectangular shape of duration greater than 100 ns. These pulses were applied at the input of the two channels and the coincidence pulse from the amplifier following the time-to-pulse height converter were displayed on a 100 channel amplitude analyser of which the channel width was adjusted to about 0.5 ns time interval. This curve is shown in fig. 4 for two values of relative time delay and gives an average value of time resolution (full width at half maximum) of about 0.5 ns.

5. Calibration

The calibration of pulse height *Vs* relative time delay was done by inserting 100 Ω cables of known delays in one channel and observing the corresponding pulse height. This is plotted in fig. 5 and shows that it is linear within the range (0–100 ns). Secondly the calibration of the coincidence resolving time Vs bias of the coincidence resolving time selector was done by inserting 100 Ω cables of known delays in steps of 10 ns in one channel and adjusting the bias for which the coincidence counting rate was reduced to half the maximum.

6. Stability

An important feature of this coincidence unit is that the coincidence resolving time for each setting of the discriminator bias can be known with an accuracy of $\pm$ 1 ns, which is a very useful requirement for the estimation of random counting rates. Besides the long time stability of the resolving time has been tested over a period of about 12 hours and shows a maximum drift of about $\pm$ 0.5 ns.

The power supplies used in this circuit are standard + 300 volt, — 150 V supplies assembled by the Electronics Laboratory of the Physics Department. The + 150 volt supplies were obtained by using a voltage regulator valve V_{16}.

7. Conclusion

This coincidence unit was used as a slow coincidence unit of variable resolving time in

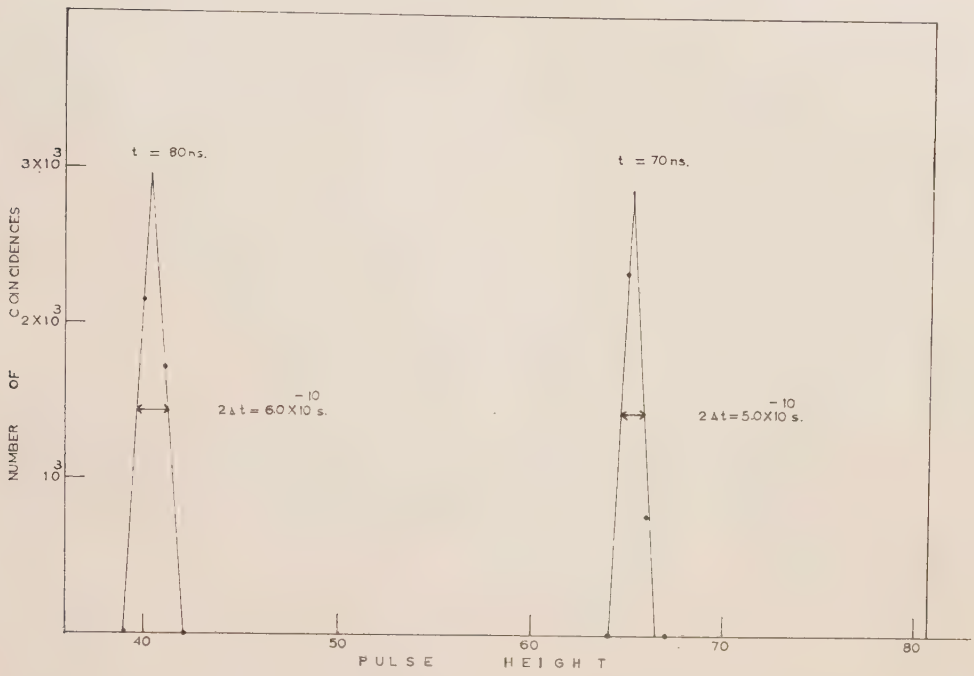

Fig. 4. Coincidence time resolution curve taken with input pulses from a fast pulser.

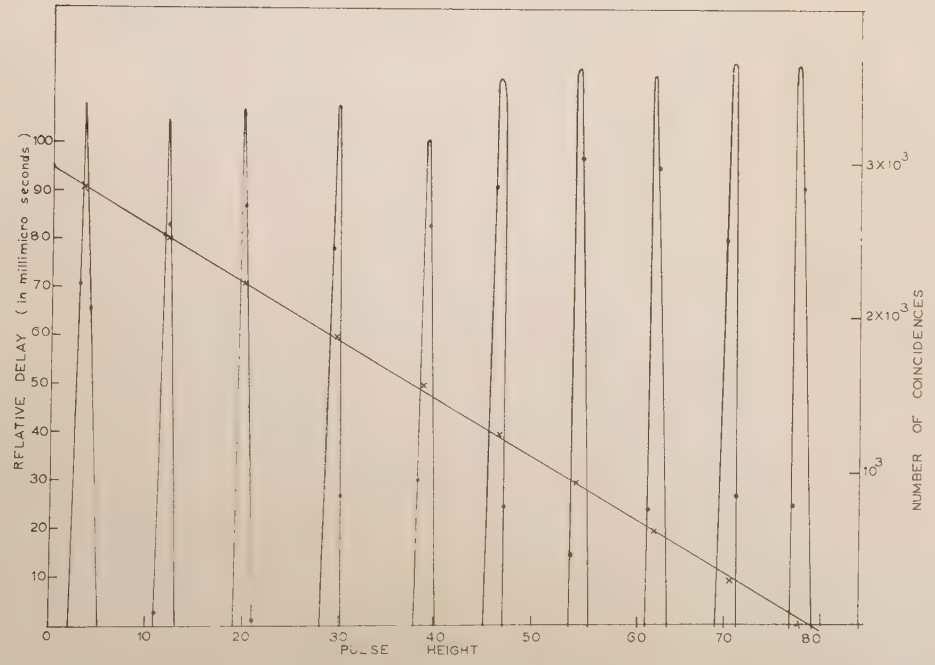

Fig. 5. Calibration curve of the pulse height *vs* relative time delay of the input pulses.

conjunction with a neutron time of flight spectrometer[5]) and gave an improved performance and utility as compared to a commercially available coincidence unit. By using this coincidence unit it was possible to measure the true and random spectrum alternately by suitable adjustment of relative delays in one of the channels of this unit. Besides the ratio of true to random counts in each channel was found to be better. Thus we see that though this unit is quite simple in circuitry it is an useful instrument for research in nuclear physics. However, the performance of this coincidence circuit is limited by the following requirement of the input pulses. The pulses must have very fast rise time and their total duration must be greater than 100 ns. Hence only pulses from fast pulser or fast scintillators and photomultipliers would give the best performance. The time resolution mentioned in the text is that obtained by using pulses from a fast pulser and consequently the time resolution with pulses from a scintillator-photomultiplier combination is expected to be worse depending upon the different combination used.

[5]) J. B. Garg, Nuclear Instruments **6** (1960) 72.

Acknowledgement

I wish to express my gratitude to Dr. D. St. P. Bunbury for his helpful criticism of the manuscript. I gratefully acknowledge the tenure of the Turner and Newall Post-Doctoral Fellowship of the University of Manchester.

NUCLEAR INSTRUMENTS AND METHODS 6 (1960) 193–200; NORTH-HOLLAND PUBLISHING CO.

BEHAVIOUR OF PHOTOMULTIPLIERS AGAINST HIGH-FREQUENCY MODULATED LIGHT

C. CERNIGOI, I. GABRIELLI and G. IERNETTI

Istituto di Fisica dell'Università, Trieste, Italy
Istituto Nazionale di Fisicaà Nucleare-Sottosezione di Trieste

Received 1 September 1959

The frequency-response of several phototubes to light modulated in intensity by an ultrasonic device has been examined. Frequency of light-modulation up to 48 Mc/sec was used. The method can be applied in order to select photomultipliers for fast-counting rates.

1. Introduction

The purpose of this work is the test of photomultipliers with light modulated in intensity, the frequency of modulation covering the range between 4 and 48 Mc/sec. If the degree of modulation is of the order of about 100%, the situation is similar to a continuous repetition of light-pulses, regularly spaced in time at a distance $1/f$, rise and decay time less than $\frac{1}{2}f$ (f = frequency of light modulation). With $f = 48$ Mc/sec, $\frac{1}{2}f$ is of the order of 10 nsec.

It has been investigated whether, in the frequency range considered, the response of the photomultipliers is getting worse or not. The intensity-modulation of light is obtained by the aid of an ultrasonic standing-wave field in a liquid. It is well-known that such a field behaves like a diffraction grating against a beam of light crossing it perpendicularly to the direction of the ultrasonic plane waves. Due to the fact that the diffraction grating disappears at every half-period of oscillation, it results that the light diffracted into any order of fringes is modulated in intensity at a frequency which is twice the frequency of the ultrasonic waves. However, it must be remembered that also progressive ultrasonic waves give rise to a diffraction pattern, but in this case the diffracted light is not modulated in intensity (see appendix). For this reason, care must be taken in order to keep a good stationary ultrasonic field.

2. Experimental Procedure

For frequencies up to 24 Mc/sec, a conventional arrangement can be used, as drawn in fig. 1a. A d.c. supplied mercury lamp, with green filter, will provide a fairly monochromatic light-source. A parallel beam of light is obtained by means of a lens and a slit in its focal plane. The beam is then diffracted by the ultrasonic field normal to it; standing waves are obtained by adjusting the distance between the reflector and the electromechanical transducer, which is a quartz, driven by a conventional R.F. power oscillator, tuned at the resonant frequency of the quartz. A second lens gives the diffraction pattern in its focal plane; a second slit is necessary for single-fringe selection.

The light then hits the photocathode area of the phototube under test, the anode output of which is connected, through a 200-ohm matched cable, to the input of the vertical amplifier of a 545-Tektronix scope. The light beam is intercepted periodically by a rotating disk, 30 cm in diameter, which has a radial window of $\frac{1}{15}$ of radian. In these conditions the light is transmitted only for a time of about 200 μsec, 50 times per second, if the angular velocity of the disk is 3000 rpm.

This method allows high peak-values of the output current with negligible average value and also fixes the position of the dark signal level on the oscilloscope. The degree of modulation is so immediately evaluated and saturation effects or failures of the high voltage divider of the phototube can be easily observed.

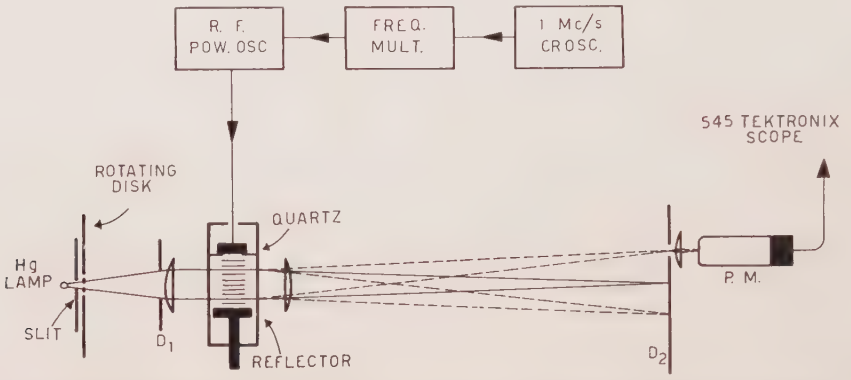

Fig. 1a. Block diagram of the experimental set-up for light modulation up to 24 Mc/sec.

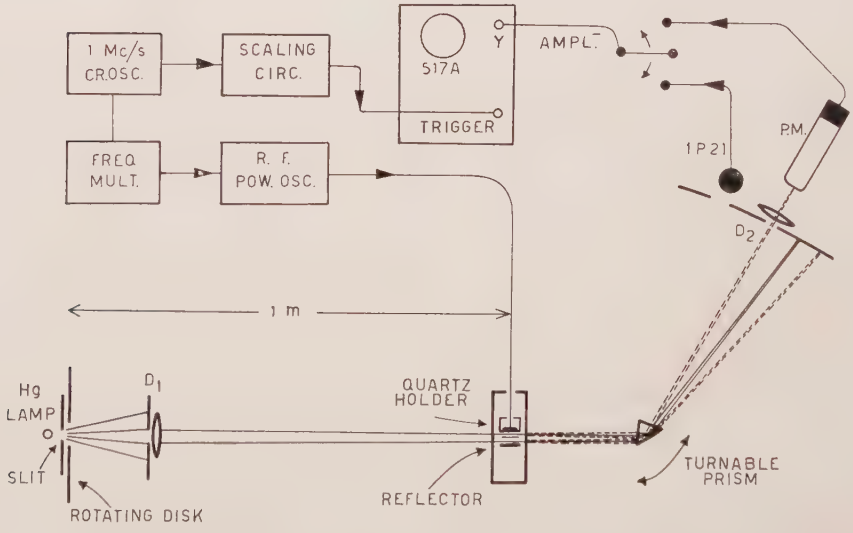

Fig. 1b. Block diagram of the experimental set-up for light modulation above 24 Mc/sec.

The R.F. power oscillator is driven, after suitable frequency multiplication, by a 1 Mc/sec quartz-controlled oscillator.

At frequencies above 24 Mc/sec, the apparatus was slightly modified, as indicated in fig. 1b. The reasons are the following:

(1) Due to the large increase, with frequency, of the ultrasonic absorption in liquids, the space between the transducer and the reflector is reduced to a value of about 1 cm. A slightly convergent light-beam, obtained with one lens only, gives the diffraction pattern in the plane where fringe-selection is performed. It is possible, in this way, to have a rather large luminous flux in the small region between the transducer and the reflector.

(2) The half-wave length of the ultrasonic waves being of the order of $\frac{1}{100}$ of mm, the parallelism between the transducer and the reflector becomes very critical. Three micrometric screws, directly supported by the transducer holder, realize the parallelism fairly well (see fig. 2). The parallelism is adjusted to

the best by keeping the output signal of a RCA-1P21 phototube to its best degree of modulation. In order to give the possibility of

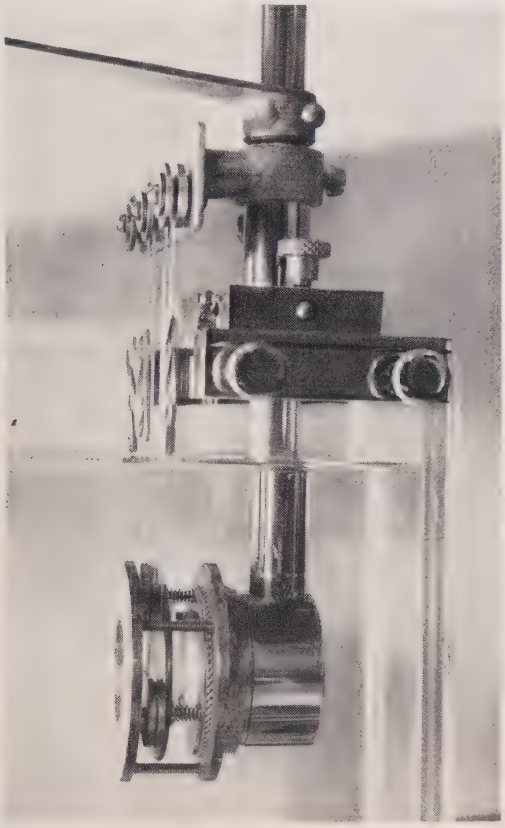

Fig. 2. Quartz and reflector holder. The glass reflector is supported on three points between a spring and a pulley adjustable from outside through nylon wires.

a continuous control of the parallelism, a turnable prism allows the light-beam to be directed either to the reference phototube (RCA-1P21), or to any other under test. The 1P21 is chosen for this control because of his very good frequency-response.

(3) The 545-scope is substituted by a 517-A Tektronix-scope, owing to its better high-frequency response. The anode-load of the phototube is reduced to 90 ohm (200 ohm in parallel with the 170 ohm input of the 517-A-scope). For higher values of the anode-load the waveforms were less clear. In order to synchronize the output signal from the phototube, the 1 Mc/sec signal from the driving oscillator is conveniently demultiplied by means of a conventional fast-scaler and fed to the trigger circuit to the 517-A-scope. The transducer was a 8 Mc/sec quartz, vibrating at the third harmonic (24 Mc/sec); the ultrasonic field-amplitude was large enough in order to obtain two orders of fringes.

3. Experimental Results

At 4 Mc/sec, the response is practically independent of the particular kind of phototube (see fig. 3) the output waveform of a 1P21 is shown. The picture is the superposition of several single-waveforms; the base-line corresponds to the dark-level. (It is kept partly out of the sensitive area of the screen, in order to reduce its brightness.) As it appears from the picture, the degree of modulation is of 100%. The vertical spread of the maxima is mainly due to the statistical behaviour of the phototube. In fact, at this frequency, the number of photons per lightpeak (about 0.25 μsec of duration) is so high that the statistics of the light-source has negligible effect.

The failure of the high-voltage divider requirements is shown in fig. 4, where the envelopes of the 200 μsec light-pulse are presented at increasing light-level. In this case, 100% of light-modulation was avoided in order to have a superposition of continuous and modulated light. The pictures 4a and 4b were taken at low light-level. In the picture 4c the increase of the alternate signal from the beginning to the end of the 200 μsec light-pulse is clearly

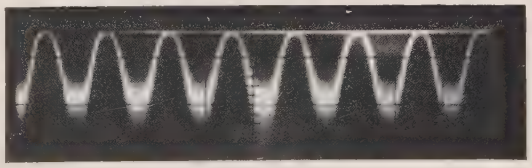

Fig. 3. Example of response at 4 Mc/sec (RCA-1P21, H.V. 1000 V).

visible. This effect, already pointed out by Engstrom and Fischer with static methods[1]), is due to the redistribution of the voltage-loss of

[1]) R. W. Engstrom and E. Fischer, Effect of the voltage-divider on multiplier phototube response, Rev. Sci. Instr. 28 (1957) 525.

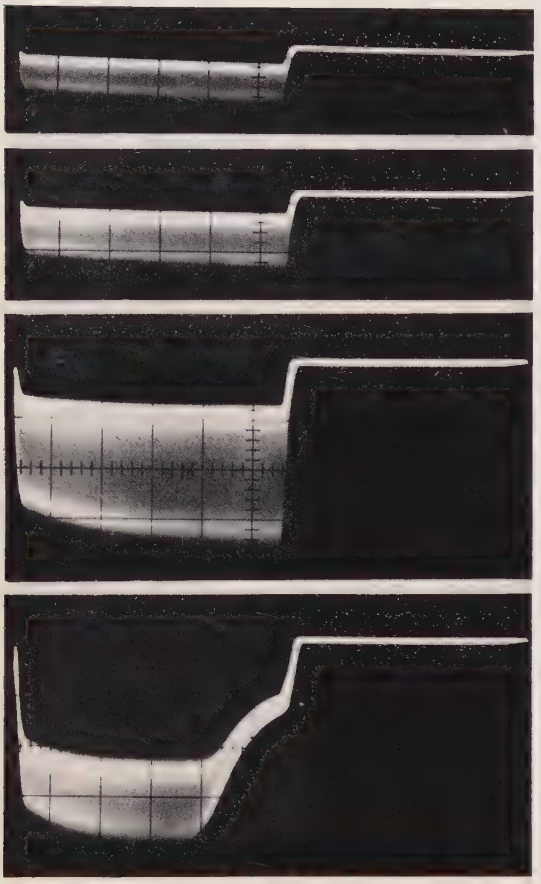

Fig. 4. Failure of the voltage-divider with increasing anode-current. RCA-1P21, H.V. 1 000 V, Light-frequency 10 Mc/sec. light increased from (a) to (d).

the last stage in the divider, which causes the increase in the gain of the first stages more rapidly than the reduction of anode collection-efficiency. Finally, in the picture 4d the above effect is followed by a strong decrease in sensitivity.

The voltage-dividers were chosen as suggested by the phototube manufacturers for the maximum output signal. A schematic list is presented in table A. The voltages of the focalization and acceleration electrodes (if any) were adjusted for the best response.

Measurements were then performed at 10, 30 and 48 Mc/sec. The tubes tested systematically were of the types: RCA-1P21, RCA-6810A and 7264, Dumont-6292, Philips-56AVP. Tubes of the types: RCA-6655A, Philips-50AVP and EMI-9514/b were occasionally tested.

The degree of modulation of the response at 10 and 30 Mc/sec can be kept close to that of the 1P21 for all the phototubes tested by us, except for the Dumont-6292 and the EMI-9514/b; the degree of modulation is still of the order of 100%. For this reason, we prefer to report and discuss only the results at 48 Mc/sec, showing some basic pictures at this frequency, i.e. the responses of the 1P21, 56-AVP, 7264 and 6292 (fig. 5). In the caption, reference is given to the similar behaviour of the other tubes tested.

The main features at 48 Mc/sec are the following:

(1) from the pictures it can be seen that the degree of modulation is lower than 100%, also for the best responses. This fact can be attributed to several causes: slight distorsions of the vertical amplifier, diffuse light collected at the photocathode, non-perfect stationary ultrasonic field and finally the fact that the phototube should have infinite frequency-bandwidth in order to follow exactly the light-intensity variations.

(2) With more intense light the degree of modulation in the response of the RCA-7264 (and 6810A) becomes smaller, showing space-charge saturation effects; this does not occur with the 1P21 and the 56AVP, even at high values of the output current.

(3) The response of the Dumont-6292 and the EMI-9514/b fails down strongly even at very low output current values.

(4) The number of photons per light-peak (about 20 nsec of duration) comes out to be very small, so that larger fluctuations occur in waveform shapes at lower light-levels.

With all phototubes of the head-on photocathode type, the light was focalized on the central point of the photocathode area; no appreciable differences have been observed spreading out the light over the whole photocathode. As above mentioned, the waveforms presented are the superposition of many single waveforms: single and few waveforms were taken with the 1P21 phototube (fig. 6). In picture 6c the small phase-jitter is due to

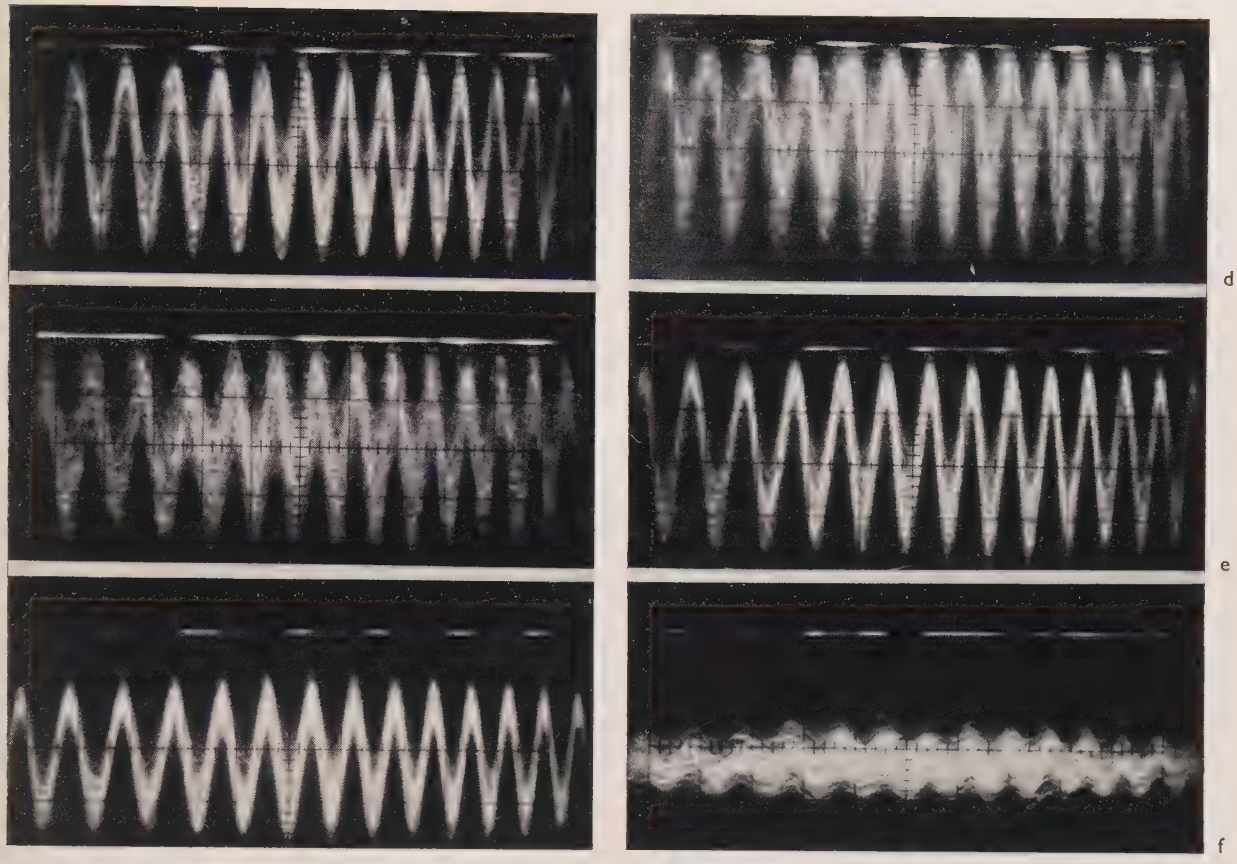

Observations. The peak-current values are calculated taking into account the anode-load (90 ohm) and the peak-to-peak voltage, evaluated from the vertical scope-sensitivity. For every picture, the vertical scope-sensitivity is determined by the value of the attenuator set and the internal calibration of the 517-A scope. Apart from the output current values, the RCA-6655A and the Philips-50AVP give similar pictures to the RCA-1P21, the RCA-6810A similar to those of the RCA-7264 and the EMI-9514/b to those of the Dumont-6292.

Fig. 5. Responses to light modulated at 48 Mc/sec

Type of photomultiplier	Total H.V. (V)	Peak-current (mA) for 200 μsec	Remarks
(a) RCA-1P21	1 000	2.7	strong light
(b) RCA-7264	2 500	8.00	weak light
(c) RCA-7264	2 200	32.0	light increased
(d) Philips-56AVP	2 500	32.0	weak light
(e) Philips-56AVP	2 200	40.0	light increased
(f) Dumont-6292	1 500	2.0	strong light

the high ratio of frequency-scaling. With the same output current, responses to unmodulated light were taken (zero-order of fringes, no ultrasound), showing clearly the need of several single waveforms in order to distinguish between modulated and unmodulated light. The pictures of fig. 6) were taken without the rotating disk in order to avoid the presence of reduced signals during the rise- and decay-time of the 200 μsec. light-pulse.

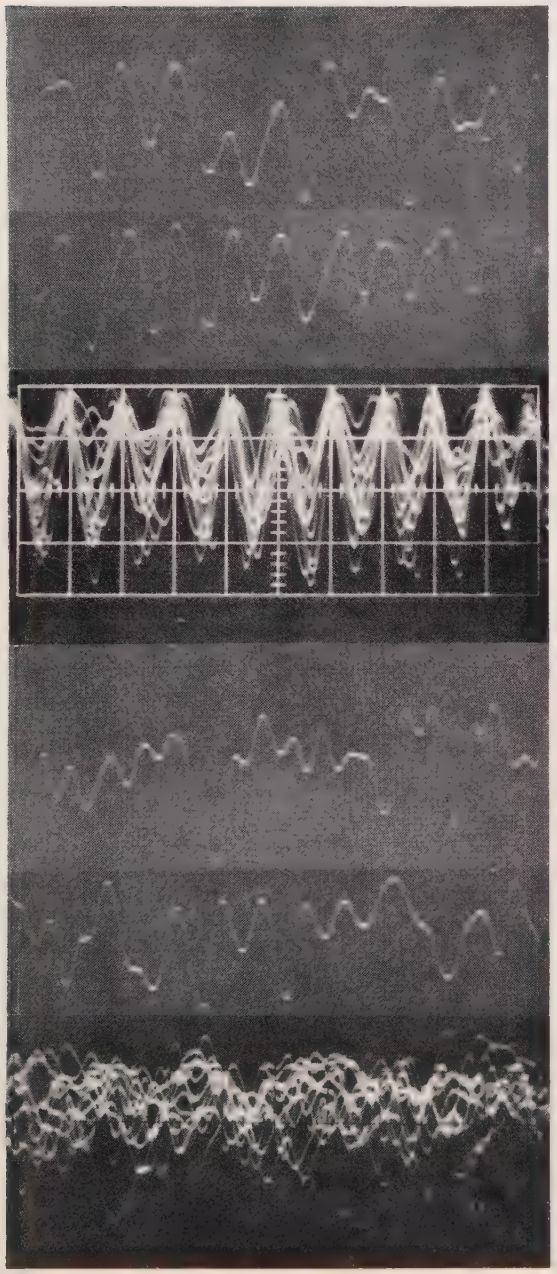

Fig. 6. Detailed response of the RCA-1P21: to light modulated at 48 Mc/sec: (a) single waveform; (b) selected single waveform; (c) few waveforms; to unmodulated light: (d), (e) single waveforms; (f) few waveforms.

4. Conclusions

The main conclusion which can be drawn from these results is that, even at the rather low value of frequency of 48 Mc/sec, there are some differences in the behaviour of the phototubes tested by us. Apart from the very poor frequency-response characteristics of the Dumont-6292 and the EMI-9514/b, the best phototubes seems to be the RCA-1P21 and the Philips-56AVP. We point out that this 14 stages tube can be adjusted to give a high-output response with a degree of modulation equal to that of the 1P21. The RCA-6810A and 7264 are somewhat less suitable, if concerned with the possibility of delivering high-level signals.

It would be interesting to compare these results with those which can be obtained by means of single short light-pulses from a hydrogen-lamp[2]). This will be done in a paper to be published shortly.

Finally, it comes out the possibility of studying experimentally the statistics of phototube-outputs. For this it would be necessary to synchronize also the 200 μsec light-pulse with the time-base of the oscilloscope. This can be accomplished either by gating the trigger signal with an auxiliary phototube, which takes the integral of the light-pulse, or by synchronizing the rotating disk by a suitable submultiple of the 1 Mc/sec, driving signal.

Appendix

The optical properties of a medium with refractive index n, are changed by the presence of an ultrasonic field; the refractive index is no longer constant but varies from point-to-point in the medium.

If we consider only a plane wave propagation of the ultrasounds, the variations Δn, of the refractive index are represented by the expression:

$$\Delta n = \Delta n_0 \sin 2\pi \left(\nu t - \frac{x}{\lambda_u} \right) \qquad (1)$$

where:

Δn_0 = maximum variation of the refractive index
ν = frequency of the ultrasounds
λ_u = wavelength of the ultrasounds.

In other terms, this is equivalent to having a medium with refractive index varying in space

[2]) J. H. Malmberg, Millimicrosecond duration light-source, Rev. Sci. Instr. **28** (1957) 1027.

according to the law: $\Delta n = \Delta n_0 \sin 2\pi x/\lambda_u$ and moving in the direction of the ultrasounds with the velocity: $v = \lambda_u \nu$.

A medium whose refractive index varies according to (1) acts as a "phase diffraction grating" against light-beams crossing it. Due to the small value of the ratio v/c (c = velocity of light), a theory of such a grating can be developed under the hypothesis that the grating itself is fixed in space.

As concerned with the light-intensity distribution in the various orders of fringes, the result is given by the theory of Raman and Nagendra-Nath[3]): the intensity, I_k, of the light diffracted in the k^{th}-order fringe, is given by:

$$I_k = CJ^2_k \left(\frac{2\pi l \Delta n_0}{\lambda_c}\right)$$

where:

C = a constant
J_k = Bessel function of the k^{th}-order
l = path of the light in the ultrasonic field
λ_c = light wavelength
Δn_0 = maximum variation of the refractive index, which is proportional to the ultrasonic field amplitude.

The effect of the movement of the grating is only a Doppler shift of the frequency of the diffracted light.

It must be pointed out that, if a large number of ultrasonic wavelengths are intercepted by the light-beam, the light in the various orders of diffraction is not modulated in intensity because the diffraction grating is present at every time. Only if the number of wavelengths intercepted by the light-beam is very small, light-modulation does occur at a frequency which is the same as the frequency of the ultrasounds. This particular kind of light-modulation was first discovered and discussed by Bär[4]). In this case, light-modulation is present either with progressive or standing ultrasonic waves.

In the case of standing waves, it is easy to demonstrate that, also with a light-beam intercepting a large number of wavelengths, light-modulation does occur. In fact, the plane diffraction grating is not travelling but it is varying in time and the variations of the refractive index can be represented by the expression: $\Delta n_0 = \Delta n_0 \sin 2\pi\nu t$, Δn_0 is zero at every half-period of oscillation and at that moment the light is not present in the fringes different from the zero-order.

For the exact evaluation of the light-intensity variations in the various orders, the same expression of Raman and Nagendra-Nath[3,5]) can be used, taking into account the fact that Δn_0 must be substituted by: $\overline{\Delta n_0} \sin 2\pi\nu t$.

Finally, the intensity of light in the various orders can be evaluated by the following formula:

$$I_k(t) = CJ^2_k \left(\frac{2\pi l}{\lambda_c} \overline{\Delta n_0} \sin 2\pi\nu t\right).$$

The Fourier analysis gives a strong component of the frequency 2ν for $I_1(t)$, if the argument variations are limited to values less than the first maximum of $J_1(t)$. Therefore, the simplest way to obtain light-modulation is to select a first-order fringe and to keep the ultrasonic field-amplitude in the limits corresponding to the above mentioned conditions. This was done in the present work, where the reported light-frequencies, f, are 2ν.

In the arrangement of fig. 1b, the slightly convergent light-beam behaves as parallel; the cross-over of the light-beam in the ultrasonic field has to be avoided, otherwise the frequency of modulation would be ν as before mentioned.

The extension of the argument variations to the second maximum of J_1 gives a light-modulation with a high component of the frequency 4ν. Also the zero-order fringe is modulated at 100% if the argument variation brings J_0 to its first zero.

By inspection of the square of the Bessel functions, it is easy to verify that different kinds of light-modulation can be obtained; e.g. if a higher-order fringe is selected, light-pulses are obtained at a repetition rate equal to the

[3]) C. V. Raman and N. S. Nagendra-Nath, The diffraction of the light by high-frequency sound waves, Proc. Ind. Acad. Sci. Part I-II, 2 (1935) 406 and 413; Part III, 3 (1936) 75.

[4]) R. Bär, Über Lichtmodulation durch fortschreitende Schallwellen, Helv. Phys. Acta Bd. 9 (1936) 367.

[5]) For a summary of ref. [3]) and useful diagrams, see: L. Bergmann, Der Ultraschall (Hirzel, Zürich, 1954), p. 282 ff

frequency of the light modulation but with duration reduced to a small fraction of the half-period of oscillation.

However, in this case, larger ultrasonic field-amplitudes are required which are not easily obtained at higher frequencies.

TABLE A

Voltage dividers

Type of phototube	Total high-voltage V	Current (mA) in the divider at the voltage V	Resistance ratio (from cathode to anode)	Capacity (pF) on the last dynode†
RCA-1P21	1 000	1	1:1:1:1:1:1:1:1:1	30 000
RCA-7264 and RCA-6810A	2 400	6.6	RCA voltage-divider arrangement for "high output pulse service"	40 000
Philips-56AVP	2 500	5	Philips, Type "B", voltage-divider arrangement	50 000
Dumont-6292	1 500	5	3:2:2:1:1:1:1:1:1:1	100 000

† Capacities are decreasing by a factor $\frac{1}{2}$ from ground to cathode.

NUCLEAR INSTRUMENTS AND METHODS 6 (1960) 201–205; NORTH-HOLLAND PUBLISHING CO.

A NEW SOLUTION OF THE FINITE RISE TIME PROBLEM BY MEANS OF A DISTRIBUTED AMPLIFIER WITH AUTOMATIC GAIN CONTROL†

B. JOHANSSON

Nobel Institute of Physics, Stockholm 50

Received 8 September 1959

In a distributed amplifier the output pulse is built up by the addition of pulses from subsequent stages. If this sum-up is stopped when the pulses have reached a certain pulse-height level then the out-put pulses will have the same height and, what is essential in time measurements, the same shape independent of the height of the input pulse within a certain pulse-height range.

A distributed amplifier based on this principle is described. It consists of 2 cascaded 5 tubes amplifiers (rise-time 8 ns) and covers a pulse-height range of 15 dB. By a conveniently chosen combination of number of tubes and cascaded amplifiers, any desired pulse-height range can be covered. The amplifier can be built for fast as well as slow phosphors.

1. Introduction

In time measurements involving scintillators and photomultipliers the main problemis to obtain a precise time determination with pulses of different pulse-heights. In cases when a large pulse-height range is involved with the measurements the finite rise-time becomes a problem also for fast phosphors. Many attempts have been made to solve this problem especially for slow phosphors. Some solutions are reviewed by Gruhle[1]).

A method to solve this finite rise-time problem is by use of an automatically gain-controlled amplifier, the output pulses of which are of the same height and the same shape independent of the input pulse-height. A very suitable type of amplifier for this purpose is the distributed amplifier because of the fact that the output pulses from such an amplifier are formed by the addition of equally shaped pulses from subsequent parallel coupled stages. By stopping the sum-up when the pulses have reached a certain height, the required conditions are satisfied.

2. Principle

The amplifier described here is a distributed amplifier supplied with automatic gain control. The tubes used are dual-controlled pentodes of the type 6AS6. A principle diagram of the amplifier is shown in fig. 1.

The pulses travelling on the anode line are lengthened and fed to the third grids of the 6AS6 tubes twice the rise-time before the input pulses appear at the first grids. Thus the anode pulses have time to adjust the amplification of the succeeding tubes before the first-grid pulses appear. The amplification can be determined in the following way. If it is assumed that the cut off of the tubes is sharp, the pulses appearing at the anodes will have pulse-heights in accordance with those indicated in fig. 1. The amplification in each stage will be decreased by a factor $(V_0 - V_v)/V_0$, where V_v is the height of the pulse at the preceeding anode and V_0 the cut off level for the third grid of 6AS6. Thus when V_v has reached the value V_0 the amplification in the following stages will be zero and the output pulse will have the height V_0. The output pulse of an ideal circuit will have the following height:

[1]) W. Gruhle, Nuclear Instruments 4 (1959) 112–114.

† This work was supported by the Research Institute of National Defence, Stockholm 80, Sweden.

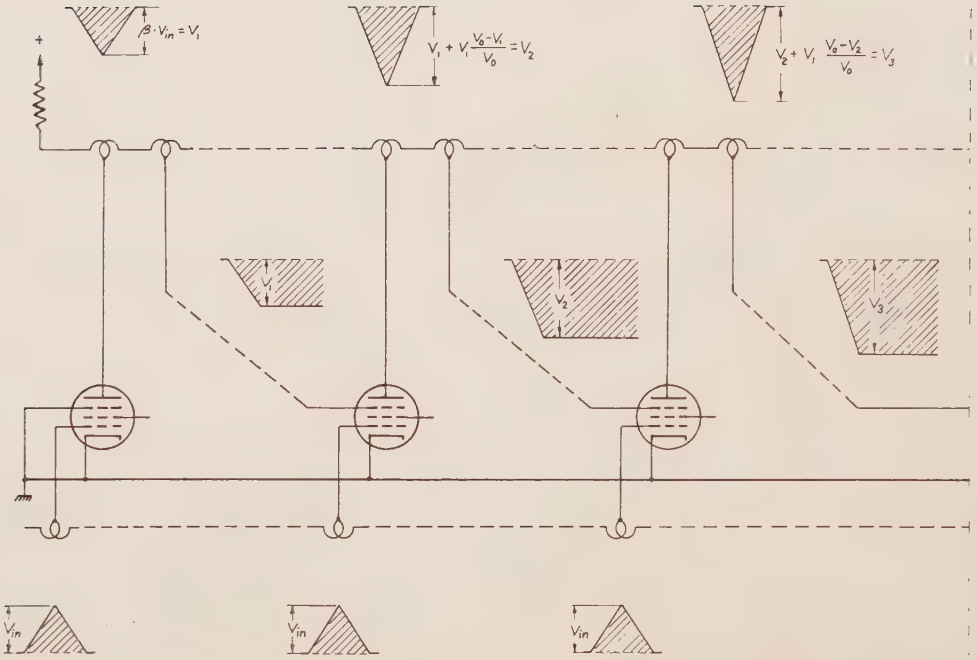

Fig. 1. Principle diagram of the automatic gain controlled distributed amplifier. The tubes are dual controlled penthodes of the type 6AS6. The D.C. voltage on the grid delay-line is set just on the cut off level of the tubes. The third grids have zero potential.

$$V_{out} = \beta V_{in} + \beta V_{in} \frac{V_0 - \beta V_{in}}{V_0} + \beta V_{in} \frac{V_0 - \beta V_{in}\left(1 + \frac{V_0 - \beta V_{in}}{V_0}\right)}{V_0} + \cdots$$

$$= \beta\alpha V_0 (1 + (1 - \alpha\beta) + 1 - \alpha\beta (2 - \alpha\beta) + \cdots$$

$$= \beta\alpha V_0 (1 + (1 - \alpha\beta) + (1 - \alpha\beta)^2 + \cdots (1 - \alpha\beta)^{n-1}$$

$$= V_0 (1 - (1 - \alpha\beta)^n) \; ; \quad \text{for} \quad 0 \leqslant \alpha\beta \leqslant 1 \; . \qquad (1)$$

For $\alpha\beta \geqslant 1$ eq. (1) reduces to $V_{out} = V_0\alpha\beta$ where

V_{out} = output pulse-height
V_{in} = input pulse-height
V_0 = cut off level for the third grid of 6AS6
β = the amplification in each stage
α = V_{in}/V_0 = relative input pulse-height
n = the number of stages.

If n is made large, then $V_{out} \simeq V_0$ independent of the input pulse-height. In practice it is not convenient to make n large, because this means a large number of tubes. A minimum for the number of tubes can be obtained in the following way.

If, for example, two matched amplifiers (the same V_0 and β) are cascaded, then the height of the output pulse of the second amplifier will be:

$$V_{out} = V_0 (1 - (1 - \alpha\beta)^{n2}) \; ;$$

where $\alpha\beta$ is the relative input pulse-height of the first amplifier. If p matched amplifiers are cascaded, the output pulse of the p^{th} as a function of the input pulse-height of the first one will be:

$$V_{out} = V_0 (1 - (1 - \alpha\beta)^{np}) \; ; \qquad (2)$$

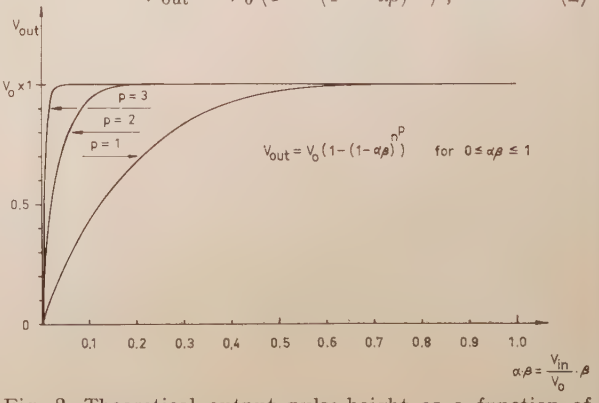
V_{out}
$V_0 \times 1$
0.5
0
p = 3
p = 2
p = 1
$V_{out} = V_0 (1 - (1 - \alpha\beta)^{np})$ for $0 \leq \alpha\beta \leq 1$
0.1 0.2 0.3 0.4 0.5 0.6 0.7 0.8 0.9 1.0
$\alpha\beta = \frac{V_{in}}{V_0} \cdot \beta$

Fig. 2. Theoretical output pulse-height as a function of input pulse-height, for three different values of p, for a five tubes amplifier ($n = 5$). p indicates the number of amplifiers in cascade.

Fig. 2 shows the function (2) for $p = 1$, 2 and 3 and $n = 5$.

The number of tubes (S) required to obtain a certain regulation factor (K) is determined by the equation

$$S = np + A\,(p - 1) = K^{1/p}p + A\,(p - 1)\,; \quad (3)$$

where A = number of tubes in the phase inverting stages connecting the cascaded amplifiers.

$$K = n^p = \frac{\log\left(1 - \frac{V_{out}}{V_0}\right)}{\log\,(1 - \alpha\beta)} = \frac{-\log 100}{\log\,(1 - \alpha\beta)}\,;$$

$$K \simeq \frac{2 \log 10}{\alpha\beta}\,.$$

for $\alpha\beta \ll 1$. The value of K determines for which α the output pulse has reached 0.99 V_0. At this point $\alpha\beta \simeq 4.6/K$.

The curves a, b and c in fig. 3 show the function ($S(p)$) for 3 different values of K. From this curve the most convenient values of n and p can be chosen. It appears that a considerably high regulation factor can be obtained with a relatively small number of tubes. For example, with 19 tubes ($n = 5$, $p = 3$ and $A = 2$), a regulation factor of $K = 125$ will be obtained. This means that input pulses between 0.04 V_0 and V_0 will all give output pulses between 0.99 V_0 and V_0.

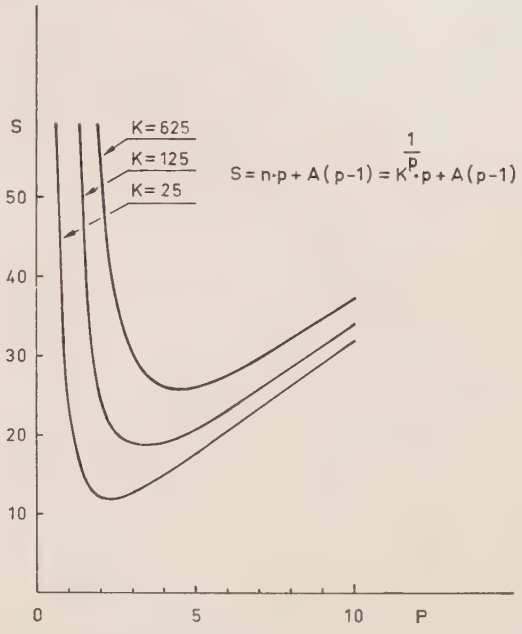

Fig. 3. Total number of tubes as a function of the number of cascaded amplifiers for three different values of K and $A = 2$. From these curves convenient values of S and p can be found.

3. Experimental Testing of the Principle

Fig. 4 shows a complete diagram of a 5 tubes amplifier. The tubes used are dual-controlled pentodes of the type 6AS6. This type is the only one with considerably high mutual conductance and at the same time small stray

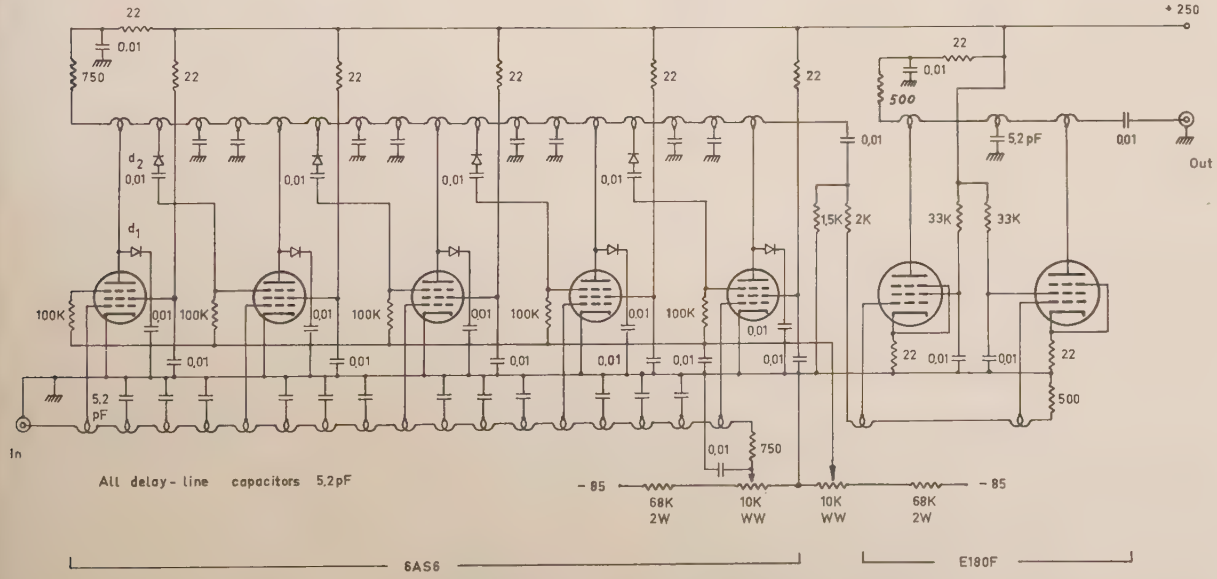

Fig. 4. Complete diagram of a 5 tubes automatic gain controlled distributed amplifier with a rise-time of about 8 ns. The crystal diodes have a rise-time of about 5 ns and are made at the Swedish research institute of semiconductors.

capacitances especially between the third grid and the anode. A disadvantage is that the cut-off with respect to the third grid is rather unsharp.

The anode and the grid lines have both an impedance of 750 Ω. This value was chosen to give an amplification factor of $\beta = 1$ for each stage. The inter-stage delay is about 15 ns in order that the negative anode-pulse shall have time to adjust the amplification in the next tube before the grid pulse appears. The D.C. voltage of the grid line is set just above the cut off level of the tubes (about 7 V) so that the negative pulse on the third grid shall give rise to as small a positive pulse as possible on the anode. This pulse is then taken away by the short circuiting diodes d_1. The output pulse-height (V_0) can be changed by adjusting the D.C. voltage on the third grids. The best condition is obtained when the potential of the third grids is a few volts negative. Fig. 5 shows the output pulse-height as a function of the input pulse-height. Curve a is the experimental curve, while curve b is the corresponding theoretical one.

For $V_{in} \geq 7$ (corresponding to $\alpha\beta \geq 1$) the output pulse will be equal to V_{in}, if $\beta = 1$, because all tubes but the first one are cut-off. For $\beta \leq 1$ is $V_{out} \leq V_{in}$ independent of the number of cascaded amplifiers. Thus no saturation effects will appear provided that the input pulse of the first amplifier is $\leq V_0$. It appears from fig. 5 that two 5 tubes amplifiers cover a pulse-height range of about 15 dB. One more amplifier added should increase this figure by a factor of two. The measuring pulses had a duration of 10 ns and were obtained from a mercury switch pulse-generator with a rise-time of about one ns. The convenient pulse-duration is determined by the inter-stage delay. If it exceeds twice this value there will be a sum-up on the anode-line also in the direction towards the input which will destroy the shape of the output pulse. Because the cut-off of the tubes is not sharp enough, the experimental curve will differ from the theoretical one at the knee. Another reason for this effect is the damping in the anode line caused by the coupling diodes d_2. Because these diodes are not conducting during the back action of the pulse, the delay of the leading edge will be larger than the delay

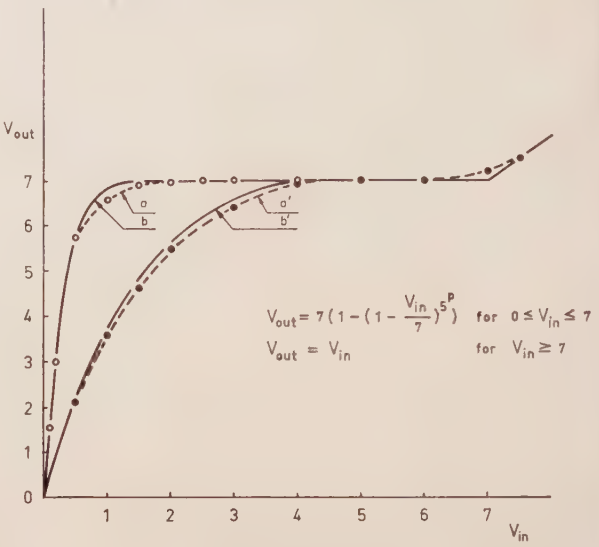

Fig. 5. The output pulse-height as a function of the input pulse-height. Curve a is the experimental curve and curve b the theoretical one for two 5 tubes amplifiers in cascade. a′ and b′ are the corresponding curves for one of the two amplifiers. No time-spread for output pulses larger than $0.99\,V_0$ was measureable with the oscilloscope used (20 ns/cm).

of the back edge, which results in a decrease of the pulse-height. In a further development of the amplifier, a different type of coupling element will be used which also permits smaller inter-stage delay. A secondary emission tube, which can give the desired output polarity, should be suitable for this purpose.

The amplifier has been tested as pulse-former in a time-of-flight arrangement at the Nobel Institute of Physics. In this arrangement a time to pulse-height converter of the Cranberg type is used. The input circuit of this converter consists of a discriminator which causes a time-spread corresponding to the variation of the pulse-height of the input pulses. By the use of the automatically gain-controlled amplifier the width at half maximum of the γ-peaks in the neutron experiments was reduced by 2 ns to at best about 3 ns. In this comparison measurement a pulse-height range of about 15 dB was accepted by the converter. The

γ-rays were detected by a plastic scintillator, the pulses of which formed start-pulses for the converter. The stop-pulses were taken from the cyclotron high-frequency source.

By changing the time-delay of the anode and grid-lines, the amplifier can be used also for pulses from slow phosphors e.g., NaI(Tl). An amplifier for this purpose is under construction at the Nobel Institute of Physics. It will have an inter-stage delay of 0.1 μs. A shorted stub in the input circuit of the first amplifier reduces the pulse duration to about 0.16 μs. The amplifier will be built in separate units, each containing 5 tubes plus one phase-inverter tube, in order that the convenient number of cascaded units for the actual purpose can be chosen.

NUCLEAR INSTRUMENTS AND METHODS 6 (1960) 206–208; NORTH-HOLLAND PUBLISHING CO.

ATTAQUE DES TUBES COMPTEURS EZ-10 PAR TRANSISTORS

P. F. GUTMANN et D. T. JOVANOVIĆ†

Centre d'Etudes Nucléaires de Saclay, Gif-Sur-Yvette, S. & O.

Received 21 September 1959

The authors describe two circuits suitable for the operation of counting tube type EZ 10. The first of these is a monovibrator supplied by a high voltage transformer and incorporates four transistors (PNP and NPN), and operates up to a frequency of 250 Hz with small consumption.

The second circuit is simpler, working on the principle of a blocking oscillator, the transformer of which has an additional high voltage winding; the upper limit of the frequency used (50 kHz) is imposed by the maximum power dissipated in the transistor.

1. Introduction

Le taux de comptage susceptible d'être atteint par les tubes compteurs décimaux à remplissage gazeux est essentiellement imposé par le temps de transfert de la décharge, la limite supérieure étant de quelques dizaines de kHz. Cependant, le tube décade miniature ELESTA EZ10 (de fabrication Suisse), permet d'obtenir dans de bonnes conditions de sécurité, une vitesse de comptage supérieure à 200 kHz en régime périodique. Le constructeur indique une limite de 300 kHz lorsque les impulsions d'attaque subissent une mise en forme convenable, mais garantit l'exploitation du tube pour une fréquence n'excédant pas 100 kHz.

Le but de cet article est de présenter la description des circuits constitutifs d'une échelle à tubes EZ10; une attention spéciale a été consacrée à l'étage d'entrée qui doit satisfaire aux éxigences de cette lampe pour obtenir la fréquence maximum de fonctionnement. Les étages suivants, de fréquençes de travail moins élevées, reposent sur l'emploi d'oscillateurs bloqués, dont le principe a déjà été appliqué à la commande de tubes compteurs à remplissage gazeux[1,2]).

2. Etage d'Entrée

Les conditions imposées au circuit d'attaque sont les suivantes:

tension d'alimentation: $\leqslant 12$ V;
amplitude de l'impulsion de sortie: $\simeq -80$ V;
durée de l'impulsion de sortie: 2 à 3 μs;
temps de résolution: $\leqslant 5$ μs;
consommation et nombre de transistors minimum;
fonctionnement indépendant de la température.

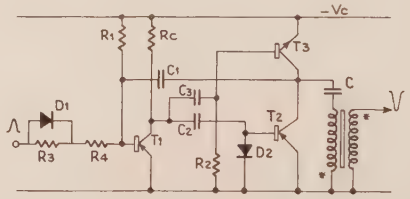

Fig. 1

Tandis que l'oscillateur bloqué satisfait à toutes ces éxigences pour des fréquences relativement basses (< 50 kHz), le montage de la figure 1 répond à l'ensemble des conditions dans toute la gamme intéressée. Le circuit d'entrée de l'échelle comporte deux parties qui seront étudiées successivement:

le monovibrateur;
le transformateur de commande.

2.1. CIRCUIT MONOVIBRATEUR

Le montage comporte une association de transistors PNP (T_1, T_2) et NPN (T_3) et son

† Détaché à Saclay par l'Institut des Sciences Nucléaires "Boris Kidrich", Belgrade, Yougoslavie.

[1]) J. B. Warman, Transistor Circuits for use with Gas-filled multicathode counter valves, Electronic Engineering (1958 march) 136.

[2]) G. B. B. Chaplin *et al.*, Dekatrons and Electromechanical Registers operated by transistors, Proc. of IEE, part B, 105, Nb. 21 (1958 may) 231.

fonctionnement est semblable à celui du monovibrateur ordinaire[3]). Dans l'état stable, T_1 et T_3 débitent, polarisés à travers R_1 et R_2 tandis que T_2 est maintenu non conducteur par l'intermédiaire de la diode D_2. Une impulsion positive appliquée dans la base de T_1 bloque celui-ci et la variation de tension négative subie par le collecteur est transmise par C_2 et C_3 aux bases de T_2 et T_3, ouvrant T_2 et fermant T_3.

Le potentiel du point commun A des collecteurs tend vers zéro, tandis que la boucle de réaction positive est fermée à travers C_1, en provoquant la transition rapide du circuit dans

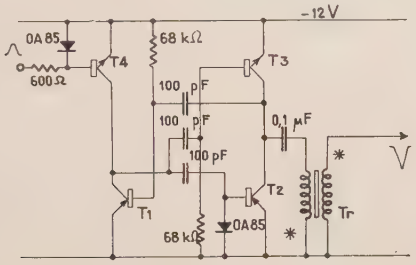

T1-0C44 2N 317 2N 136
T2-0C44 2N 317 2N 136
T3- 2N 168 A
T4- 2N 168 A
Tr - 40×600 sp N° 558

Fig. 2

l'état quasi stable. La durée de cet état est déterminée par la constante de temps R_1C_1. Lorsque la base de T_2 atteint le potentiel de déblocage, le circuit retrouve rapidement son état stable. Le résultat des 2 transitions est l'apparition d'une impulsion positive en A. Du fait qu'il existe toujours un transistor dans l'état conducteur (soit T_3, soit T_2, soit T_2 et T_3 pendant la transition), le point A demeure toujours sous basse impédance.

Afin d'éviter l'influence de l'impédance interne de la source des impulsions de commande, on utilise le circuit modifié représenté par la figure 2, dans lequel le réseau R_3, R_4, D_1 du schéma initial a été remplacé par un transistor NPN T_4. Dans ce cas, une meilleure précision sur la durée de l'impulsion délivrée par le monovibrateur est obtenue, la polarisation de la base de T_1 étant alors rendue indépendante des conditions de l'attaque. La figure 3 reproduit la forme des signaux observés.

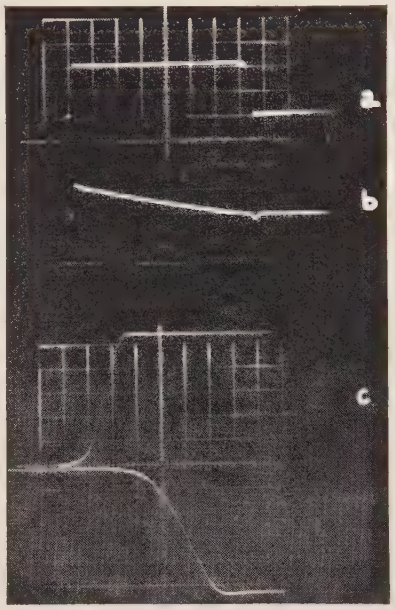

Fig. 3. a = Collecteurs communs de T_2 et T_3 en A (5 V/cm, 0.4 μs/cm); b = Base de T_1 (5 V/cm, 0.4 μs/cm); c = Temps de montée et de descente de l'impulsion en A (2 V/cm, 0.04 μs/cm).

2.2. TRANSFORMATEUR DE COMMANDE

L'amplitude du signal délivré par le monovibrateur n'est pas suffisante pour commander le tube EZ10. L'impulsion négative nécessaire est fournie par l'intermédiaire d'un transformateur élévateur (fig. 1 et 2) qui charge les transistors T_2 et T_3. Comme la durée du signal

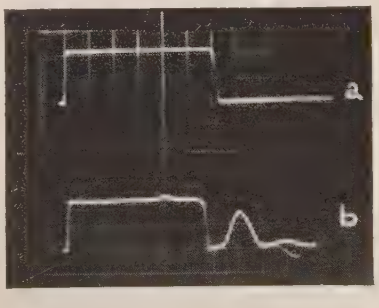

Fig. 4. Impulsions aux collecteurs communs (point A) a = Sans charge (2 V/cm, 0.5 μs/cm); b = Avec charge (EZ 10) (2 V/cm, 0.5 μs/cm).

[3]) D. T. Jovanović, Multivibrator Circuits using PNP and NPN Junction Transistors, Electronic Engineering (1959 may) 301 (lettre).

est déterminée par les constantes de temps du circuit, la valeur de l'inductance de l'enroulement primaire n'est pas critique et par suite, la construction du transformateur est simplifiée †. Il suffit d'éviter les distorsions de l'impuslion transmise. La figure 4 montre l'influence du transformateur chargé sur la forme des signaux du monovibrateur.

Le tableau suivant indique la valeur de la consommation en courant mesurée pour différentes fréquences de fonctionnement du circuit:

f (kHz)	i (mA)
0	0.34
0.1	0.35
1	0.4
10	1.4
33	3.2
100	5.8
200	8.5

3. Circuit de Couplage et Etages Suivants

Le schéma détaillé du circuit de couplage est montré sur la figure 5. Au repos, le transistor T_5 conduit; il peut être bloqué par le signal positif

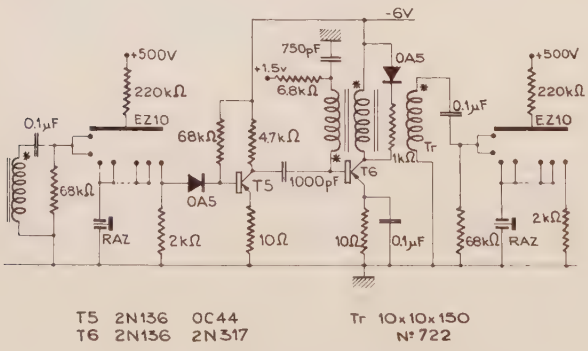

Fig. 5

recueilli dans la cathode du tube précédent et fournit alors dans son collecteur un signal négatif qui après dérivation, attaque l'étage suivant consitué par un oscillateur bloqué. La puissance importante dissipée dans le transistor limite à 50 kHz la fréquence maximum d'utilisation de ce dernier circuit bien que le temps de résolution obtenu soit égal à 7 μs.

† Circuit LTT-1002 – D4904 – 80 × 600 spires (CEA 558).

†† Circuit LTT-1002 – D4904 – 10 × 10 × 230 spires (CEA 708).

Toutefois, le même montage, équipé d'un groupement de 2 transistors en cascade (transistor composite) permet d'atteindre un temps de résolutions de 4 μs.

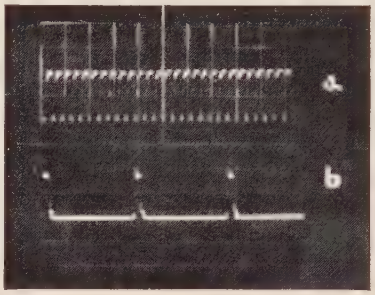

Fig. 6. a = Guides du tube EZ 10 (50 V/cm, 150 kHz); b = Cathode de sortie du tube EZ 10 (1 V/cm, 150 kHz).

Contrairement au cas précédent, le transformateur à 3 enroulements utilisé, exige un certain soin pour sa construction, car de lui dépend en partie, la durée de l'inpulsion créée dans le circuit †.

La figure 6 montre la forme du signaux de commande et des signaux de sortie du tube EZ10.

4. Conclusion

Les schémas décrits ci-dessus ont été utilisés pour construire le prototype d'une échelle de 1000 transistorisée. Un bon fonctionnement a été observé jusqu'à des fréquences dépassant 250 kHz à l'entrée du 1er étage. Il convient cependant de remarquer que la radioactivité actuelle des tubes EZ10 peut être considérée comme un obstacle à leur emploi en Physique Nucléaire, dans les applications de comptage à faible bruit de fond[4]). Par ailleurs, la faible luminosité de la décharge rend la lecture de l'affichage délicat.

Les auteurs tiennent à exprimer leur reconnaissance à M. Surdin, Directeur du Département d'Electronique, qui leur a permis de réaliser ce travail et à MM. H. Guillon et V. Goursky pour les utiles discussions qu'ils ont eues avec eux au cours de l'étude. Ils remercient la direction du Commissariat à l'Energie Atomique de les avoir autorisés à publier cet article.

[4]) J. Mey *et al.*, Radioactivité des tubes EZ 10 (rapport interne).

NUCLEAR INSTRUMENTS AND METHODS 6 (1960) 209–212; NORTH-HOLLAND PUBLISHING CO.

A GAS ČERENKOV DETECTOR FOR THE ACCURATE DETERMINATION OF ELECTRON BEAM ENERGY

R. E. JENNINGS and P. I. P. KALMUS

Department of Physics, University College London, England

Received 12 August 1959

Details are given of a variable pressure gas Čerenkov detector which is being used to measure the energy of the electron beam from the U. C. L. 4.5 MeV microtron. Nitrogen which has a Čerenkov threshold at a pressure of about 18 atmospheres for 4.5 MeV electrons is used, but many other gases would also be suitable. The detector is capable of giving an absolute value of the electron energy to a accuracy of about $\pm$ 0.25%.

1. Introduction

It has previously been shown[1]) that the average energy of the electrons in a beam can be determined by finding the threshold for Čerenkov radiation in a gas. The apparatus used was simple, and indicated that the method was very suitable for measuring the energy of the electrons from the University College London 4.5 MeV microtron.

Electron scattering experiments, using this accelerator, are now in progress, and a more refined Čerenkov detector has been incorporated into the experimental apparatus. The present system which is described in this paper, is capable of giving an accurate value for the electron beam energy. The main refinements of the system are as follows:

(1) A high pressure interferometer has been incorporated into the pressure system to enable the refractive index to be determined directly and absolutely. At first sight this might appear to be an unnecessary complication, but accurate values for the refractive indices of gases at high pressures are not readily available. In addition if the refractive index is measured directly an absolute pressure measurement is not required nor need the gas be pure.

(2) An improved mechanical system is used which allows the Čerenkov detector to be pushed in and out of the electron beam without breaking the vacuum.

(3) The electron beam intensity can be accurately monitored during the determination of the Čerenkov threshold. The Faraday chamber used in the scattering experiments is used for this.

(4) Dispersion effects are reduced by inserting a narrow band-width interference filter in front of the photomultiplier.

2. Principle of the Method

The Čerenkov effect has been used for velocity determination on a number of occasions and has been treated comprehensively in review articles and in a book by Jelley[2]). The theory relevant to the determination of the electron energy using beams rather than single particles has been described fully by Bhiday, Jennings and Kalmus[1]).

Briefly the method consists of passing a high energy beam of electrons into a vessel containing gas. The pressure can be varied and the threshold for Čerenkov radiation found. At this point the electron velocity v is equal to c/n, and is thus determined provided the refractive index n of the gas is known.

[1]) M. R. Bhiday, R. E. Jennings and P. I. P. Kalmus, Proc. Phys. Soc. **72** (1958) 973.

[2]) J. V. Jelley, Čerenkov Radiation (Pergamon Press, 1958).

3. Description of the Apparatus

The design of the detector itself is shown in fig. 1. It consists of a small cylindrical steel pressure chamber on the end of a steel tube, arranged in a housing so that it can slide in or out of the electron beam as required. The beam

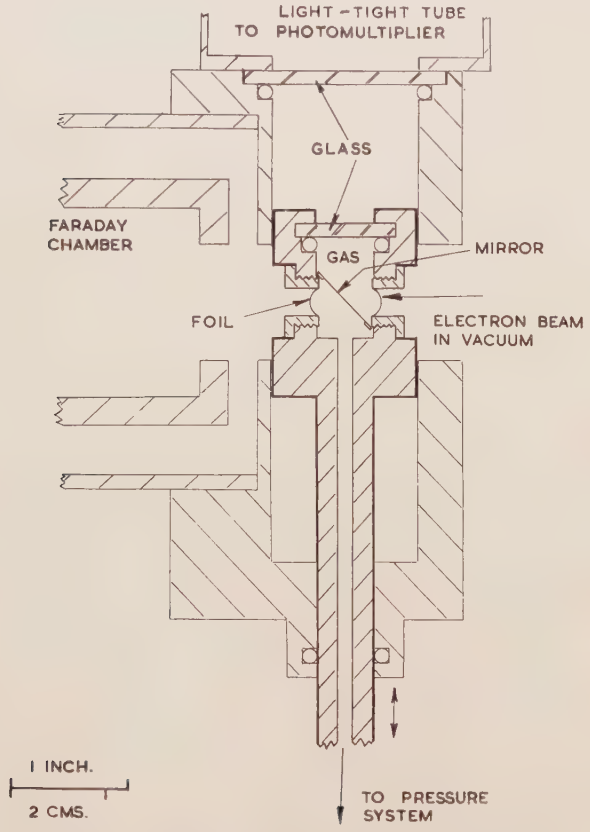

Fig. 1. Simplified diagram of Čerenkov detector.

is passed into and out of the chamber in a direction perpendicular to its axis through $\frac{1}{4}$ inch diameter windows made of "Melinex" foil 0.002 inch thick, this thickness being sufficient to withstand the pressures used (up to 20 atmospheres for nitrogen). The thin windows are glued on to the ends of hollow steel plugs with "Araldite" epoxy resin, the plugs being screwed into place and sealed with rubber gaskets. The "Melinex" is aluminium-coated on the inside to prevent Čerenkov light formed in these foils from entering the chamber. At pressures just above the threshold, the Čerenkov radiation from the gas itself is emitted in a narrow cone in the forward direction and this light is reflected upwards by a plane mirror mounted at 45° to the beam direction. The mirror also consists of a 0.002 inch "Melinex" foil coated with aluminium on its front surface. After reflection the Čerenkov radiation leaves the pressure chamber through a glass window and, after passing through an optical filter, enters a photomultiplier. The filter is an interference type having a bandwidth of about 100 A.U. centred on the wavelength of a mercury spectral line (4358 A.U.).

The pressure vessel itself can slide up or down so as either to intercept the beam or to allow it to pass freely into a Faraday chamber during electron scattering experiments. Even when the beam passes through the pressure vessel a large fraction of the electrons still enter the Faraday chamber enabling the beam current to be monitored while the Čerenkov radiation is measured.

The rest of the pressure system comprises a nitrogen cylinder, an interferometer, a Bourdon pressure gauge and a rotary vacuum pump together with a number of taps which allow fine control of the pressure in the system.

A Jamin interferometer is used to measure the refractive index of the gas. The tubes were formed by accurately drilling two parallel holes about 6 inches long in a block of aluminium alloy, the tubes being closed by $\frac{1}{2}$ inch thick windows of optically flat glass. This robust construction prevents appreciable deformation of the tubes under pressure: no variation in length to an accuracy of 0.001 inch was found for a pressure change of 20 atmospheres down to the vacuum obtainable with a rotary pump.

A mercury lamp is used as a source of light and fringes can be viewed through a telescope. An interference filter similar to the one used in the Čerenkov detector is placed in front of the telescope to select only the fringes formed by the 4358 A.U. line. In order that the fringes can be counted mechanically, a narrow slit was placed in the focal plane of the telescope and the consequent variation in light intensity is observed by means of a photomultiplier which

was substituted for the normal eye piece. This system, in which the passage of a fringe is made to operate a mechanical counter, was kept fairly simple and is efficient provided the fringes are passing at a fairly uniform rate of a few per second. The amplified photomultiplier output is also displayed on a meter and thus the fringes can also be counted by observing the motion of the pointer. This was useful when the fringes were passing very slowly.

Care is taken to allow for any possible differences in temperature between the Čerenkov detector and the interferometer. Before any measurements are begun, gas at a pressure just above the threshold is left in the system for a considerable time so that any difference in temperature would be given by thermometers immediately outside the two parts of the system. While the threshold point is being determined the gas pressure is decreased slowly so that the gas will have time to reach equilibrium with the metal of the chambers. Once this point has been reached the pressure can be decreased more rapidly to zero as any temperature changes during this part of the measurement are immaterial since the number of fringes passing is unaffected.

The energy loss of the electron beam in the Čerenkov vessel causes a slight rise in temperature. However, calculations showed that this is negligible, as gas conduction is sufficient to prevent a temperature rise of more than 0.02° C for an electron current of 10^{-10} amps.

4. Experimental Procedure

The normal procedure followed when making a measurement, is to start at a pressure a little above the expected threshold, and to decrease the pressure in small steps, each step corresponding to the passage of 10 fringes in the interferometer. At each pressure the corresponding Čerenkov signal is noted. Owing to small variations in the electron beam flux it was found to be more reliable to use an integrated value of the Čerenkov signal for a given amount of charge collected in the Faraday chamber, rather than taking spot readings. As a 50 channel pulse height analyser is being used in the main electron scattering experiments, it is convenient to use this as an integrator for the Čerenkov signal. About 15 measurements at intervals of 10 fringes are made, the fringes being counted by observing the meter as already mentioned. The pressure is then reduced effectively to zero and the remaining fringes (approximately 1700) are allowed to pass at a rate of two or three a second and automatically counted, the last few fringes again being watched on the meter to avoid any spurious counts.

5. Results and Errors

A typical set of results is shown in fig. 2 where the Čerenkov signal is plotted against a measure of the refractive index. The treatment of these results has been considered in ref. [1]) where it was shown that the intersection at α occurs at a refractive index corresponding to the threshold for electrons having the mean velocity in the detector. The only corrections required are for energy loss in the "Melinex" window and gas, and when necessary a further correction for temperature differences between the Čerenkov vessel and the interferometer.

Various factors which might affect the accuracy of the determinations will now be considered.

The statistical fluctuations in the number of Čerenkov photons which is a limitation when observing single particles, is negligible here, where a mono-energetic beam of electrons is used (average current 10^8 electrons/second, pulsed at 50 p.p.s., energy spread $\pm$ 4 keV).

Dispersion is also negligible since the filter limits acceptance of photons to a bandwidth of about 100 A.U. (corresponding range in refractive index is about 0.15%).

The lengthening of gas path with pressure due to the bowing of the "Melinex" window was investigated. After being strained at pressure for some time, the "Melinex" aquired a permanent set (nearly hemispherical) and thereafter only bowed by about 0.015 cm for the full pressure change 0 to 20 atmospheres. This corresponds to a negligible path change for the pressure range used near the threshold.

Fluctuations in beam height can however cause much more serious path differences, since the mirror is at 45° to the beam direction. In practice the height of the detector relative to background from the microtron. A graph of integrated photomultiplier signal against time, for the passage of a fixed number of electrons is found to be a straight line. Thus by timing each

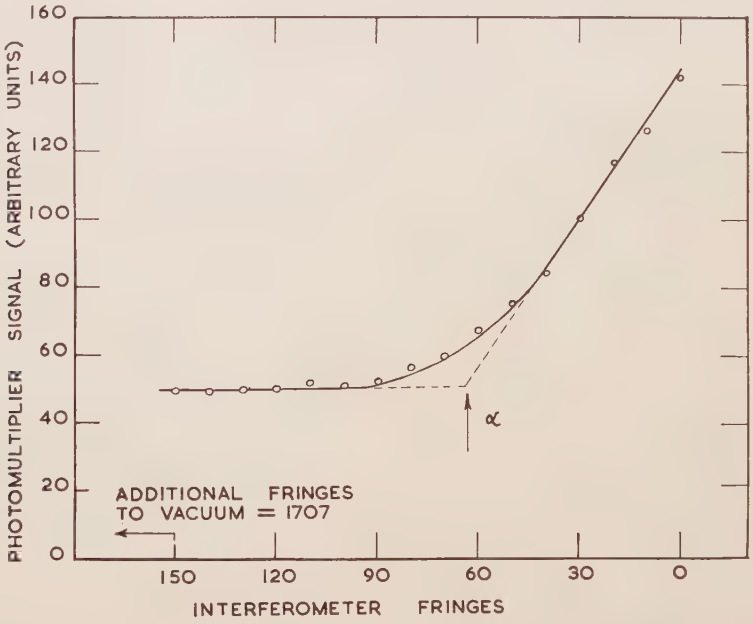

Fig. 2. Typical graph showing variation of photomultiplier signal with refractive index. Changes in refractive index are measured in fringes from an arbitrary pressure above threshold. After taking readings during the first 150 fringes, the remaining number down to zero pressure are automatically counted.

the beam was adjusted until the beam entered the window above the half way region where it was found that the Čerenkov signal was fairly insensitive to detector position (here the path length between the 45° mirror and the bowed out entrance window tends to be constant).

The variation with gas pressure of the fraction of electrons reaching the Faraday chamber was found to be small and in any case the threshold location is not appreciably affected by this.

The limiting factor affecting the accuracy of the experiment is found to be due to fluctuations of the electron beam current. It is found that the integrated background signal (below threshold) from the photomultiplier depends not only on the charge entering the Faraday chamber but also on the time taken for collecting this charge. This is presumably due to the X-ray collection of charge during the threshold determination a correction can be made. When this is applied it is found that results are repeatable to a location of the threshold to better than $\pm$ 10 fringes in about 1800, which corresponds to an absolute accuracy of about $\pm$ 0.25% for the electron energy. The error in calculating the average energy loss of the beam in the detector does not add appreciably to this figure.

Acknowledgements

We would like to thank Mr. R. V. Thornton for constructing most of the apparatus, and Dr. M. R. Bhiday for assistance during the energy determinations. This work forms part of the electron scattering programme which is supported by the Department of Scientific and Industrial Research.

NUCLEAR INSTRUMENTS AND METHODS 6 (1960) 213–216; NORTH-HOLLAND PUBLISHING CO.

ON A DESIGN OF WIDE RANGE MAGNET FOR CYCLOTRON

HIROO KUMAGAI

Institute for Nuclear Study, University of Tokyo, Tanashi-machi, Kitatama-gun, Tokyo

Received 15 August 1959

A design principle of electromagnets is described in which the magnetic induction B in the pole iron is constant. By this design, we can have a constant relative distribution of magnetic field in the gap for a wide range of field. Results of applications in two cases are described.

1. Introduction

In many electromagnets which are used for cyclotron or other apparatus, the relative distribution of magnetic field changes when the magnitude of the field varies for a wide range. Especially, it changes remarkably when the field is larger than about 1.5 Wb/m². These circumstances may be a result of local saturation of iron in the pole and the pole tip. In the followings, a design principle is described by which we avoid the local saturation of iron and can reduce the variation of relative distribution of field.

2. Principle

The principle may be expressed briefly as that we take into account the distribution of magnetic field in the pole iron. In fig. 1, a, d, c and f are points within the iron near the surface. By the integral theorem of the magnetic field, we have

$$\int_{ab}^{c} H_s \, ds = \int_{a}^{d} H_s \, ds + \int_{de}^{f} H_s \, ds + \int_{f}^{c} H_s \, ds .$$

If the integral in the iron from a to d and from f to c are negligible for a wide range of field, we have

$$\int_{ab}^{c} H_s \, ds = \int_{de}^{f} H_s \, ds$$

and, as the result, the relative distribution can be expected to be constant for a wide range of field.

There may be two ways to reduce the integral in iron; the first is to reduce the magnitude of the magnetic field avoiding the saturation of iron and the second to make the magnetic field perpendicular to the integral path. These circumstances may be realized by the B-constant type described in the followings.

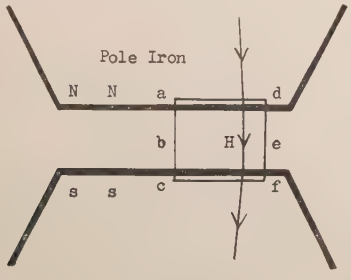

Fig. 1. Integral of field.

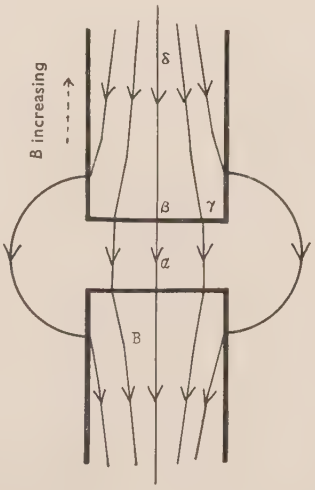

Fig. 2. B-increasing type.

The type of pole of electromagnet may be classified into 3 types shown in fig. 2, 3 and 4. The type shown in fig. 2 is a rather ordinary one, in which magnetic induction B increases at a distant point from the gap, on account of the

leakage flux. We should call this type as B-increasing one. In this case, the magnitudes of B at various points (α, β, γ and δ in the figure) are distributed in the following way $B_\delta > B_\gamma > B_\beta \doteqdot B_\alpha$. The direction of B and H at the surface of the gap is not perpendicular to the

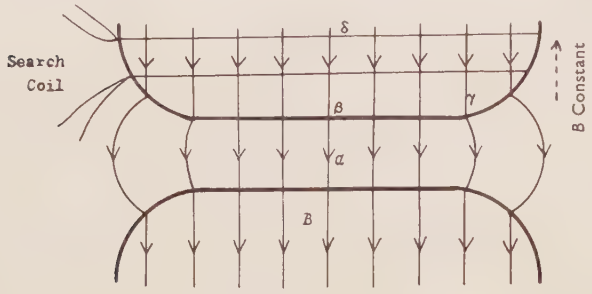

Fig. 3. B-constant type.

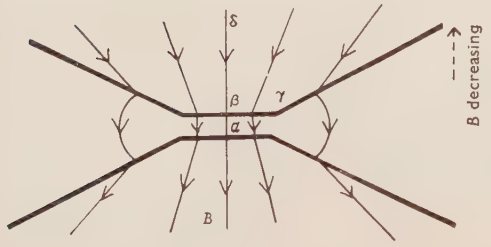

Fig. 4. B-decreasing type.

surface, this fact being checked by our measurements with search coils within the iron.

The type shown in fig. 3 is B-constant type in which the magnetic induction B is constant within the pole iron. In this case, $B_\delta = B_\gamma = B_\beta \doteqdot B_\alpha$ and then we can avoid local saturation. The direction of B is perpendicular to the surface of the gap. The type shown in fig. 4 is a B-decreasing one, in which $B_\delta < B_\gamma < B_\beta \doteqdot B_\alpha$.

3. Check of B-constant Design

The check of B-constant design is performed in a simple way. Search coils are wound at various parts of the pole as shown in fig. 3. Total flux Φ passing through the coils is measured by switching off or reversing the current of the magnet. When the cross section of the pole at the search coil is S, and if $B = \Phi/S$ is constant at various points of the pole, it is certain that B in the pole is constant. Such a measurement of B in the pole iron has been performed by Villard in 1924[1]). We have made such measurements on 2 or 3 magnets and the profiles of magnets for cyclotrons were determined by these experiences.

4. Examples of Application

The principle has been applied to two cyclotrons, the 16″ variable energy cyclotron[2]) at the Institute of Solid State Physics, Univ. of Tokyo and the 63″ variable energy cyclotron[3]) at the Institute for Nuclear Study, University of Tokyo. The 63″ cyclotron latter mentioned is also used as a synchrocyclotron.

In both cases, the design principle of B-

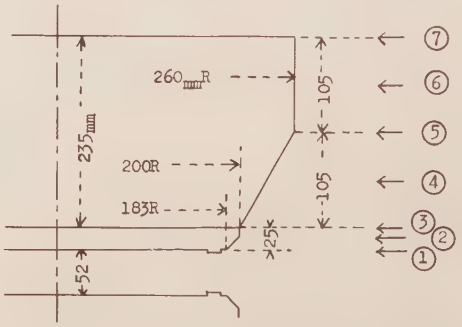

Fig. 5. Pole profile of 16″ cyclotron magnet and positions of search coils.

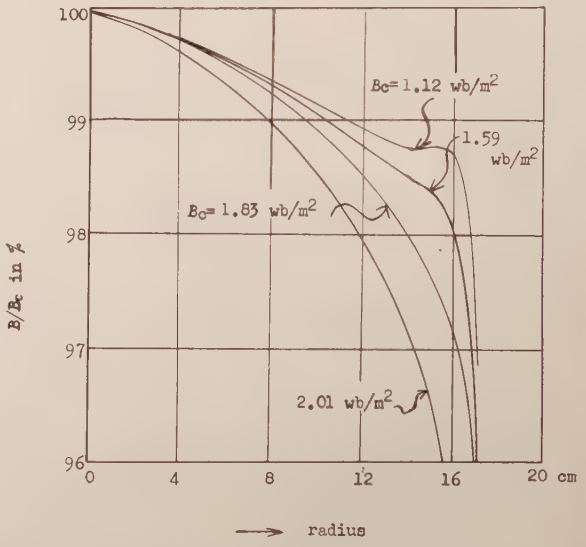

Fig. 6. Relative radial distribution of field in 16″ cyclotron magnet. B_c is the field at the centre.

[1]) P. Villard, Comptes Rendus **179** (1924) 1365.
[2]) H. Kumagai and others, J. Phys. Soc. Jap. **14** (1959) 1.
[3]) Will be published soon in J. Phys. Soc. Jap.

constant has been very successful for varying the energy of accelerated particles, as the field is varied by changing only the magnet current and the field can be used for cyclotron accel-

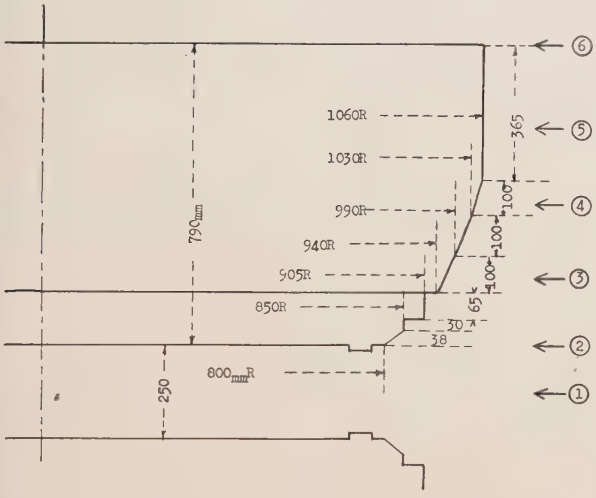

Fig. 7. Pole profile of 63″ cyclotron magnet and positions of search coils.

eration without any change of so called shim.

The pole shape in the 16″ cyclotron is shown in fig. 5, and the ratios of Φ, S and $B = \Phi/S$ at points in the figure are shown in table 1. Fig. 6 shows the obtained relative field distribution where B_c is the field at the centre. The small hump of field near the edge at a low field is due to the too thick Rose shim. In this case the thickness of the real shim has been doubled as that required by Rose's paper[4]), and just the same quantity required by Rose's paper may have been adequate.

The corresponding data of the 63″ cyclotron are shown in fig. 7, table 2 and fig. 8.

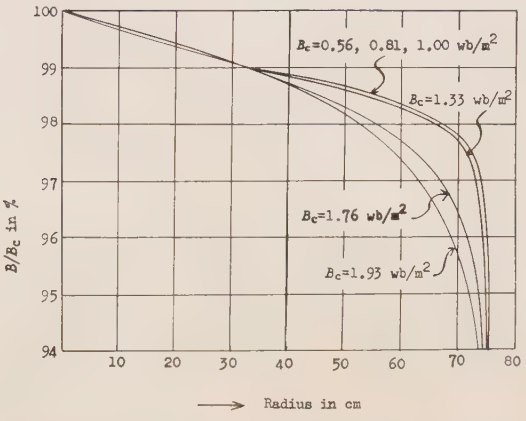

Fig. 8. Relative radial distribution of field in 63″ cyclotron magnet. B_c is the field at the centre.

The vertical lines of profile of the magnet pole in both cyclotrons are for vacuum connection with the accelerating chamber. The real surfaces of the magnet gap are not plane in both cases and they are of slightly cone type to give adequate inclination of magnetic field as shown in figs. 6 and 8.

[4]) M. H. Rose, Phys. Rev. **53** (1938) 715.

Table 1

Check of B-constant profile in 16″ cyclotron magnet

Position of search coil (fig. 5)	1	2	3	4	5	6	7
Ratio of total flux Φ	1.00	1.21	1.26	1.58	1.83	1.93	1.92
Ratio of cross section S	1.00	1.16	1.20	1.58	2.02	2.02	2.02
Ratio of $B = \Phi/S$	1.00	1.04	1.05	1.00	0.91	0.95	0.95

Table 2

Check of B-constant profile in 63″ cyclotron magnet

Position of search coil (fig. 7)	1	2	3	4	5	6
Ratio of total flux Φ	1.00	1.02	1.43	1.73	1.88	1.88
Ratio of cross section S	1.00	1.00	1.44	1.69	1.76	1.76
Ratio of $B = \Phi/S$	1.00	1.02	1.00	1.02	1.07	1.07

5. Some Calculations on the Profile of *B*-constant Pole

We have calculated the profile of B-constant pole by following simplified assumptions. (1) We treat the problem as two dimensional and select the coordinate as shown in fig. 9, where the x-axis is the centre of the gap and z-axis is at the end of the parallel surface of the gap. (2) Let a be a point on the surface of the pole and b the intersection of line of induction and x-axis, then

$$\int_a^b B_s \, ds$$

is constant independent of the position of a. We introduce this condition simply as magnitudeof B at the surface multiplied by the coordinate z of the surface is constant. (3) We regard the magnetic permeability of iron to be sufficiently large.

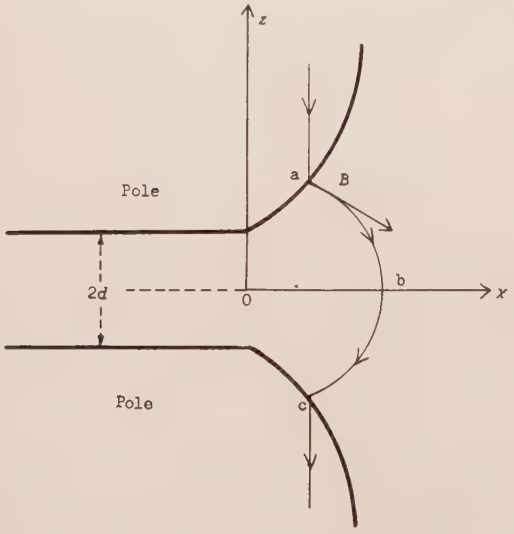

Fig. 9. Calculation of B-constant profile.

By these assumptions, we can easily calculate the profile and obtain

$$\frac{x}{d} = \ln\left[\frac{z}{d} + \sqrt{\left(\frac{z}{d}\right)^2 - 1}\right] \qquad (1)$$

where $2d$ is the gap length.

The calculated curve and the real profile in 63″ cyclotron are compared in fig. 10[5]). As the real profile must be considered to be an approx-

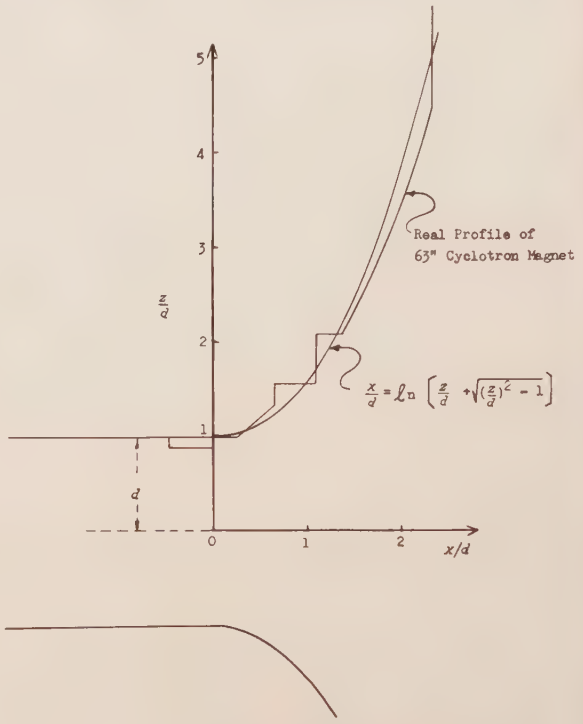

Fig. 10. Comparison of calculation and real profile.

imation by group of straight lines, the two curves are fitted by the general trend but not by the end of the parallel plane. As the agreement is rather good inspite of rough assumptions, eq. (1) may be used so as to give an approximation of B-constant profile.

I wish to express my gratitudes to the staff of 16″ cyclotron in the Institute for Solid State Physics and 63″ cyclotron in the Institue for Nuclear Study for their works in design and measurements of the properties of magnets.

[5]) INSJ-2. H. Kumagai and others, Reports on the Wide Range Magnet for 160 cm synchrocyclotron.

NUCLEAR INSTRUMENTS AND METHODS 6 (1960) 217; NORTH-HOLLAND PUBLISHING CO.

LETTERS TO THE EDITOR

NACHTRAG ZU UNSEREM BEITRAG: ZUR HERSTELLUNG SEHR DÜNNER ELEKTRISCH LEITENDER PRÄPARAT-UNTERLAGEN FÜR ABSOLUTE β-ZÄHLUNG

(Nuclear Instruments 3 (1958) 213–217)

E. HUSTER und W. RAUSCH

Institut für Kernphysik, Universität Münster

und

Physikalisches Institut, Universität Marburg

In the paper mentioned above we had described a method of preparing very thin and electrically well conducting formvar foils used as backings of large sources for absolute low-level β-counting. In the meantime it has been found that this method does not work unless there is some mercury vapour in the chamber used to evaporate silver on the foil.

In dem oben genannten Beitrag hatten wir über ein Verfahren zur Herstellung sehr dünner, elektrisch leitender Präparatunterlagen berichtet.

Die von uns untersuchten, auf "bekernte" Formvar-Folien aufgedampften Ag-Schichten waren in einer Aufdampfanlage hergestellt worden, welche durch eine Hg-Diffusionspumpe evakuiert wurde und bei der eine mit flüssiger beschickte Kühlfalle vom Deckel des Verdampfungsgefässes durch dieses hindurch in den Ansaugstutzen der Hg-Diffusionspumpe hineinragte.

Seitdem haben wir in gleicher Weise Ag-Schichten in einer Aufdampfanlage hergestellt, welche durch eine Öldiffusionspumpe evakuiert wurde.

Diese Schichten wiesen jedoch eine sehr viel geringere elektrische Leitäfhigkeit auf als die Schichten, welche in der Anlage mit Hg-Diffusionspumpe hergestellt waren. Der Einbau einer mit flüssigen Luft beschickten Kühlfalle brachte keine Verbesserung. Erst als zusätzlich zu der Kühlfalle noch ein Tropfen Quecksilber in das Verdampfungsgefäss gebracht wurde, konnten wieder die Werte für die Leitfähigkeit der Ag-Schichten erzielt werden, wie wir sie in der Anlage mit Hg-Diffusionspumpe erhalten und in dem obengenannten Artikel angegeben haben.

Wir halten es für erforderlich, hierauf hinzuweisen, da offenbar ein gewisser Hg-Restdampfdruck für die Bildung der gut leitenden Ag-Schichten von Bedeutung ist.

Zur Zeit können wir noch keinerlei Aussagen darüber machen, welche Rolle der Hg-Dampf bei der Bildung der Ag-Aufdampfschichten spielt.

NUCLEAR INSTRUMENTS AND METHODS 6 (1960) 218–219; NORTH-HOLLAND PUBLISHING CO.

ALUMINIUM OXIDE FILMS FOR NUCLEAR SPECTROSCOPY

K. SEVIER Jr. and W. PARKER

Institute of Physics, University of Uppsala, Uppsala, Sweden

Received 15 November 1959

It has been pointed out[1]) that aluminium oxide films have a quite uniform thickness and are chemically and thermally more resistant than organic films. Because of the effective low Z-value, these films are very useful as source backings in nuclear spectroscopy. In addition, because of their excellent properties, they are of interest for a variety of applications. For these reasons an attempt has been made to overcome certain difficulties often encountered in the conventional preparation of these films.

The most convenient and common procedure of preparation of thin aluminium oxide films is that of anodization of a piece of aluminium metal. The aluminium metal to be anodized can be in one of several forms, i.e., aluminiumized mirror[2,3]), mechanically shaped[4]), and aluminium foil[5]). The anodization takes place on both sides of the foil. After the anodization the oxide film is first removed from one side by the application of a strong solution of NaOH. When all of the oxide film on that side has been dissolved away, a clean aluminium metal surface remains. A solution of HCl is then applied to dissolve the aluminium metal. The oxide film on the other side, being inert to acid, is all that remains.

The complications that may set in are as follows:

1. During the anodization there is great suceptibility to sparking of the foil at the intersection of the foil and the surface of the anodizing solution depending on the purity of the materials used.

2. When one side of the anodized foil is treated with NaOH, care must be taken that the base is not washed away too soon which would result in the remaining of a very thin layer of oxide film. When the metal is dissolved away, the bubbles of hydrogen may become trapped between the remaining two layers of

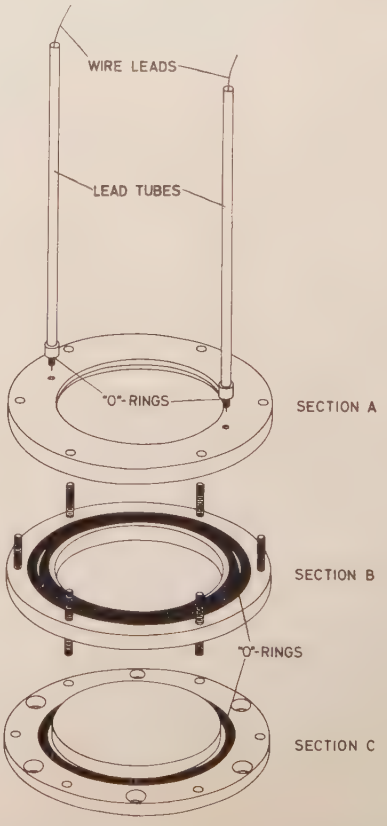

Fig. 1. Diagram of aluminium oxide film preparation device.

[1]) K. Strohmaier, Z. Naturf. 6a (1951) 508.

[2]) L. Holland, Vacuum Deposition of Thin Films (Chapman and Hall, London, 1956).

[3]) G. Hass, Vacuum **11**, No. 4 (1952) 331.

[4]) U. Hauser and W. Kerler, Rev. Sci. Instr. **29**, No. 5 (1958) 380.

[5]) L. Harris, J. Opt. Soc. Amer. **45**, No. 1 (1955) 27.

oxide film and cause fracturing of the thicker film. Also, if any NaOH comes into contact with the film being prepared either by direct contact or by the NaOH dissolving through the metal, partial dissolution of the film will result. These complications have been overcome by the authors by dispending with both the intersection of the metal and surface of the solution and the NaOH treatment. This is done by using a device which allows only one side of the metal foil to be anodized. A diagram of this device is shown in fig. 1 and the procedure of film preparation is as follows: The piece of aluminium foil to be anodized is in the form of a circle of a diameter such that the circumference will lie between the two "○"-rings of section B in the diagram (100 mm for our use). This foil is put in place between sections A and B, and the device is put together with bolts in the order A, B, C. The lucite lead tubes are screwed into place giving water tightness to the annular ring-shaped space between the two "○"-rings of section B where the edge of the foil is situated, and the wire in each is in contact with this edge. The aluminium face is now ready for anodization in the usual manner. After the desired thickness of oxide film is obtained, section C may be removed, inverted, and fastened to section A after the lucite lead tubes have been removed. The nuts already protruding from section A are housed in holes drilled for this purpose in section C and the fastening is done with extra nuts. It should be noticed that section C is so constructed as to lend support to the oxide film. HCl can now be placed on the exposed layer of aluminium. After the metal is dissolved, the film may be mounted by pressing an adhesive covered mounting ring onto the film. Alternatively, the whole circle of anodized aluminium may be removed from the device, cut into suitably sized pieces, and each treated and mounted individually. Caution should be taken to insure purity conditions and distilled water should be used for rinsing after each step of the process. The complete device is made from lucite except for the "○"-rings and bolts.

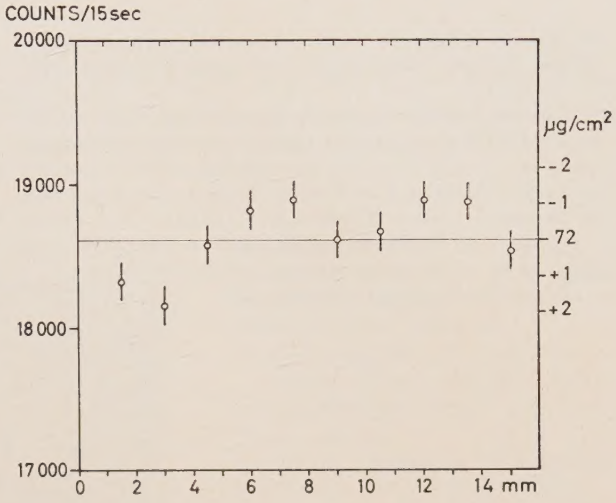

Fig. 2. Thickness distribution of an aluminium oxide film.

Aluminium oxide films are much more fragile when wet than when dry. They are electrically non-conducting and have been found to withstand temperatures in the region 1500°–2000° C. The films have also found use as windows for Geiger counters. The thickness distribution of aluminium oxide films, found by the use of the method of alpha-absorption†, is very uniform as is shown by the sample in fig. 2. When used as a source backing, a thin metal substrate of aluminium has been evaporated on the film to prevent charging of the source. This substrate greatly increased the strength of the film so that its endurance becomes comparable with that of a film of the same thickness of zapon.

† To be published.

ERRATUM

R. Meunier et J. Teiger: Circuit de coïncidence rapide à trois diodes (Nuclear Instruments, Vol. **5**, No. 3 (1959) p. 148).

Dans le schéma du circuit de coïncidence il y a une erreur. En effet, sur les deux triodes extrêmes, nous devons sortir sur les anodes au lieu des cathodes, avant d'attaquer le circuit d'addition à résistances. Nous devons donc avoir un circuit CR où $C = 5$ kpF et $R = 150$ kΩ.

Quant à la triode du milieu, nous sortons, avec une capacité de 5 kpF, sur la cathode, au lieu de l'anode.

Le schéma du circuit est le suivant:

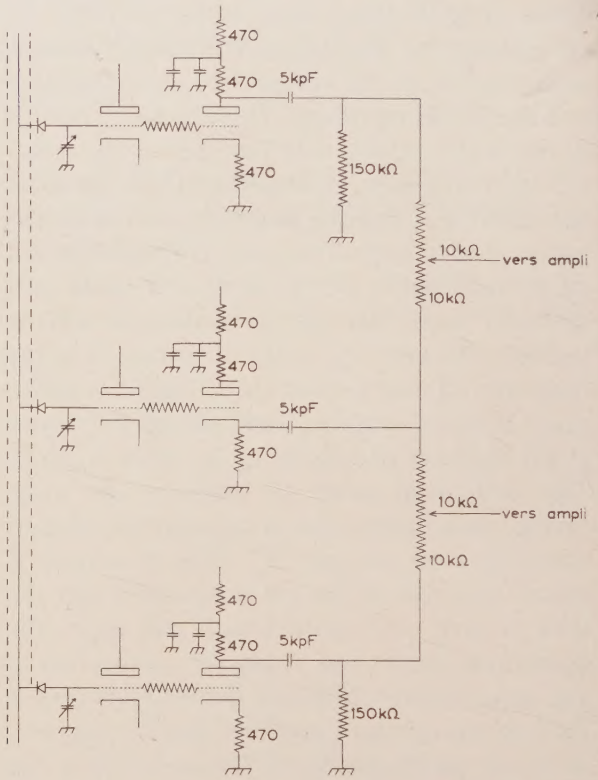

NEWS ITEM

FOIRE INTERNATIONALE DE LIEGE (BELGIQUE)

JOURNEE INTERNATIONALE D'INFORMATION SUR L'ENERGIE NUCLEAIRE

P. FOURMARIER

A.I.M. Association des Ingénieurs Electriciens, 31, Rue Saint-Gilles, Liège (Belgique)

(9 juin 1960)

Cette journée comportera une série de conférences qui seront consacrées aux thèmes suivants relatifs au développement de l'énergie nucléaire au cours des dernières années:

1. Réacteurs de puissance actuellement en service ou en construction et conceptions d'avant garde.

2. Incidence de l'énergie nucléaire sur le développement industriel, notamment par le développement de fabrications existantes ou la création d'industries nouvelles (métallurgie, etc.).

3. Etat actuel des connaissances en fusion nucléaire.

4. Coordination des programmes de recherche dans les divers pays de la Communauté de l'Euratom.

Des détails relatifs à l'organisation de cette journée ainsi que les noms des conférenciers, vous seront communiqués ultérieurement.

Spotlight on Industry

This section appears each month and features various happenings of interest in the nuclear industrial world and objective information on products of the nuclear manufacturers. It is offered entirely as a service and all nuclear manufacturers are cordially invited to submit clearly objective and descriptive material on their endeavours and product developments for consideration for use in this section.

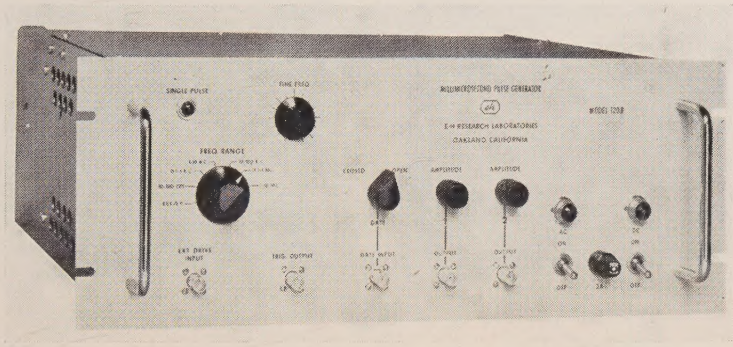

MILLIMICROSECOND PULSE GENERATOR, MODEL 120B

E-H Research Laboratories, Inc., 1922 Park Boulevard, Oakland 6, California

A new Millimicrosecond Pulse Generator, Model 120B is offered, featuring a rise time of less than 2.5 millimicroseconds. Two independent outputs are available providing precision pulse widths from 2.5 to 25 millimicroseconds, and repetition rates from 10 cps to 10 Mc/s which may be controlled externally. A fast flexible gating input is avialable for complex pulse-time and pulse-amplitude selection. A positive 15 volt trigger output may be used to initiate timing cycles or trigger an oscilloscope.

---

330 MW CLOSED CYCLE PLANT

Westinghouse Electric International Company, Wall Street, New York

Power Ratings

Gross Electric Generator Output, 360 MW. Plant Net Electrical Output, 330 MW. Steam Conditions at Turbine Throttle, 650 psia, Dry and Saturated.

Primary System

Number of Heat Transfer Loops, 5. Normal Operating Pressure, Primary Design, 2150 psia. Total Reactor Flow, 75×10^6 lb/hr.

Reactor Vessel

Material, Carbon Steel with Stainless Steel Clad. Design Pressure, 2500 psia. Design Temperature, 650° F. Over-all Length of Assembled Vessel and Closure Head, 41 ft. Inside Diameter of Vessel Shell, 142 in. Thickness of Vessel Shell (excluding cladding), 10″ approx. Nominal Clad Thickness, $\frac{1}{4}$ in. Weight of Vessel, 300 tons.

Steam Generators

Number of Units, 5. Type, Vertical U-Tube with Integral Steam Drum. Design Pressure, Tube Side, 2500 psia. Tube Material, Stainless Steel. Over-all Length, 45 ft. Shell Outside Diameter, 114 in. Shell Material, Carbon Steel. Weight, 300 000 lbs.

Main Coolant Pumps

Number of Units, 5. Type, Vertical, Single Stage Radial Flow with Bottom Suction and Horizontal Discharge. Design Capacity, 40 500 gpm. Design Pressure, 2500 psia.

Main Coolant Loops

Number of Loops, 5. Main Piping and Fittings Material, Stainless Steel. Design Pressure, 2500 psia.

Thermal and Hydraulic Design of Core

Coolant Flow, 75×10^6 lbs/hr. System Pressure, Design, 2500 psia.

Nuclear Design

Loading Technique, 3 region–3 cycle.

Initial U-235 Enrichment, w/o

Outer Region, 2.9 approx. Middle Region, 2.6 approx. Inner Region, 2.1 approx.

Turbine Generator

Rated Capacity, 330 MW. Type, Tandem Compound Quadruple Flow. Speed, 1800 rpm. Stages Steam Separation, 1.

---

22 MW INTEGRAL BOILING SUPERHEAT REACTOR

Westinghouse Electric International Company, 40 Wall Street, New York

Power Rating

Net, Electrical, 20.0 MW.

Fuel Assembly

Type, Road Bundles. Fuel Material, UO_2 Pellets.

Core Design

Number of Pressure Tubes, Total, 80 approx. Number of Tubes in Superheat Region, 24 approx. Number of Tubes in Boiling Region, 56 approx. Pressure Tube Design Condition, 1100 psig. (Superheat Region) 1000°F. Pressure Tube Desing Condition, 1200 psig. (Boiling Region), 650°F.

Reactor Tank

Design Condition, 100 psig 650°F. Material, Carbon Steel. Outside Diameter, 12.5 ft. Wall Thickness, $\frac{1}{2}$ in.

Steam Conditions
Throttle Temperature, 900° F. Throttle Pressure, 865 psia.

Graphite Core
Cylinder Height, 14 ft. approx. Cylinder Diameter, 11 ft. approx.

Steam Drum
Design Condition, 1200 psig 600° F. Outside Diameter, 4 ft. Length, 11 ft. Number required, 2.

Circulating Pump
Number Required, 2. Capacity, 2570 gpm.

Helium Circulator
Number Required, 1. Inlet Temperature, 740° F. Capacity, 14 300 lbs/hr.

---

225 MW GROSS COMBINATION NUCLEAR POWER PLANT

Westinghouse Electric International Company, 40 Wall Street, New York

Power Rating
Net, Electrical, 215 MW. Reactor Contribution, 60%. Superheater Contribution, 40%.

Fuel Assembly
Type, Rod Bundles. Fuel Material, UO_2. Clad Material, Zr-2 or Stainless Steel. Fuel, Pellets.

Thermal and Hydraulic
Operating Temperature, Dry and Saturated. Reactor Operating Pressure 2100 psi.

Reactor Vessel
Material, Carbon Steel with Stainless Steel Clad. Design Pressure, 2500 psia. Inside Diameter, 9 ft. 3 in. Over-all Length, 34 ft. approx.

Steam Separators
Number, 2. Design Pressure, 2500 psia. Inside Diameter, 78 in. Over-all Length, 21 ft.

Recirculating Pumps
Number, 4. Design Pressure, 2500 psia. Flow, gpm each, 12 500.

Superheater and Reheater Unit
Type, Pressurized Furnace. Over-all Dimensions, 146′ × 76′ × 65′.

Turbine Generator
Operating Pressure, 1800 psig. Operating Temperature, 1000° F/1000° F. Type, Tandem Compound Triple Flow.

VIBRATION MONITOR

Kahn and Company, Inc., 541 Windsor Street, Hartford, Connecticut

This Vibration Monitor, Model KC-524 provides a means of sensing vibration levels in machinery and motors. If excessive vibration occurs, the affected unit is automatically shut down or an alarm can be sounded. This Vibration Monitor is made up of two units—a scanning unit, which is used with vibration pick-ups and an electronic trigger unit. Power requirement is 115 volts, 60 cycles AC.

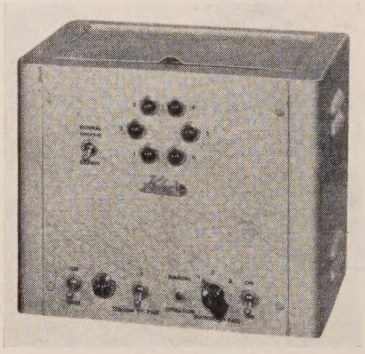

Scanning unit.

The scanning unit (which measures 8″ × 10″ × 8″ and weighs 10 lbs) can be used with up to 10 vibration pick-ups. Each station is monitored in sequence for a preset time interval. The scanning unit is provided with either station indicator lights or an indicator tube which remains energized after a shutdown or alarm, thus pinpointing the location of the excessive vibration.

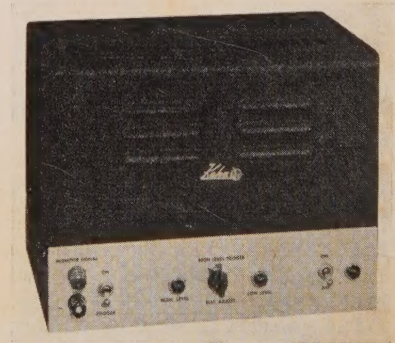

Monitor unit

The trigger unit (which measures 9″ × 12″ × 10″ and weighs 21 lbs) amplifies the vibration signals and feeds them to a trigger circuit and a fail-safe circuit. A shut-down or alarm relay is energized when a preset vibration level is reached at any station. An electronic or pickup failure also causes a shutdown or alarm relay to activate.

ANALOGUE TUTOR

Solartron Electronic Group Ltd., Surrey, England

This new addition is in fact a simplified analogue computer intended for educational applications. It is

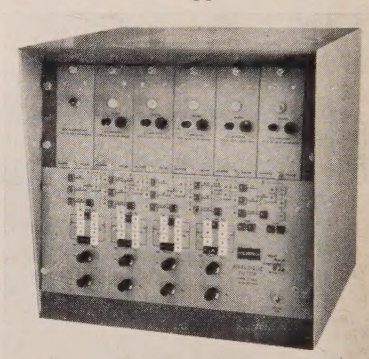

capable of representing any form of the linear second-order differential equation using the built-in computing components and demonstrating, for example, the effects of velocity and acceleration limits using external diodes as additional computing impedances. Within the limitations imposed by the total complement of five amplifiers, a wide range of physical systems may be represented. These include simple servos, electrical networks, the motion of a particle under gravity, and so on.

The Solartron Analogue Tutor is virtually "Student Proof" in that the unit will suffer no permanent damage should incorrect operation be programmed by unskilled users.

Incorporating five Operational DC Amplifiers, the Analogue Tutor is a fully self-contained unit, complete with stabilised power supplies and adequate patching and control facilities. Interchangeability of component assemblies—a feature of all Solartron "SPACE" Series Analogue Computers—permits elements from the Analogue Tutor to be incorporated into more complex analogue computer installations at any time should this be required.